





Universitat Autònoma de Barcelona

ADVERTIMENT. L'accés als continguts d'aquesta tesi queda condicionat a l'acceptació de les condicions d'ús establertes per la següent llicència Creative Commons:  http://cat.creativecommons.org/?page_id=184

ADVERTENCIA. El acceso a los contenidos de esta tesis queda condicionado a la aceptación de las condiciones de uso establecidas por la siguiente licencia Creative Commons:  <http://es.creativecommons.org/blog/licencias/>

WARNING. The access to the contents of this doctoral thesis it is limited to the acceptance of the use conditions set by the following Creative Commons license:  <https://creativecommons.org/licenses/?lang=en>

The background of the cover is a photograph of a large geothermal drilling rig. The rig is a tall, complex structure with a central vertical shaft, surrounded by various mechanical components, cables, and platforms. It is situated outdoors on a flat, paved area. The sky is a clear, pale blue. The overall scene is industrial and technical.

Evaluation of reservoir potential and induced seismicity of deep geothermal systems

Guillem Piris Casanovas

Tesi Doctoral

2022

UAB

**Universitat Autònoma
de Barcelona**

Facultat de Ciències

Departament de Geologia



**Universitat Autònoma
de Barcelona**

Facultat de Ciències
Departament de Geologia

Evaluation of reservoir potential and induced seismicity of deep geothermal systems

Memòria presentada per Guillem Piris Casasnovas per l'obtenció del títol de
Doctor en Geologia

Abril de 2022

Tesi doctoral dirigida per:

Dr. Albert Griera Artigas, Departament de Geologia, Universitat Autònoma de Barcelona

Dr. Enrique Gómez Rivas, Departament de Mineralogia, Petrologia i Geologia Aplicada,
Universitat de Barcelona

Tutors industrials:

Dr. Joan Palau Ramírez, Àrea d'Enginyeria i Recursos Geològics de l'Institut Cartogràfic i
Geològic de Catalunya

Sr. Ignasi Herms Canellas, Àrea de Recursos Geològics de l'Institut Cartogràfic i Geològic de
Catalunya

Dr. Albert Griera Artigas

Dr. Enrique Gómez Rivas

Dr. Joan Palau Ramírez

Sr. Ignasi Herms Canellas

Guillem Piris Casasnovas

Cover image: Blanc-Mesnil Geothermal district heating, Paris basin (photo: Institut Cartogràfic i Geològic de Catalunya, Jan. 2016)

This research was supported by a PhD grant of the Industrial Doctorate programme sponsored by the AGAUR (Agència de Gestió d'Ajuts Universitaris i de Recerca) of the Government of Catalonia (reference number 2016-DI-031), and funded and maintained by the Institut Cartogràfic i Geològic de Catalunya (ICGC).

A la meva família i a tots els professors i professores que m'han dut fins aquí

*Sèi un país e ua flor
E ua flor, e ua flo)
Que l'aperam la de l'amor
La de l'amor, la de l'amor*

*Haut Peiròt, vam caminar, vam caminar
De cap tà l'immortèla
Haut Peiròt, vam caminar, vam caminar
Lo país vam cercar*

*Au som deu malh, que ia ua lutz
Que ia ua lutz, que ia ua lutz
Qu'l cau gurardar los uelhs dessus
Los uelhs dessus, los uelhs dessus*

*Que'ns cau traucar tot lo segàs
Tot lo segàs, tot lo segàs
Tà ns'arrapar, sonque las mans
Sonque las mans, sonque las mans*

*Lhèu veiram pas jamei la fin
Jamei la fin, jamei la fin
La libertat qu'ei lo camin
Qu'ei lo camin, qu'ei lo camin*

*Après lo malh, un aute malh
Un aute malh, un aute malh
Après la lutz, ua auta lutz
Ua auta lutz, ua auta lutz*

*Haut Peiròt, vam caminar, vam caminar
De cap tà l'immortèla
Haut Peiròt, vam caminar, vam caminar
Lo país vam cercar*

Nadau, De cap tà l'immortèla

Índex

ABSTRACT	5
RESUM	6
RESUMEN	7
1 Introduction	10
1.1 Phases in deep geothermal projects.....	12
1.2 Geo-thermo-hydro-mechanical and induced seismicity processes in EGS and their modelling.....	15
1.2.1 Modelling approaches	15
1.2.2 Integrating the fracture network.....	16
1.2.3 Stimulating the fracture network.....	17
1.2.3.1. Stimulation typologies.....	17
1.2.3.2. Principal stimulation mechanisms.....	19
1.2.3.3. Parameters in fracture network stimulation.....	23
1.3 Seismic hazard assessment	26
1.4 Geothermal potential assessment	28
1.5 A view on public acceptance and communication	29
1.6 Interest and objectives of the thesis.....	30
1.7 Thesis structure	31
1.8 References.....	33
2 Rate-and-State friction law and slip regimes analysis of a single fluid pressurized fault. Comparison between thermal-hydromechanical continuous (Toughreact-Flac3D) and discontinuous (CFRAC) modelling.....	40
2.1 Introduction	40
2.2 Numerical approaches	42
2.2.1 TOUGHREACT-FLAC3D (TF3D).....	42
2.2.2 CFRAC	43
2.3 Methods	44
2.3.1 Rate-and-state friction law.....	44
2.3.2 Model set-up: rate-and-state benchmark	46
2.3.3 Model set-up TF3D and CFRAC: slip regime analysis.....	46
2.4 Results	49
2.4.1 Benchmark model	49
2.4.2 Slip regimes: TF3D.....	50
2.4.3 Slip regimes: CFRAC	54
2.5 Discussion.....	56

2.5.1 Slip regimes.....	56
2.5.2 Comparison between numerical approaches	62
2.6 Conclusions	63
2.7 References.....	65
2.8 Supplementary materials rate-and-state implementation into TF3D.....	69
3 Fluid pressure drops during stimulation of segmented faults in deep geothermal reservoirs	71
3.1 Introduction	71
3.2 Methods	73
3.3 Model set-up	74
3.4 Results	77
3.4.1 Model “88-60”.....	77
3.4.2 Model “60-88”.....	80
3.4.3 Model “60-hydro”	82
3.4.4 Sensitivity analysis	83
3.5 Discussion.....	85
3.5.1 Pressure drop mechanism	85
3.5.2 Seismicity and pressure drops	87
3.5.3 Rittershoffen sensitivity analysis	89
3.6 Conclusions	91
3.7 References.....	92
4 On the influence of fault geometry in seismic cycle under fluid injection scenarios: a numerical approach	95
4.1 Introduction	95
4.2 Methodology	96
4.3 Model set-up	97
4.4 Results	100
4.4.1 Fluid pressure.....	101
4.4.2 Seismicity	103
4.4.3 Seismic ruptures propagation.....	103
4.5 Discussion.....	106
4.5.1 Pressure front propagation.....	106
4.5.2 Seismic production	109
4.5.3 Seismic front propagation.....	110
4.6 Conclusions	113
4.7 References.....	116
5 3DHIP-Calculator - A new tool to stochastically assess deep geothermal potential using the Heat-In-Place method based on 3D geological models	120

5.1 Introduction	120
5.2 Materials and methods.....	122
5.2.1 Mathematical background of the HIP method	122
5.2.2 Mathematical background of the Monte Carlo method.....	123
5.2.3 Program description	124
5.2.3.1. Pre-processing: Input data.....	125
5.2.3.2. Post-processing: Output data	126
5.2.3.3. Modelling scenarios depending on data availability.....	127
5.3 Example case study—The Reus-Valls Basin (NE, Spain)	128
5.3.1 Geological setting.....	128
5.3.2 The potential hot deep sedimentary aquifers	129
5.3.2.1. Example 1: Using a single-voxel 1D geological model	131
5.3.2.2. Example 2: Using a 3DGM but not a 3DTM.....	132
5.3.2.3. Example 3: Using both a 3DGM and a 3DTM.....	135
5.3.2.4. Example 4: The use of the Recoverable Heat (Hrec) values.....	138
5.4 Discussion and conclusions.....	139
5.5 References.....	142
6 Discussion and Conclusions	149
7 Acknowledgments / Agraïments.....	154

Abstract / Resum / Resumen

ABSTRACT

The effects of the climate change have boosted the transition to and the search for new renewable energy resources in recent years, such as geothermal energy. The exploration and exploitation of deep geothermal reservoirs has grown significantly around the world. However, many deep medium- and high-temperature geothermal reservoirs are still untapped due to the high costs of their exploration and production, the social impact that projects generate and the induced seismicity they can trigger in cases in which their production requires hydraulic stimulation. In addition, the uncertainties associated with the lack of capacity for the assessment of the resource increase the risks of project failure. For this reason, scientific and technological efforts are focused both on improving the existing knowledge about the processes that give rise to the risks associated with geothermal energy production and on generating predictive models to reduce uncertainty and anticipate and minimize risks. Within this framework, numerical simulations stand out as a key method to model the dynamic behaviour of geothermal reservoirs in order to forecast their behaviour in terms of the production of the resource (energy) and when phases of hydraulic stimulation are required to improve energy extraction. Hydraulic stimulation operations are responsible for producing the so called microseismicity (low-intensity seismicity), which can sometimes trigger earthquakes perceived by the population and that can negatively affect project. For these reasons, one of the main objectives of this PhD thesis is to evaluate by means of numerical simulations the processes that give rise to induced seismicity in a context of injection of fluids in deep geothermal reservoirs. These works are carried out through the numerical simulation codes CFRAC and TOUGHREACT-FLAC3D that allow evaluating the phenomenon from a discontinuous and a continuous point of view, respectively. The study focuses on the analysis of the different sliding regimes and the transitions between seismic and aseismic behaviour and the seismic cycles that are generated from them. This knowledge is used to address the pressure drops observed in the hydraulic stimulation phase of the Rittershoffen reservoir (France), and to analyze the seismic behaviour of geometrically complex faults.

As mentioned above, another key aspect that hampers the development of deep geothermal reservoir exploration is the ability to predict the resources they contain. Thus, in the framework of the thesis, a tool has been developed for the generation of probabilistic maps of the deep geothermal potential using as input data 3D geological and thermal models. The tool, called 3DHIP-Calculator, has the dual aim of generating maps of geothermal potential and of favouring the diffusion of deep geothermal resources to the society.

RESUM

En els darrers anys els efectes del canvi climàtic han potenciat la transició i la cerca de noves fonts d'energia renovables, entre elles la geotèrmia. L'exploració i explotació de reservoris geotèrmics profunds ha crescut de forma significativa al llarg dels darrers anys arreu del món. No obstant, molts reservoris geotèrmics profunds de mitja i alta temperatura encara resten sense aprofitar degut als elevats costos d'exploració i producció, l'impacte social que generen i la sismicitat induïda que poden generar en els casos en què requereixen estimulació hidràulica. A més, les incerteses associades a la manca de capacitat per poder avaluar la capacitat productiva del recurs incrementen els riscos alhora de fer-ne prediccions. Per aquest motiu, els esforços científics i tecnològics es centren alhora en la generació de models predictius per reduir la incertesa i en millorar el coneixement sobre els processos que donen lloc als riscos associats i poder anticipar-se als perills que comporten. Dins d'aquestes eines o models, destaquen les simulacions numèriques com a eina per a modelitzar el comportament dinàmic dels reservoris geotèrmics i poder-ne avaluar, amb antelació, el seu comportament davant l'extracció dels recursos (energia) o davant de fases d'estimulació hidràulica per a millorar-ne les seves capacitats productives. Aquestes fases d'estimulació hidràulica són les responsables de produir el que s'anomena sismicitat de baixa intensitat (i. e. microsismicitat), però que a vegades pot desencadenar en terratrèmols percebuts per la població i que poden afectar de forma capdalt en el desenvolupament dels projectes on succeeixen. Per aquests motius, un dels objectius principals de la tesi es avaluar mitjançant simulacions numèriques els processos que donen lloc a la sismicitat induïda en un context d'injecció de fluids en reservoris geotèrmics profunds. Aquests treballs es duen a terme a través dels codis de simulació numèrica CFRAC i TOUGHFLAC3D que permeten avaluar el fenomen d'es d'un punt de vista de medi discontinu i continu respectivament. Els treballs es centren en l'anàlisi dels diferents règims de lliscament i en les transicions entre comportament sísmic vs. asísmic i els cicles sísmics que se'n generen. Aquests coneixements, s'utilitzen per abordar les caigudes de pressió observades en la fase d'estimulació hidràulica del reservori de Rittershoffen (França) i per analitzar el comportament sísmic de falles amb complexitat geomètrica. També s'aborda la problemàtica de la capacitat d'exploració y predicció dels recursos, un dels aspectes crítics que frena el desenvolupament de l'explotació dels reservoris geotèrmics profunds. Així, s'ha desenvolupat una eina capaç de generar mapes probabilístics dels potencial geotèrmic profund utilitzant com a dades d'entrada models geològics i termals 3D. L'eina, 3DHIP-Calculator té el doble objectiu de generar mapes de potencial geotèrmic i d'afavorir la difusió dels recursos geotèrmics profunds a la societat.

RESUMEN

En los últimos años los efectos del cambio climático han potenciado la transición y búsqueda de nuevas fuentes de energía renovables, entre ellas la geotermia. La exploración y explotación de reservorios geotérmicos profundos ha crecido significativamente en los últimos años. No obstante, muchos reservorios geotérmicos profundos de media y alta temperatura aún no se aprovechan debido a los elevados costes de exploración y producción así como el impacto social que generan como consecuencia de la sismicidad inducida que pueden producir durante la fase de estimulación hidráulica del reservorio. Además, las incertidumbres asociadas a la falta de capacidad para poder evaluar la capacidad productiva del recurso incrementan los riesgos a la hora de hacer predicciones. Por este motivo, los esfuerzos científicos y tecnológicos se centran al mismo tiempo en la generación de modelos predictivos para reducir la incertidumbre y en mejorar el conocimiento sobre los procesos que dan lugar a los riesgos asociados para poder anticiparse a los peligros que comportan. Dentro de estas herramientas o modelos destacan las simulaciones numéricas como una herramienta para modelizar el comportamiento dinámico de los reservorios geotérmicos y poder evaluar, con antelación, su comportamiento durante el proceso de extracción del recurso (energía) o durante las fases de estimulación hidráulica para mejorar su producción. Durante estas fases de estimulación se puede producir una sismicidad de baja intensidad (i.e. microsismicidad), pero que en ocasiones puede desencadenar terremotos percibidos por la población y que pueden afectar negativamente la viabilidad de los proyectos. Por estos motivos, uno de los objetivos principales de esta tesis doctoral es evaluar mediante simulaciones numéricas los procesos que dan lugar a la sismicidad inducida en un contexto de inyección de fluidos en reservorios geotérmicos profundos. Estos trabajos se llevan a cabo mediante los códigos de simulación numérica CFRAC y TOUGHFLAC3D que permiten evaluar el fenómeno desde un punto de vista de medio discontinuo y continuo, respectivamente. Los trabajos se centran en el análisis de los diferentes regímenes de deslizamiento en fracturas y en las transiciones entre comportamientos sísmicos vs. asísmicos y en los ciclos sísmicos que se generan. Estos conocimientos, se utilizan para abordar las caídas de presión observadas en la fase de estimulación hidráulica del reservorio geotérmico de Rittershoffen (Francia) y para analizar el comportamiento sísmico de las fallas con complejidad geométrica. También se aborda la problemática de la capacidad de exploración y predicción de los recursos geotérmicos profundos, que es uno de los aspectos críticos que frena el desarrollo de la explotación de los reservorios geotérmicos profundos. Así, se ha desarrollado una herramienta capaz de generar mapas probabilísticos del potencial geotérmico profundo utilizando como datos de entrada modelos geológicos y termales 3D. La herramienta 3DHIP-Calculator tiene el doble objetivo de generar mapas de potencial geotérmico y de favorecer la difusión de recursos geotérmicos profundos a la sociedad.

Capítol 1

1 Introduction

The traditional system of energy production currently presents some problems and challenges. Two key issues are the constant increase of energy demand and the supply security. For example, the European Union (EU) is nowadays energy-dependent on the rest of the world. The EU, the world's third-largest economy, consumes one fifth of the world's energy but has limited reserves (Eurostat, 2015, 2017). The continuous increase in greenhouse gas emissions associated with energy production has severe environmental and public health consequences. Furthermore, several accidents in nuclear power plants in the past also question the use of this type of energy as a long-term solution for energy generation in high-demand areas. These problems have fostered the research and development of new green energy resources in the EU and other countries, with the combined objective of becoming more energetically independent and, at the same time, producing energy in a sustainable way that affects the environment as less as possible. Among these new energy resources a promising option is geothermal energy. The exploration and exploitation of deep geothermal reservoirs have significantly increased during the last few years around the world, with the aim of exploiting these renewable energy sources (Király et al., 2015, Moeck et al., 2015, Lukawski et al., 2016, Gnatus et al., 2011, among others). However, high- and medium-deep geothermal energy is still underexplored and underexploited due to the exploration and well-drilling costs, and the social impact that induced seismicity and potential environmental issues generate. Additionally, the uncertainties in terms of evaluating and producing the resource (Lukawski et al., 2016, Capuano, 2016) result in a high risk when it comes to forecasting production and risks (Majer et al., 2007). Despite these challenges, the potential of geothermal energy is enormous (Tester et al., 2006) and its contribution to electricity and heat production will likely be strategical for the energy transition.

Reservoirs for the production of high and medium temperature geothermal energy ($> 60^{\circ}\text{C}$) are located in deep aquifers or crystalline basement rocks ($> 1,000$ m deep) and regions with high geothermal gradients. Heat and/or electricity can be produced from these reservoirs by exchanging heat between fluids and their host rocks. Two main types of deep geothermal resources can be distinguished depending on the reservoir hydraulic properties: (i) deep hydrothermal systems (i.e., water-bearing deep geological formations) and (ii) petrothermal systems (those with none or relatively low permeability, mainly in crystalline basement rocks that require a phase of hydraulic stimulation; Gnatus et al., 2010, Tester et al., 2006).

This Ph.D. thesis focuses on the exploitability of petrothermal resources and the assessment of deep geothermal potential in such settings. As mentioned above, petrothermal reservoirs are preferentially located in crystalline rocks, where permeability is typically controlled by the pre-existing fracture network

given that the rock matrix is normally considered impermeable. Although fracture networks provide some permeability, this is most of the times not high enough to guarantee fluid injection and production flow rates to ensure the economic feasibility of the project. In those cases, and to increase the reservoir production, a stimulation phase is needed.

Enhanced Geothermal Systems (EGS), originally called 'hot dry rock' systems, and nowadays also called Engineered Geothermal Systems, are characterized by a phase of hydraulic and/or chemical stimulation that aims to improve the reservoir permeability. This is carried out by stimulating the pre-existing fracture network or by generating new fractures to increase fluid flow and heat transfer between injection and extraction wells. This stimulation phase is characterized by the injection of fluids (normally water) at high pressure, aiming at causing opening and/or sliding of pre-existing fractures, together with the generation of new fractures that increase fracture connectivity. The reservoir permeability is thus increased due to stimulation and the well production rate can rise by an order of magnitude or more (Tester et al., 2006). The hydraulic stimulation phase can be coupled or followed by a chemical stimulation phase (Schill et al., 2017), with the aim of dissolving the host rock or the fracture precipitates and enhance the reservoir porosity and permeability. The simplest configuration of such a stimulated reservoir is based on a doublet system, consisting of a production and an injection well, with the aim of ensuring optimal flow rates with averages ranging between 50 and 100 kg/s. These rates would result in an electric power of 3 – 10 MW (Jung, 2013) or heat rates for heating purposes normally on the order of 5 – 10 kWt.

A serious limitation of the hydraulic stimulation process is that it might result in induced seismicity during the generation of new fractures or the stimulation of pre-existing fractures during the deployment of the reservoir, but also throughout the phases of geothermal exploitation (Majer et al., 2007). When the resulting event magnitude is low this type of seismicity is referred to as microseismicity. Nevertheless, these events can sometimes be felt at the Earth's surface (e.g., Grigoli et al., 2018; Mignan et al., 2015). To mitigate this issue, the monitoring, control, and understanding of the mechanisms responsible for this induced seismicity are key points for the public acceptance and viability of EGS projects (Majer et al., 2007). In the last years, there have been several cases of relatively high-seismicity events (of moderate magnitude) associated with the initial stages of stimulation projects (Dempsey & Suckale, 2015). For example, the Deep Heat Mining project that was initiated in Basel (Switzerland) in 1996 by the Geopower Basel (GPB) consortium, caused a 3.4 magnitude earthquake in 2006, producing slight damage in some buildings, and finally leading to the cancellation of the project (Håring et al., 2008).

The first important aspect for the viability of EGS projects is to be able to carry out an accurate prediction of the induced seismicity phenomena associated with hydraulic stimulation, as well as to foresee the development of strategies for risk mitigation (Bruhn et al., 2015). This requires the development of tools

capable of simulating the different geomechanical processes involved in induced seismicity and quantifying their relative importance in the geothermal system. These include parameters such as pore pressure changes, fracture distribution, initial stress state, thermal effect, and static stress transference (Bruhn et al., 2015; Catalli et al., 2016). Accordingly, this process needs to take into account the thermo-hydro-mechanical behaviour of fractured geological reservoirs. The second important aspect in EGS projects is to develop an exhaustive monitoring process with a complete seismic network (both in-depth and at the surface) to locate, quantify and plot the seismic sources, with the objective of controlling and continuously updating our knowledge of seismic production associated with the stimulation and heat production activity.

Another topic to be considered in this kind of project is its public acceptance, even if the exploitation of geothermal energy can theoretically be considered as a way towards progress and an energetically sustainable society. The development of EGS entails costs and benefits that the society needs to know and understand through all the stages of the project, from the first exploration stages until the end of the reservoir lifetime (Duijn et al., 2013). This public knowledge and acceptance will make the project successful and will allow facing the inconveniences with more transparency and margin of manoeuvre.

1.1 Phases in deep geothermal projects

This chapter starts with an overview of geological uncertainties in deep geothermal energy project development. Projects that are based or interact with geological systems always present a relatively high uncertainty. Uncertainty and risk of failure decrease as the project progresses and when the investment in geological exploration and investigation increases. However, there is always a certain uncertainty (residual risk), with which the project should deal with.

EGS and deep geothermal projects can be divided into different stages or phases. The successful development of each phase allows progressing to the following one. Figure 1 shows the main scenarios of the different phases of a deep geothermal project (“go” or “not go” to the next phase) and the principal activities and objectives for each phase. The phase diagram is based on the one employed for the St. Gallen (Moeck et al., 2015) and Soultz (Dezayes et al., 2005; Schill et al., 2017) projects. If the project is developed in a hydrothermal reservoir, the stimulation phases can be omitted in the diagram of Figure 1.

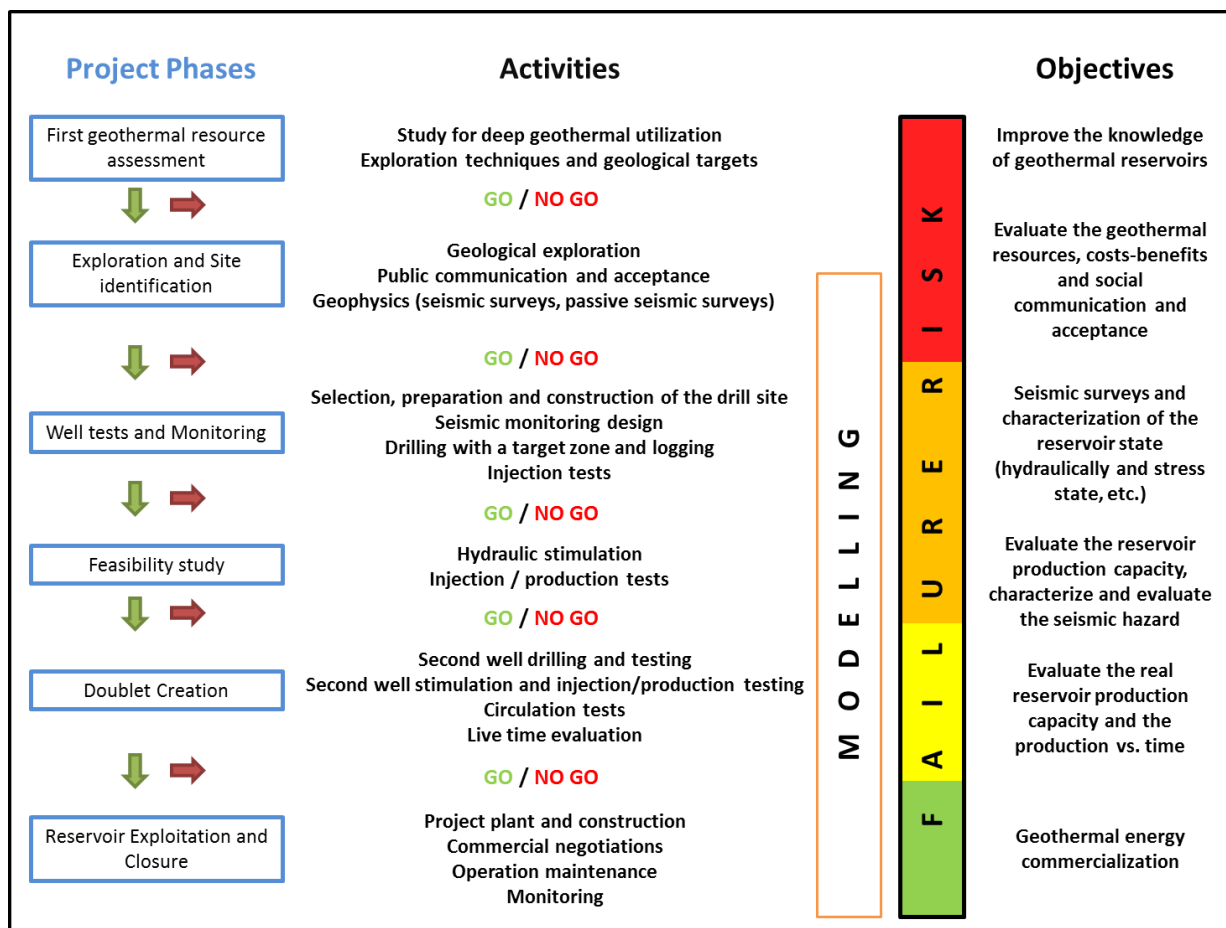


Figure 1. Phase diagram of a deep geothermal project, including the activities and the main objectives for each phase. The colours of the failure risk bar show the quantification of project failure risk for each phase. On a scale from 0 to 3 (where 0 is minimum risk and 3 is maximum risk), 0 is shown in green, 1 in yellow, 2 in orange and 3 in red.

Each phase increases the knowledge of the reservoir properties and geothermal potential assessment in this kind of projects, and also the response of the reservoir in terms of injection, hydraulic stimulation, production, and induced seismicity. The knowledge accumulated in each phase is used to reduce the geological uncertainties for the following phase. As the project progresses, the geological conceptual model of the reservoir gets continuously updated with new and more accurate data. When the first well is drilled in and the first hydraulic tests are carried out, a first numerical model can be built based on the previous geological model and using real data of the specific location. The objective during these initial stages is to predict the reservoir response for the different working conditions that may be encountered by developing numerical simulations. As real data is collected during testing, the models can be continuously calibrated according to the project progress. The modelling process could be divided into three steps: pre-stimulation, stimulation, and monitoring (Rutqvist et al., 2015). In the first step, the model includes all the knowledge acquired before the stimulation and drilling processes and some estimated parameters (e.g. stress state, fluid pressure, material properties, etc.) from the geological exploration, injection tests, literature, and analogous reservoirs.

When real data from the first hydraulic stimulation and injection/production test has already been collected, it can be used to calibrate the model and with this, improve its capacity to predict scenarios, a key point for decision making to define the next development phase. Finally, when the second well is built and the interference test (with the doublet) is done, all this new knowledge is incorporated into the model, and then, long-time reliable simulations can be developed to predict the behaviour of the reservoir with time. Besides, as the reservoir characterization improves, maps of geothermal fluid flow can be built, reducing the risk to locate future wells and increasing their productivity (Siler et al., 2016).

Another topic to be taken into account is the risk of failure of the project, i.e. the likelihood that the feasibility of the project will be disallowed. This risk dependence is based on the activities of each phase. At the end of each phase, the viability of the project is estimated to decide if it is possible to go to the next phase or abandon the project. One of the main issues to be tackled is the induced seismicity produced during the hydraulic stimulation phase (for EGS), together with the capacity of quantifying the energy that can be extracted from the reservoir through time, either for electricity or heat production. For this reason, a *First geothermal resource assessment* phase is one of the most important phases, because it can considerably reduce the potential risks. The following key phase is *Well tests and Monitoring*, where the unknown reservoir properties have to be characterized.

Finally, and not less important, is the public acceptance concept involved in the *Exploration and Site identification* phase. The society and the residents near the geothermal plant should understand, approve and accept the project (with their costs and benefits) that will be built. A poor or directly bad public communication can hinder a promising project.

To better understand the relationships between the risks, cost, and project phases a diagram is displayed in Figure 2.

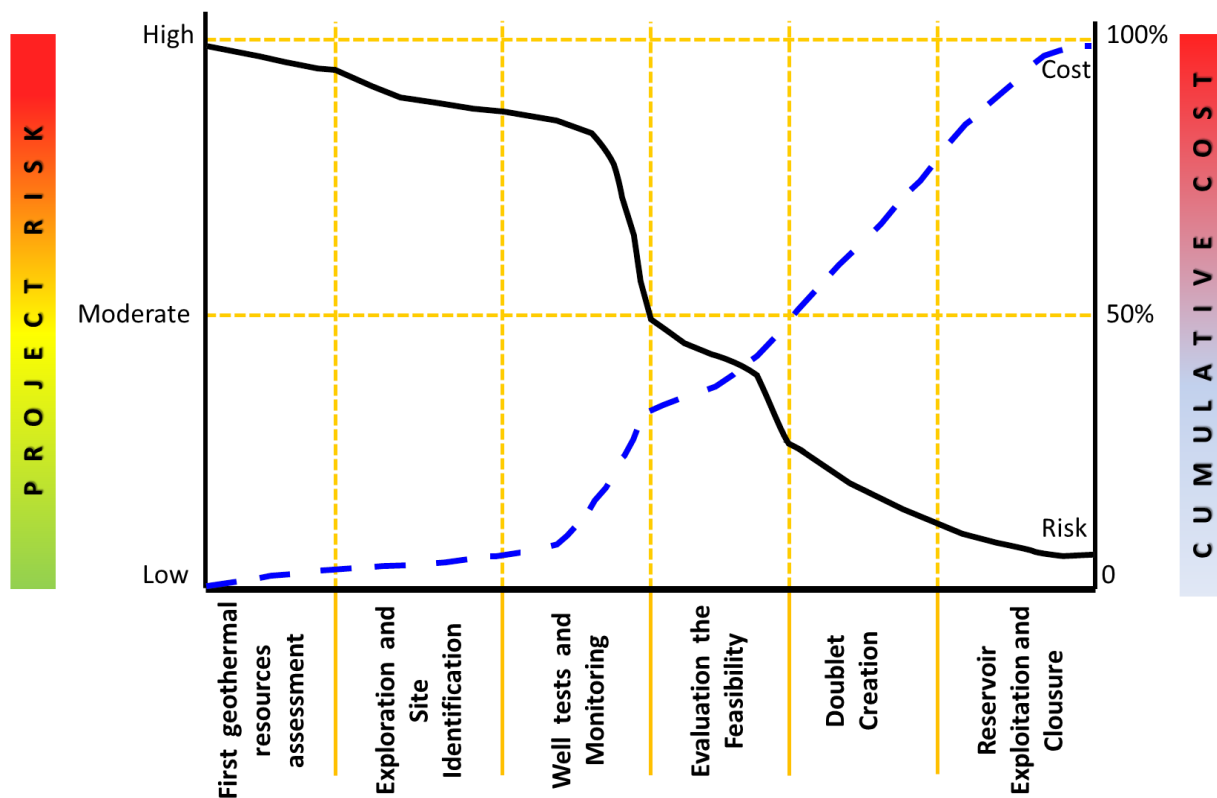


Figure 2. Cost and risk evolution through the project phases. The high-risk level reduction is related to the ‘Well tests and monitoring’ and ‘Evaluation the feasibility’ phases. In these phases, there is also the biggest uncertainty reduction. On the other side, the high-cost increases are related to the drilling of the wells (adapted from Sameting, 2009).

1.2 Geo-thermo-hydro-mechanical and induced seismicity processes in EGS and their modelling

1.2.1 Modelling approaches

Several numerical approaches and methodologies can be used to investigate the phenomena of induced seismicity during fluid injection in a fractured reservoir (Lei et al., 2016; White et al., 2018). The main differences between these approaches depend on the strategy used for solving the thermo-hydro-mechanical (THM) problem and the discretization method chosen to represent the geological media (i.e., continuous vs. discontinuous modelling approaches). Continuous approaches consist in subdividing the whole domain into small, simple parts, called elements. This method assumes continuity of functions or fields like stress, fracture displacement, etc. between elements. The discretized model can then be solved using an approximation based on the difference finite solution of the differential equations (DFM; e.g. Flac3D, Gan & Elsworth, 2014a) or by inverting the differential equation matrix formed by element assembly of the entire problem (FEM - Finite element methods; e.g. CodeBright; De Simone et al., 2013). The main limitations of these approaches are that (i) the hydraulic, thermal, and mechanical problem are usually not solved at the same time (coupled models), (ii) they are not efficient for solving discontinuous problems such as sliding along very thin fractures, and (iii) they are in general restricted to rock bodies with low fracture density or large fractures (Jing, 2003). On the other hand, discretization in discontinuous approaches can be carried out assuming an assembly of spherical elements or “particles”

able to slide (or flow) pass each other (Particle Flow Codes; e.g. PFC; Zhao & Young, 2011), or assuming a network of planar elements (fractures) immersed in an impermeable (or low-permeable) matrix (DFN; Discrete Fracture Network; e.g. CFRAC; McClure, 2012). Therefore, these approaches are efficient to handle and solve discontinuous functions, but they have the handicap on transfer variables (e.g., fluid flow, heat) between fracture and the surrounding matrix.

1.2.2 Integrating the fracture network

Once the different modelling strategies are evaluated, it is time to consider the ways to introduce or develop the fracture system or discrete fracture network (DFN) in the model. Normally this DFN has the properties or relations between the different fracture sets (fracture interactions and intersections) and their characteristics (orientation, dip, length, spacing, mechanical or hydraulic aperture, position etc.). This DFN can be generated by three main ways: a) by means of field mapping to characterize fracture systems at the outcrops (Bertrand et al., 2015), b) by generating the DFN using stochastic modelling (Gan & Elsworth, 2016) or c) by employing geomechanical modelling (Lei et al., 2016).

The first approach consists of mapping and obtaining the fracture patterns from the rock outcrops and using logging (Vidal et al., 2017), fracture description, LIDAR data, seismic surveys, excavations, rock sampling and/or laboratory measurements (Zhang et al., 2015) in order to define the fault and fracture networks at different scales and the characterization of structural parameters (e.g., fracture length, orientation, aperture, etc). This approach has as the advantage that data is from nature, preserves the geological settings, and integrates the different processes to produce the DFN. However, the resolution or the consideration of different fracture scales as well as the uncertainty in deep of the outcrop DFN sometimes represent a disadvantage for this method.

The second approach tries to solve the big complexity to measure, characterize and integrate all the natural fractures in 2D and 3D, by applying statistical methods to generate stochastic DFNs. This aims to simplify the natural fracture networks but keeping their statistical properties and hydro-mechanical behaviour. The idea is to capture representative values (orientation, length (Weiss, 2008), distribution, aperture) of the real fracture sets from outcrops or drill core (Zhang & Einstein, 2000) to generate artificial DFNs with the same properties and behaviour. The simplicity, the efficient generation, and the applicability for 2D and 3D are the benefits or the strengths of these methods. However, the possibility of developing too simplistic models and obtaining some statistical parameters are weak points of this method.

The third approach tries to integrate the geological and geomechanical history in the natural fracture generation from field observations (Lei & Wang 2016, Scholz 2002). The main objective is to generate a

geomechanically-based DFN that incorporates the fracture growth physics and that simulates the evolution of the fracture networks as a response to the stress state and strain changes. In this approach, the DFN model solves the evolution of the discrete fractures (i.e., nucleation, propagation, interaction, and arrest). A linear-elastic fracture mechanics based method (LEFM) is frequently adopted (Paluszny & Matthäi, 2009). This method has the advantage that the dependence on geomechanical properties and geological history are already included in the fracture network.

1.2.3 Stimulating the fracture network

The efficiency and the success of an EGS project depend on managing two different processes: 1) maintaining a commercial heat flow between the injection and extraction wells, and 2) keeping the induced seismicity below the acceptable risk. In this section, the processes to commercially produce heat flow are evaluated.

As mentioned above, one of the biggest challenges in an EGS project is the development of an appropriate fracture network that works as a subsurface pipeline heat exchanger and fluid pathway (Hofmann et al., 2016). This fracture network should satisfy both a commercial heat flow capacity (i.e. require an enhancement of the reservoir permeability) and, at the same time, maximize the exploited area of the reservoir (i.e. large fracture networks, large fluid transmissibility). It must be ensured that the residence time of fluid circulation and the distance between the injector well (cold water) and the producer well (hot water) are large enough to heat the circulating fluid. Inadequate permeability and short-circuiting are both related to the properties of the fracture network created during stimulation (McClure & Horne, 2014a). The generation of an intricate (tortuous) pathway for the fluid subsurface circulation rather than simply following high-permeability fractures, was proposed as a key for economically viable EGS energy systems in a way that maximization of the rock volume accessed and increase of the lifetime of the exploitation (Hofmann et al., 2016; Tester et al., 2006). This permeability enhancement and the generation of an optimal fracture network can be obtained by stimulating the pre-existing fractures making them open or sliding them and, at the same time, generating new fractures to increase their connectivity.

1.2.3.1. Stimulation typologies

Depending on whether the activity consists principally of stimulating pre-existing fractures (pure shear stimulation), generating new ones (pure opening or tensile stimulation), or a mixed scenario between stimulation of pre-existing fractures and hydraulic fracturing generation (mixed shear and opening mode) (McClure & Horne, 2014a), the conceptual model of the fracture network generation changes and has different implications. In pure shear stimulation only the pre-existing fractures are taken into account for permeability enhancement, either by sliding them when the shear stress is higher than the shear

strength (generating a permeability enhancement due to the dilatancy process) or by opening them when the fluid pressure is higher than the normal stress on the fracture (generating a permeability enhancement due to fracture opening) but with few or no new fracture production. To keep this option, the injection pressure must be under the minimum principal stress (σ_3) to prevent hydrofracture generation. This is the common stimulation mechanism assumed in EGS projects given that the injection pressure is kept under or near the minimum principal stress (Gischig 2015; Häring et al. 2008; McClure & Horne 2013).

On the other hand, if the injection pressure is kept above the minimum principal stress (σ_3), new planar fractures perpendicular to that minimum principal stress (σ_3) can propagate from the well (generating a permeability enhancement by a new fracture opening). This is the most common stimulation mechanism accepted in the oil and gas industry for the generation of new permeability since normally sedimentary shale beds do not have enough pre-existing fractures to be stimulated (Economides & Nolte, 2000).

Finally, some authors (McClure & Horne, 2014a; Norbeck et al., 2016; Wang et al., 2016; Zhang & Li, 2016) present the mixed stimulation process as the combination of pre-existing fracture stimulation and new fracture generation for permeability enhancement. The main goal is to propagate new fractures between pre-existing ones. This process can prevent the formation of large planar fractures forcing the fluid to pass through a tortuous fracture network, which involves pre-existing and new fractures. The stress concentration in the pre-existing fracture stimulation should be enhanced to generate this kind of stimulation. Fractures not oriented perpendicular to the minimum principal stress (σ_3) can be forced to open, or partially open, by both increasing the fluid pressure and local stress concentration, created by the stimulation of surrounding fractures. These local stress concentrations can allow fractures to open and propagate from their tips with fluid pressures below the least principal stress, or form splay fractures that initiate next to pre-existing fracture tips due to tensile stress concentration by fracture shearing (Mutlu & Pollard, 2008). With the fluid pressure above the minimum principal stress (σ_3), splay fractures can propagate extensively through the formation. However, when the fluid pressure is below the minimum principal stress (σ_3) splay fractures are limited by the stress perturbations produced by the stimulation of pre-existing fractures.

The last proposed scenario is another possible mechanism assumed for EGS when the stimulation of the pre-existing fracture network is not high enough to produce high permeability but the stress concentration around pre-existing fractures is consciously (or unconsciously) enhanced by the operational procedures up to induce new fractures. The enhancement of this kind of stimulation mostly depends on the operational procedures (injection pressure increments, injection rate schemes, flow back rates, etc.) and the reservoir properties (geological parameters), as discussed below. Furthermore, in a large majority of EGS projects, the well bottom-hole pressure during injection exceeds or approaches the

minimum principal stress (McClure & Horne, 2014a). This should produce the propagation of new hydraulic fractures from the wellbore, parallel to the maximum horizontal stress direction. However, field experiences in EGS projects show that fluid expansion in the reservoir is also localized following discrete zones and correlates with the orientation of pre-existing fractures. Therefore, the mixed stimulation scenario can be a good explanation when reactivation of pre-existing fractures and generation of new hydraulic fractures are observed.

These mixed stimulation processes could have previously been omitted as an explanation for EGS because seismic magnitude production is bigger in sliding stimulation than in opening stimulation i.e. the produced seismicity for mixed stimulation and pure shear stimulation could be very similar (McClure & Horne, 2014a). This is due because the stress drop produced by sliding stimulation is higher than that produced by tensile stimulation (Fischer & Guest, 2011; Norbeck et al., 2016; Zielke et al., 2017).

1.2.3.2. Principal stimulation mechanisms

The previous section has presented the main typologies for basement reservoir stimulation using fluid injection. In this section, the main rock mechanic concepts related to fluid stimulation are briefly introduced.

The injection of a fluid pressurized in a well produces a perturbation of the local stress state. The main effect is the build-up of fluid pressure and fluid propagation into the reservoir, increasing pore pressure in rocks and bringing the effective stress state close to the failure condition. Two main end-members of failure are possible: tensile and shear fracturing. For an intact rock, tensile failure will occur when the effective minimum principal stress σ_3 exceeds the tensile strength of the rock T_0 (i.e. $\sigma_3 \leq T_0$). The resulting new fracture propagates following a plane normal to the minimum principal stress. Shear failure normally happens under compressive stress when shear stress on rock exceeds shear strength. Several criteria are used to describe shear failure, with the Mohr-Coulomb criterion being the simplest approach:

$$\tau_r = \tau_{0r} + \mu\sigma_n \quad (1)$$

where τ_r is the shear strength of the intact rock, τ_{0r} is the cohesion of the rock, μ is the coefficient of internal friction and σ_n is the normal stress applied on the point.

For a fractured rock, the tensile strength is the normal stress applied to the fracture. The slip strength on a closed fracture requires that the shear stress be less or equal than the slip strength. This relation is also described by the Mohr-Coulomb law. However, in this case, the terms are related to the fracture properties not to the intact rock properties:

$$\tau_F = \tau_{0F} + \mu_f\sigma_n \quad (2)$$

where τ_F is the shear slip resistance of the fracture, τ_{0F} is the cohesion of the fracture and the μ_f is the friction coefficient of the fracture.

The failure condition in a fault plane is inherently two-dimensional (King et al., 1994) and for the bidimensional stress case, the stress tensor in a point can be described by a Mohr circle in a reference system defined by normal and shear stresses. The Mohr-Coulomb failure criterion for intact rock and fracture are represented by positive slope lines and taking into account the assumption that the resistance of a fracture is less than the resistance of intact rock (Figure 3).

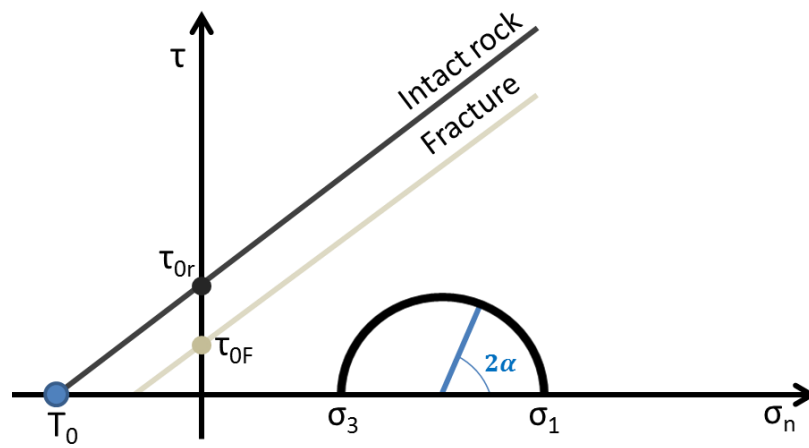


Figure 3. Mohr-coulomb diagram showing the stress state, and the fracture and intact rock envelopes. The fracture envelope is characterized by fracture orientation (α) and its fracture cohesion (τ_{0F}).

When fluid is injected there is an increase of the pore pressure (ΔP), and the initial pore pressure (P_0) increases producing a reduction in the effective normal stress (σ_n') defined as:

$$\sigma_n' = \sigma_n - (P_0 + \Delta P) \tag{3}$$

This effect can be observed in the shear and normal stress system (Figure 4).

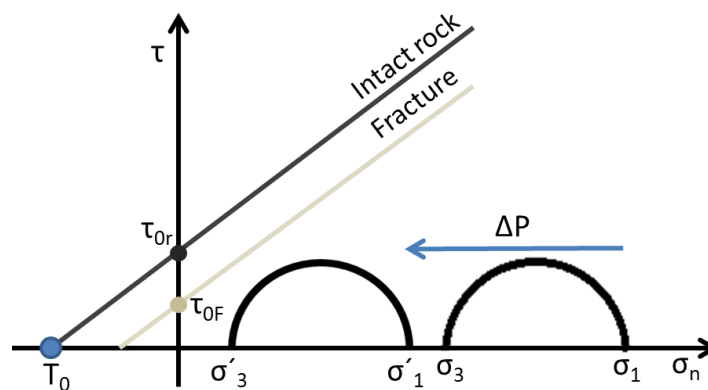


Figure 4 Pore pressure increment effect on the shear and normal stress plane. The pore pressure increment is reducing the distance between the stress state and the failure stress state.

For the intact rock body, if the stress state is higher than the failure envelope a shear failure or a tensile failure (hydraulic fracture) will occur depending on the location where the failure envelope is attached. Also for the fracture, shear slip or aperture will occur differently with the modes commented above (Figure 5 from Fischer & Guest 2011).

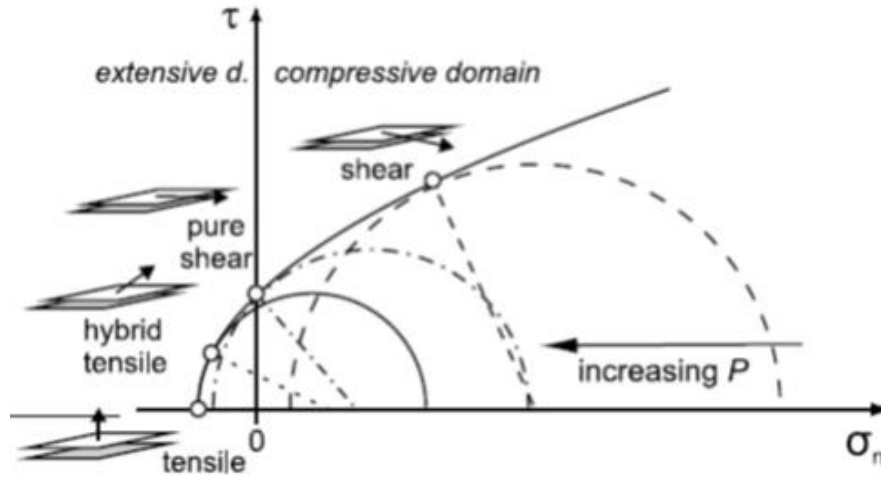


Figure 5 According to the relations between τ and σ_n the tensile, hybrid tensile, pure shear and shear failure modes are defined. The diameter of semi-circles shown by full and broken lines indicate the maximum differential stress for tensile and hybrid tensile faulting (from Fisher and Guest, 2011)

The pore pressure increase is the principal mechanism to stimulate the rock medium. Nevertheless, there are some other mechanisms, such as the thermal effect produced by fluid injection, which is normally colder than the host rock. This produces a thermo-elastic response of the rock body. Thermal effects involve cooling contraction of the reservoir rock, which results in stress changes that can strongly contribute to stimulation and result in micro seismic activity. Thermal effects normally occur at a slower rate than pore pressure changes, given that a certain time is required to cool the surrounding rock body (Gan & Elsworth, 2014b). The rock mass near the preferential fluid flow paths and the injection well will cool faster than other regions do. These regions experience thermal stress that reduces the effective compressive stress (unloading the pre-existing fractures), acting on preferential fluid flow paths by increasing fracture aperture (Guo et al., 2016) and tending to lose their frictional resistance. All these effects enhance the fractures to be reactivated with pressure changes (Rutqvist et al., 2015). Besides, thermal cooling can cause the rock to have a more brittle behaviour, especially if the working area is on the ductile-brittle transition.

However, the consequences of the thermal effect in terms of induced seismicity are still poorly explained. Some studies evaluate the thermal effect in different kinds of reservoirs. In reservoirs dominated by some large and simple structures, the thermo-mechanical processes are driven by poroelasticity processes, increasing the fracture shear strength, balancing traction and opening effects and reducing the likelihood of the shear failure developing. On the contrary, in more complex reservoirs where the

fracture network is denser, the cooling of the rock can trigger repeated ruptures at places where an initial failure was produced during early stimulation phases (Gan & Lei, 2020). The delay of a new seismic event to occur is controlled by heat diffusion in the rock zones adjacent to the fracture. In this case, renewal of seismicity can be observed after a couple of years of exploitation, but the new seismic moments seem to be bounded by the initial stress drop generated during initial reservoir stimulation (Bruehl et al., 2010).

This seismic reactivation produced by the thermal drawdown of the reservoir is also correlated with the injection rate, fracture spacing, and the injection and extraction wells (Gan & Elsworth, 2014a, 2014b; Gan & Lei, 2020). These parameters produce by this effect, together with the reservoir characteristics control the thermal drawdown of the reservoir and the timing and magnitude of the seismicity (Gan & Elsworth, 2014b).

Another derivative mechanism is the static stress redistribution produced by the earthquake nucleation. When an earthquake occurs, the region adjacent to the nucleation zone can undergo instantaneous stress changes, and such changes can trigger secondary seismicity in other locations. To quantify this stress change and find the place with a positive decrease of stability, the Coulomb stress change (ΔCFF) is used (King et al., 1994):

$$\Delta CFF = \Delta\tau - \mu' \Delta\sigma \quad (4)$$

where $\Delta\tau$ is the change in shear stress (positive in the slip direction), $\Delta\sigma$ is the change in normal stress (positive when the fault is unclamped) and μ' is the apparent friction coefficient after accounting for the pore fluid pressure effect, where μ' is defined as:

$$\mu' = \mu \cdot (1 - B) \quad (5)$$

and B is the Skempton coefficient. This term is added to take into account the fluid pressure and the effect of stress change faster than the fluid pressure change through flow (King et al., 1994). The Skempton coefficient varies between 0 and 1 as a function of fluid pressure. Its value is zero when the fluid pressure is 0, and 1 when the fluid pressure is equal to the normal stress.

The effect of the Coulomb stress change has been widely used in studies of natural seismicity (Harris, 1998; King et al., 1994; Lin, 2004; Mildon et al., 2016). However, this effect has not been fully considered in studies focused on induced seismicity due to the dominance of fluid pressure changes. However, the importance of this effect was recently evaluated for the Basel project-induced seismicity (Catalli et al., 2013) and the Castor project (Saló, 2016; Vilarrasa et al., 2021). These studies described how these mechanisms can be responsible for a non-insignificant percentage of the induced earthquakes. For this

reason, it should be considered as a coexistent mechanism with the pore pressure variation and an explanation for the earthquakes triggered outside of the pressurized front (Catalli et al., 2016).

1.2.3.3. Parameters in fracture network stimulation

Different parameters are involved during the stimulation process in a fractured basement reservoir. These parameters can enhance the stimulation, act as inhibitors or determine the shape and properties of the post-stimulated fracture network. The parameters can be divided into two main groups:

- a) Natural parameters: stress state, pre-existing fracture network (shape, size, spacing, roughness, orientation, permeability, etc.), and the lithology, among others.
- b) Operational parameters: injection parameters (rate, pressure, schedule, temperature, etc.) and parameters related to the well configuration (depth, orientation, etc.).

The effect and importance of these parameters are evaluated in this section in terms of the efficiency and sensitivity of the fracture network stimulation and also in terms of induced seismicity. Although these parameters are considered partially independent, their effects can be the same in terms of stimulation, modifying or limiting the others. For example, natural parameters can determine the optimal operational methodologies for each location or the lithology can be critical for frictional parameters.

As natural parameters are characteristic for each reservoir, and based on them, different methodologies or exploitation strategies can be proposed. During the initial stages of exploration, they are the first ones to be evaluated. At the level of reservoir evaluation, natural parameters include from reservoir-scale parameters (lithology, stress state, fracture network, etc.) to fracture-scale (fracture roughness, fracture apertures, frictional coefficient, etc.).

In EGS, the required moderate/high temperatures of the reservoir forces to work at high depth or in regions with anomalous high-temperature gradients (different geothermal plays; Moeck, 2014). The lithology of the reservoir constrains the elastic properties and frictional parameters but, at the end, it does not have a direct correlation with the fracture network stimulation or induced seismicity. However, the geological history has a deep influence in terms of fault development and the complexity of the fracture network. The reservoir behaviour will be different if the faulting process has only produced isolated cracks or, alternatively, has created large faults surrounded by large damage zones. This state of the art of fault development in the reservoir area is important for the fracture network because it determines the fracture density and their properties (with implications in terms of permeability, fracture connectivity, etc.). But it could also be important for seismic production because it determines the size

and continuity of faults, and it could eventually have implications for the induced seismic hazard (McClure & Horne 2014b).

The stress state of the reservoir and its surrounding area, together with the initial (pre-existing) fracture network, are among the most important parameters to characterize. With the stress field and the fracture network orientations, the stress state of all the fractures can be determined and the limiting fluid pressure to generate hydraulic fractures can be established. By knowing this relation it is possible to catalogue the sliding regime of the fractures and their potential stress drops, making it possible to predict the seismic behaviour and stimulation capacity (Fischer & Guest, 2011; Gischig, 2015; Norbeck et al., 2016). Besides, a prediction of the stimulation behaviour of the fracture network can also be done in terms of fracture network propagation (interaction between pre-existing fractures and new hydrofractures). If the higher principal stress σ_1 is perpendicular to the pre-existing fracture set, the tendency will be to generate complex networks of new fractures. But if the maximum principal stress is parallel to the pre-existing fracture network, the tendency will be then to stimulate the pre-existing fracture network (Zhang et al., 2015; Zhang & Li, 2016). The relationship between the fracture network and the stress field exerts a control on the main stimulation mechanism (shear stimulation, tensile stimulation, or mixed shear/tensile stimulation), which in turn is characterized by a predominant seismic behaviour. At the same time, the shape of the fracture network defines the connectivity relations and the stimulation capacity in terms of induced seismicity and the stimulated fracture network ratio. Zhang et al., (2013) evaluated the effect of the fracture network density, in a way that a sparse network show a flat microseismic distribution zone with few events (indicating high production of hydrofracturing), while a dense network cases showed a complex microseismic map that indicate intensive interaction between natural and hydraulic fractures.

Another parameter to consider is the reservoir capacity to increase permeability with shear stimulation or dilatancy, i.e., increase of the permeability by dilatancy in the pre-existing fracture network. The above commented stimulation mechanism is also influenced by the capacity of the pre-existing fracture network to accommodate fluid. If the permeability and storability of the initial fracture network are high enough to accommodate fluid without a building up the fluid pressure, the pure shear stimulation will be the most possible stimulation mechanism. But if the permeability and storability of the natural fracture network are not high enough, then the pressure will build up to reach the tensile strength and propagate as a tensile fracture (McClure & Horne 2014a).

Together with the natural parameters, operational parameters also define the response and evolution of the reservoir (e.g., at the level of fracture network and seismic evolution). Operational parameters are those that can be controlled directly during the reservoir exploitation phases. The injection schedule, or specifically the injection rate, can be the most representative parameter among the operational ones.

This parameter eventually controls the reservoir stimulation rhythm and is linked to the evolution of the injection pressure and the expansion of the fluid in the reservoir. The relation between injection and induced seismicity is unequivocal, although the reservoir response can be different in each case. Dempsey and Suckale (2015) studied the relationship between injection rates and seismicity rates for some EGS projects. They observed a direct relationship between injection volume in the reservoir and induced seismicity. Also, they noted that in general a reduction of the injection rate produces a decrease of the seismicity rate, but with different behaviour depending on the reservoir properties. However, the relation of the injection rate and the induced seismicity depends on the characteristics of the fracture network and the pressure evolution with injection (McClure & Horne, 2014b; Michelle et al., 2019). If injection results in fluid pressures under the minimum principal stress, it will produce shear stimulation and reactivation of inherited fractures in the reservoir. For cases in which the fluid pressure reaches the minimum principal stress, coetaneous to potential reactivation of natural fractures, hydro-fractures can be produced. The injection rate also plays a role in the efficiency of reservoir stimulation. On the one hand, smaller injection rates will result in a greater total volume of the stimulated reservoir, as the affected fracture surface area is larger and the fluid can slowly expand through the fracture network, preventing overpressure. On the other hand, hydro-fractures will be created when injection rates are preferentially high and overpressure reaches the minimum principal stress, but both the affected surface area and the shear stimulated area will be reduced (Riahi & Damjanac, 2013). The selection of a high/low injection rate setting must be done depending on the mechanical and geometrical properties of the fracture network (i.e., connectivity, permeability, aperture, etc.). For this, the injection rate should be determined according to the properties of the natural fracture network during the design of the stimulation treatment (Zhang & Li, 2016). The associated induced seismicity will depend on the stimulation mechanism and the properties of the pre-existing fracture network.

Another concept related to operational conditions is the injection rate setting, i.e., the injection rhythm or scheme (increasing and decreasing of the injection rate, or continuous vs. cyclic injections). Numerical investigations show that continuous fluid injection may lead to more complex fracture networks (higher seismic hazard scenarios) compared to cyclic rate injections (Yoon et al., 2015). Cyclic schemes have the advantage that there is time for the reservoir rock mass to relax and reduce the pressure in the fracture network developing (Hofmann et al., 2016). Wang et al. (2016) suggested that a sudden increase in the injection rate produces hydraulic fracture propagation along many branching fracturing points. McClure and Horne (2014a) discussed the propagation of pre-existing fractures with pressures under the minimum principal stress, empowering that injection rate could favour the stress concentration at fracture tips and enhance the generation of splay fractures by hydrofracturing. In terms of seismic production, Huenges et al., (2017) observed a major reduction of microseismicity during cyclic stimulation than in continuous stimulation scenarios.

Another operational parameter is the well distribution and their completion design. Hofmann et al., (2016) investigated the effect of the well distribution and stimulation schedule on fracture production and fracture branching. They pointed out that these parameters also exert an influence on the fracture network evolution and the reservoir volume stimulated.

1.3 Seismic hazard assessment

The most important challenge associated with the deployment of EGS projects is the prediction and mitigation of induced seismicity, in particular the risk of inducing seismic events that can be felt by people during the stimulation phases and then during the lifetime of the geothermal plants. For this reason, the main objective for the seismic hazard assessment is to be able to predict induced seismicity for a specific site (Shapiro et al., 2010) and, more specifically, the evolution of the induced seismicity in terms of magnitude and frequency. However, the capacity of accurately predicting seismicity before the stimulation phase is difficult. The maximum magnitude (M_{max}) is inferred from the largest potentially active fault in the geothermal reservoir (Majer et al., 2007). However, in some cases, reservoir faults cannot be directly detected by geophysical instruments. For these reasons, different methodologies and correlations have been proposed to constrain or predict the number of events and then M_{max} . Such methodologies are based on the injected fluid volume, the total injected mass, the injection rate, or the energy introduced in the system (Dempsey & Suckale, 2015). However, these correlations still have high uncertainties. In order to increase the capacity to predict induced seismicity, different strategies have been proposed. One option is to combine real data (injection, induced seismicity, reservoir properties) with a statistical model (Mena et al., 2013; Mignan et al., 2015). This hybrid model is recalibrated each step a stimulation phase is done and/or new microseismicity is detected to improve the prediction capability (eg., Király et al. 2015; Bachmann et al., 2012). To apply this approach a good deployment of seismic stations and knowledge of the reservoir properties are required during monitoring. This information provides knowledge about the fracture network distribution and the reservoir properties. Besides, a good historic model of fault development is a key point to properly characterize the main fault surfaces that could potentially be stimulated and then derive the maximum magnitudes that can be expected.

Another strategy is the development of geomechanical models capable of reproducing the stress changes in the reservoir and the induced seismicity (e.g., McClure, 2012; Wang & Ghassemi, 2012; Gischig & Wiemer, 2013). Different scenarios can be evaluated in terms of the effect on the seismicity rate, and recommendations can be provided to reduce the seismicity rate. Nevertheless, these models need a good calibration phase during all the project phases to increase the prediction capacity and reduce uncertainty.

One of the widely used tools to date for hazard and risk management in EGS projects are the 'Traffic Light Systems'. They represent new strategies for risk mitigation in induced seismicity because it is possible to manage the risk to control the hazard, in contrast with standard seismic risk mitigation where only intervention in vulnerability reduction is made (Mignan et al., 2015). Traffic Light Systems were proposed to determine when the risk associated with induced seismicity reaches a threshold value and, thus, a decision to modify or stop the operations should be made (Bommer & Abrahamson, 2006; Convertito et al., 2012). The traffic light system is based on three components: 1) public response, 2) observed local magnitudes, and 3) peak ground velocities. In a four-stage action plan, the injection follows as it was planned (green light), continued but not increased (yellow light), stopped (orange light), or stopped and initiation of fluid extraction (red light) (Bruhn et al., 2015).

Nevertheless, it has been observed in recent cases that these systems present some handicaps. First, in some cases, the larger events are produced after the shut-in (Dempsey & Suckale, 2015; McClure, 2015). Second, uncertainty associated with the project can result in wrong decisions. Third, some unexpected operational issues can occur (Mignan et al., 2015). The accumulated experience demonstrates that the conventional 'Traffic Light Systems' are not capable enough to adequately manage the seismic hazard. Bruhn et al. (2015) under the GEISER project proposed an 'Advanced Traffic Light', which should have the capacity of predicting the future seismicity, not only working with the observed events (Figure 6). Thus, these new systems should include:

- Forward-looking: Prediction capacity based on the reservoir and injection parameters (seismicity, injection, stress changes, pressure evolution, stress state, etc.). For this, robust physics-based models are needed to forecast the likely future seismicity and optimize reservoir exploitation.
- Probabilistic: Forecasts are made within a fully probabilistic framework, considering the physical uncertainties related to the lack of knowledge during the stimulation/operational phases, and the aleatory variability involved in the processes themselves. They should also integrate the seismic hazard analysis for the critical structures, by including the forecasted rates for all magnitudes and possible events (unlikely extreme events), avoiding that they become an obstruction for public communication and acceptance.
- Dynamic: All new data both reservoir evolution properties and new seismicity, are introduced in the models to produce better forecasts. All data are integrated combining prior knowledge with the newly acquired data.

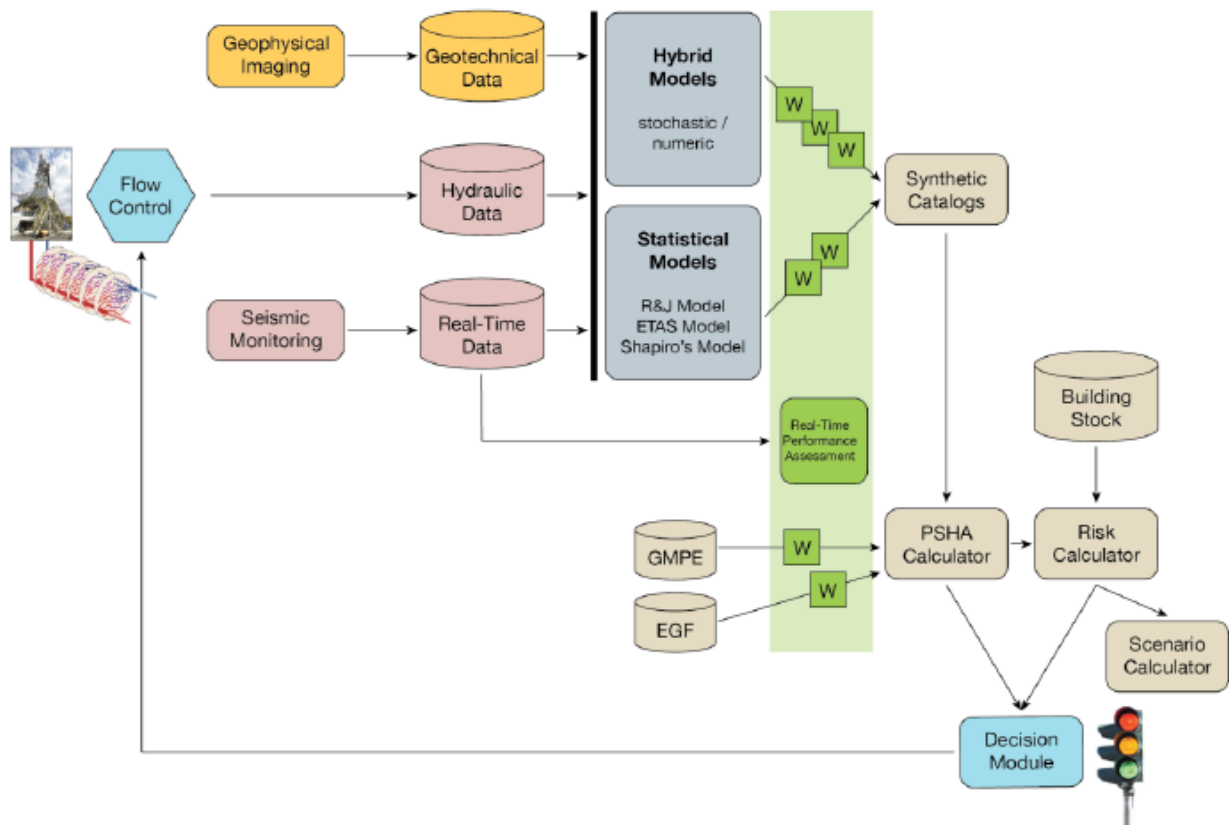


Figure 6. Advanced Traffic Light System scheme. Schematic overview of the foreseen software framework. W=weighting. GMPE= ground motion prediction equation. EGF=empirical green's function. PSHA = probabilistic seismic hazard assessment. (from Bruhn et al., 2015).

1.4 Geothermal potential assessment

One of the first steps during the initiation of a geothermal project is the geothermal potential assessment of the reservoir. This must be done independently of the project aim, either heat or power production, or the reservoir type, either a deep aquifer (i.e., hydrothermal) or low-permeability crystalline rock (i.e., petrothermal). The geothermal potential assessment is quantified as the base resource and in terms of energy stored in the reservoir (Agemar et al., 2018).

This quantification is needed to estimate the potential energy that can be produced from the geothermal reservoir for power generation or direct uses (district heating, greenhouses, etc.). It is essential to carry out preliminary evaluations of the viability of the project based on the investment and exploitation cost of the geothermal resource. A handicap of the geothermal potential assessment is that it is done during the early stages of exploration and, therefore, large uncertainties in the geological knowledge must be considered when carrying out these preliminary assessments. The main uncertainties are related to the prediction of petrophysical properties, the temperature distribution, and the reservoir geometry.

The volumetric “Heat In Place” (*HIP*) method implemented by the United States Geological Survey (USGS) (Muffler & Cataldi, 1978), beyond its subsequent revisions and reformulations (Garg & Combs, 2010, 2015), is still the most widely used evaluation technique to estimate the available stored heat and the recoverable heat fraction (*Hrec*) of deep geothermal reservoirs (Limberger et al., 2018; Trumpy et al., 2016; Miranda et al. 2020). This method takes into account the volume of the reservoir (surface and thickness), the petrophysical properties of rocks and fluids (e.g., porosity, specific heat capacity, rock, and fluid densities, etc.) as well as the reservoir and reinjection (or reference) temperatures. The method is sensitive to certain parameters that are normally not well constrained during the early stages of exploration, including the reservoir geometry, the distribution of the petrophysical properties, or the volume of fluids stored in the reservoir. Due to the potential influence of these uncertainties, the HIP method is normally applied by carrying out multiple stochastic calculations using approaches such as the Monte Carlo method. This approach systematically varies the parameters considered over a defined range of values by using probability distribution functions (*PDF*) (e.g., triangular, normal, lognormal, etc.) (Garg & Combs, 2010; Shah et al., 2018).

To obtain a quantification of the HIP two main approaches can be used. In the first one, calculations are normally performed on the entire reservoir scale or on a specific part, where the selected part is treated conceptually as a single-cell model. However, a weak point of this approach is that the analyzed domain is treated with a homogeneous distribution of the parameters in the entire calculated volume. But local variability of the assessment is expected in reservoirs, mainly due to variation of the petrophysical properties, the temperature distribution, or the reservoir geometry (thickness, depth, etc.). For this reason, the second approaches are based on GIS (Geographic Information System) capabilities coupled with 3D subsurface models that explicitly allow the application of the volumetric method using 3D voxel models as inputs. For this reason, nowadays the tools that use GIS capacities for the geothermal potential assessment at a regional scale can be considered as a reference to be followed. These tools, also allow showing the geothermal potential distribution as maps in an easy untestable way. Thus, the geothermal energy potential can be distributed and promoted through society.

1.5 A view on public acceptance and communication

The introduction of new technologies in the public domain is always difficult and can produce an initial repulse if the public is inadequately informed (Duijn et al., 2013). Normally the rejection of a new project happens because there is a lack of public information on some key aspects. The capacity of the EGS and geothermal projects developers to involve the citizens of the geothermal project location as an active part is fundamental for the successful development of the project. The key dilemmas or the question that should be responded are the following (Duijn et al., 2013):

First, a cost and benefits relation: Who will be benefited by the development, implementation and exploitation the new technology? The associated risks should be accounted for as a cost of the project. Given that, from this moment on they will become quotidian new risks for the site citizens.

Second, the disturbance of daily life: How will the project development affect the daily lives of the local population? Is it going to change their routines?, do they need new knowledge? Is it going to affect their privacy? What impact will it have on the physical aspects?, environmental systems?, society relations?

Third, the uncertainty of the novelty: What do we know about the performance and impact of the new technology? Will it meet the expectations and/or deliver the promises made? Is it going to improve the actual situation? Will the new technology have negative consequences that have yet to be discovered?

With all this knowledge or part of it, the objective is to provide the local population with enough background to free decide the convenience or not of the project. At the end, the final decision goes through the acceptance of the project by the citizens of the location place. Otherwise the project will always be walking on thin ice and the people will be waiting for a little problem to protest. On the other side with the population betting for the project the difficulties can be treated as challenges for the society.

1.6 Interest and objectives of the thesis

During this introduction, a broad view of the aspects surrounding the initial phases of a high/moderate temperature geothermal project and the reason for its growing development have been exposed. Focusing, above all, on those projects that require a phase of hydraulic stimulation (i.e., Enhanced Geothermal Systems; EGS), the risk of induced seismicity that they entail and how to deal with them. A key step is to understand the processes surrounding the generation of induced seismicity and how to prevent and control them. For this reason, a research direction related to this issue is to improve our capacity to numerically simulate the processes that give rise to this induced seismicity and understand how the seismicity and the stimulation of the fracture network are related is critical for the development and success of such projects. This relationship is important, both for risk management and for improving the reservoir hydraulic properties for the economic viability of the project. Among these parameters, the ones that have a major effect are those related to the geometry and mechanical properties of the fracture network. A fundamental process is how fracture sliding and opening improves the hydraulic properties of the reservoir while generating seismicity. Thus, this thesis mainly focuses on the numerical simulation of induced seismicity due to the injection of high-pressure fluids into a geothermal reservoir hydraulically dominated by a fracture network.

As previously explained, during the initial phases of EGS projects there is a great deal of uncertainty that should be considered when characterizing the geothermal potential. This uncertainty, which plays an

inhibitory role in the development of these projects, is due to the lack of representative data of the reservoir, such as its petrophysical properties (e.g. porosity, thermal properties) and their spatial distribution (e.g. volume, temperature) as well as the high cost of obtaining them from the reservoir itself.

Accordingly, in order to be able to include this uncertainty in the initial assessments of the deep geothermal potential, tools are required to characterize in a stochastic way the deep geothermal resources at the regional scale including the spatial variation of the parameters involved in these calculations. Thus, the development of methodologies, workflows, and numerical tools to be able to include geological and petrophysical uncertainties in the assessment of deep geothermal potential, is another of the main challenges of this thesis.

The development of these methodologies and tools within the context of the thesis is framed in locations of geothermal interest at the local level in Catalonia. However, obtaining methodologies and tools for stochastic resolution of local geothermal potential also represent global solutions that can be implemented in other areas of study and exploration contexts.

The specific objectives of this thesis are to:

- Evaluate the fluid injection induced seismicity in geothermal reservoirs from a numerical point of view, using different numerical approaches to understand the processes that give rise to this phenomenon and how to model them.
- Numerically analyze the relationship between the different fracture slip regimes, the seismicity their activity induces, and the orientation of the fractures in a context of fluid injection in stimulated geothermal reservoirs.
- Develop methodologies, workflows, and specific tools for stochastically evaluating the deep geothermal potential focusing on cases of study of local deep reservoirs in the area of Catalonia.
- Integrate local solutions of deep geothermal potential analyses in a global context in other study areas.

1.7 Thesis structure

This PhD thesis is organized in a classical format as a standalone volume. However, each main chapter has been written in the format of a scientific article format for their publication (**chapters 2, 3, 4 and 5**), being **chapters 3 and 5** already published on the date of submission of this thesis. Finally, chapter 6 contains a general discussion and the main conclusions of this thesis. The bibliographic references of each chapter are included in the corresponding References section.

Chapters 2, 3, and 4 are focused on the analysis of induced seismicity in relation to the reservoir fracture network, while **chapter 5** shows the 3DHIP-Calculator application, a new application developed for the deep geothermal potential assessment. **Chapter 2** explores the relationship between the different fracture slip regimes (slip velocity distribution during seismic rupture) and fracture orientation. This relationship is analyzed using two different numerical approaches based on discrete and continuous modelling. Special attention is paid to the analysis of the differences between approaches and to the exploration of the concept of dynamic rupture and dynamic evolution of the coefficient of friction. **Chapter 3** uses the concepts worked on in **chapter 2** to propose explanations to the phenomenon of pressure drops at bottom-well observed in stimulated geothermal reservoirs. This phenomenon is explained by numerical simulations, through the mixed stimulation process produced by the interrelation between fractures stimulated by sliding (and producing micro-seismicity) and fractures stimulated by opening (and generally aseismic). **Chapter 4** deals with the seismic cycle and the pressurization process resulting from the interaction between concatenated fractures with different orientations. The chapter analyses the importance of considering macro-roughness (metric to large-scale) in the seismic behaviour of fractures during fluid injection process.

Finally, **chapter 5** is conceptually different from the previous ones as it focuses on another fundamental aspect in the study of geothermal reservoirs: the evaluation of deep geothermal potential using stochastic approaches. In this case, the 3DHIP-Calculator tool is presented, which allows to stochastically estimate the geothermal resources and the recoverable part (reserves) using geological and thermal 3D models as input data. The approach considers the spatial distribution of the petrophysical parameters and geological units in the evaluation of deep geothermal potential. This software has been designed, developed, implemented and tested within the framework of the thesis.

In **chapter 6**, a general discussion of the main results and summary of the main conclusions are presented.

1.8 References

- Agemar, T., Weber, J., & Moeck, I. S. (2018). Assessment and Public Reporting of Geothermal Resources in Germany : Review and Outlook. *Energies*, 11(332). <https://doi.org/10.3390/en11020332>
- Bachmann, C. E., Wiemer, S., & Woessner, J. (2012). Influence of pore-pressure on the event-size distribution of induced earthquakes. *Geophysical Research Letters*, 39, 1–7. <https://doi.org/10.1029/2012GL051480>
- Bertrand, L., Géraud, Y., Diraison, M., Le Garzic, E., & Place, J. (2015). The Use of Outcrops on the Catalonian Coastal Ranges (Spain) as Analogue for Deep Geothermal Reservoir Characterization in the Upper Rhine Graben (France). *World Geothermal Congress 2015*, Melbourne, Australia .
- Bommer, J. J., & Abrahamson, N. A. (2006). Why Do Modern Probabilistic Seismic-Hazard Analyses Often Lead to Increased Hazard Estimates ?. *Bulletin of the Seismological Society of America*, 96, 6, 1967–1977, doi: <https://doi.org/10.1785/0120060043>
- Bruel, D., Van Wees, J.-D., & Charalampidou, E. (2010). Geothermal Engineering Integrating Mitigation of Induced Seismicity in Reservoirs - GEISER. D4.4 - Role of temperature changes. Retrieved from <http://www.geiser-fp7.fr/ReferenceDocuments/Pages/ReferenceDocuments.aspx>
- Bruhn, D., Huenges, E., Agustsson, K., Zang, A., Rachez, X., Wiemer, S., Van Wees, J. D., & Calcagno, P. (2015). Summary of the European GEISER Project (Geothermal Engineering Integrating Mitigation of Induced Seismicity in Reservoirs). *Proceedings World Geothermal Congress*, Melbourne, Australia.
- Capuano, L. E. J. (2016). 5 - *Geothermal well drilling*. *Geothermal Power Generation*. Elsevier, Woodhead Publishing. Ltd. <https://doi.org/10.1016/B978-0-08-100337-4.00005-X>
- Catalli, F., Meier, M. A., & Wiemer, S. (2013). The role of Coulomb stress changes for injection-induced seismicity: The Basel enhanced geothermal system. *Geophysical Research Letters*, 40(1), 72–77. <https://doi.org/10.1029/2012GL054147>
- Catalli, F., Rinaldi, A. P., Gischig, V., Nespoli, M., & Wiemer, S. (2016). The importance of earthquake interactions for injection-induced seismicity: Retrospective modeling of the Basel Enhanced Geothermal System. *Geophysical Research Letters*, 43(10), 4992–4999. <https://doi.org/10.1002/2016GL068932>
- Convertito, V., Maercklin, N., Sharma, N., & Zollo, A. (2012). From Induced Seismicity to Direct Time-Dependent Seismic Hazard, *Bulletin of the Seismological Society of America*, 102, 6, 2563–2573, doi: [10.1785/0120120036](https://doi.org/10.1785/0120120036)
- Dempsey, D., & Suckale, J. (2015). Induced Earthquake Sequences in Geothermal Settings : Data Trends and Modeling Approaches. *Proceedings of 40th Stanford Geothermal Workshop*.
- Dezayes, C., Gentier, S., & Genter, A. (2005). Deep Geothermal Energy in Western Europe: The Soultz Project, (BRGM/RP-54227-FR), 48.
- Duijn, M., Puts, H., & Boxem, T. (2013). Geothermal Engineering Integrating Mitigation of Induced Seismicity in Reservoirs - GEISER. D6.4 - Laying the Groundwork for Public Acceptance of Enhanced Geothermal Systems (Vol. Final version). Delft, the Netherlands.
- Economides, M. J., & Nolte, K. G. (2000). *Reservoir Stimulation* (3rd Editio). Chichester, England: John Wiley & Sons Ltd. <https://doi.org/10.1017/CBO9781107415324.004>
- Eurostat (2015). Sustainable development in the European Union: 2015 monitoring report of the EU Sustainable Development Strategy. European Union. Luxembourg: Publications Office of the European Union, 2015. ISBN 978-92-79-49391-1 ISSN 2443-8480 doi: 10.2785/999711
- Eurostat (2017). Energy balance sheets 2015 DATA. European Union. Luxembourg: Publications Office of the European Union, 2017. ISBN 978-92-79-69844-6 ISSN 1830-7558 doi: 10.2785/032728
- Fischer, T., & Guest, A. (2011). Shear and tensile earthquakes caused by fluid injection. *Geophysical Research Letters*, 38(5), 2–5. <https://doi.org/10.1029/2010GL045447>

- Gan, Q., & Elsworth, D. (2014a). Analysis of fluid injection-induced fault reactivation and seismic slip in geothermal reservoirs. *Journal of Geophysical Research: Solid Earth*, 119, 3340–3353. <https://doi.org/10.1002/2013JB010500>. Received
- Gan, Q., & Elsworth, D. (2014b). Thermal drawdown and late-stage seismic-slip fault reactivation in enhanced geothermal reservoirs. *Journal of Geophysical Research: Solid Earth*, 119, 8936–8949. <https://doi.org/10.1002/2014JB011323>. Received
- Gan, Q., & Elsworth, D. (2016). A continuum model for coupled stress and fluid flow in discrete fracture networks. *Geomechanics and Geophysics for Geo-Energy and Geo-Resources*, 2(1), 43–61. <https://doi.org/10.1007/s40948-015-0020-0>
- Gan, Q., & Lei, Q. (2020). Geothermics Induced fault reactivation by thermal perturbation in enhanced geothermal systems. *Geothermics*, 86, <https://doi.org/10.1016/j.geothermics.2020.101814>
- Garg, S. K., & Combs, J. (2010). Appropriate use of USGS volumetric heat in place method and Monte Carlo calculations. *Proceedings: Thirty-Fourth Workshop on Geothermal Reservoir Engineering, Stanford University, Stanford, California*. Retrieved from <https://pangea.stanford.edu/ERE/pdf/IGAstandard/SGW/2010/garg.pdf>
- Garg, S. K., & Combs, J. (2015). A reformulation of USGS volumetric “heat in place” resource estimation method. *Geothermics*, 55, 150–158. <https://doi.org/10.1016/j.geothermics.2015.02.004>
- Gischig, V. S. (2015). Rupture propagation behavior and the largest possible earthquake induced by fluid injection into deep reservoirs. *Geophysical Research Letters*, 42(18), 7420–7428. <https://doi.org/10.1002/2015GL065072>
- Gischig, V. S., & Wiemer, S. (2013). A stochastic model for induced seismicity based on non-linear pressure diffusion and irreversible permeability enhancement. *Geophysical Journal International*, 1229–1249. <https://doi.org/10.1093/gji/ggt164>
- Gnatus, N. A., Khutorskoy, M. D., & Khmelevskoi, V. K. (2011). Petrothermal Energy and Geophysics. *Moscow University Geology Bulletin, Vol. 66, No. 3, pp. 151–157*. <https://doi.org/10.3103/S0145875211030045>
- Grigoli, F., Cesca, S., Rinaldi, A. P., Manconi, A., López-Comino, J. A., Clinton, J. F., Westaway, R., Cauzzi, C., Dahm, T., & Weimer, S. (2018). The November 2017 Mw 5.5 Pohang earthquake: A possible case of induced seismicity in South Korea. *Science*, 10.1126/science.aat2010.
- Guo, B., Fu, P., Hao, Y., Peters, C. A., & Carrigan, C. R. (2016). Thermal drawdown-induced flow channeling in a single fracture in EGS. *Geothermics*, 61, 46–62. <https://doi.org/10.1016/j.geothermics.2016.01.004>
- Häring, M. O., Schanz, U., Ladner, F., & Dyer, B. C. (2008). Characterisation of the Basel 1 enhanced geothermal system. *Geothermics*, 37(5), 469–495. <https://doi.org/10.1016/j.geothermics.2008.06.002>
- Harris, R. a. (1998). Introduction to Special Section: Stress Triggers, Stress Shadows, and Implications for Seismic Hazard. *Journal of Geophysical Research*, 103(B10), 24347. <https://doi.org/10.1029/98JB01576>
- Hofmann, H., Babadagli, T., Yoon, J. S., Blöcher, G., & Zimmermann, G. (2016). A hybrid discrete/finite element modeling study of complex hydraulic fracture development for enhanced geothermal systems (EGS) in granitic basements. *Geothermics*, 64, 362–381. <https://doi.org/10.1016/j.geothermics.2016.06.016>
- Huenges, E., Zang, A., & Kim, K. Y. (2017). Soft stimulation and induced seismicity. In *2nd Induced Seismicity Workshop*. Davos, Switzerland.
- Jing, L. (2003). A review of techniques, advances and outstanding issues in numerical modelling for rock mechanics and rock engineering. *International Journal of Rock Mechanics and Mining Sciences*, 40(3), 283–353. [https://doi.org/10.1016/S1365-1609\(03\)00013-3](https://doi.org/10.1016/S1365-1609(03)00013-3)
- Jung, R. (2013). EGS — Goodbye or Back to the Future. Chapter 5. *Effective and Sustainable Hydraulic Fracturing* (p. 1072). InTech. <https://doi.org/10.5772/56458>
- King, G. C. P., Stein, R. S., & Lin, J. (1994). Static Stress Changes and the Triggering of Earthquakes. *Bulletin of the Seismological Society of America*, 84(3), 935–953. [https://doi.org/10.1016/0148-9062\(95\)94484-2](https://doi.org/10.1016/0148-9062(95)94484-2)

- Király, E., Zechar, J. D., Gischig, V., Karvounis, D., Heiniger, L., & Wiemer, S. (2015). Modeling and Forecasting Induced Seismicity in Deep Geothermal Energy Projects. *Proceedings World Geothermal Congress*, Melbourne, Australia.
- Lei, Q., Latham, J., & Tsang, C. (2016). The use of discrete fracture networks for modelling coupled geomechanical and hydrological behaviour of fractured rocks. *Computers and Geotechnics*, 85, 151–176. <https://doi.org/10.1016/j.compgeo.2016.12.024>
- Lei, Q., & Wang, X. (2016). Tectonic interpretation of the connectivity of a multiscale fracture system in limestone. *Geophysical Research Letters*, 43(4), 1551–1558. <https://doi.org/10.1002/2015GL067277>
- Limberger, J., Boxem, T., Pluymaekers, M., Bruhn, D., Manzella, A., Calcagno, P., Beekman, F., Cloetingh, S. & van Wees, J.-D. (2018). Geothermal energy in deep aquifers : A global assessment of the resource base for direct heat utilization. *Renewable and Sustainable Energy Reviews*, 82, 961–975. <https://doi.org/10.1016/j.rser.2017.09.084>
- Lin, J. (2004). Stress triggering in thrust and subduction earthquakes and stress interaction between the southern San Andreas and nearby thrust and strike-slip faults. *Journal of Geophysical Research*, 109(B2), 1–19. <https://doi.org/10.1029/2003JB002607>
- Lukawski, M. Z., Silverman, R. L., & Tester, J. W. (2016). Uncertainty analysis of geothermal well drilling and completion costs. *Geothermics*, 64, 382–391. <https://doi.org/10.1016/j.geothermics.2016.06.017>
- Majer, E. L., Baria, R., Stark, M., Oates, S., Bommer, J., Smith, B., & Asanuma, H. (2007). Induced seismicity associated with Enhanced Geothermal Systems. *Geothermics*, 36(3), 185–222. <https://doi.org/10.1016/j.geothermics.2007.03.003>
- McClure, M. W. (2012). Modeling and Characterization of Hydraulic Stimulation and Induced Seismicity in Geothermal and Shale Gas Reservoirs. *Stanford PhD Dissertation*, 1–369.
- McClure, M. W. (2015). Generation of large postinjection-induced seismic events by backflow from dead-end faults and fractures. *Geophysical Research Letters*, 42, 6647–6654. <https://doi.org/10.1002/2015GL065028>. Received
- McClure, M. W., & Horne, R. N. (2013). Characterizing hydraulic fracturing with a tendency for shear stimulation test. *Society of Petroleum Engineers, SPE166332*, 1–17. <https://doi.org/10.2118/166332-MS>
- McClure, M. W., & Horne, R. N. (2014a). An investigation of stimulation mechanisms in Enhanced Geothermal Systems. *International Journal of Rock Mechanics and Mining Sciences*, 72, 242–260. <https://doi.org/10.1016/j.ijrmms.2014.07.011>
- McClure, M. W., & Horne, R. N. (2014b). Correlations between formation properties and induced seismicity during high pressure injection into granitic rock. *Engineering Geology*, 175, 74–80. <https://doi.org/10.1016/j.enggeo.2014.03.015>
- Mena, B., Wiemer, S., & Bachmann, C. (2013). Building Robust Models to Forecast the Induced Seismicity Related to Geothermal Reservoir Enhancement. *Bulletin of the Seismological Society of America*, 103(1), 383–393. <https://doi.org/10.1785/0120120102>
- Michelle, A., Pierre, D., Hervé, C., & Frédéric, P. (2019). Effect of the Injection Scenario on the Rate and Magnitude Content of Injection-Induced Seismicity : Case of a Heterogeneous Fault. *Journal of Geophysical Research: Solid Earth*, 124, 8426–8448. <https://doi.org/10.1029/2019JB017898>
- Mignan, A., Landtwing, D., Kästli, P., Mena, B., & Wiemer, S. (2015). Induced seismicity risk analysis of the 2006 Basel, Switzerland, Enhanced Geothermal System project: Influence of uncertainties on risk mitigation. *Geothermics*, 53, 133–146. <https://doi.org/10.1016/j.geothermics.2014.05.007>
- Mildon, Z. K., Toda, S., Faure Walker, J. P., & Roberts, G. P. (2016). Evaluating models of Coulomb stress transfer: Is variable fault geometry important? *Geophysical Research Letters*, 407–414. <https://doi.org/10.1002/2016GL071128>
- Miranda, M.M., Raymond, J., & Dezayes, C. (2020). Uncertainty and Risk Evaluation of Deep Geothermal Energy

- Source for Heat Production and Electricity Generation in Remote Northern Regions. *Energies*, 13, 4221. <https://doi.org/10.3390/en13164221>.
- Moeck, I. S. (2014). Catalog of geothermal play types based on geologic controls. *Renewable and Sustainable Energy Reviews*, 37, 867–882. <https://doi.org/10.1016/j.rser.2014.05.032>
- Moeck, I., Bloch, T., Graf, R., Heuberger, S., Kuhn, P., Naef, H., Sonderegger, M., Uhlig, S., & Wolfgramm, M. (2015). The St. Gallen Project: Development of Fault Controlled Geothermal Systems in Urban Areas. *Proceedings World Geothermal Congress*, Melbourne, Australia.
- Muffler, P., & Cataldi, R. (1978). Methods for regional assessment of geothermal resources. *Geothermics*, 7, 53–89. [https://doi.org/https://doi.org/10.1016/0375-6505\(78\)90002-0](https://doi.org/https://doi.org/10.1016/0375-6505(78)90002-0)
- Mutlu, O., & Pollard, D. D. (2008). On the patterns of wing cracks along an outcrop scale flaw: A numerical modeling approach using complementarity. *Journal of Geophysical Research: Solid Earth*, 113(6), 1–20. <https://doi.org/10.1029/2007JB005284>
- Norbeck, J. H., McClure, M. W., & Horne, R. N. (2016). Revisiting stimulation mechanism at Fenton Hill and an investigation of the influence of fault heterogeneity on the Gutenberg-Richter b-value for rate-and-state earthquake simulations. *41st Workshop on Geothermal Reservoir Engineering*, Stanford, California.
- Paluszny, A., & Matthäi, S. K. (2009). Numerical modeling of discrete multi-crack growth applied to pattern formation in geological brittle media. *International Journal of Solids and Structures*, 46(18–19), 3383–3397. <https://doi.org/10.1016/j.ijsolstr.2009.05.007>
- Riahi, A., & Damjanac, B. (2013). Numerical Study of Interaction Between Hydraulic Fracture and Discrete Fracture Network. *Effective and Sustainable Hydraulic Fracturing*. In D. R. Jeffrey (Ed.). <https://doi.org/10.5772/56416>
- Rutqvist, J., Jeanne, P., Dobson, P. F., Garcia, J., Hartline, C., Hutchings, L., Singh, A., Vasco, D. W., & Walters, M. (2015). The Northwest Geysers EGS Demonstration Project, California - Part 2: Modeling and interpretation. *Geothermics*, 63, 120–138. <https://doi.org/10.1016/j.geothermics.2015.08.002>
- Saló, L. (2016). Improving the knowledge of the 2013 Castor UGS (Spain) seismic sequence from a seismological and geomechanical standpoint. *Master Final Thesis*.
- Sameting, K. (2009). How to invest in geothermal. *Renewable Energy Focus*, 9(7), 84–86. [doi:10.1016/s1755-0084\(09\)70048-1](https://doi.org/10.1016/s1755-0084(09)70048-1)
- Schill, E., Genter, A., Cuenot, N., & Kohl, T. (2017). Hydraulic performance history at the Soultz EGS reservoirs from stimulation and long-term circulation tests. *Geothermics*, 70, 110–124. <https://doi.org/10.1016/j.geothermics.2017.06.003>
- Scholz, C. (2002). *The mechanics of earthquakes and faulting* (2nd editio). New York: Cambridge University Press.
- Shah, M., Vaidya, D., & Sircar, A. (2018). Using Monte Carlo simulation to estimate geothermal resource in Dholera geothermal field, Gujarat, India. *Multiscale and Multidisciplinary Modeling, Experiments and Design*. <https://doi.org/10.1007/s41939-018-0008-x>
- Shapiro, S. A., Dinske, C., & Langenbruch, C. (2010). Seismogenic index and magnitude probability of earthquakes induced during reservoir fluid stimulations. *The Leading Edge - Special Section: Microseismic*, 304–309.
- Siler, D. L., Hinz, N. H., Faulds, J. E., & Queen, J. (2016). 3D analysis of geothermal fluid flow favorability: Brady's, Nevada, USA. *The 41st Workshop on Geothermal Reservoir Engineering, Stanford University*, SGP-TR-209.
- De Simone, S., Vilarrasa, V., Carrera, J., Alcolea, A., & Meier, P. (2013). Thermal coupling may control mechanical stability of geothermal reservoirs during cold water injection. *Physics and Chemistry of*

the Earth, 64, 117–126. <https://doi.org/10.1016/j.pce.2013.01.001>

- Tester, J. W., Anderson, B. J., Batchelor, A. S., Blackwell, D. D., & DiPippo, R. (2006). The Future of Geothermal Energy - Impact of Enhanced Geothermal Systems (EGS) on the United States in the 21st Century. *MIT - Massachusetts Institute of Technology*, 358.
- Trumpy, E., Botteghi, S., Caiozzi, F., Donato, A., Gola, G., Montanari, D., Pluymaekers, M.P.D., Santilano, A., van Wees, J.D., & Manzella, A. (2016). Geothermal potential assessment for a low carbon strategy: A new systematic approach applied in southern Italy. *Energy*, 103, 167–181. <https://doi.org/10.1016/j.energy.2016.02.144>
- Vidal, J., Genter, A., & Chopin, F. (2017). Permeable fracture zones in the hard rocks of the geothermal reservoir at Rittershoffen, France. *Journal of Geophysical Research: Solid Earth*, 1–24. <https://doi.org/10.1002/2017JB014331>
- Vilarrasa, V., De Simone, S., Carrera, J., & Villaseñor, A. (2021). Unraveling the Causes of the Seismicity Induced by Underground Gas Storage at Castor, Spain. *Geophysical Research Letters*, 48, 1–10. <https://doi.org/10.1029/2020GL092038>
- Wang, X., & Ghassemi, A. (2012). A 3D thermal-poroelastic model for geothermal reservoir. In *Thirty-Seventh Workshop on Geothermal Reservoir Engineering*. Stanford University, Stanford, California.
- Wang, Y., Li, X., & Zhang, B. (2016). Numerical Modeling of Variable Fluid Injection-Rate Modes on Fracturing Network Evolution in Naturally Fractured Formations. *Energies*, 9(6), 414. <https://doi.org/10.3390/en9060414>
- Weiss, M. (2008). Techniques for estimating fracture size: A comparison of methods. *International Journal of Rock Mechanics and Mining Sciences*, 45(3), 460–466. <https://doi.org/10.1016/j.ijrmms.2007.07.010>
- White, M., Fu, P., McClure, M., Danko, G., Elsworth, D., Sonnenthal, E., Kelkar, S., & Podgorney, R. (2018). A suite of benchmark and challenge problems for enhanced geothermal systems. *Geomechanics and Geophysics for Geo-Energy and Geo-Resources* (Vol. 4). Springer International Publishing. <https://doi.org/10.1007/s40948-017-0076-0>
- Yoon, J. S., Zimmermann, G., & Zang, A. (2015). Discrete element modeling of cyclic rate fluid injection at multiple locations in naturally fractured reservoirs. *International Journal of Rock Mechanics and Mining Sciences*, 74, 15–23. <https://doi.org/10.1016/j.ijrmms.2014.12.003>
- Zhang, F., Nagel, N., Lee, B., & Sanchez-Nagel, M. (2013). Fracture Network Connectivity — A Key To Hydraulic Fracturing Effectiveness and Microseismicity Generation. *Effective and Sustainable Hydraulic Fracturing*. <https://doi.org/10.5772/56302>
- Zhang, L., & Einstein, H. (2000). Estimating the intensity of rock discontinuities. *International Journal of Rock Mechanics and Mining Sciences*, 37(5), 819–837. [https://doi.org/10.1016/S1365-1609\(00\)00022-8](https://doi.org/10.1016/S1365-1609(00)00022-8)
- Zhang, Z., & Li, X. (2016). Numerical Study on the Formation of Shear Fracture Network. *Energies*, 9(4), 299. <https://doi.org/10.3390/en9040299>
- Zhang, Z., Li, X., Yuan, W., He, J., Li, G., & Wu, Y. (2015). Numerical analysis on the optimization of hydraulic fracture networks. *Energies*, 8(10), 12061–12079. <https://doi.org/10.3390/en81012061>
- Zhao, X. P., & Young, R. P. (2011). Numerical modeling of seismicity induced by fluid injection in naturally fractured reservoirs. *Geophysics*, 76(6), Wc167-Wc180. <https://doi.org/10.1190/Geo2011-0025.1>
- Zielke, O., Galis, M., & Mai, P. M. (2017). Fault roughness and strength heterogeneity control

earthquake size and stress drop. *Geophysical Research Letters*, 777–783.
<https://doi.org/10.1002/2016GL071700>

Capítol 2

2 Rate-and-State friction law and slip regimes analysis of a single fluid pressurized fault. Comparison between thermal-hydromechanical continuous (Toughreact-Flac3D) and discontinuous (CFRAC) modelling.

2.1 Introduction

Fluid injection into subsurface reservoirs has the risk of inducing earthquakes. In recent years, the increase of subsurface geoengineering operations has largely increased injection-induced earthquakes and has caused a social impact on these projects. Examples are related to diverse energy applications, such as due to stimulation in geothermal reservoirs (Gaucher et al., 2015; Grigoli et al., 2018; Kwiatek et al., 2019; Majer et al., 2007), wastewater disposal (Norbeck & Rubinstein, 2018; Yeck et al., 2016), shear gas – oil operations (Atkinson et al., 2016; Hui et al., 2021), gas storage (Saló et al., 2017; Vilarrasa et al., 2021), gas extraction (Dempsey & Suckale, 2017), or CO₂ sequestration (Johnson & Morris, 2009; Stork et al., 2015; Vilarrasa et al., 2019). In this context, diverse processes are involved when seismicity is triggered by pressure build up, as the increase of pore pressure (Norbeck & Rubinstein, 2018; Schill et al., 2017), Coulomb stress change (Catalli et al., 2016), or porothermoelastic effects (Gan & Lei, 2020; Norbeck & Horne, 2015). If we focus on the exploration and production of geothermal reservoirs, careful consideration of the coupled thermal-hydro-mechanical (THM) processes must be done to correctly model all the potential effects related to fluid flow, permeability evolution, and heat transfer in the system. Moreover, such effects are also critical to predict and minimize induced seismicity associated with fluid injection during stimulation phases of Enhanced Geothermal Systems (EGS).

In general, injection-induced earthquakes in EGS are low magnitude earthquakes (and normally called “micro-seismicity”), but occasionally relative large magnitude have been observed such as the Basel Mw=3 earthquakes between 2006 and 2007, or the Pohang Mw=5.5 in 2017. To prevent large magnitude seismicity, several operation strategies have been developed to maintain fluid pressure below a critical threshold (e.g. Hofmann et al., 2019). However, in general, these approaches do not consider the conditions which control the evolution of nucleation and/or arrest of the rupture or the transitions between seismic or aseismic slips (Bie & Ryder, 2014; Cappa et al., 2019).

From a theoretical point of view, the pioneering work by Garagash and Germanovich (2012) established the basics of the conditions for nucleation and arrest during dynamic slip on a non-dilatant, frictional pressurized 2D fault. Posteriorly, this work was extended to include hardening dilatancy effects by Ciardo and Lecampion (2019), the relationship between hydraulic fracturing injection, and the potential of a seismic slip by Azad et al., (2017), or generalization to planar 3D faults by Galis et al., (2017). All these approaches are based on a linear weakening of the frictional coefficient with slip. However, experimental

data indicate that phenomenological more complex frictional behaviour is required to include conditions in which the friction coefficient evolves dynamically and, therefore, allows reproducing the seismic cyclicity (i.e. from the pre-seismic and earthquake nucleation to the coseismic and post-seismic stages; e.g. Dieterich & Kilgore, 1994; Rubín & Ampuero, 2005). For this reason, a friction evolution model based on the rate-and-state constitutive law is potentially a more capable way to simulate friction evolution due to changes in slip velocity along a pressurized fault.

Other critical issues are the way that the fracture is simulated and the strategy in which the coupled thermal-hydraulic-mechanical (THM) problem is solved (e.g. Zareidarmiyán et al., 2020). From a numerical scheme, the problem to treat a fracture zone can be done using continuous or discontinuous mechanical approaches. On the one hand, continuous approaches represent faults using finite thickness elements, and therefore, the approach is limited in the way to describe the discrete nature of faults (i.e. thin surfaces). On the other hand, discontinuous approaches are efficient to handle the discrete nature of faults, but present limitations to simulate the interactions between surrounding medium and fracture (e.g. fluid flow, mechanical behaviour of matrix).

Simultaneous solving of the equations of the full-couple thermal-hydraulic-mechanical (THM) problem is not straightforward, as many of the involved equations imply non-linear relationships. For this reason, strategies based on sequential solving of the THM problem (for example a first step solving the mechanical and then the hydraulic problem) has been proposed to handle it more efficiently.

The goal of this study is to investigate the slip behaviour and induced seismicity due to fluid injection into a dilatant fault using a rate-and-state friction law. For this goal, two different numerical strategies are used to compare results and predictions. On one hand, the THM simulator TOUGHREACT-FLAC3D (TF3D; Taron and Elsworth, 2009) provides a continuum and sequential simulation approach which links the multiphase flow and non-isothermal heat transfer solver TOUGHREACT (Xu et al., 2011) with the geomechanics simulator FLAC3D (Itasca, 2009). TF3D has been used to simulate the thermal drawdown along a fault to trigger fault reactivation (Gan & Elsworth 2014a, 2014b), or to evaluate the role of localized thermal drawdown along faults triggering fault reactivation (Gan & Lei, 2020). A limitation of this simulator is that does not incorporate a rate-and-state frictional behaviour and for this reason, a new approach was implemented in the TF3D approach.

On the other hand, the code CFRAC (McClure & Horne 2011, 2013) provides a fully coupled hydro-mechanical simulator that links the fluid flow with the stresses induced by deformation in discrete fracture networks. This code has been used to investigate the stimulation mechanisms in EGS (McClure & Horne 2014), rupture behaviour propagation and sliding regimes (Gischig, 2015) or pressure drop formation during EGS stimulation (Piris et al., 2018).

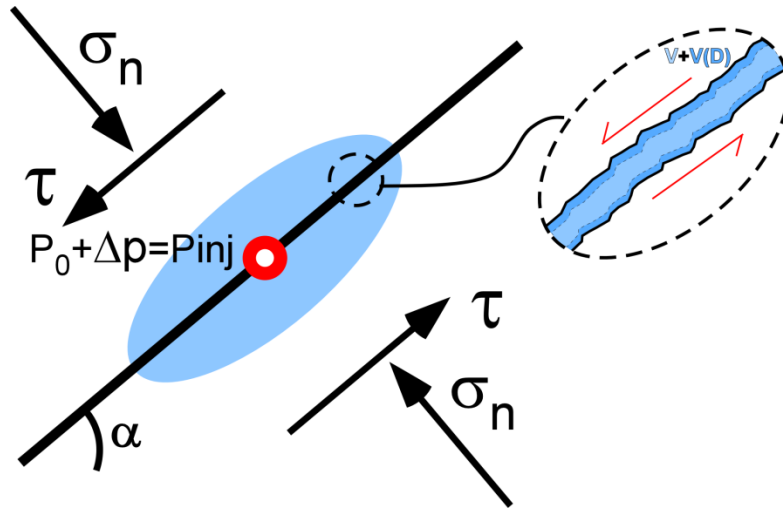


Figure 1. Schematic model of fluid injection in a dilatant and stress-loaded fault. Zoom represents schematically the dilatant process (i.e. increment of fault volume, dV) that occurs during shear displacement (D).

In this work, we use two different modelling approaches (discrete fracture and effective continuum; White et al., 2018) to simulate the fluid injection into a dilatant fault (Segall, 2010) (Fig. 1) using the rate-and-state friction law.

The main aspects investigated using both approaches were (1) the nucleation and arrest of the dynamic slip along stimulated faults, (2) the seismic vs. aseismic behaviour, and (3) the influence of the fault orientation with respect to the main stresses directions.

2.2 Numerical approaches

2.2.1 TOUGHREACT-FLAC3D (TF3D)

TF3D is a sequential coupled thermal-hydro-mechanical numerical code based on the coupling between TOUGHREACT and FLAC3D (Taron and Elsworth, 2009). TOUGHREACT uses a finite volume method to simulate reactive multicomponent and multiphase fluid and heat flow in porous and fractured materials (Pruess & Wu, 1993). FLAC3D (Itasca, 2009) is a mechanical continuum code that solves the stress-strain evolution in an elastic-plastic material using the finite-difference scheme. The sequential approach has been extensively validated and applied to simulate geothermal systems (Taron & Elsworth, 2009; Gan & Elsworth, 2014a, 2014b). The coupling between both codes is facilitated because both codes use the same mesh to simulate the system, and data (permeability, porosity, aperture, effective stress, etc.) only need to be interpolated between elements and nodes. This transfer of data between both codes is done through an external module (Taron & Elsworth, 2009). Additionally, the module also calculates the pressure and temperature dependence on the compressibility of fluids, poroelasticity response to stress, fracture aperture changes to bulk permeability, and evolves fractures according to several constitutive equations.

TF3D has different options to simulate frictional behaviour. The onset of brittle-plastic deformation is mainly based on the Mohr-Coulomb criteria. The onset of shear failure starts when the shear stress exceeds the shear strength. The different approaches implemented in TF3D have the limitations that friction coefficient is constant during deformation or it can only evolve using pre-defining tables between accumulated plastic strain and coefficient friction. Therefore, modifications based on current sliding velocity are unable to incorporate. For this reason, a rate-and-state frictional law was implemented using the internal programming functions incorporated in FLAC3D. The new functions recalculate the dynamic friction coefficient using the current slip velocity during each computational time step (see Supplementary materials for more detail).

Fracture permeability is characterized in TF3D by the Warren-Root model, relating to the fracture aperture b and fracture spacing s as (Warren & Root, 1963):

$$k = \frac{b^3}{12s} \quad (1)$$

The constitutive model for predicting the aperture evolution is governed by the fracture stiffness and effective stress, given as (Min et al., 2009):

$$b_s = b_r + (b_{max} - b_r)e^{(-\gamma(\sigma' - \sigma'_0))} \quad (2)$$

where, b_r represents the residual aperture (m), b_{max} is the maximum aperture at zero stress level (m), and γ is the non-linear fracture stiffness (1/ MPa). To consider the shear dilatancy effect, the shear displacement in fractures D contributes to increasing the normal aperture b_{dila} according to the following equation:

$$b_{dila} = D \tan \varphi_{dil} \quad (3)$$

where, φ_{dil} is the fracture dilation angle. Thus, b is the sum of b_s and b_{dila} and Eq (1) includes both normal closure and shear dilation effects.

2.2.2 CFRAC

CFRAC (Complex Fracturing ReseArch Code; McClure, 2012) is a two-dimensional discrete boundary element that solves the fully coupled hydro-mechanical problem related to the fluid injection through a fracture network embedded in an impermeable matrix (McClure & Horne 2011, 2013, 2014). Additionally, CFRAC can also handle the location and magnitude calculation of the associated induced seismicity using sliding velocity thresholds. CFRAC has been extensively benchmarked and validated (e.g. White et al. 2016) and used in multiple geothermal applications (Gischig, 2015; McClure & Horne, 2014; Norbeck et al., 2018; Piris et al., 2017). The code incorporates a rate-and-state frictional law, and it will be used as the reference solution to compare with the TF3D predictions.

CFRAC initializes the simulations assuming initial homogeneous, anisotropic stress field conditions and homogeneous fluid pressure distribution. It can simulate both pre-existing fractures and new hydraulically-formed fractures, although the location of potentially new forming fractures is defined in advance. The frictional resistance to slip is given by Coulomb's law (Segall, 2010):

$$|\tau - \eta v| = \mu_f (\sigma_n - P_f) + S_0 \quad (6)$$

where τ is the shear stress, η is the radiation damping coefficient, v is the sliding velocity of the fracture walls, μ_f is the friction coefficient, σ_n is the normal stress, P_f is the fluid pressure and S_0 is the fracture cohesion. The evolution of the friction coefficient is done using a rate-and-state formulation where friction coefficient depends on the sliding velocity and the sliding history of the fracture (Scholz, 2002; Segall, 2010). In terms of aperture changes due to fluid pressure and/or slip, the approach evaluates separately the changes in fracture conductivity (i.e. hydraulic aperture “ e ”) and pore volume (i.e. void or mechanical aperture “ E ”) using similar equations. but using different dilatation angles and constant values for the hydraulic or mechanical aperture cases (McClure 2012).

Fracture permeability is evaluated using the cubic law (Jaeger et al., 2007):

$$k = \frac{e^2}{12} . \quad (7)$$

The aperture of a closed fracture is defined as (Willis-Richards et al., 1996; Rahman et al., 2002; Kohl & Mège, 2007):

$$e = \frac{e_0}{1+9\sigma'_n/\sigma_{enref}} + D \cdot \frac{\tan(\phi_{edil})}{1+9\sigma'_n/\sigma_{enref}} + e_{res} \quad (8)$$

where, e_0 , σ'_n , σ_{enref} , ϕ_{edil} and e_{res} are the initial hydraulic aperture, normal effective stress, reference normal traction stress (is the effective normal stress applied to cause a 90% reduction in the compliant aperture), dilation angle, and residual hydraulic aperture respectively. Thus, hydraulic aperture takes into account both normal closure and shear dilation effects.

2.3 Methods

In this section, the theoretical definition of the rate-and-state friction law is presented, together with benchmarking of the numerical approach. Following, the configuration setups used for the different simulations are explained.

2.3.1 Rate-and-state friction law

Different experimental studies have shown that the friction coefficient does not only depend on the strain or accumulated displacement, but also on the sliding velocity and the holding time after the last displacement (Fig. 2) (Dieterich & Kilgore, 1994; Rubín & Ampuero, 2005; Segall, 2010). The rate-and-state friction law (Dieterich & Kilgore, 1994; Scholz, 2002; Segall, 2010) relates the evolution of friction

coefficient as a function of sliding velocity and a state variable depending on the aging and expressed as:

$$\mu_f = f_0 + a \cdot \ln\left(\frac{v}{v_0}\right) + b \cdot \ln\left(\frac{\theta v_0}{d_c}\right) \tag{9}$$

where, f_0 , v_0 , a , b , and d_c are material constants and v is the sliding velocity. The variable d_c accounts for the characteristic displacement scale. The parameters a and b are around 0.01, much smaller than f_0 , which has values between 0.6 and 0.9. Their relatively small value is consistent with the observation that only a fraction of the stress borne by a fracture is usually released during a seismic event. Conceptually, the a and b values are related with the friction coefficient reduction due to the sliding velocity change and the d_c with the sliding displacement required to stabilize the friction coefficient (Dieterich & Kilgore, 1994) (Fig. 2).

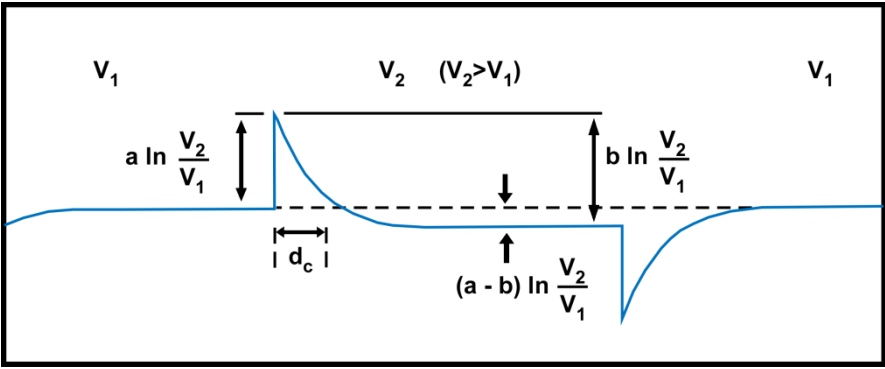


Figure 2. Example of the friction coefficient response with slip velocity predicted by Eq (9) and Eq (10) (Dieterich & Kilgore, 1994).

Under a rate-and-state framework, all fractures slip at all times. However, fractures can have very low slip velocities (or aseismic), which are physically meaningless on the time scale of hydraulic stimulation. However, this does not produce a critical issue because these fractures behave approximately as if they were locked.

The state variable can be interpreted as the average contact time of asperities on the fault. The “aging law” of state evolution θ is defined as (Segall, 2010):

$$\frac{d\theta}{dt} = 1 - \theta \frac{v}{d_c} \tag{10}$$

Dieterich (1979) associated the state variable with the asperity contact time. Dieterich and Kilgore (1994) experimentally demonstrated that the surface contact area increases with the contact time due to the creep of asperities. This rate-and state-friction law is widely used to describe and simulate fracture sliding and earthquake nucleation (e.g. Abe et al., 2002; Avouac & Al, 2017; Cueto-Felgueroso et al., 2017; Elst & Savage, 2015; Gischig, 2015; McClure, 2012; Norbeck et al., 2018; Piris et al., 2018; Rice, 1993; Romanet et al., 2018; Rubin & Ampuero, 2005).

2.3.2 Model set-up: rate-and-state benchmark

To validate the rate-and-state implementation in TF3D code, we performed a numerical simulation consisting of a single, horizontal, weak, and planar fault immersed in a homogeneous elasto-plastic matrix (Fig. 3). The mechanical behaviour of the fault was defined using a linear strain-hardening/softening ubiquitous-joint plasticity model with a Mohr-Coulomb as the plastic envelope. The joint friction coefficient property was used to implement the rate and state law according to the parameters shown in Table 1 (values for the benchmark scenario). The rest of the sample follows a strain-hardening/softening plasticity model with a Mohr-Coulomb envelope with a constant friction coefficient high enough to prevent sliding on it.

We applied constant velocity boundary conditions in one of the fault walls. During the simulation, the velocity was several times modified and the evolution of the frictional coefficient with time was registered to compare with the analytical solution described by Eq (9) and Eq (10) (Fig. 2).

This simulation reproduces a cubic elongated sample with a weak plane in dry conditions (Fig. 3). The dimensions of the model are $X=1$ m, $Y=0.1$, and $Z=0.2$ m. The weak plane is indicated by the red line. The boundary conditions were defined by fixing the block below the weak plane and forcing it to slide the upper part of the sample at a fixed controlled velocity imposed on the upper left side part of the sample (Fig. 3). The condition of no displacement in Z directions is imposed on the vertical side of the model.

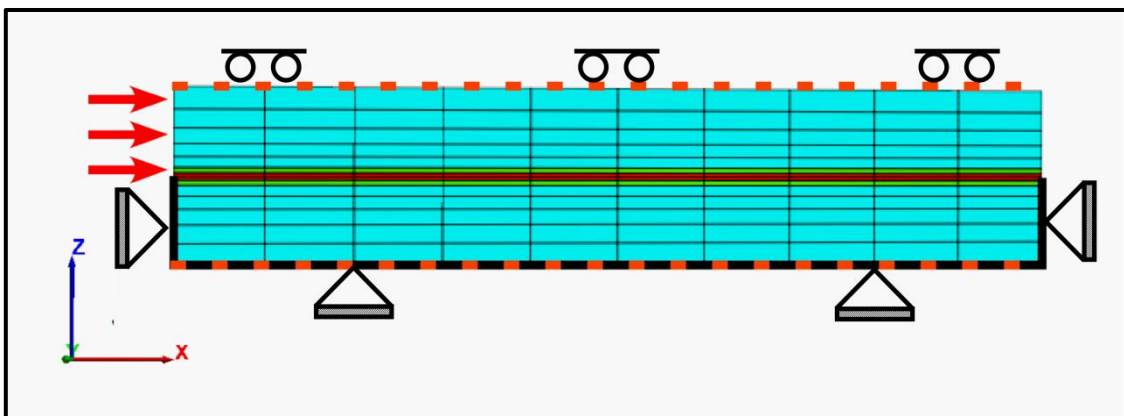


Figure 3. Geometry of the model used for benchmarking the rate-and-state approach. The model consists in a single horizontal fault (red line) immersed in a homogenous matrix. The model dimensions were $X=1$, $Y=0.1$ m, and $Z=0.2$ m. The solid black lines and dashed orange lines indicate the regions with X and Z displacements fixed, respectively. The Y displacement (i.e. out-of-plane direction) was fixed in the entire domain. On the left upper part, the sliding velocity was fixed (as indicated with red arrows).

2.3.3 Model set-up TF3D and CFRAC: slip regime analysis

To test the influence of the modelling approach (sequential continuous vs. full-coupled discontinuous) on the slip regime behaviour, we tested a series of models of a single fracture immersed in a homogenous

matrix. The fracture is defined in all simulations with a length of 600 m, with a fractured core with a thickness of 0.8m and surrounded by a fractured damage zone of 0.6m thickness (Fig. 4). The tips of the fracture do not reach boundary conditions to prevent potential numerical instabilities (Fig. 4). The dimensions of the models are variable attending the fracture orientation (α) and x ranges approx. from 310 - 760 m, Z ranges 600-800 m, and the length in the direction normal to the model (i.e. y-direction) is always 100 m. The mesh is defined using hexahedral elements, with a resolution of 20 elements in the x-direction, 80 elements in the z-direction, and 2 elements in the y-direction. The element size varies in function of the orientation and distance to the fracture, with a refinement near to the fracture.

A strike-slip stress field was applied, with the maximum compressive stress $\sigma_1= 50$ MPa parallel to the z-direction, the minimum compressive stress $\sigma_3= 29$ MPa parallel to the x-direction, while $\sigma_2= 45$ MPa is applied normal to the model section. The orientation of the fracture α is defined as the angle between the normal of the fracture respect to σ_1 (Fig. 4). To evaluate the transition between dynamic seismic ruptures to aseismic slip conditions or the capacity of the seismic rupture to propagate/arrest along a fracture, models with different orientations of the fracture to the stress field were done. To test realistic conditions to geothermal reservoir fields, these simulations were done using stress conditions close to those observed at the Rittershoffen geothermal reservoir (Baujard et al., 2017; Cornet et al., 2007; Meyer et al., 2017).

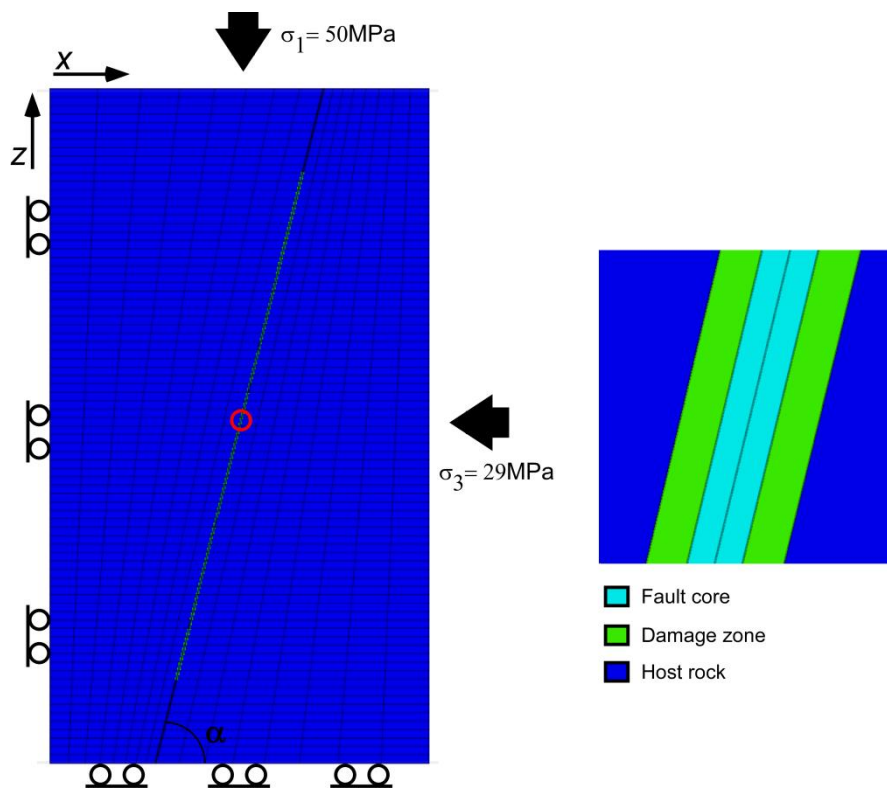


Figure 4. Geometry, mesh and boundary conditions of the models to explore slip regimes. The fault is simulated as a fault core and a damage zone, inside a homogenous host rock. Example for a fault with $\alpha=76^\circ$. Free-slip parallel to the boundaries is used for the left and bottom sides. Red circle indicates the injection point.

For boundary conditions, the left and basal sides are implanted using free-slip conditions with free-displacement parallel to the boundaries. The displacement out-of-plane is not allowed on top and bottom sides (y position fixed).

Fault core elements were simulated using an elasto-plastic ubiquitous-joint model implemented in FLAC3D. This model assumes Mohr-Coulomb criterion and shear failure takes place when the shear stress exceeds the shear strength. Here, we use the new implementation in which the joint friction coefficient evolves following the rate-and-state law. The fault damage zones and the host rock domains were simulated using the elasto-plastic strain-hardening/softening model. Table 1 summarizes the material properties of the different materials and the rate-and-state parameters (see Table 1 for the rate-and-state parameters and material properties).

The water was injected in the middle of the fault damage zone at a constant pressure of 26 MPa (P_{inj}). An additional series was done using $P_{inj}=28\text{MPa}$. The initial temperature field was set as uniform at 190 °C, and the initial pore pressure (P_0) was defined as 23MPa. To avoid overpressure excess at the boundaries of the model, a condition of extraction of fluid (withdrawal wells at pressure 1MPa below the P_{inj}) was placed at both fault tips. At the level of permeability, the fault core is considered low permeability ($k=1\text{e-}15\text{m}^2$), flanked by high-permeability $k=1\text{e-}12\text{m}^2$ damage zones (Faulkner et al., 2003; Gan & Lei, 2020). The host rock has a very low permeability $k=1\text{e-}16\text{m}^2$ to keep the fluid preferentially within the fault. Implicit time-stepping was used, spanning time steps from 10s to 1e-2s (reduced to prevent numerical stability during seismic stages).

The set-up of CFRAC models was very similar to that used in TF3D. In this case, a 600 m length fault discretized using constant 0.5 m long elements. A constant “thickness” of 100 m was considered in the out-of-plane direction of the model. Matrix was considered impermeable and isotropic, and it was not discretized. Therefore, injected fluid is only allowed to flow along the fracture. The stress state, injection pressures, parameters of the rate and state equations, and range of fault orientations were similar to TF3D models (Table 1). Some difference between codes exists in the way to simulate the hydraulic aperture. The initial parameters were selected to produce initial fault permeability similar to the imposed in the damage zone of the TF3D model.

In CFRAC models the edges of the model were treated like no-flow boundaries. The stresses induced by deformation were calculated assuming an elastic whole-space. The model was initialized with a homogeneous distribution of fluid pressure and stress, and the stress field was permitted to be anisotropic. At each element during every time step, the fluid pressure, and opening and sliding displacements were calculated to satisfy the steady-state mass balance equation and stress conditions. An implicit time-stepping was used, spanning time steps from 10s to 1e-5s.

Rate and state parameters for joint core fault zones	Parameter	Values for the benchmark scenario	Values for the fluid injection scenarios	
	f_0	0.8	0.8	
	a	0.01	0.01	
	b	0.02	0.015	
	dc	1e-4m	1e-5m	
	v_0	1e-6 m/s	1e-5 m/s	
	θ_0	100s	2.6e3s	
Material properties for TOUGHREACT-FLAC3D	Parameters	Host Rock	Fault damage zone	Fault core zone
	Matrix permeability, m^2 (k)	1e-16	1e-12	1e-15
	Fracture permeability, m^2 (k)	7.7e-15	7.7e-11	7.7e-14
	Bulk modulus, GPa	25	25	25
	Poisson ratio	0.25	0.25	0.25
	Fracture spacing, m	13	0.1	0.3
	Cohesion, MPa	1	0.1	0.1
	Porosity	0.01	0.3	0.01
	Matrix friction angle, deg	40	40	40
	Tensile strength, MPa	0.1	0.1	0.1
	Joint cohesion MPa	-	-	0
	Joint tensile strength, MPa	-	-	0
	Rock density, kg/m^3	2490	2490	2490
	Dilation angle (ϕ_{dil}), degrees	5	5	5
	Non-linear stiffness, 1/MPa (γ)	0.218	0.218	0.218
Residual aperture, m (b_r)	2.12e-5	9.03e-5	1.33e-5	
Maximum aperture, m (b_{max})	1.06e-4	4.52e-4	6.50e-5	
Material properties for CFRAC	Initial mechanical aperture (E_0)	-	-	1.2 e-3 m
	Reference normal traction (mechanical aperture) (σ_{Enref})	-	-	25 MPa
	Residual mechanical aperture (E_{res})	-	-	2.6e-6 m
	Dilatation angle (mechanical aperture) (ϕ_{Edil})	-	-	5°
	Initial hydraulic aperture (e_0)	-	-	4.52 e-4 m
	Reference normal traction (hydraulic aperture) (σ_{enref})	-	-	25 MPa
	Residual hydraulic aperture (e_{res})	-	-	9.03e-5 m
	Dilatation angle (hydraulic aperture) (ϕ_{edil})	-	-	5°
	Radiation damping coefficient (η)	-	-	3 MPa/(m/s)
	Cohesion (S_0)	-	-	0 MPa
Shear modulus (G)	-	-	15 GPa	

Table 1. Material and frictional properties for the simulations. The Poisson ratio is the same for both simulation approaches.

2.4 Results

2.4.1 Benchmark model

The comparison between the benchmark simulation and the theoretical solution is shown in Fig. 4. The friction coefficient evolution was calculated using equation 9 and 10 (red curve, Fig. 4) and compared with numerical simulation (blue curve Fig. 4). The reference element used to calculate was the first left zone on the weak plane. The initial sliding velocity was fixed to $v_1=1e-6$ m/s, changed to $v_2=1e-5$ m/s after 15 seconds, and was reduced again to the initial v_1 after 140 seconds. This cycle was repeated also at 500, 625, 950, and 1075 s. Although the results are quite similar between the numerical and the theoretical response, the numerical results tend to be more conservative both during hardening and

softening peaks. However, differences between theoretical and numerical solutions are reduced during the second and third cycles.

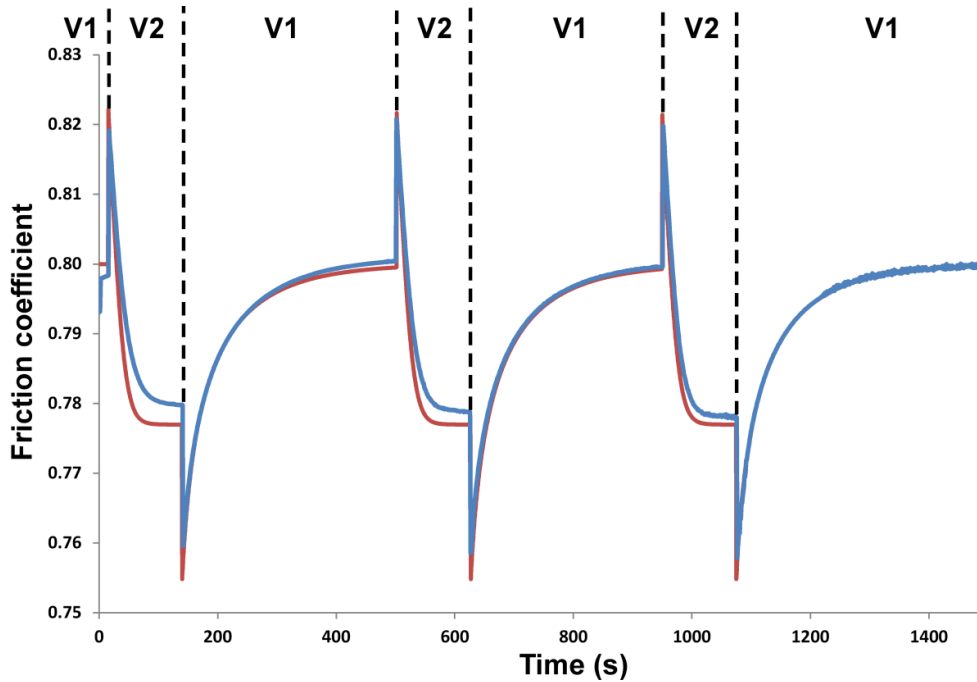


Figure 5. Friction coefficient evolution on the weak plane with the sliding velocity changes. The red curve describes the theoretical response while the blue the obtained from numerical simulation. The adjustment of both curves during the second and third cycles are satisfactory.

2.4.2 Slip regimes: TF3D

The evolutions of the friction coefficient in the injection point for the different fault orientations are shown in Fig. 6. As expected, the friction coefficient evolves in different ways according to the fault orientation (α). For a fracture with $\alpha=85^\circ$ (i.e. subparallel to maximum compressive direction), the fluid injection produces an initial stage of hardening (an increase of the friction coefficient), followed by a moderate reduction. This friction reduction is related to a peak of the sliding velocity of $1e-4m/s$ (Fig. 6A), after which the velocity gets reduced to below $1e-6m/s$ and remains approximately constant throughout all the simulation, keeping the friction coefficient near-constant (approx. 0.825), although small oscillations are visible (Fig. 6A). For the case with $\alpha=80^\circ$, the simulation starts with a friction hardening followed by a gradually weakening. The friction drop is related to a peak of the sliding velocity of $5e-4m/s$. However, after the sliding velocity peak, the velocity is reduced below $1e-5m/s$ and continuously oscillates close to this value throughout the whole simulation (Fig. 6B). The friction value also oscillates but is always above a value of 0.8 (Fig. 6B). For the $\alpha=76^\circ$, the simulation shows an initial friction hardening followed by a sudden weakening related to a peak velocity of $5.3e-3m/s$ (Fig. 6C). After this initial weakening stage, the friction coefficient recovers and remains constant until the time step 125. After this period, characterized by constant values, a series of non-steady cycles are observed (Fig. 6C). In the $\alpha=65^\circ$ case, the simulation starts with a strong hardening (Fig. 6D) followed by a sudden weakening related to

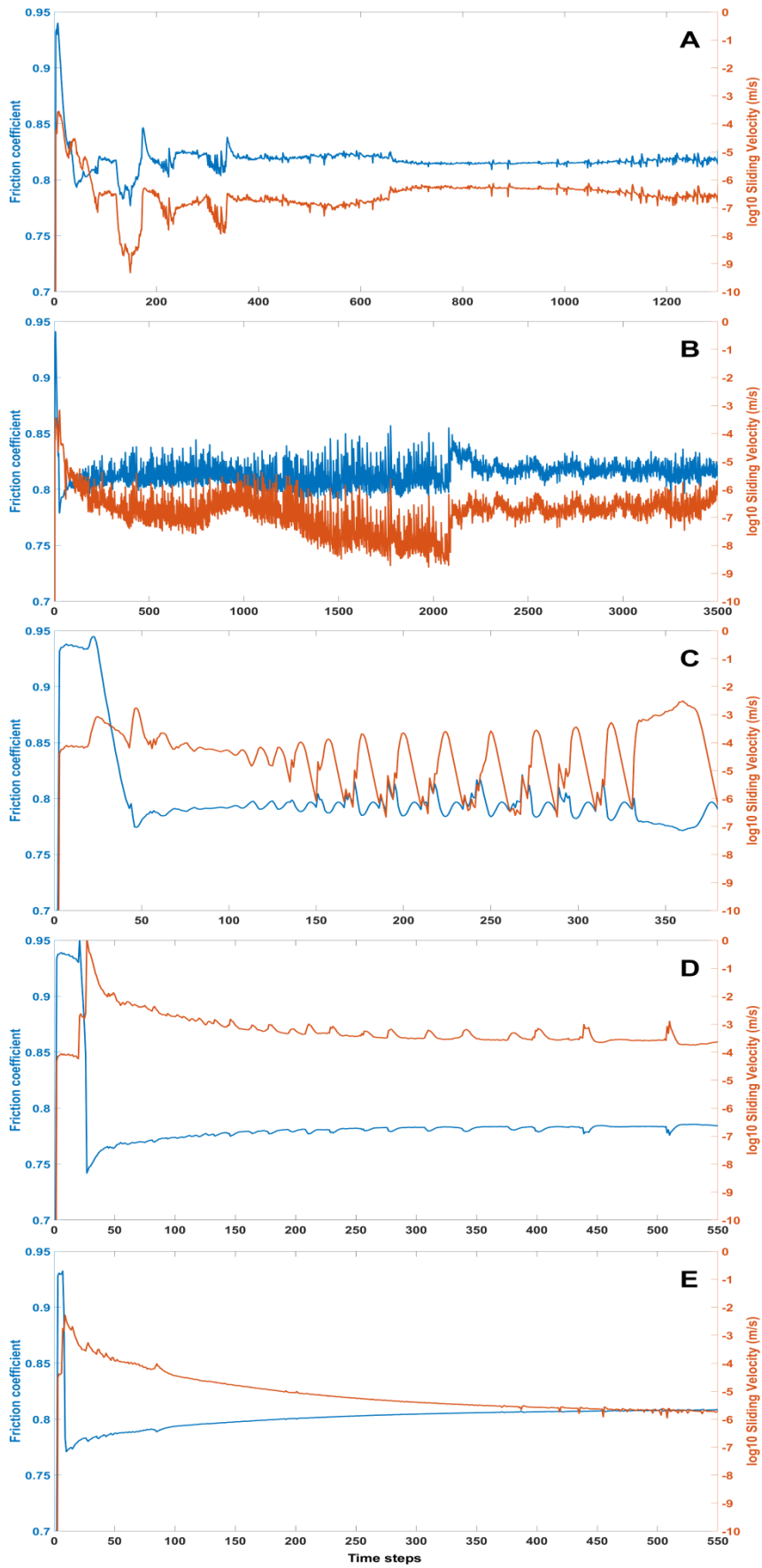


Figure 6. Evolution of the friction coefficient (blue curve) and the sliding velocity (red curve) in the injection point predicted by TF3D. A. $\alpha=85^\circ$, B. $\alpha=80^\circ$, C. $\alpha=76^\circ$, D. $\alpha=65^\circ$, and E. $\alpha=50^\circ$.

a peak velocity of 0.5 m/s (Fig. 6D). Then the friction value progressively recovers until it reaches a value of 0.79 with small quickly drops of 0.01 (Fig. 6D). Finally, the model for $\alpha=50^\circ$ fracture starts with a hardening followed by weakening (Fig, 6E) related to a sliding velocity peak of $8e-3$ m/s (Fig. 5E). After this weakening, the friction coefficient progressively recovers until it reaches a value of 0.81, only showing some friction small drops until the time step 100 (Fig. 6E).

To understand the behaviour of the entire fracture domain for the different fault dips, the sliding velocity and the fluid pressure evolution are shown for $\alpha=80^\circ$ (Fig. 7A-B), 76° (Fig. 7C-D), 65° (Fig. 7E-F) and 50° (Fig. 7G-H) models. The injection point for all the configurations was located at $Y=5$ m. Following the predefined thresholds on sliding velocity, a seismic event is when the sliding velocity is higher than $1e-3$ m/s and is considered aseismic if the sliding velocity is below this value (McClure, 2015; Romanet et al., 2018). Seismic events are easier to detect in the skidding velocity field, and it's marked by sharp and high velocities propagating along the fault.

For the $\alpha=80^\circ$ case, the fluid pressure front shows a progressive expansion through the whole fracture with the development of a low-pressure gradient. In the pressurized zone, the sliding velocity indicates a continuous sliding at aseismic velocities between $1e-5$ and $1e-6$ m/s. The $\alpha=76^\circ$ model starts with a period where the fluid pressurization is limited near the injection point. Around the time step equal to 50, the pressure front starts to expand progressively and constantly with a moderate pressure gradient, until the time step 350 where the pressure front expands abruptly and expands to the entire fracture. These changes in fluid pressure are also observed in the evolution of the sliding velocity. In the beginning, low-to-medium velocities ($1e-5$ to $1e-3$ m/s) are observed along the entire fracture. However, close to the injection point, the sliding velocities reached seismic values close to the $1e-3$ m/s, and therefore eventually nucleate a micro-seismic event, but the rest of the fracture remains with low velocities. Cyclic periods with increasing-decreasing velocity and expansion through fracture are observed, with increasing the affected fracture length with increasing simulation time. A drop in the velocities is observed when the pressurization front is crossed. While the sliding velocities are near seismic conditions inside the pressurization zone (approx. $1e-3$ m/s), the velocities are aseismic (approx. $1e-5$ m/s) beyond the pressurized region. When the pressurized front almost reaches the fault tips, the propagation of the higher velocities can expand along the entire fracture with velocities around or higher than $1e-3$ m/s, Therefore all the fracture is stimulated and velocities decreases to values of $1e-5$ m/s.

For $\alpha=65^\circ$ the pressurized region is limited close to the injection point while the entire fault can slide seismically at high velocities (>1 m/s). After a sharp seismic rupture at the beginning of the simulation, the sliding velocity is reduced in seismic and intersismic cycles of $1e-4$ m/s. Finally, for $\alpha=50^\circ$ the pressurized region is limited to the injection point until the pressure gradient is too high (approx. time step 50), to expand quickly the entire fracture. This expansion of the pressurized front expansion is

related to a previous seismic event nucleated in the injection point and able to propagate along the entire fracture up to the tips. After this seismic event the sliding velocity decreases, showing values of $1e-5$ and $1e-6$ m/s.

Although in general fluid pressure and sliding velocity tend to show a symmetric distribution to the injection point, higher velocities are observed in the upper part of the model (Y positive values in Fig. 7) respect to the lower part of the model.

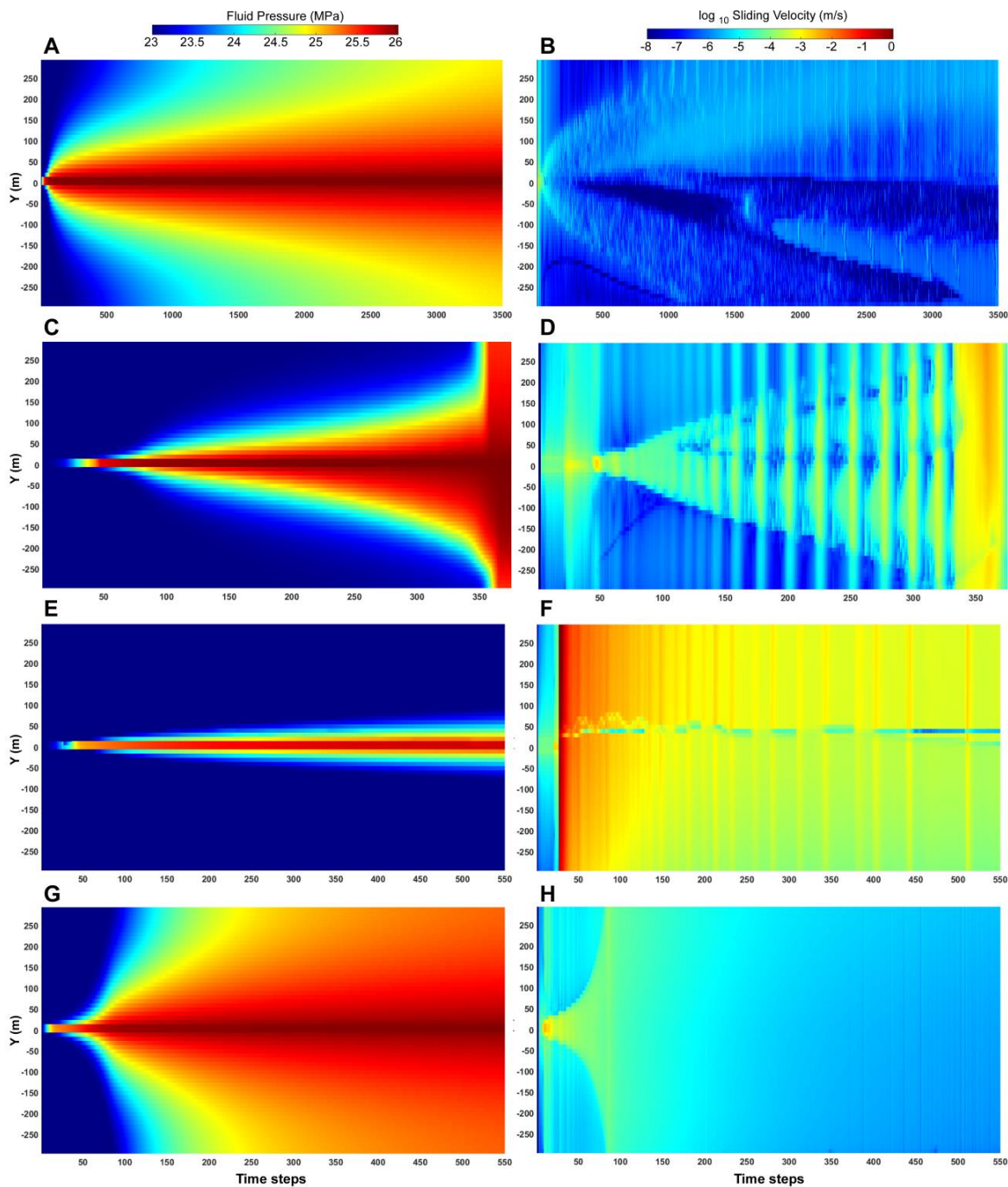


Figure 7. Fluid pressure (MPa) and sliding velocity (m/s) along fracture length and time steps for TF3D model; $\alpha = 80^\circ$ (A-B), $\alpha = 76^\circ$ (C-D), $\alpha = 65^\circ$ (E-F) and $\alpha = 50^\circ$ (G-H).

2.4.3 Slip regimes: CFRAC

The evolution of the friction coefficient in the injection point is shown in Fig. 8, while the evolution of fluid pressure and sliding velocities along the fracture are shown in Fig. 9.

For the case of a fracture with $\alpha=85^\circ$, the evolution of the friction coefficient shows a stable and slight increase (Fig. 8A). The sliding velocity of this simulation is nearly constant, with values equal to $1e-10$ m/s. For the $\alpha=80^\circ$ model, the friction starts with a hardening followed by a weakening, related to a peak velocity close to $1e-2$ m/s. A series of sudden ups and downs in the frictional behaviour are observed after the initial weakening. However, after some time (approx. time step 150), the friction behaviour becomes more stable and follows an increasing tendency with variations related with low velocity peaks between $1e-5$ m/s and $1e-6$ m/s (Fig. 8B). The $\alpha=76^\circ$ case starts with a hardening followed by a weakening and by a series of seismic cycles related to peak velocities of $1e-2$ m/s. These cycles are repeated up to the friction coefficient becomes more stable (approx. time step 125) and the friction oscillations are related to relative low sliding velocities of $1e-5$ m/s (Fig. 8C). The $\alpha=65^\circ$ case starts with a hardening followed by a prolonged weakening related to an instability with a peak velocity of $6e-2$ m/s. After this weakening (time step 100), there are some friction oscillations related to sliding velocity reduction to $1e-5$ m/s. Then the friction coefficient becomes constant at a value of 0.77 with some small drops related to seismic events with velocities of $1e-2$ m/s (Fig. 8D). Finally, the fracture with a dipping angle of $\alpha=50^\circ$ starts with three cycles of hardening-weakening related to seismic velocities of $1.5e-1$ m/s. After these events, the friction coefficient starts to progressively increase and the sliding velocity is kept under $1e-7$ m/s (Fig. 8E).

The $\alpha=80^\circ$ case shows a pressure front that progresses continuously without sharp expansions and with low-pressure gradients. The pressurized region shows cyclic seismicity related to the pressurized front that progressively moves away from the injection point. When the entire fault becomes pressurized, the fracture becomes almost aseismic with low-velocity events (Fig. 9A-B). Reducing the dipping angle to $\alpha=76^\circ$ the behaviour is similar, but now the pressure gradient is higher and the seismicity related with the pressure front is higher too. There is a reduction of the time between seismic and an increase of the sliding velocity (average and peak velocities). The seismicity is not only related to the pressure front but also can propagate inside the pressurized region (Fig. 9C-D). For an orientation of $\alpha=65^\circ$, the simulation starts with a long seismic high-velocity event that propagates through the entire fault with the pressurized region limited almost to the injection point (high seismic events produce a strong reduction of the incremental time step (approx. $1e-5$ s) generating a huge amount of time steps which are traduced in triangle areas e.g. Fig. 8F first 100 time steps). After this initial seismic event, a series of seismic sliding occur propagating beyond the pressurized region (Fig. 9E-F). Finally for $\alpha=50^\circ$ pressure front is also related to the seismic production. However, for this orientation this phenomenon occurs suddenly and with high-velocity ruptures, becoming completely pressurized and relaxed at time step 200 (Fig. 9G-H).

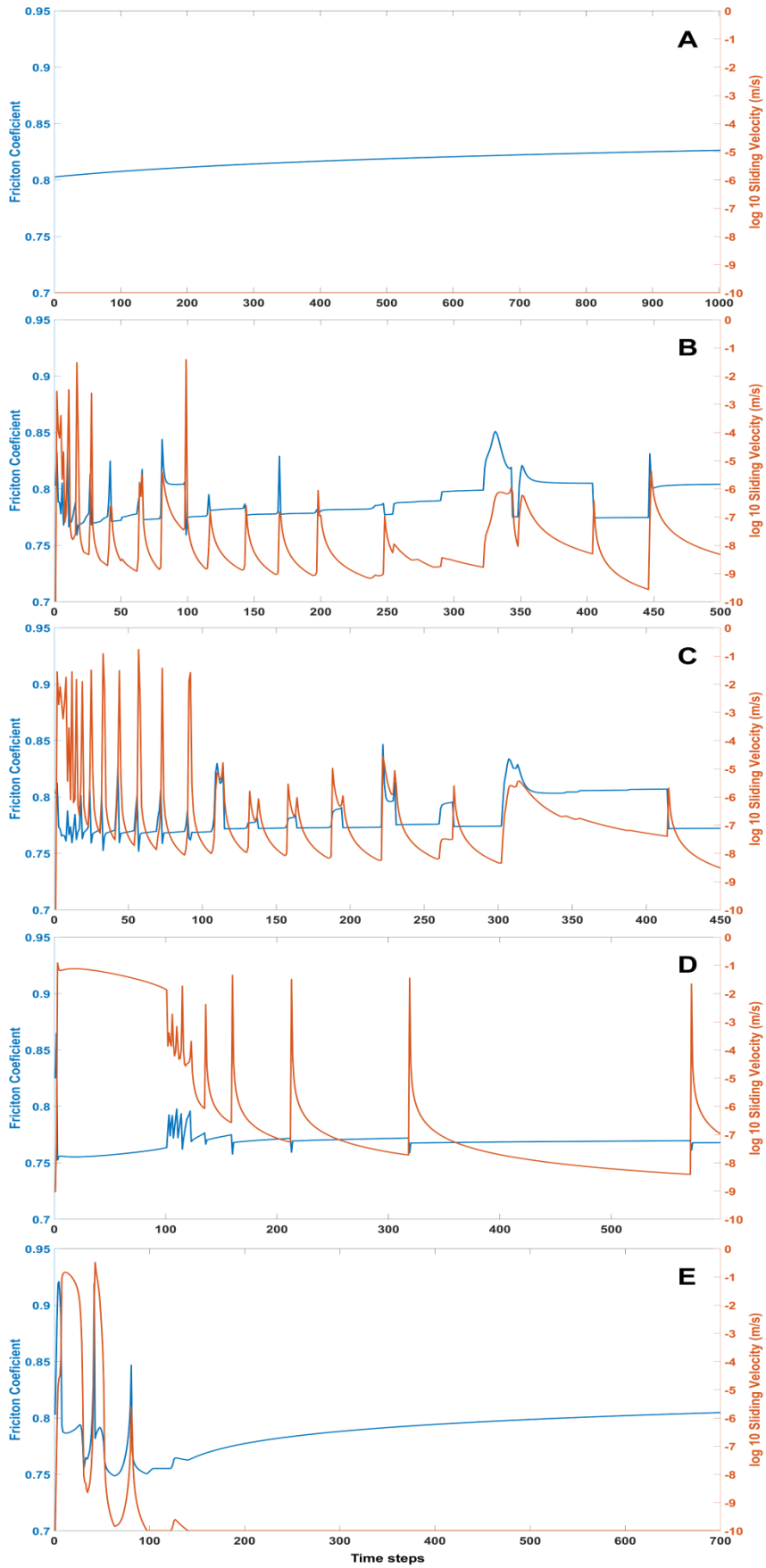


Figure 8. Evolution of the friction coefficient (blue curve) and the sliding velocity (red curve) in the injection point resulting from CFRAC simulations. A. $\alpha=85^\circ$, B. $\alpha=80^\circ$, C. $\alpha=76^\circ$, D. $\alpha=65^\circ$ and E. $\alpha=50^\circ$.

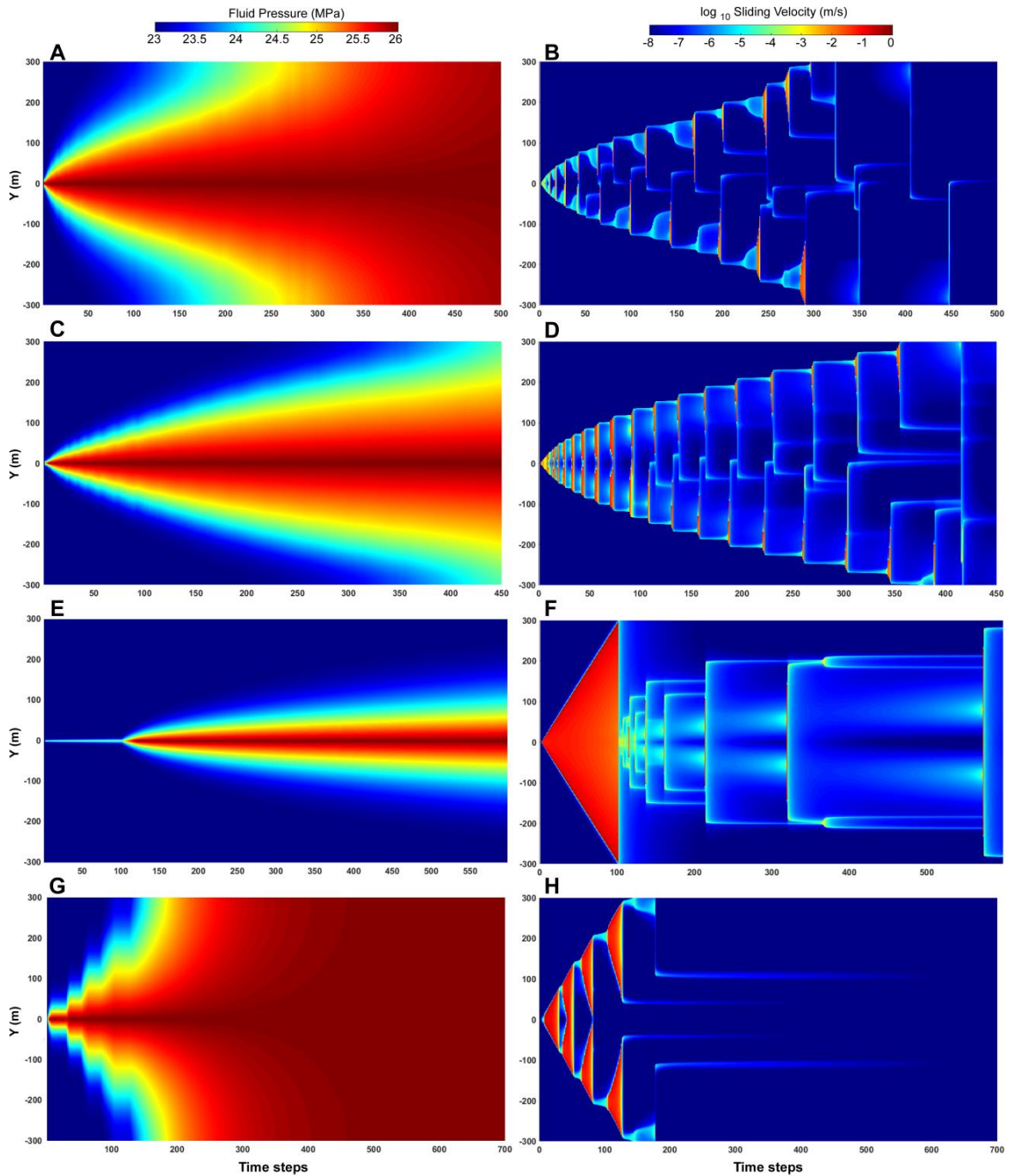


Figure 9. Fluid pressure (MPa) and sliding velocity (m/s) along fracture distance and time steps for CFRAC model $\alpha = 80^\circ$ (A-B), $\alpha = 76^\circ$ (C-D), $\alpha = 65^\circ$ (E-F) and $\alpha = 50^\circ$ (G-H). Triangle areas in F and H are related to seismic events with high velocities that produced a strong reduction of the incremental time step (approx. $1e-5$ s) in the numerical simulation, and they needed more time steps before recovery of the usual incremental time (10s).

2.5 Discussion

2.5.1 Slip regimes

The results show that the seismic behaviour (i.e., sliding velocities, microseismicity) during fluid injection is strongly influenced by the fracture orientation, at least for single-fracture cases. Different slip or sliding regimes can clearly be distinguished. A **first type** of slip regime corresponds to fractures that with a

small overpressure patch can induce a slip that propagates through the entire fracture length, producing a large rupture surface. The onset of seismic instabilities is reached at the beginning of fluid injection, without requiring a substantial increment of the pressurized region and with very high sliding velocities ($>1\text{m/s}$). This type of slip regime, in which the rupture is not controlled by the fluid pressurization front, is observed for fracture orientations of $\alpha=65^\circ$ for both simulation codes (Fig. 7 E-F, Fig. 9 E-F). A **second type** of slip regime is observed in fractures that require longer injection times before the onset of moderate/large slip events. In this case, the onset of dynamic slip requires that a large part of the fracture is first uniformly pressurized. This behaviour is characterized by high slip velocities ($>1\text{m/s}$) and surface run-outs that rarely expand outside of the pressurized region. When the rupture can occasionally expand outside the sliding velocity it gets is strongly reduced and finally arrested. This is due to the velocity strengthening and increasing of the friction coefficient. For this case, the rupture front propagation is pressure-controlled. This implies that, although the dynamic slip behaviour is efficient and there is a weakening of the friction coefficient, the residual friction is still high enough to arrest and stabilize the perturbation beyond the pressurized region. This type would correspond to orientations of 76° to 80° for both simulation codes (Fig. 7 C-D, Fig. 9 A-B, C-D). An intermediate case between types one and two regimes is such of fractures oriented at $\alpha=50^\circ$ (Fig. 7 G-H and Fig. 9 G-H.). While in the second type, the slip regime is controlled by the propagation of the pressure front, for this last case it looks like the pressure front is seismically controlled and progresses as a result of the subsequent ruptures. Thus, the fracture pressurization rate is higher than that observed in the purely second type, and with strong seismicity. This probably corresponds to a transition case between the **first** and **second types**. Another particular case is the $\alpha=80^\circ$ of the TF3D in which the slip behaviour is a little different than in the other cases. Dynamic slip is not observed for this **third type** of slip regime and fracture propagation is arrested due to the increase of the dynamic friction coefficient during the raise of the slip velocity. The accommodation of loading, and therefore the accumulation of a finite displacement along the fracture, takes place through slow sliding velocity or by aseismic flow ($\sim 5\text{e-}5\text{m/s}$). This type would also correspond to orientations of 85° for both simulation codes.

All these observations can be correlated with the analytical model developed by Garagash and Germanovich (2012) on the nucleation and arrest of dynamic slip on a pressurized fault and the numerical simulations done by Gischig (2015). The influence of fracture orientation (α) can be evaluated using the Garagash and Germanovich (2012) slip regime diagram (Fig. 10 A) and the Mohr-Coulomb failure criterion (Fig. 10 B). Although the Mohr-Coulomb failure envelope is defined using the static friction coefficient and the Garagash and Germanovich (2012) uses a slip-weakening dynamic friction coefficient for non-dilatant fractures, the comparison between both diagrams can improve our understanding of the implications of dynamic friction coefficient using the traditional static Mohr-Coulomb envelope.

Garagash and Germanovich (2012) proposed a diagram defined by the relationship between the understress and the overpressure. The understress $((\tau_p - \tau) / \tau_p)$ is defined as the normalized difference between shear stress (τ_p) at which slip initiates, based on the Mohr-Coulomb failure criterion, (i.e., $\tau_p = f_0 \cdot \sigma_n'$), and the initial shear stress on the fault (τ). The overpressure $(\Delta p / \sigma_n')$ is defined as the incremental fluid pressure ($\Delta p = P_{inj} - P_0$) normalized by the normal effective stress on acting on the fracture (σ_n'). Combinations of shear stress, normal stress, and injection pressure (P_{inj}) are represented by plotting the understress on the x-axis and the overpressure on the y-axis.

On the one hand, when understress approaches zero the fault becomes critically stressed (i.e., it is on the limit of rupture), while a value of understress equal to one means that there is no shear stress on the fault (Fig. 10 A). On the other hand, when overpressure approaches zero the fault rests without pressurization (i.e., it is on the verge of stability), while an overpressure equal to one means a total reduction of the effective stress due to fluid pressure increment and, therefore, a hydrofracture closure condition. For a more detailed description of the mathematical formulation and definition of the different sliding regime fields see Garagash and Germanovich (2012) or Ciardo and Lecampion (2019).

However, for our simulations in which we used a dynamic approach of the friction coefficient using the rate and state friction law, the transition or differences between the regions 2 and 3 (cases of ultimately stable faults ($\tau < \tau_r$) for which most of the fracture growth is due to aseismic velocities, although transient seismic slip may occur (region 2)) are not fully conservative with the Garagash and Germanovich (2012) diagram (Fig. 10), even with the dilatancy stabilizing effect defined by Ciardo and Lecampion (2019). For the rate-and-state friction law, the friction weakening is defined by the sliding velocity and holding time variation rather than the amount of sliding displacement as in slip-weakening friction laws. This characteristic of our approach tends to intensify the seismic response in the simulations and expand the corresponding region 2 of Garagash and Germanovich (2012). A similar tendency was also recognized by Gischig (2015).

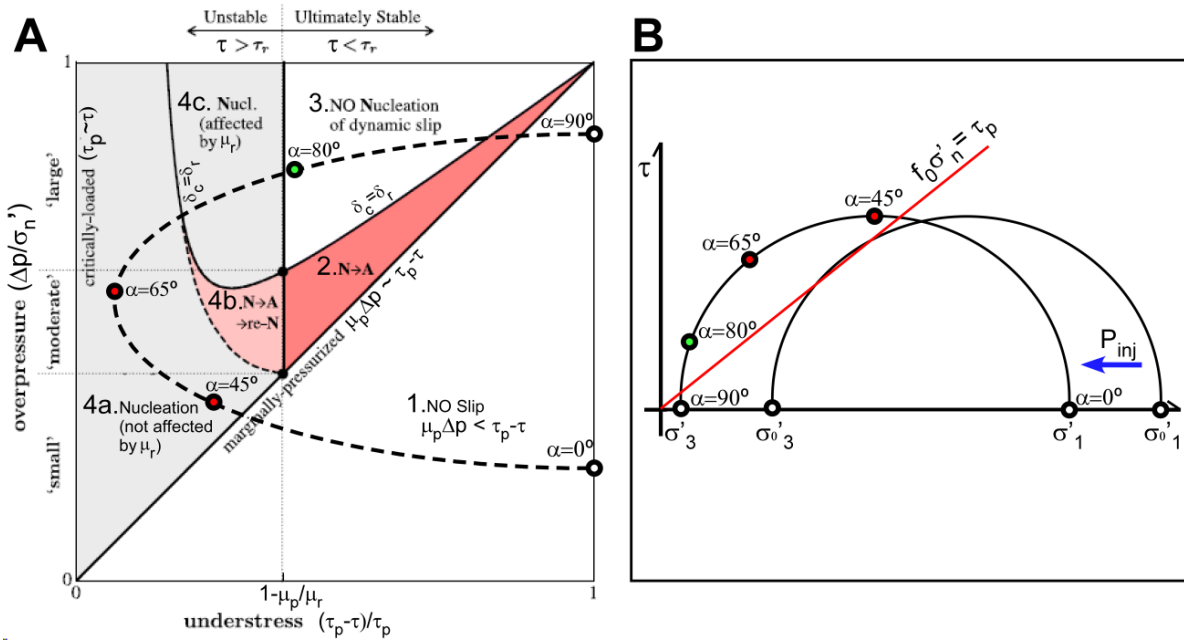


Figure 10. Diagram of Garagash and Germanovich (2012) that describes the different sliding regimes of propagation for a non-dilatant fault as a function of the dimensionless fluid overpressure $\Delta p/\sigma_n'$ and the understress $(\tau_p - \tau)/\tau_p$. Region 1 corresponds to injection scenarios without fault reactivation. Regions 2 and 3 correspond to the cases of ultimately stable faults ($\tau < \tau_r$) for which most fracture growth is produced in aseismic velocities, although transient seismic slip may occur (region 2). Regions 4a, 4b, and 4c correspond to unstable fault cases for which an unabated dynamic rupture occurs as the residual shear strength (defined at ambient conditions) is lower than the in situ shear stress ($\tau_r < \tau$). The region is subdivided depending on whether the residual friction coefficient affects nucleation. The dark dashed parabola represents the evolution trajectory as a function of fracture orientation (α), with several representative orientations analyzed (white, green and red indicate orientations with no slip, no dynamic slip or unstable faults regimes, respectively). B. Mohr-Coulomb diagram that describes the different stability regimes as a function of the shear stress (τ) and effective normal stress (σ_n'). Orientations above the failure envelope ($\tau_p = f_0 \cdot \sigma_n'$) will slip and orientations below will be stable. An additional circle with P_0 (23MPa) is included to visualize the pressure increment effect (reducing the effective normal stress) in terms of stability. Both diagrams are performed using the stress state defined in Fig.4, with $P_{inj} = 28MPa$, $f_0 = 0.8$, a relation of $0.6\mu_p = \mu_r$ and $\sigma_0'1 = \sigma_1 - P_0$.

Thus, the **first type** would correspond to cases in which the nucleation of the dynamic slip produces an uncontrolled fracture front propagation (regions 4a, 4b, and 4c of Garagash & Germanovich (2012)). The **second type** would correspond to situations in which the dynamic slip is not enough and the rupture front propagation is pressure-controlled (region 2 of Garagash and Germanovich (2012)), Eventually, the **third type** results in aseismic or non-dynamic slip nucleation (region 2 of Garagash and Germanovich (2012)).

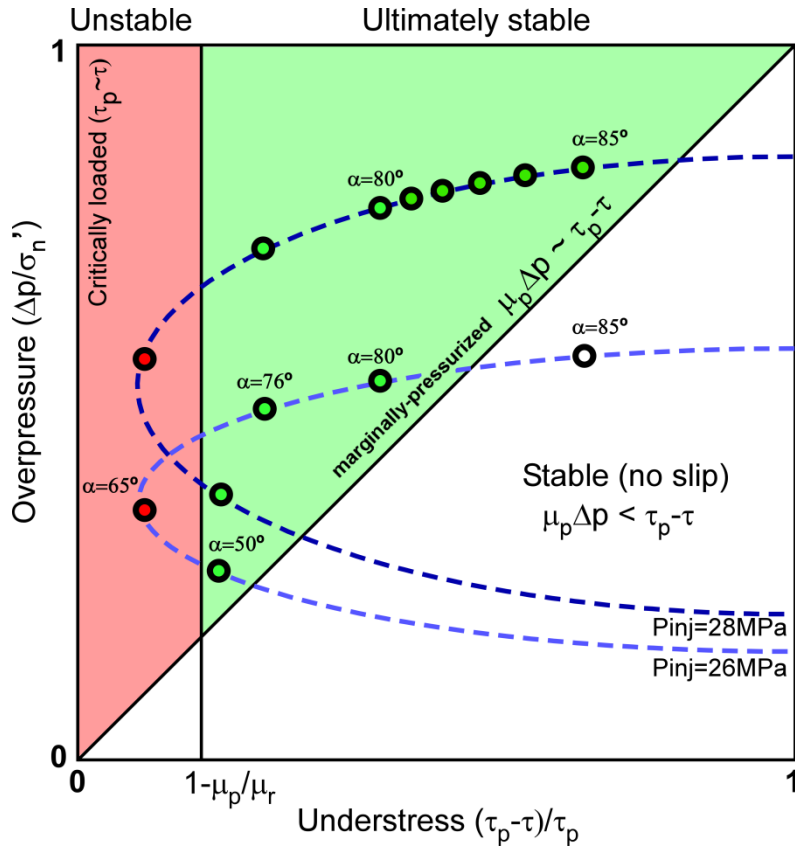


Figure 11. Main slip regimes as a function of the overpressure and the understress fields. The dashed curves represent the evolution trajectory as a function of the fracture orientation (from $\alpha=0^\circ$ to $\alpha=90^\circ$). The white, green and red circles indicate orientations with no slip, no dynamic slip or unstable faults regimes, respectively. The relation between μ_p (peak of friction coefficient) and μ_r (residual friction coefficient) was established at $0.84\mu_p = \mu_r$ based on the mean values of the numerical simulations. The α increment from simulations between $\alpha=80^\circ$ to $\alpha=85^\circ$ is one degree. Modified the diagram from Garagash and Germanovich (2012)

However, looking at the prediction of Fig. 11, the $\alpha=80^\circ$ case should follow a dynamic slip regime with a pressure-controlled rupture front propagation. This behaviour was observed in the CFRAC simulation for $\alpha=80^\circ$ (Fig. 9 A-B), but results from TF3D show a clear tendency towards aseismic behaviour (Fig. 7 A-B). This contradiction between both codes and the analytical solution of Garagash and Germanovich (2012) open three hypotheses:

- a) The result misfits are related to the differences between the two simulation codes.
- b) The result misfits are related to the use of a rate and state formulation (Segall, 2010) instead of a dynamic slip weakening as a function of the shear displacement (Garagash & Germanovich, 2012). Therefore, it would be necessary to define the transition between the dynamic slip regime with a pressure-controlled rupture front propagation and the aseismic or no dynamic slip nucleation.

c) The result misfits are related to a mixture of hypotheses a) and b)

To investigate the different hypotheses, we carried out additional simulations with both codes to investigate the transition between the **second** and **third types**. We developed a new series of simulations using $P_{inj}=28\text{MPa}$ (dark blue curve in Fig. 11), equivalent to just displacing the curve in the overpressure axis (y -axis) and including more orientations in the analysis of this transition. The results obtained are coherent with the sliding regimes shown in Figs. 7 and 9. However, from $\alpha=80^\circ$ for $P_{inj}=28\text{MPa}$ we see the beginning of the transition from the dynamic slip regime (**second type**) with a pressure-controlled rupture front propagation to the aseismic slip regime (**third type**). The results of CFRAC and TF3D show a mixture of the **second and third types** where the pressure front (with lower overpressure) slides seismically and the zones close to the injection point (with higher overpressures) slide aseismically. However, the TF3D results reveal a more marked aseismic regime than those of CFRAC, in which seismicity is well recognized. For $\alpha=85^\circ$ a completely stable regime (no slip) was obtained using CFRAC while TF3D models resulted in an aseismic regime with sliding velocities $<5\text{e-}5\text{m/s}$.

Accordingly, the transition between the second and third types should be related to the overpressure stabilizing effect, when the overpressure at the fluid source is equal to the ambient effective stress normal to the fault. In this limit, the instability is suppressed entirely on ultimately stable faults (Garagash & Germanovich, 2012). This overpressure stabilizing effect is also observed in hydraulic fracturing operations where pure open fracture mode is related to low seismicity and the injection pressure is normally close to or higher than the least principal stress (Fisher and Guest. 2011; Holland, 2013; Skoumal et al., 2015). To constrain this transition, we explored more orientations for the $P_{inj}=28\text{MPa}$ reducing overpressure, i.e. $\alpha=81^\circ$ to 84° (with one degree as α interval). TF3D results reveal a light transition reducing the sliding velocity as α increases, from peak values of $6\text{e-}5\text{m/s}$ for $\alpha=80^\circ$ to $1\text{e-}5\text{ m/s}$ for $\alpha=85^\circ$. CFRAC results show a transition where the pressure front seismic patch gets continuously reduced while the aseismic patch grows until $\alpha=84^\circ$ where the fault follows a stable regime (no slip).

Although an increase of the injection pressure, nearly close to, or equal to the less principal stress, can be used to better constrain the overpressure stabilization effect it can also result in unrealistic scenarios (for single fractures) where hydrofracture production (perpendicular to the least principal stress) would be more favourable than the sliding of pre-existing fractures. At least, these scenarios need to be evaluated by combining the presence of new hydrofracture production with the pre-existing fractures (McClure & Horne, 2014).

2.5.2 Comparison between numerical approaches

The results from numerical simulation show how TF3D can reproduce the rate and state behaviour both for a shear benchmark experiment and fracture fluid injection scenarios.

For the benchmark simulation, a misfit was observed between the theoretical and numerical simulation results. The results show a more conservative response with a slow friction reduction when the model velocity changes from v_1 (slow) to v_2 (fast) conditions, and on the hardening and weakening peaks. These effects are produced because the velocity used for the rate and state calculations is obtained as the average of the eight grid points of each zone (see supplementary material) and normally there is a velocity attenuation effect due to the surrounding zones. This misfit effect is mainly observed at the beginning of the simulation during the first slow- (v_1) fast- (v_2) and fast- (v_2) slow- (v_1) cycles and progressively reduced for the second and third cycles. Additionally, the initial friction coefficients start with values lower than expected in all the simulations and they are normalized to those expected after the first time step. This effect and the higher misfits between the theoretical and numerical results at the beginning of the simulation are surely related to the internal calculations of the initial conditions in TF3D that evaluate the initial conditions with zero velocity at time equal to zero, and in the first time step the velocity change produces a friction coefficient below the expected one producing anomalously higher sliding velocities than expected (e.g. Fig. 6D). However, these initial condition effects are quickly attenuated in the following steps (e.g. Fig. 6, see beginning of the simulation) and in terms of physical time(s) are related to the first second of the simulation.

For the fluid injection scenarios differences between both codes used to perform the numerical simulations can be identified. The results of simulations based on a continuous and sequential approach (TF3D) tend to show an attenuation of the friction hardening and weakening evolution and to show higher background oscillations. Simulations based on the discrete approach (CFRAC) reveal that the model tends to accommodate friction changes in single abrupt episodes. If we focus on the frictional evolution, CFRAC uses an explicit third-order Runge-Kutta time-stepping with an adaptive time step to force the model to produce very short time steps to accurately simulate the events production and sliding behaviour (McClure, 2012). Also, fine element spatial discretization must be used to prevent numerical instabilities (Lapusta, 2001). We used an element size of 0.5m in our simulations, a value smaller than the critical maximum element size of 4.7 m using the Lapusta (2001) condition (for $\sigma_n=50\text{Mpa}$ and 8.1m for $\sigma_n=29\text{Mpa}$). The sliding velocity is calculated in CFRAC by treating velocity as an unknown and calculating the velocity at each element to enforce the frictional equilibrium equation (McClure, 2012). On the other hand, TF3D uses an integral finite difference approach to solve the mechanics and fluid flow equilibrium with a low adaptive time step. The time step is forced to be reduced in function of fluid pressure changes for an imposed tolerance (Taron et al., 2009; Taron and Elsworth, 2009). Thus, the

obtained velocity resulting from the stress equilibrium is used to calculate the friction coefficient and then to evaluate the frictional resistance to slip. Although the current version allows reproducing the different sliding regimes shown previously, the adaptive time step is not able to drastically reduce the time step to accurately simulate the events production/nucleation and sliding details as in CFRAC.

To test the time step reduction vs the spatial discretization we re-ran all the CFRAC models to analyze this effect using a spatial discretization similar to that used in the TF3D models (i.e., length of 10m). We observe that, although the spatial sliding resolution decreases and evolves to the TF3D results, the nucleation processes can keep the resolution. However, the obtained seismicity includes a huge number of low-magnitude events and this must be related to numerical instabilities. Anyway, the sliding regimes were coherent with the previously shown from a broad point of view even with this sparse spatial discretization.

For this reason, TF3D shows good results in terms of the sliding regime using a 3D approach and without needing a fine spatial discretization but is not able to correctly reproduce seismic nucleation, because fine time discretization has a higher ponderation in seismic nucleation than spatial discretization.

2.6 Conclusions

Through this chapter, we have evaluated the transition between seismic and aseismic slip using two different modelling approaches, a discrete fracture (CFRAC) or a continuum (TF3D) approach, both using a rate-and-state friction law. For that purpose we have firstly introduced the rate-and-state friction law on TF3D and tested it on a pure shear benchmark simulation. The pure shear benchmark experiment shows a good correlation between the theoretical and numerical results, although the numerical results follow a more conservative evolution related to the velocity average and with initial conditions.

The transition between seismic and aseismic slip was modelled using the background theory of Garagash and Germanovich, (2012) for sliding regimes in non-dilatant faults and crossing the results between TF3D and CFRAC. The results reveal that both codes using the rate-and-state law can reproduce the sliding regimes analytically defined Garagash and Germanovich (2012) and simulated by Gischig (2015). However, we identified the need to better constrain the transition between the dynamic slip regime with a pressure-controlled rupture front propagation (**second type**) and the aseismic or non-dynamic slip nucleation (**third type**) due to the misfits between the analytical solution and the numerical results and showing higher instability using the rate-and-state friction law respect using slip-weakening friction law, even with the dilatant faults that should increase the stability (Ciardo and Lecampion, 2019).

The transition seismic-to-aseismic is clearly marked by the overpressure stabilizing effect and the numerical simulation differences between TF3D and CFRAC. The sliding regimes can be distinguished from a global point of view without a fine spatial discretization but with implications in the transitions between the sliding regimes and losing information about sliding nucleation.

The seismicity analysis and the seismic nucleation require a fine adaptive time step that TF3D currently does not have. For this reason, we did not expand the work toward seismic production comparisons. Additionally, a sensitivity analysis of the rate-and-state friction law parameters should be carried out to better constrain the transition seismic-aseismic using this friction solution.

2.7 References

- Abe, S., Dieterich, J. H., Mora, P., & Place, D. (2002). Simulation of the influence of rate- and state-dependent friction on the macroscopic behavior of complex fault zones with the lattice solid model. *Pure and Applied Geophysics*, 159(9), 1967–1983. <https://doi.org/10.1007/s00024-002-8718-7>
- Atkinson, G. M., Eaton, D. W., Ghofrani, H., Walker, D., Cheadle, B., Schultz, R., Shcherbakov, R., Tiampo, K., Gu, J., Harrington, R. M., Liu, Y., Van der Baan, M., & Kao, H. (2016). Hydraulic Fracturing and Seismicity in the Western Canada Sedimentary Basin. *Seismological Research Letters*, 87(3), 631–647. <https://doi.org/10.1785/0220150263>
- Avouac, J., & Al, T. E. T. (2017). Rate-and-state friction properties of the Longitudinal Valley Fault from kinematic and dynamic modeling of seismic and aseismic slip. *Journal of Geophysical Research: Solid Earth*, 122, 1–23. <https://doi.org/10.1002/2016JB013615>. Abstract
- Azad, M., D. I. Garagash, & M. Satish (2017). Nucleation of dynamic slip on a hydraulically fractured fault. *Journal of Geophysical Research: Solid Earth*, 122, 2812–2830, doi:10.1002/2016JB013835.
- Baujard, C., Genter, A., Dalmais, E., Maurer, V., Hehn, R., Rosillette, R., Vidal, J., & Schmittbuhl, J. (2017). Hydrothermal characterization of wells GRT-1 and GRT-2 in Rittershoffen, France: Implications on the understanding of natural flow systems in the rhine graben. *Geothermics*, 65, 255–268. <https://doi.org/10.1016/j.geothermics.2016.11.001>
- Bie, L., & Ryder, I. (2014). Recent seismic and aseismic activity in the Ashikule stepover zone, NW Tibet. *Geophysical Journal International*, 198(3), 1632–1643. <https://doi.org/10.1093/gji/ggu230>
- Cappa, F., De Barros, L., & Wynants-Morel, N. (2019). From aseismic slip to seismicity during fluid injection controlled by interactions between stress perturbation, permeability increases and fault structure. *American Rock Mechanics Association*, 19–140, 1–7.
- Catalli, F., Rinaldi, A. P., Gisichig, V., Nespoli, M., & Wiemer, S. (2016). The importance of earthquake interactions for injection-induced seismicity: Retrospective modeling of the Basel Enhanced Geothermal System. *Geophysical Research Letters*, 43(10), 4992–4999. <https://doi.org/10.1002/2016GL068932>
- Ciardo, F., & Lecampion, B. (2019). Effect of dilatancy on the transition from aseismic to seismic slip due to fluid injection in a fault. *Journal of Geophysical Research: Solid Earth*, <https://doi.org/10.1029/2018JB016636>
- Cornet, F. H., Bérard, T., & Bourouis, S. (2007). How close to failure is a granite rock mass at a 5 km depth? *International Journal of Rock Mechanics and Mining Sciences*, 44(1), 47–66. <https://doi.org/10.1016/j.ijrmms.2006.04.008>
- Cueto-Felgueroso, L., Santillán, D., & Mosquera, J. C. (2017). Stick-slip dynamics of flow-induced seismicity on rate and state faults. *Geophysical Research Letters*, <https://doi.org/10.1002/2016GL072045>
- Dempsey, D., & Suckale, J. (2017). Physics-based forecasting of induced seismicity at Groningen gas field, the Netherlands. *Geophysical Research Letters*, 7773–7782. <https://doi.org/10.1002/2017GL073878>
- Dieterich, J. (1979). Modeling of rock friction 1. Experimental results and constitutive equations. *Journal of Geophysical Research*, 84, 2161–2168.
- Dieterich, J. H., & Kilgore, B. D. (1994). Direct observation of frictional contacts: New insights for state-dependent properties. *Pure and Applied Geophysics*, 143(1–3), 283–302. <https://doi.org/10.1007/BF00874332>
- Elst, N. J., & Savage, H. M. (2015). Frequency dependence of delayed and instantaneous triggering on laboratory and simulated faults governed by rate-state friction. *Journal of Geophysical Research: Solid Earth*, 1–24. <https://doi.org/10.1002/2014JB011611>. Received
- Fischer, T., & Guest, A. (2011). Shear and tensile earthquakes caused by fluid injection. *Geophysical Research Letters*, 38(5), 2–5. <https://doi.org/10.1029/2010GL045447>
- Galis, M., Ampuero, J. P., Mai, P. M., & Cappa, F. (2017). Induced seismicity provides insight into why earthquake ruptures stop. *Science Advances*, 3(12), eaap7528. doi:10.1126/sciadv.aap7528

- Gan, Q., & Elsworth, D. (2014a). Analysis of fluid injection-induced fault reactivation and seismic slip in geothermal reservoirs. *Journal of Geophysical Research: Solid Earth*, 119, 3340–3353, doi:10.1002/2013JB010679.
- Gan, Q., & Elsworth, D. (2014b). Thermal drawdown and late-stage seismic-slip fault reactivation in enhanced geothermal reservoirs. *Journal of Geophysical Research: Solid Earth*, 119, 8936–8949, doi:10.1002/2014JB011323.
- Gan, Q., & Lei, Q. (2020). Geothermics Induced fault reactivation by thermal perturbation in enhanced geothermal systems. *Geothermics*, 86, 101814. <https://doi.org/10.1016/j.geothermics.2020.101814>
- Garagash D.I., & Germanovich LN. (2012). Nucleation and arrest of dynamic slip on a pressurized fault. *Journal of Geophysical Research : Solid Earth*, 117:1–27. <https://doi.org/10.1029/2012j b0092 09>.
- Gaucher, E., Schoenball, M., Heidbach, O., Zang, A., Fokker, P. A., Van Wees, J. D., & Kohl, T. (2015). Induced seismicity in geothermal reservoirs: A review of forecasting approaches. *Renewable and Sustainable Energy Reviews*, 52, 1473–1490. <https://doi.org/10.1016/j.rser.2015.08.026>
- Gischig, V. S. (2015). Rupture propagation behavior and the largest possible earthquake induced by fluid injection into deep reservoirs. *Geophysical Research Letters*, 42(18), 7420–7428. <https://doi.org/10.1002/2015GL065072>
- Grigoli, F., Cesca, S., Rinaldi, A. P., Manconi, A., López-Comino, J. A., Clinton, J. F., Westaway, R., Cauzzi, C., Dahm, T., & Weimer, S. (2018). The November 2017 Mw 5.5 Pohang earthquake: A possible case of induced seismicity in South Korea. *Science*, 10.1126/science.aat2010.
- Hofmann, H., Farkas, M., Huenges, E., Zang, A., Leonhardt, M., Kwiatek, G., Martinez-garzon, P., Bohnhoff, M., Min, K., Fokker, P., Westaway, R., Bethmann, F., Meier, P., Yoon, K. S., Choi, J. W., Lee, T. J., & Kim, K. Y. (2019). First field application of cyclic soft stimulation at the Pohang Enhanced Geothermal System site in Korea. *Geophysical Journal International*, 217, 926–949. <https://doi.org/10.1093/gji/ggz058>
- Holland, A. (2013), Earthquakes triggered by hydraulic fracturing in south-central Oklahoma. *Bulletin of the Seismological Society of America*, 103(3), 1784–1792, doi:10.1785/0120120109.
- Hui, G., Chen, S., Gu, F., Pang, Y., Yu, X., & Zhang, L. (2021). Insights on Controlling Factors of Hydraulically Induced Seismicity in the Duvernay East Shale Basin. *Geochemistry, Geophysics, Geosystems*, 22, 1–13. <https://doi.org/10.1029/2020GC009563>
- Itasca, F., (2009). Fast Lagrangian Analysis of Continua in 3 Dimensions, Version 4.0. Minneapolis. Itasca Consulting Group, Minnesota, pp. 438.
- Jaeger, J. C., Cook, N. G.W., & Zimmerman R.W. (2007). Fundamentals of rock mechanics: Blackwell Publishing. ISBN: 978-0-632-05759-7
- Johnson, S., & Morris, J. (2009). Hydraulic fracturing mechanisms in carbon sequestration applications. In 43rd US Rock Mechanics Symposium & 4th US-Canada Rock Mechanics Symposium. American Rock Mechanics Association.
- Kohl, T., & Mège, T. (2007). Predictive modeling of reservoir response to hydraulic stimulations at the European EGS site Soultz-sous-Forêts. *International Journal of Rock Mechanics & Mining Sciences*, 44, no. 8, 1118–1131
- Kwiatek, G., Saarno, T., Ader, T., Bluemle, F., Bohnhoff, M., Chendorain, M., Dresen, G., Heikkinen, P., Kukkonen, I., Leary, P., Leonhardt, M., Malin, P., Martínez-Garzón, P., Passmore, K., Passmore, P., Valenzuela, S. & Wollin, C. (2019). Controlling fluid-induced seismicity during a 6.1-km-deep geothermal stimulation in Finland. *Science Advances*, 5(5), eaav7224. <https://doi.org/10.1126/sciadv.aav7224>
- Majer, E. L., Baria, R., Stark, M., Oates, S., Bommer, J., Smith, B., & Asanuma, H. (2007). Induced seismicity associated with Enhanced Geothermal Systems. *Geothermics*, 36(3), 185–222. <https://doi.org/10.1016/j.geothermics.2007.03.003>
- McClure, M. W. (2012). Modeling and Characterization of Hydraulic Stimulation and Induced Seismicity in Geothermal and Shale Gas Reservoirs. Stanford PhD Dissertation, 1–369.

- McClure, M. W. (2015). Generation of large postinjection-induced seismic events by backflow from dead-end faults and fractures. *Geophysical Research Letters*, 42, 6647–6654. <https://doi.org/10.1002/2015GL065028>. Received
- McClure M.W., & Horne R.N. (2011). Investigation of injection-induced seismicity using a coupled fluid flow and rate/state friction model. *Geophysics*, 76:181. <https://doi.org/10.1190/geo2011-0064.1>.
- McClure M.W., & Horne R.N. (2013). Characterizing hydraulic fracturing with a tendency for shear stimulation test. *Society of Petroleum Engineers*, 166332:1–17. <https://doi.org/10.2118/166332-ms>
- McClure, M. W., & Horne, R. N. (2014). An investigation of stimulation mechanisms in Enhanced Geothermal Systems. *International Journal of Rock Mechanics and Mining Sciences*, 72, 242–260. <https://doi.org/10.1016/j.ijrmms.2014.07.011>
- Meyer, G., Baujard, C., Hehn, R., Genter, A., & McClure, M. W. (2017). Analysis and Numerical Modelling of Pressure Drops Observed During Hydraulic Stimulation of GRT-1 Geothermal Well (Rittershoffen, France). Proceedings of the 42nd Workshop on Geothermal Reservoir Engineering, 1(1), 14.
- Min, K.B., Rutqvist, J., & Elsworth, D. (2009). Chemically and mechanically mediated influences on the transport and mechanical characteristics of rock fractures. *International Journal of Rock Mechanics Mining and Science*, 46 (1), 80–89.
- Norbeck, J. H., McClure, M. W., & Horne, R. N. (2018). Field observations at the Fenton Hill enhanced geothermal system test site support mixed-mechanism stimulation. *Geothermics*, 74, 135–149. <https://doi.org/10.1016/j.geothermics.2018.03.003>
- Norbeck, J. H., & Rubinstein, J. L. (2018). Hydromechanical Earthquake Nucleation Model Forecasts Onset, Peak, and Falling Rates of Induced Seismicity in Oklahoma and Kansas. *Geophysical Research Letters*, <https://doi.org/10.1002/2017GL076562>
- Norbeck, J., & Horne, R. (2015). Injection-Triggered Seismicity: An Investigation of Porothermoelastic Effects Using a Rate-and- State Earthquake Model, (2011), Proceedings, Fourtieth Workshop on Geothermal Reservoir Engineering Stanford University, Stanford, California, SGP-TR-204.
- Piris, G., Griera, A., Gomez-rivas, E., Herms, I., & Goula, X. (2017). Induced Seismicity in pressurised single fractures : a numerical approach. *Geogaceta*, 61, 95–98.
- Piris, G., Griera, A., Gomez-Rivas, E., Herms, I., McClure, M. W., & Norbeck, J. H. (2018). Fluid pressure drops during stimulation of segmented faults in deep geothermal reservoirs. *Geothermal Energy*, 6(24). <https://doi.org/10.1186/s40517-018-0110-7>
- Pruess, K., & Wu, Y.-S. (1993). A new semi-analytical method for numerical simulation of fluid and heat flow in fractured reservoirs. *SPE Advanced Technology Series*, 1(2), 63–72.
- Rahman, M. K., Hossain, M. M., & Rahman, S. S. (2002). A shear-dilation based model for evaluation of hydraulically stimulated naturally fractured reservoirs. *International Journal for Numerical and Analytical Methods in Geomechanics*, 26, 5, 469–497.
- Rice, J. R. (1993). Spatio-temporal complexity of slip on a fault. *Journal of Geophysical Research*, 98(B6), 9885. <https://doi.org/10.1029/93JB00191>
- Romanet, P., Bhat, H. S., Jolivet, R., & Madariaga, R. (2018). Fast and slow earthquakes emerge due to fault geometrical complexity. *Geophysical Research Letters*. <https://doi.org/10.1029/2018GL077579>
- Rubin, A. M., & Ampuero, J. P. (2005). Earthquake nucleation on (aging) rate and state faults. *Journal of Geophysical Research: Solid Earth*, 110(11), 1–24. <https://doi.org/10.1029/2005JB003686>
- Saló, L., Frontera, T., Goula, X., Pujades, L. G., & Ledesma, A. (2017). Earthquake static stress transfer in the 2013 Gulf of Valencia (Spain) seismic sequence. *Solid Earth*, 8(5), 857–882. <https://doi.org/10.5194/se-8-857-2017>
- Schill, E., Genter, A., Cuenot, N., & Kohl, T. (2017). Hydraulic performance history at the Soultz EGS reservoirs from stimulation and long-term circulation tests. *Geothermics*, 70, 110–124.

<https://doi.org/10.1016/j.geothermics.2017.06.003>

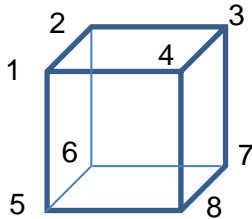
- Scholz, C. (2002). *The mechanics of earthquakes and faulting* (2nd editio). New York: Cambridge University Press.
- Segall, P. (2010). *Earthquake and volcano deformation*. New Jersey: Princeton University Press.
- Skoumal, R. J., M. R. Brudzinski, and B. S. Currie (2015), Earthquakes induced by hydraulic fracturing in Poland Township, Ohio. *Bulletin of the Seismological Society of America*, 105(1), 189–197
- Stork, A. L., Verdon, J. P., & Kendall, J. M. (2015). The microseismic response at the In Salah Carbon Capture and Storage (CCS) site. *International Journal Greenhouse Gas Control*, 32, 159-171, <https://doi.org/10.1016/j.ijggc.2014.11.014>.
- Taron, J., & Elsworth, D. (2009), Thermal–hydrologic–mechanical–chemical processes in the evolution of engineered geothermal reservoirs. *International Journal of Rock Mechanics Mining and Science*, 46(5), 855–864.
- Taron, J., Elsworth, D., & Min, K. (2009). Numerical simulation of thermal- hydrologic-mechanical-chemical processes in deformable, fractured porous media. *International Journal of Rock Mechanics and Mining Sciences*, 46, Issue 5, 842-854, <https://doi.org/10.1016/j.ijrmms.2009.01.008>.
- Vilarrasa, V., Carrera, J., Olivella, S., Rutqvist, J., & Laloui, L. (2019). Induced seismicity in geologic carbon storage. *Solid Earth*, 10, 871–892, <https://doi.org/10.5194/se-10-871-2019>, 2019.
- Vilarrasa, V., De Simone, S., Carrera, J., & Villaseñor, A. (2021). Unraveling the Causes of the Seismicity Induced by Underground Gas Storage at Castor , Spain. *Geophysical Research Letters*, 48, 1–10. <https://doi.org/10.1029/2020GL092038>
- Warren, J.E., & Root, P.J. (1963). The behavior of naturally fractured reservoirs. *Old Spe Journal*, 3 (03), 245–255.
- White, M., Fu, P., McClure, M., Danko, G., Elsworth, D., Sonnenthal, E., Kelkar, S., & Podgorney, R. (2018). A suite of benchmark and challenge problems for enhanced geothermal systems. *Geomechanics and Geophysics for Geo-Energy and Geo-Resources* (Vol. 4). Springer International Publishing. <https://doi.org/10.1007/s40948-017-0076-0>
- Willis-Richards, J., Watanabe, K., & Takahashi, H. (1996). Progress toward a stochastic rock mechanics model of engineered geothermal systems. *Journal of Geophysical Research*, 101, 17, 481–17, 496.
- Xu, T., Spycher, N., Sonnenthal, E., Zhang, G., Zheng, L., & Pruess, K. (2011). TOUGHREACT Version 2.0: A simulator for subsurface reactive transport under non-isothermal multiphase flow conditions. *Computers & Geosciences*, 37(6), 763–774. doi:10.1016/j.cageo.2010.10.007
- Yeck, W. L., Hayes, G. P., McNamara, D. E., Rubinstein, J. L., Barnhart, W. D., Earle, P. S., & Benz, H. M. (2016). Oklahoma experiences largest earthquake during ongoing regional wastewater injection hazard mitigation efforts. *Geophysical Research Letters*, 711–717. <https://doi.org/10.1002/2016GL071685>
- Zareidarmiyani, A., Salarirad, H., Vilarrasa, V., Kim, K., Lee, J., & Min, K. (2020). Comparison of numerical codes for coupled thermo-hydro-mechanical simulations of fractured media. *Journal of Rock Mechanics and Geotechnical Engineering*, 12(4), 850–865. <https://doi.org/10.1016/j.jrmge.2019.12.016>

2.8 Supplementary materials rate-and-state implementation into TF3D

To introduce the rate and state friction law, we created two Fish functions able to rewrite the friction coefficient each time step following the Eq. (9) regardless of the constitutive model which the user was using (Fish is the Flac3D console language).

These functions introduced the Eq. (9) and Eq. (10) parameters, calculate the friction coefficient through the Eq. (9) and rewrote this parameter each time step. To generate all the extra parameters we used the Flac3D extra zones configuration.

The friction coefficient is obtained from the zone sliding velocity. This sliding velocity is the result of an average of the modulus sliding velocity on the fault direction of each grid point in each zone:



$$slipvel = \frac{\sum_{i=1}^8 \sqrt{xvel_i^2 + zvel_i^2} \cdot \cos\left(\tan^{-1}\left(\frac{zvel_i}{xvel_i}\right) - \gamma \cdot \frac{\pi}{180}\right)}{8} \quad (11)$$

Where, $xvel$ and $zvel$ are the zone grid points sliding velocity in x and z direction respectively and γ is the fracture angle in degrees.

The resulting sliding velocity is used to obtain the θ variable in function of time through the Eq. (10). Finally the friction coefficient was calculated using the Eq. (9) and replaced in the constitutive model for each time step.

To ensure that the sliding velocity coming from Flac3D is coherent we activated the *Creep*time dependence option (see FLAC3D manual, Itasca, 2009). If not, the grid point sliding velocity should be rejected and use the grid point displacement and then obtain the sliding velocity using the time step.

Capítol 3

3 Fluid pressure drops during stimulation of segmented faults in deep geothermal reservoirs

3.1 Introduction

Geothermal energy development, either for electricity generation or for direct applications of geothermal heat, can be carried out in a wide range of geological settings. In the case of active tectonic zones with abnormally high geothermal gradients, such as Iceland, Italy, New Zealand or Turkey (Moeck 2014), geothermal energy can be widely exploited at shallow depths. However, geothermal projects usually need to exploit deeper reservoirs in regions where radiogenic igneous rocks are not present or where the tectonic activity is minor. In recent years, the exploration and exploitation of deep geothermal reservoirs have significantly increased worldwide (e.g. Tester et al. 2006; Breede et al. 2013; Király et al. 2015). In this context, geothermal projects focusing on heat distribution (low and medium enthalpy) have mainly targeted crystalline basement rocks or large and deep sedimentary basins, such as intracratonic basins and foredeep orogenic belts, as well as continental rifts. Projects focusing on power generation in high-temperature, low-permeability settings generally need to be developed as Enhanced Geothermal Systems (EGS), either in fractured crystalline basement rocks, in sedimentary and volcanic rocks (Zimmermann and Reinicke 2010; Elders et al. 2014).

Although deep, naturally fractured tight reservoirs are normally characterized by the presence of pre-existing fracture networks that provide some permeability. In most cases, the presence of rocks with low permeability prevents the economic feasibility of the project. Exploitation of low-permeability geothermal reservoirs requires the use of hydraulic stimulation techniques to enhance the permeability of the reservoir, increasing fluid flow and heat transfer between injection and extraction wells (Zimmermann and Reinicke 2010; Schill et al. 2017). However, stimulation processes sometimes produce induced seismicity, a hazard that needs to be mitigated to ensure the social acceptance and viability of the project. Normally, when this type of seismicity is low in magnitude, it is rarely felt and is referred to as microseismicity. Nevertheless, in some cases, the events may have high enough magnitude to be noticed at the Earth's surface, putting in risk the viability of the project (e.g. Majer et al. 2007; Häring et al. 2008; Dempsey and Suckale 2015). In such contexts, it is essential that we understand the fundamental processes involved in the hydraulic stimulation phase to reduce seismic risks and characterize the uncertainty of seismic hazard estimates.

Recently, Meyer et al. (2017) reported a strange phenomenon observed during the stimulation of the GRT1 well of the Rittershoffen geothermal power plant (Baujard et al. 2017). This consisted of a series of pressure drops (between $4 \cdot 10^{-3}$ MPa and 0.16 MPa, Fig.1A) during fluid injection that, according to

these authors, seemed to be linked with or followed by a cluster of seismic events (with magnitudes ranging between 0.3 and 1.3; Meyer et al. 2017; Fig 1B). For systems where permeability is dominated by the pre-existing fracture network, key factors that could produce a sudden pressure drop in the system are the rapid generation of permeability or the sudden increase of fluid storage capacity of the fracture network. Although most EGS projects have typically assumed that stimulation occurs principally through shear reactivation of pre-existing fractures, an alternative explanation is the so-called mixed-mechanism stimulation (McClure and Horne 2014; Norbeck et al. 2018). The mixed-mechanism stimulation involves both (1) shear stimulation by reactivation of previous fractures and (2) the development of new tensile fractures as bridges between pre-existing fractures.

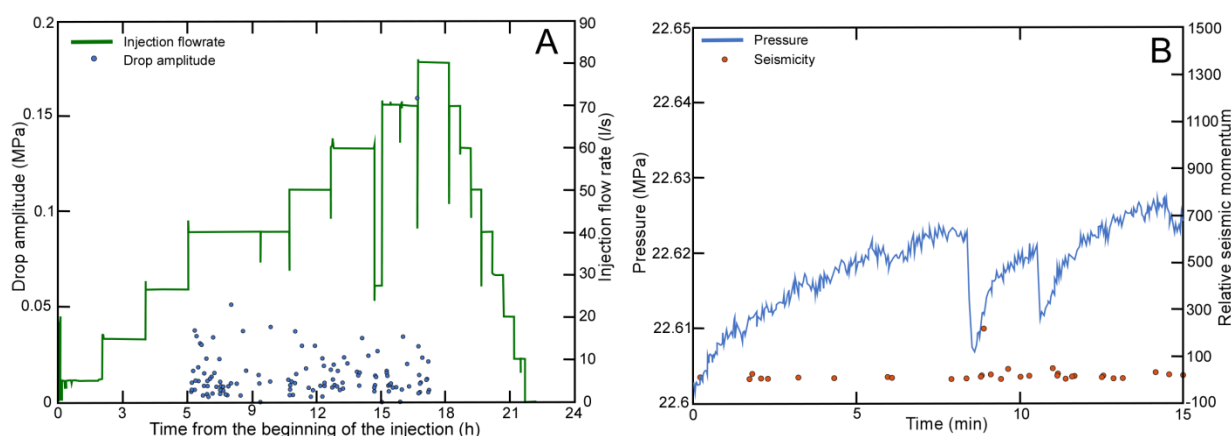


Figure 1. (A) Injection flow rate and fluid pressure drop amplitude during fluid stimulation of the GRT1 well at the Rittershoffen geothermal reservoir. (B) A detail of the fluid pressure registered at the well showing two examples of pressure drops and the associated seismicity swarm. Figure modified from Meyer et al. (2017).

Meyer et al. (2017) proposed three main hypotheses to explain the mechanisms associated with pressure drops and the triggering of induced seismicity. The first hypothesis considers that pressure drops are caused by fracture reactivation and slip with associated microseismicity. In the second hypothesis, they suggest that the phenomenon can be due to pressure equilibration during the connection between the stimulated/hydraulic fractures and the pre-existing ones. When a pressurized hydrofracture (i.e., a new fracture in the reservoir formed during hydraulic stimulation) gets connected with an unpressurized pre-existing fracture, additional fluid storage space is suddenly generated and, as a consequence, a pressure drop can occur. When fluid pressure recovers, stimulation of the newly connected fracture causes instability and slip takes place creating a swarm of seismic events. Finally, the third hypothesis considers that the pressure drop is produced by the propagation and opening of new cracks (i.e., tensile fractures) as wing cracks growing from pre-existing fractures (e.g. Norbeck et al. 2018). During the sliding stimulation phase of a pre-existing fracture, there is a relative displacement between the two fracture walls. This can induce the growth of tensile cracks at their tips if the tensile strength of the rock is overcome. Such new cracks would also cause a sudden increase of permeability and an associated pressure drop. After running a series of numerical models, Meyer et al. (2017)

concluded that the most plausible hypothesis to explain pressure drops is the propagation of new tensile fractures, although their study was not conclusive and suggested that further work was required.

Both hypotheses 2 and 3 proposed by Meyer et al (2017) share the condition that pressure drops occur in systems that contain or develop at least two sets of fractures at different orientations with respect to the stress field. As previously demonstrated by several studies (e.g. Garagash and Germanovich 2012; Gischig 2015; Piris et al. 2017), rupture propagation and sliding/tensional behaviour on fluid pressurized fractures depend on their relative orientation with respect to the principal stress axes. Fractures with strikes oriented at moderate angles with the maximum compressive stress (σ_1) are characterized by reactivation by sliding and/or opening, and are considered seismically active. In contrast, fractures at low angles with σ_1 have the capacity of being stimulated by opening mode and present either an aseismic behaviour or very low-magnitude seismicity (Piris et al. 2017). The new formation or reactivation of the latter set of fractures (i.e., at low angles with σ_1) can potentially result in a sudden permeability increase due to their ability to dilate at relatively low fluid pressure. Accordingly, if both fracture sets are connected when a fracture at a moderate angle is reactivated, the slip would induce opening of the aseismic fracture and will thus cause a pressure drop. The understanding of this process can potentially be used to identify patterns of the mixed-mechanism stimulation during hydraulic stimulation treatments.

In this study, we present a conceptual model where natural fractures are hydraulically connected by tensile splay fractures. Our overarching aim is to understand the influence of different properties of fracture sets on the system pressurization and their consequences for seismicity propagation and fault pressurization in a generic deep geothermal reservoir. We present numerical simulations based on simple fracture geometries, avoiding complex fracture networks, to investigate how pressure drops are related to stimulation and induced seismicity. Our results reveal a direct link between pressure drops and seismicity in systems involving two different fracture sets that are hydraulically connected. Seismicity is produced by sliding of a shear-mode fracture that induces a sudden opening of connected hydraulically tensile fractures, thus triggering the pressure drop.

3.2 Methods

The numerical simulations were carried out with the two-dimensional version of the boundary element reservoir simulation code CFRAC (McClure 2012). This software is able to solve the fully-coupled hydro-mechanical problem related to the injection of fluid through a fracture network embedded in an impermeable matrix and the associated induced seismicity (McClure and Horne 2011, 2013, 2014). These conditions are those typically found in deep geothermal reservoirs in crystalline basement rocks, where matrix permeability is nearly zero and flow occurs predominantly through fracture networks. The full-field fluid flow evolution and the reactivation of pre-existing fractures (by opening and/or sliding) are

solved simultaneously. In these simulations, the fluid is assumed to be single-phase (liquid water) and thermal effects are neglected (i.e., simulations are carried out in isothermal conditions). The simulation is initialized under homogeneous, anisotropic stress field conditions and with a homogeneous fluid pressure distribution. CFRAC can simulate both pre-existing fractures and new hydraulically formed fractures. However, the location of potentially forming fractures is defined in advance. The frictional resistance to slip is given by Coulomb's law (Segall 2010):

$$|\tau - \eta v| = \mu_f(\sigma_n - P) + S_0 \quad (1)$$

where τ is the shear stress, η is the radiation damping coefficient, v is the sliding velocity of the fracture, μ_f is the friction coefficient, σ_n is the normal stress, P is the fluid pressure and S_0 is the fracture cohesion. The evolution of the friction coefficient was defined using a rate-and-state formulation where this parameter depends on the sliding velocity and the sliding history of the fracture (Scholz 2002; Segall 2010). In terms of aperture change with slip, the approach evaluates separately the changes in fracture conductivity (i.e., hydraulic aperture) and pore volume (i.e., void or mechanical aperture) using two dilatation angles. For a more detailed description of the mathematical formulation used by CFRAC see McClure (2012) or McClure and Horne (2013).

3.3 Model set-up

The initial geometry of the model consisted of a single fracture defined by several linked segments with different orientations with respect to the maximum compressive stress (σ_1). Each individual fracture had a length of 60 m and was discretized into 20 cm-long elements (Fig. 2). The fracture element size was further refined near fracture intersections (with a minimum element size of 0.02 m). A constant out-of-plane thickness of $h=100\text{m}$ was considered for all models. Segments were orientated at $\alpha=60^\circ$ and $\alpha=88^\circ$, where α is the angle between σ_1 and the normal of the fracture segment (Fig. 2). These angles were selected because previous studies demonstrated that these orientations result in a highly variable range of seismic behaviour during fluid injection (Garagash and Germanovich 2012; Gischig 2015; Piris et al. 2017). Fractures at $\alpha=60^\circ$ are characterized by a critically loaded behaviour, with high associated seismicity and ruptures that can propagate through the entire fracture. Fractures at $\alpha=88^\circ$ are characterized as having an aseismic orientation, with slow sliding velocities and are thus unable to produce seismicity (e.g. Piris et al. 2017).

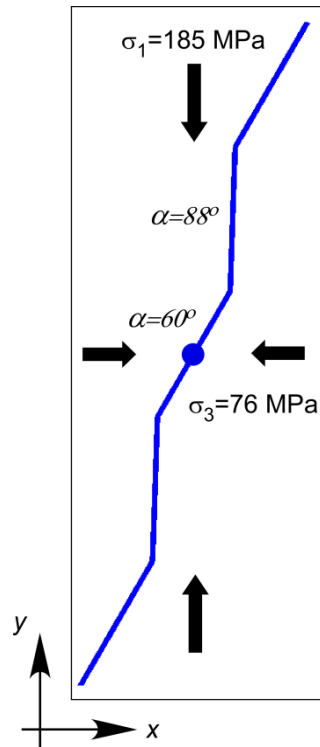


Figure 2. Geometry of the “60-88” model. The blue line represents the fracture configuration and the blue dot the injection point. Each fracture segment is 60 m long. Orientation and values of principal stresses are indicated.

Fluid injection was performed at the centre of the model. To evaluate the influence of the orientation of fractures in which the fluid was injected, two types of models were investigated: (1) the model named “60-88” in which the segment chosen for injection had an orientation of $\alpha=60^\circ$ (as shown in Fig. 2) and (2) the model “88-60” in which the segment where the fluid was injected was oriented at $\alpha=88^\circ$. Finally, we carried out additional simulations on a modified version of the “60-88” model to evaluate the effect of pressure drops with the propagation of hydraulic fractures. In such models (termed model “60-hydro”), we combined $\alpha=60^\circ$ segments with hydrofractures (i.e., tensile opening fractures) as wing cracks. In terms of numerical simulation, the main differences between the simulation setup of a pre-existing fracture or wing crack models are that (1) the tensile strength has to be overcome to initiate the wing crack and (2) the rate of fracture generation or propagation is determined by calculating a stress intensity factor at the fracture tips. This approach is similar to that used by other authors who modelled hydrofracture stimulation (McClure 2014; Zeeb and Konietzky 2015; Meyer et al. 2017). A summary of the mechanical parameters used in this study is shown in Table 1.

For all the models, the geothermal reservoir was assumed to be at a depth of 4,500 m, with an initial fluid pressure defined by the hydrostatic gradient. We assumed a strike-slip regime in which the principal stresses σ_1 and σ_3 are horizontal (parallel to the y - and x -axis of our model, respectively; Fig. 2) while σ_2 is vertical (i.e., oriented out-of-plane in the models). A minimum in-situ stress of 76 MPa was imposed in the x -direction, while a maximum horizontal stress of 185 MPa was applied in the y -direction. A constant

injection pressure of 70 MPa was imposed, with a maximum injection rate of 10 kg/s. The duration of simulation was set to be high enough to pressurize almost the entire domain (50,000 s).

A series of additional models were run in order to evaluate the influence of key parameters on the pressure drop phenomenon. These include the dilatancy effect, the scale effect and the model setup similar to that of the Rittershoffen geothermal reservoir. To evaluate the sensitivity of the models to the mechanical dilation angle (i.e., the dilatancy effect, defined as the increase of fracture volume by shear displacement), additional models were run with dilation angles (ϕ_{Edil}) of 2.5° and 5°. The potential sensitivity of the length scale was evaluated in the model “88-60” using fracture segments with lengths of 50m, 40m, 30m, 20m, 15m, and 6m. Finally, with the aim of comparing numerical predictions with field observations of seismicity coupled with pressure drops, several models with different length scales (i.e., 80m, 60m, 50m, 40m, 30m, 20m, 15m and 6m) were run using a configuration similar than that utilized during the stimulation of the Rittershoffen geothermal reservoir (Cornet et al. 2007; Baujard et al. 2017; Meyer et al. 2017). For these models, the only parameters that were varied with respect to the previous ones were the stress state ($\sigma_1=50$ MPa, $\sigma_3= 29$ MPa), the initial fluid pressure of 23.7 MPa and a constant injection pressure of 28 MPa.

Parameter	Description	Value	Source
E_0	Mechanical aperture	1,200 μm	Arbitrary (common values)(McClure 2010; Gischig 2015)
σ_{Enref}	Reference normal traction (mechanical aperture)	25 MPa	
E_{res}	Residual mechanical aperture	2 μm	
ϕ_{Edil}	Dilatation angle (mechanical aperture)	0° / 2.5° / 5°	(Willis-Richards et al. 1996; Kohl and Mège 2007)
e_0	Hydraulic aperture	120 μm	Arbitrary (common values) (McClure 2010; Gischig 2015)
σ_{enref}	Reference normal traction (hydraulic aperture)	25 MPa	
e_{res}	Residual hydraulic aperture	0.2 μm	
ϕ_{edil}	Dilatation angle (hydraulic aperture)	2.5°	Arbitrary (good coupling)
ρ	Fluid density	1,000 kg/m^3	Water values at 20°C
μ	Fluid viscosity	0.001 Pa·s	
h	Out-of-plane dimension	100 m	To obtain representative magnitudes
η	Radiation damping coefficient	3 $\text{MPa}/(\text{m/s})$	Arbitrary (common value) (McClure 2012)
S_0	Cohesion	0 MPa	Assumption
G	Shear modulus	15 GPa	Arbitrary (common value)
ν_r	Poisson's ratio	0.25	Arbitrary (common value)
f_0	Nominal friction coefficient	0.85	Arbitrary (common value) (Håring et al. 2008; Gischig 2015)
d_c	Characteristic displacement scale	100 μm	Gouge material (Marone and Scholz 1988; Scholz 2002; Gischig 2015)
a	Velocity effect coefficient	0.01	(Scholz 2002)
b	State effect coefficient	0.02	
v_0	Reference velocity	10 ⁻⁶ m/s	Arbitrary (common value)
Θ_{RS}	State	2.6·10 ⁶ s	(Rubin and Ampuero 2005; Gischig 2015)
T_{str}	Matrix tension strength	3 MPa	Arbitrary (common value)(McClure 2014)
$K1crithf$	Stress intensity factor	1.5 $\text{MPa}\cdot\text{m}^{1/2}$	Arbitrary (common value)(Zeeb and Konietzky 2015; Meyer et al. 2017)

Table 1. Friction and fracture parameters used in the simulations.

3.4 Results

The main parameters analyzed in our simulations were the fluid pressure evolution, the fracture apertures, the earthquake hypocentre locations, and the earthquake magnitudes. These parameters were used to highlight differences between models.

3.4.1 Model “88-60”

The evolution of fluid pressure, fracture aperture and hypocentre locations are shown in Fig. 3. Microseismicity was observed in both segment orientations, with magnitude events spanning up to $M=2.5$. The events with the highest magnitudes were systematically located along the $\alpha=60^\circ$ segments, while the segments oriented at $\alpha=88^\circ$ recorded lower-magnitude events (with maximum magnitudes of $M<1.5$). The fluid pressurization of the fracture was not homogeneous, with several abrupt events in which fluid pressure drops were linked with seismic events. Initially, the fluid batch expanded homogeneously along the $\alpha=88^\circ$ segment until it reached the intersection between two fracture segments. Seismic events and local pressure drops were generated from this point. Most of the hypocentres were located next to the intersection between fracture segments and near the pressurization front. However, low-magnitude events were also observed in the central part of the model, along the $\alpha=88^\circ$ segment. With progressing injection, the fluid reached the following fracture intersections and hypocentres thus shifted to these regions. Larger magnitude events ($M>1.5$) were able to produce stronger pressure drops able to be transmitted along the entire fracture system, and thus being ultimately detectable at the well (Fig. 4A). Pressure drops in the well ranged between 0.5 to 3 MPa. Furthermore, pressure drops felt in the well were correlated with increases in injection rate due to permeability enhancement (Fig. 4B). The time lapse between the main earthquake event and the associated well pressure drop was found to be lower than 2 s. This time-lapse increases with the distance from hypocentre to the well. The evolution of fracture apertures was characterized by two stages. In the early stage, before the stimulation of $\alpha=60^\circ$ segments, fracture apertures increased from the well in the same direction than that of the migration of the fluid pressure front ($t<0.5\times 10^4$ s; Fig. 3B). In the second stage, after stimulation of the $\alpha=60^\circ$ segments, fracture apertures expanded from fracture intersections towards the well, in a direction opposite to that of the expansion of the fluid pressure front. The highest observed apertures corresponded to the $\alpha=88^\circ$ fractures, with values reaching 0.027 m, while apertures slightly increased for $\alpha=60^\circ$ segments.

Snapshots of the fluid pressure before ($t-10$ s, where t is the time of the main seismic event) and after ($t+10$, $t+400$ and $t+2000$ s) the main seismic event of $M=1.96$ (indicated by the red dashed line in Fig. 3) are shown in Fig. 5. Strong variations of fluid pressure were observed before the onset of the seismic event near the intersection between segments. At $t+10$ s after the seismic event, a strong fluid pressure decrease was observed in the intersection segment and along $\alpha=88^\circ$ segment fractures. With increasing

time ($t=400$ s and $t=2000$ s in Fig. 5) the fluid pressure recovered quickly in the injection segment next to the well, while fluid pressure recovery was slow in the rest of the fracture, especially at the intersection near the location of the seismic event.

The evolution of fracture aperture is displayed for the same event in Fig. 6 for several control points next to the fracture intersections. Fracture apertures showed different trends depending on the distance to the intersections, and an aperture increase was not always observed for all monitoring points. While fracture apertures at the points located at the seismic segment remained approximately constant or slightly decreased (points 3 and 4 in Fig. 6), the evolution of apertures for the $\alpha=88^\circ$ segment showed aperture increases for control points next to the intersections (points 2 and 5 in Fig. 6). Apertures initially decreased and then increased (or remained constant) for control points located away from the intersections (points 1 and 6 in Fig. 6).

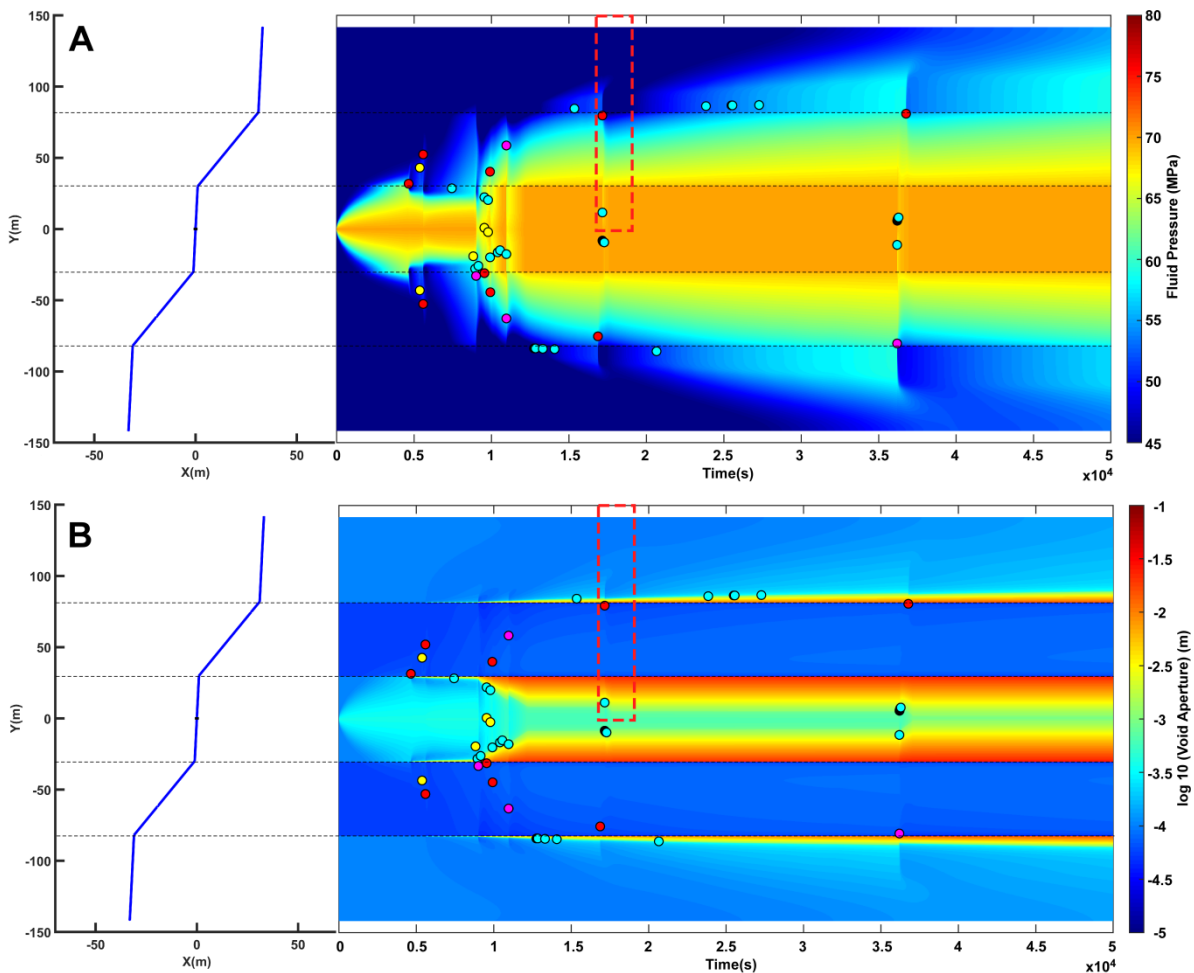


Figure 3. Sketches of the simulated fracture network (blue lines on the left), and the evolution of (A) fluid pressure and (B) fracture aperture for the model “88-60”. Dashed lines indicate the location of fracture segment intersections. Coloured points indicate the location of the earthquake hypocentres and magnitudes (cyan: $M < 0$, green: $0 \leq M < 1$, yellow: $1 \leq M < 1.5$, red: $1.5 \leq M < 2$ and pink: $M \geq 2$). The red dashed area indicates the data shown in Figures 5 and 6.

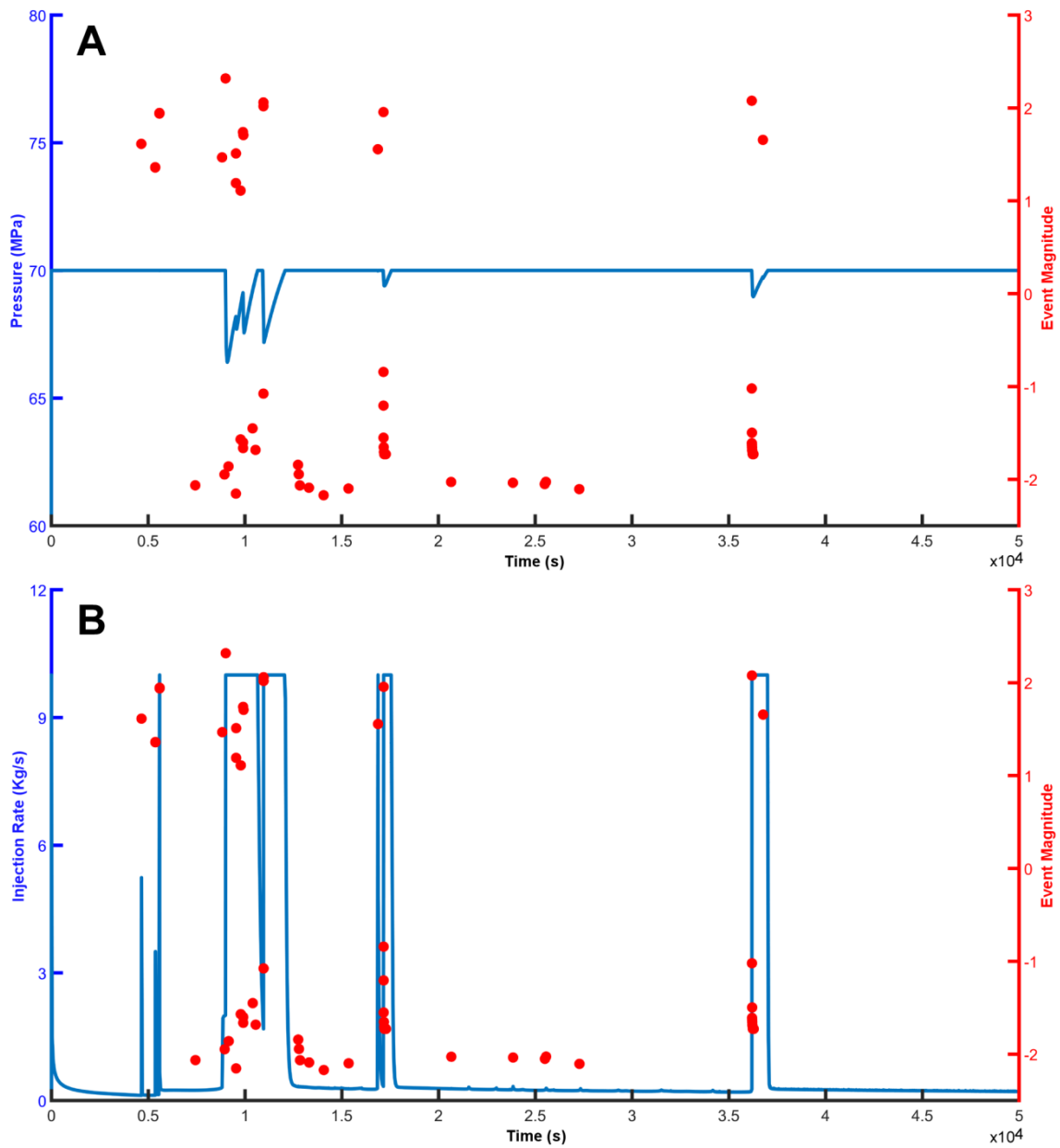


Figure 4. Variation of the (A) fluid pressure in the well and (B) the injection rate with increasing stimulation time. The magnitude of the seismic events is indicated by red circles. In general, events with larger magnitudes are linked to fluid pressure drops in well, although a swarm of low magnitude earthquakes is observed after pressure drops. Additionally, pressure drops are linked to peaks of the injection rate.

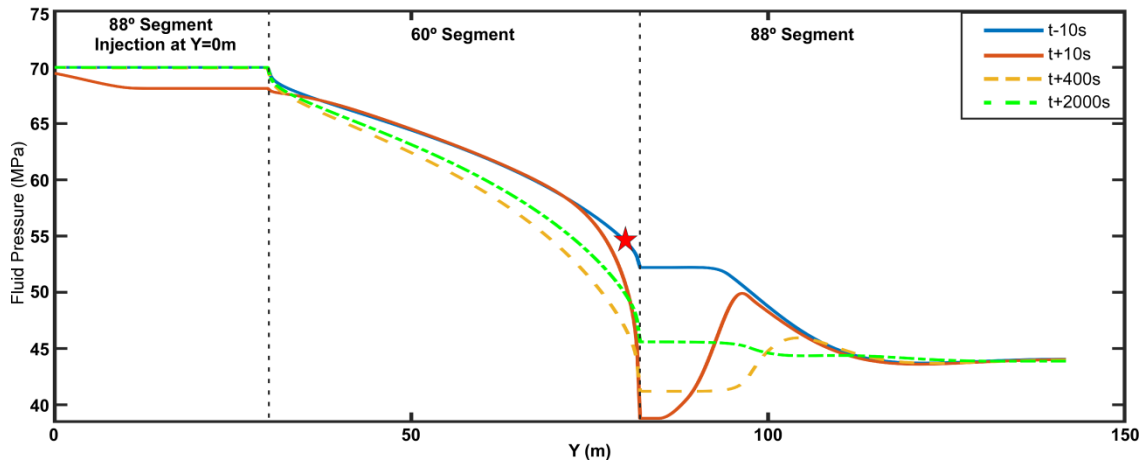


Figure 5. Fluid pressure evolution with the distance to the well (Y) before ($t-10s$) and after ($t+10s$, $t+400s$ and $t+2000s$) a seismic event (indicated by a red star) for the “88-60” model. The event corresponds to the red dashed area indicated in Fig. 3. Vertical dashed lines indicate the location of fracture segment intersections.

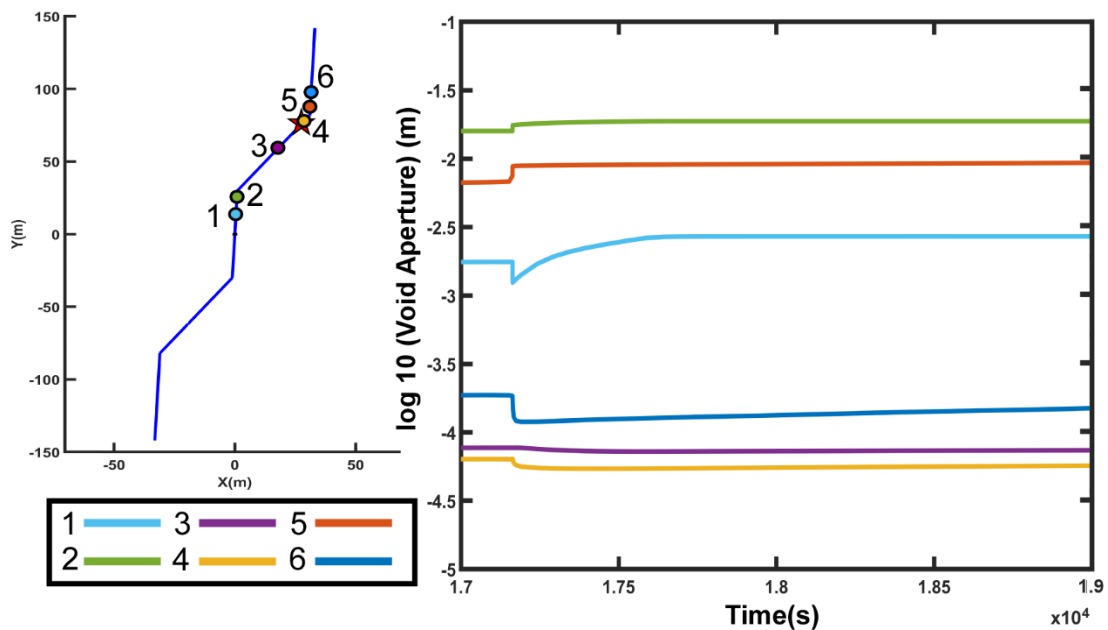


Figure 6. Right, fracture network (in blue) and location of control points (coloured dots). Left, evolution of \log_{10} (void aperture) at the control points through time. The time interval and region monitored by control points is indicated with the red dashed area in Fig. 3. The hypocentre location is the same as that of Fig. 5.

3.4.2 Model “60-88”

Fluid pressure and fracture aperture evolution through time are shown in Fig. 7. In this case, the well was located at a critical seismic fracture ($\alpha=60^\circ$). Microseismicity was detectable from early stages of injection and expanded from the well towards the first fracture intersection (Fig. 7). Abrupt decays of fluid pressure were linked with seismicity, although they did not produce detectable pressure drops at the well. In general, microseismic events occurred near the intersection regions, although several low-magnitude events were observable in the $\alpha=88^\circ$ fractures behind the pressurization front. Progression of the fluid along the fracture produced a migration of hypocentres until they reached the intersection of the

last fracture, producing a large batch of events with strong ruptures (Fig. 7, at approx. $t=4.5 \times 10^4$ s). The evolution of fracture apertures showed similar patterns as in the previous case (88-60 model), with the maximum apertures propagating from fracture intersections following the aseismic $\alpha=88^\circ$ fractures (Fig. 7B).

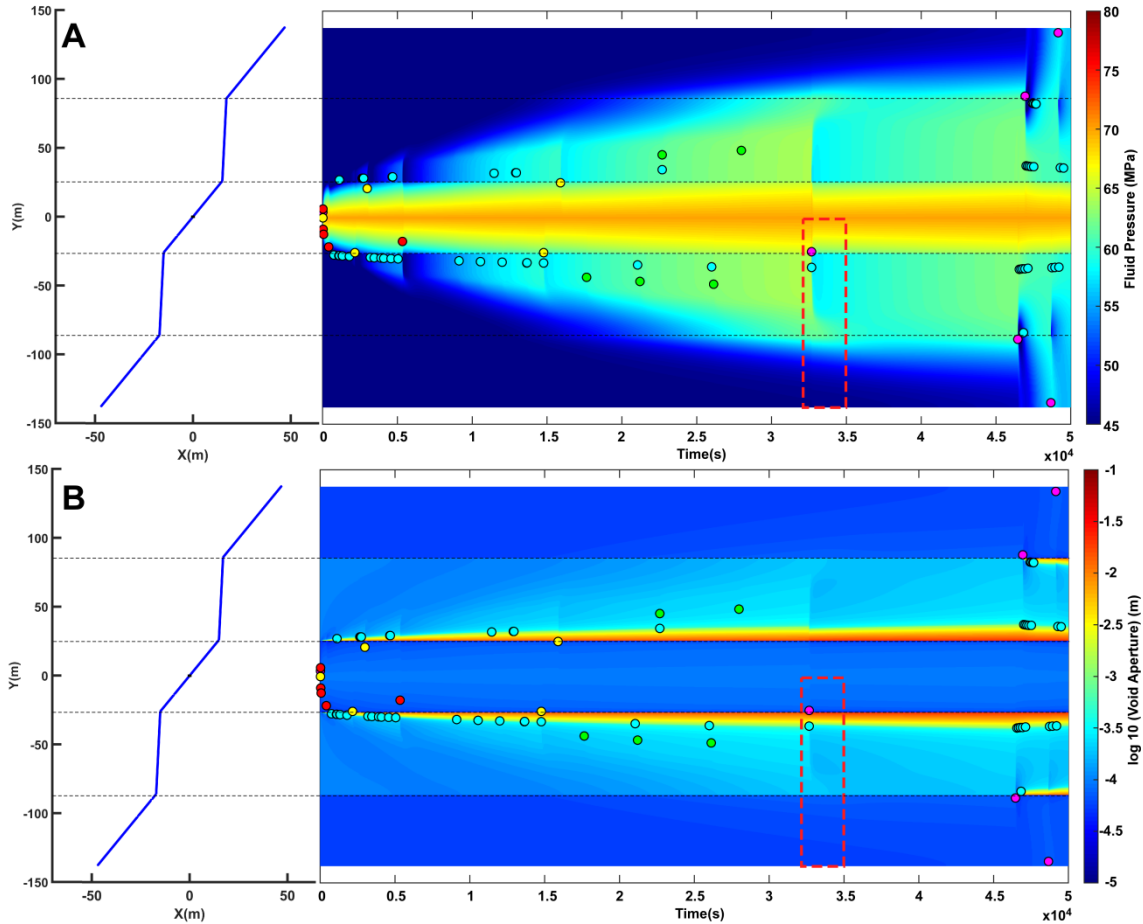


Figure 7. Sketches of the simulated fracture network (blue lines on the left graphs), and the evolution of (A) fluid pressure and (B) fracture aperture for the model “60-88”. Dashed lines indicate the location of fracture segment intersections. Coloured points indicate the location of the earthquake hypocentres and magnitudes (cyan: $M < 0$, green: $0 \leq M < 1$, yellow: $1 \leq M < 1.5$, red: $1.5 \leq M < 2$ and pink: $M \geq 2$). The red dashed area indicates the data shown in Figures 8 and 9.

The event with magnitude $M=2.1$ and hypocentre in the $\alpha=60^\circ$ segment was analyzed for the model “60-88” (Figs. 8, 9) (red dashed line in Fig. 7). In general, fluid pressure curves and patterns are similar to those of the previous case (Fig. 8). For this configuration, the pressure drop was not felt at the well (Fig. 8). The aperture evolution was not homogenous and control points generally showed a decrease of the fracture aperture. Aperture increases occurred only next to the intersection and along the $\alpha=88^\circ$ segment (point 3 in Fig. 9), followed by a region where the aperture decrease was followed by a constant increasing value (point 2 in Fig. 9).

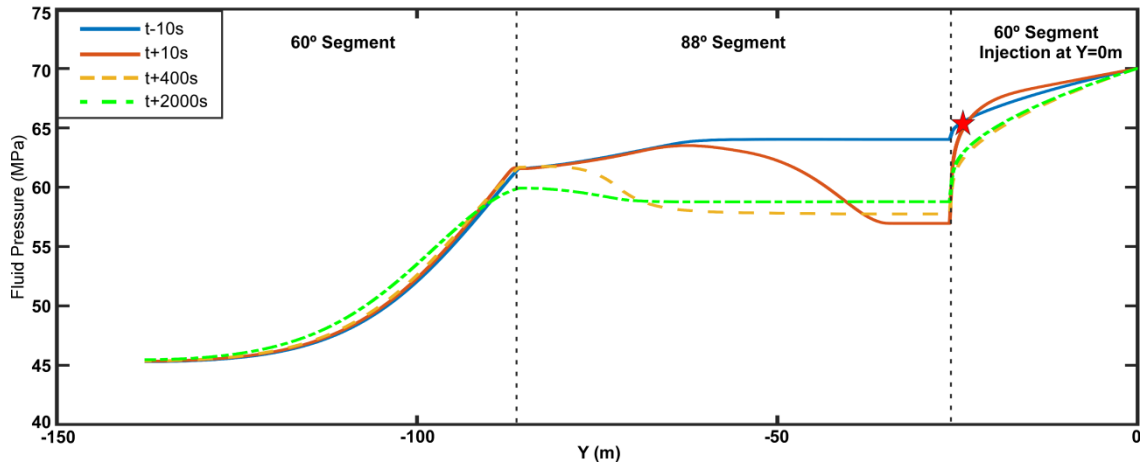


Figure 8. Fluid pressure evolution depending on distance to the well (Y) before ($t-10s$) and after ($t+10s$, $t+400s$ and $t+2000s$) a large magnitude seismic event (red star, $M=2.1$, red dashed rectangle in Fig. 7) for the “60-80” model. Vertical dashed lines indicate the location of intersections between fracture segments.

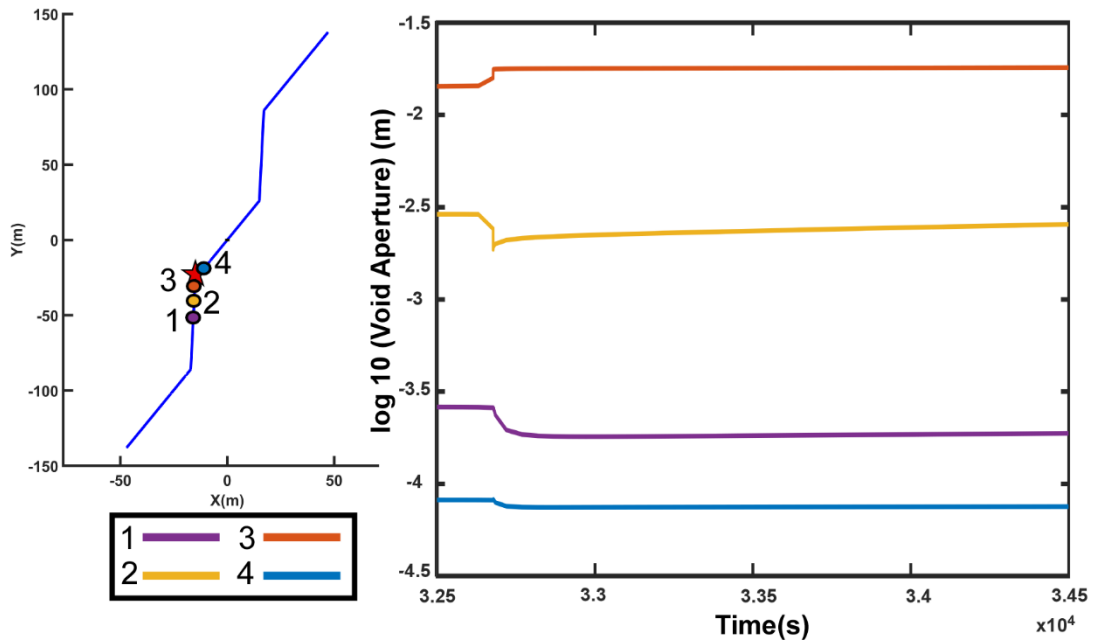


Figure 9. Right, fracture network (in blue) and location of control points (coloured dots). Left, evolution of \log_{10} (void aperture) of the control points through time. The interval of time and region monitored by control points is the red dashed area shown in Fig. 7. The hypocentre location is the same than in Fig. 8.

3.4.3 Model “60-hydro”

Figure 10 shows the evolution of fluid pressure, fracture aperture and microseismic event magnitude and location of the model defined by a pre-existing fracture with two potential tensile cracks at their tips (i.e., wing cracks; red lines in Fig. 10). As in previous models, the events with higher magnitudes were located at the pre-existing segment ($\alpha=60^\circ$), while wing cracks only registered low-magnitude events linked to the propagation of the fluid pressure front. The propagation of this front along wing cracks was relatively slow compared to previous models with pre-existing fractures (models “88-60” or “60-88”). Pressure drops were also identified and linked to seismic events at the $\alpha=60^\circ$ segment (Fig. 10 at around

$t=1 \times 10^4$ s). The widest fracture apertures were observed along wing cracks, while the aperture of the natural fracture slightly increased.

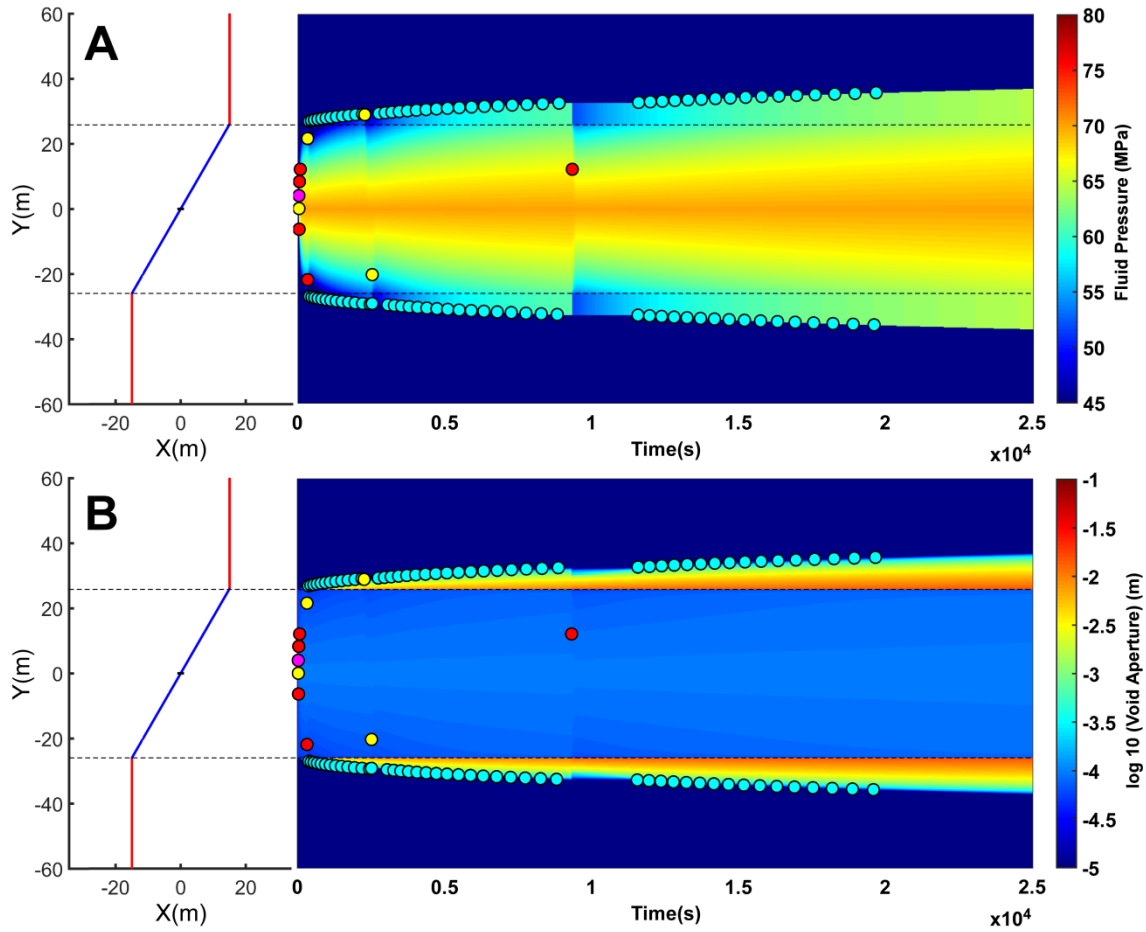


Figure 10. Sketch of the fracture network on the left (the blue line is the pre-existing fracture and red lines represent the wing cracks) and evolution of (A) fluid pressure and (B) fracture aperture. Black dashed lines indicate the fracture segment intersection points. The coloured points indicate the seismic hypocentres and their magnitudes (cyan: $M < 0$, green $0 \leq M < 1$, yellow: $1 \leq M < 1.5$, red: $1.5 \leq M < 2$ and pink: $M \geq 2$).

3.4.4 Sensitivity analysis

All the model configurations (i.e., models “88-60”, “60-88” and “60-hydro”) were run with different values of mechanical dilation angles ($\varphi_{E_{dil}} = 0^\circ, 2.5^\circ$ and 5°) in order to test their influence on fracture aperture and pressure drops. The cumulative apertures increased half an order of magnitude in the seismic segments ($\alpha = 60^\circ$) when large dilation angles were used, while apertures only slightly increased in the aseismic segments ($\alpha = 88^\circ$) (Fig. 11). The total aperture change (normalized by length) was between two and one and a half order of magnitude higher in the aseismic segment than that produced in the seismic segment (Fig. 11). The sharp steps of the accumulated aperture in Fig. 11 correlate with seismic events, while slight and progressive fracture aperture increases characterize the progressive aseismic deformation.

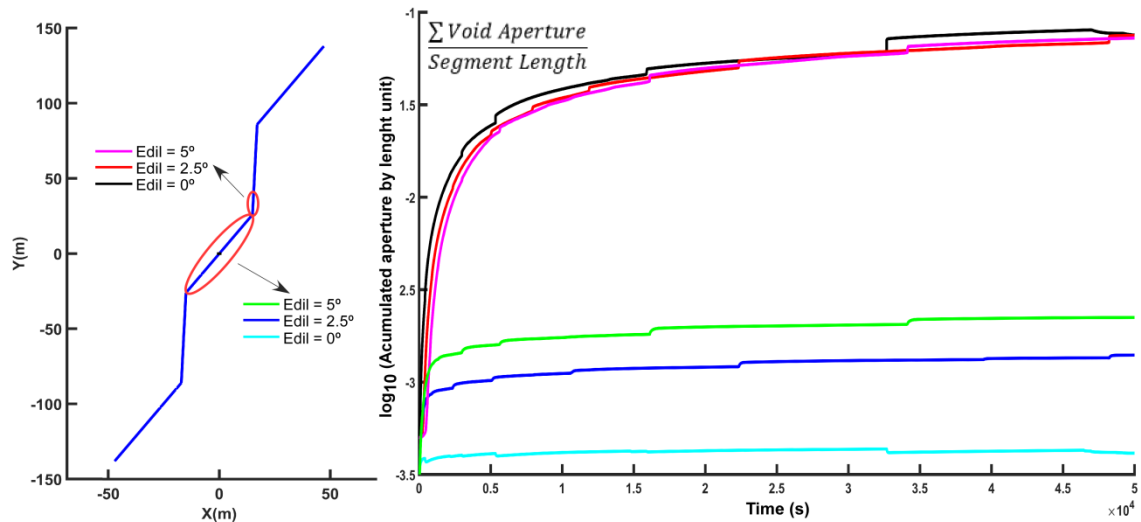


Figure 11. Accumulated aperture by length unit in the injection seismic segment and in the opening region of the aseismic segment with different dilation angles (0° , 2.5° and 5°) for the “60-88” model.

The dilatation angle also plays a secondary role in the occurrence of pressure drops at the well and in the bulk model (Fig. 12A). This tendency depends on the geometrical configuration of the model. While in the “88-60” model configuration there was a pressure drop decrease at the well with increasing dilatation angles (from an average of 1.25 to 0.4 MPa), in the “60-88” models the tendency was the opposite, in a way that pressure drops raise with increasing dilatation angles (from 0 to 1 MPa on average). The “60-hydro” model followed a similar tendency than that observed in the “60-88” model.

Finally, the influence of the length scale of the fracture segments on the pressure drops is summarized in Fig. 12B. Using as a reference the model “88-60” and $\varphi_{Edil} = 0^\circ$, different runs were carried out with different segment sizes (60m, 50m, 30m, 20m, 15m, and 6m). Systematic pressure drops in the well and in the entire domain were identified and the mean values were calculated. There was a systematic decrease of the pressure drop values throughout the system with decreasing segment length (from 6 MPa for the 60 m length model to 1.5 MPa for the 6m model). Pressure drop values in the well were very similar, although there was an increase of ranging between 30 and 15 m (Fig. 12B).

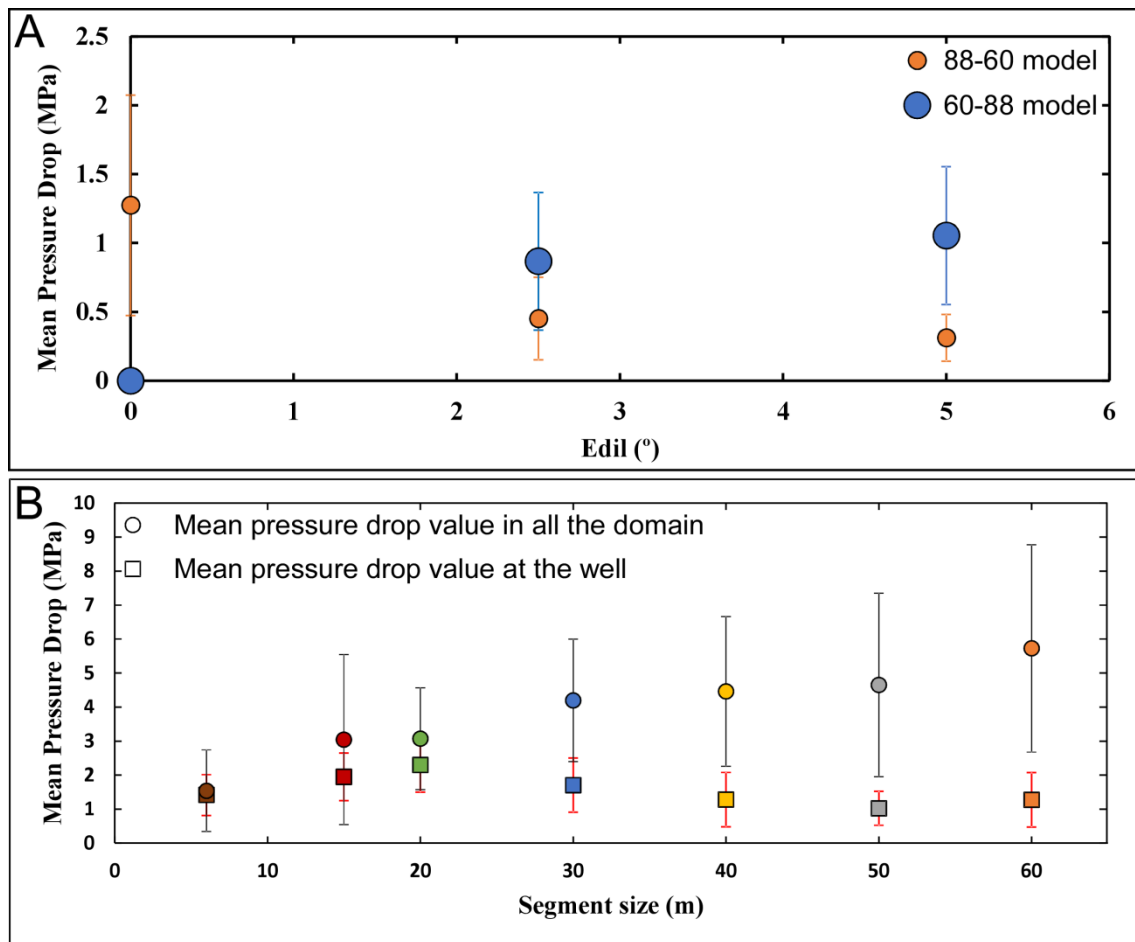


Figure 12. **A.** Mean well pressure drops against different mechanical dilatation angles for the “88-60” and “60-88” configuration models. **B.** Mean pressure drop values observed for all the simulation domain (circles) and felt at the well (squares) for different segment sizes. Error bars indicate the standard deviation.

3.5 Discussion

3.5.1 Pressure drop mechanism

The results of our numerical simulations demonstrate that a direct link between seismicity and pressure drops can be established. The formation of pressure drops seems to be related to the activation of slip along a pre-existing fracture during seismic events in regions near fracture intersections. This process operates in a series of steps summarized in Fig. 13.

In situations where the fluid is injected in a fracture segment at a low angle with σ_1 (e.g., model “88-60”), the fracture high fluid storage capacity or transmissibility allows it to be initially pressurized without seismicity. Once the pressure front reaches the intersection between fracture segments, and a seismic segment is stimulated, microseismicity occurs. When the tensile strength is overcome in the seismic segment (i.e., $\alpha=60^\circ$), the fracture slides and the relative displacement between walls induces stress concentration at fracture tips. In our models this stress was high enough to open the tensional segments, producing a slight decrease of fluid pressure next to the intersection zones (for example see Fig 3

around $t=0.5 \times 10^4$ s). After that, a time lapse is required to re-pressurize the region prior to the onset of a new pressure drop. This pressurization is followed by new seismic events that assist the opening of additional tensional segments. These processes are repeated until all the seismic segments are completely stimulated. While the injected fluid progressively flows from the well throughout the fracture network, seismic events migrate from intersections located next to the injection well to more distant ones. Tensional segments are stimulated as aseismic segments or result in seismic events with very low magnitude. Larger events are located along seismic fractures and tend to occur near the intersections. With ongoing stimulation seismic events progressively occur at longer distances from the injection point and the induced pressure drops are thus hardly observable by looking at the fluid pressure measured at the well. Nevertheless, they are continually happening, as illustrated in Figs. 3, 7 and 10 or in Fig. 12B, in which the difference between pressure drops at the well and in the simulation domain increases with increasing of fracture length.

In cases where fluid injection is carried out in a low-transmissivity fracture segment (model “60-88”; Fig. 7) pressure drops are difficult to be detected at the injection point. The fracture acts as a barrier for the pressure drop propagation due to its low storage capacity and low hydraulic aperture. The process producing pressure drops operates in a similar way as in the model previously described. When the tensile strength is overcome in a seismic segment, a sudden aperture change of the intersection is induced, causing the aseismic/tensional segments (i.e., high-capacity fractures) to get open, generating a new volume and producing the pressure drop (for example, see those at $t=3.25 \times 10^4$ s in Figs. 7, 8 and 9 or between $t=4$ and 4.5×10^4 s in Fig. 7).

Another process associated with void aperture can be detected when pressure drops are analyzed in detail (Figs. 5, 6, 8 and 9). The opening of aseismic fractures was not homogenous in our models, and regions along the same fracture segment experienced closing and opening during stimulation of the fracture intersections. Some regions are opened suddenly, while others are closed suddenly (e.g., points 1 and 6 in Fig. 6). Since a sudden fracture opening should imply a pressure drop, its sudden close should be associated with a local fluid pressure rise. Such local pressure rises, which get quickly dissipated, are likely to be felt more intensively in low-permeability fractures, i.e., in fractures that are shear-stimulated (this can be detected for example in the curve $t+10$ s in Fig. 8 for injection in the 60° segment).

Models “60-88” and “88-60” were carried out to explore the influence of the orientation of the fracture in which the fluid was injected. Despite the initial differences between the two models, their dynamic behaviour is very similar, and both show similar pressure drop phenomena. Similarly, the variation of the dilation angle or the length scale does not modify the described processes, but only determines the absolute values of pressure drops (Fig. 12) and the magnitude of microseismicity. Increasing the

dilatational angle produces a permeability increase in the shear-stimulated fractures, allowing the propagation of pressure drops up to the well (Fig. 12A). However, the pressure drop process is similar than that in models “60-88” and “88-60”, and is related to the reactivation by sliding of a shear stimulated fracture and the opening of the tensile conjugated fractures. Fig.13 shows a synthesis of the processes related to pressure drops. The influence of the injection rate was tested (from 2 kg/s up to 100 kg/s), producing a reduction of pressure drop values. However, the main pressure drop values in the system are independent of this parameter.

The same pattern was observed in the model with wing cracks (model “60-hydro”). When the seismic segment is stimulated, the wing crack is forced to open, producing a pressure drop and enhancing its propagation. In our simulations, pressure drops were not related to wing crack propagation, which was associated with the stress concentration at the edges of the pre-existing fracture. Sliding of the seismic segment allowed wing crack propagation, given that injection pressure in our models was lower than the minimum principal stress (σ_3). This resulted in hydrofracture propagation with injection fluid pressures below σ_3 and in accordance with the model proposed by McClure and Horne (2014), as an explanation of the mixed-mechanism stimulation for EGS projects (i.e., shear stimulation operates jointly with new tensile fracture generation).

As previously mentioned, Meyer et al. (2017) concluded that pressure drops could be produced by the propagation of tensile fractures as a wing crack. This process could be interpreted in a similar way, as observed in breakdown tests and used to identify the minimum principal stress (Prabhakaran et al. 2017). In these tests, the generation of a new hydrofracture produces a pressure drop because the fluid quickly migrates into the newly formed fracture, oriented normal to the minimum stress. However, the process of hydraulic fracture propagation as a wing crack due to the stress concentration at fracture tips was achieved under conditions of fluid pressure below σ_3 . According to the modelling parameters used in our simulations (specifically the injection fluid pressure and the tensile strength of the material), sudden changes as those observed in breakdown tests (in which the injection pressure reaches σ_3) are not observed. Moreover, as discussed above, pressure drops in our models are linked with the tensile fracture opening rather than its propagation, regardless of whether this fracture is a pre-existing or a newly formed one.

3.5.2 Seismicity and pressure drops

In terms of the seismicity associated with pressure drops, we can distinguish two types of events. The first type of seismic event is produced in the seismic segments by fluid pressurization, acting as a trigger for the pressure drop phenomenon and usually producing high magnitudes ($M > 1.5$). The second type of seismic event is produced at the aseismic fracture segments next to the regions that are opening. Normally, the latter events appear as low-magnitude seismic swarms (events with magnitude below one

or zero), produced to accommodate the displacement generated by the sliding of seismic segments and the opening of the aseismic ones. A similar behaviour can be observed in the model containing a pre-existing fracture combined with wing cracks. This duality of the system's seismicity was proposed and analyzed by Fischer and Guest (2011). In their model the higher magnitude events are located at the critically-stressed natural fractures, while lower magnitudes occur at pre-existing tensile fractures or new hydrofractures. Such behaviour would be expected in a mixed-stimulation mechanism, where these different stimulation mechanisms operate jointly (McClure and Horne 2014; Norbeck et al. 2018).

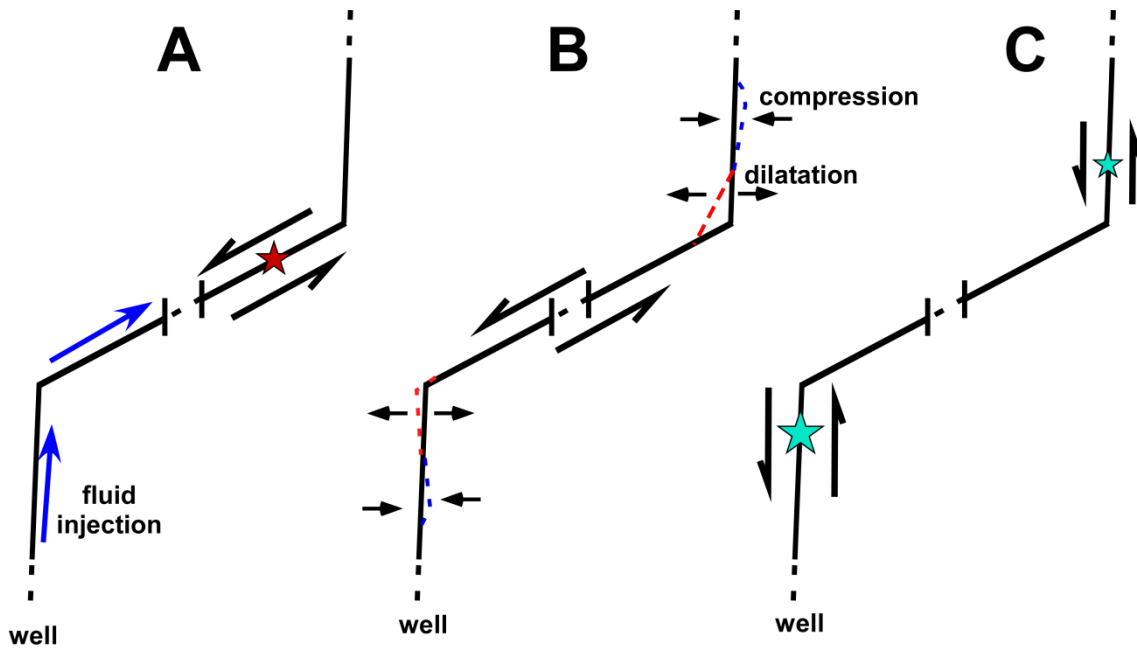


Figure 13. Sketch representing the different processes involved in a fluid pressure drop. **A.** Start of the pressure drop process, in which a seismic event is produced at the seismic segment (red star), with arrows indicating the sliding direction. **B.** Dynamic aperture (red dashed lines) and closure (blue dashed lines) on the aseismic tips connected with the seismic segment. **C.** Low-magnitude events at the aseismic tips occur to accommodate the opening generated. Seismicity is higher in the already pressurized segment than in the new stimulated segment (blue stars).

A key aspect in our simulations is the tendency of microseismicity to cluster next to the intersections between fractures. The influence of intersections between fractures on the seismicity population and location was already proposed by Rutledge et al. (2004). Their interpretation of microseismicity generated during fluid stimulation in the Cartage Cotton Gas field (Texas) showed anomalous dense clusters of seismic events following intersections between fractures. Clusters showed location patterns diverging in time, progressively migrating from the injection zone to far away regions. Additionally, clustering of events was related to fewer and larger precursor events along critically-stressed fractures, while other segments oriented at low angles to σ_1 experienced an aseismic behaviour. After injection shut-in, new large-magnitude and clustered seismic events were observed. This phenomenon was interpreted by Rutledge et al. (2004) as a result of fluid flow forced by slip-induced loading along critical seismic fractures. During injection the increase of fluid pressure critically stimulated pre-existing fractures and fracture intersections, allowing fluid migration along the fracture network.

3.5.3 Rittershoffen sensitivity analysis

To evaluate the applicability of our results, stress drops and microseismicity data from the stimulation of the GRT1 well in Rittershoffen (Meyer et al. 2017) were analyzed using a sensitivity analysis similar to that presented here. The stress and injection conditions used for these models are described in the Model Setup section. For this setup, pressure drops and seismic magnitudes are lower than those previously described, as stress magnitudes are substantially lower. The relationship between pressure drops mean values in the well and in the simulation domain with respect to the seismic magnitudes are shown in Fig. 14. Pressure drops were not detected at the well for fractures with length scales below 30 m. The maximum was observed for 50 m-long fractures, while those longer than 80 m produced pressure drops that could hardly be detected at the well. As expected, a proportional relationship between the seismic magnitude and pressure drops in the system was observed. For the range of seismic magnitudes and pressure drops observed in the Rittershoffen case (box grey area in Fig. 14; from Meyer et al. 2017), we can infer that fracture sizes of stimulated fractures could range between 40 and 60 m. A better constraint could potentially be obtained if pressure drop data were linked to magnitude and epicentre (unreported in Meyer et al., 2017), because in such case the distance to the well could be utilized for the analysis. However, a handicap is that large uncertainty is normally associated with earthquake location data, normally longer than hundreds of meters (e.g., Kinnaert, 2016).

Furthermore, our models show that the time lapse between the main earthquake event and the pressure drop at the well occurs after a few seconds (less than 2-4 s). This very short time interval probably implies that both phenomena will be almost simultaneously detected in real cases, requiring a highly precise time synchronization between injection and seismicity data.

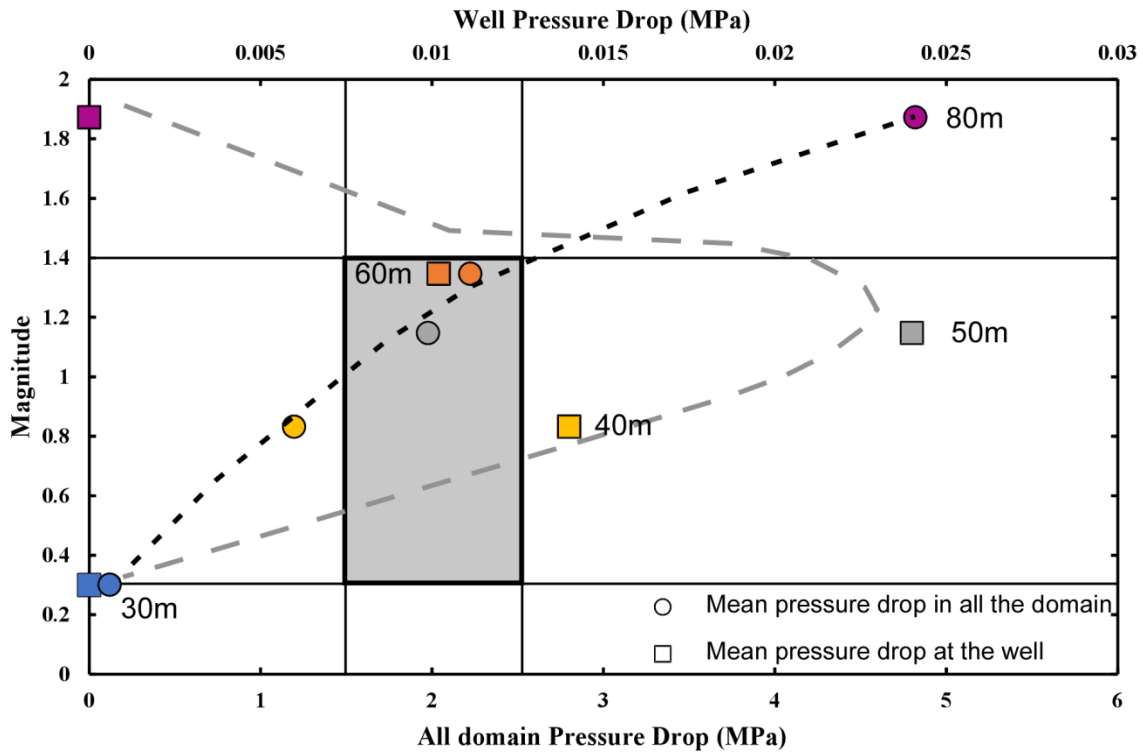


Figure 14. Mean seismic magnitude against mean pressure drop in all the domain (circle symbols, lower x-axis) and at the well (square symbols, upper x-axis). Each colour represents a different segment size, ranging from 30 to 80 m. Pressure drops were not observed in models with length size lower than 30m. The black dashed curve indicates the general tendency of pressure drops measured in all the domain, while the grey dashed curve represents the general tendency of pressure drops at the well. The dashed area indicates the range of pressure drops and seismic events observed during stimulation in the Rittershoffen reservoir (Meyer et al., 2017).

Our models use simplified geometries and are intended to help investigate and understand physical processes, rather than provide a perfect representation of reality. We chose not to use a model with complex multifracture networks, such as that utilized by Meyer et al. (2017), in order to isolate the main processes controlling pressure drops and seismicity. With a more complex network, the superposition of effects could attenuate the phenomena. Simulations by Meyer et al. (2017) with multifracture networks also produced pressure drops next to the intersections between fractures. However, their signal in the fluid pressure evolution at the well was attenuated. Additionally, there is a higher chance that more fractures can act as barriers to the propagation of transient variations of fluid pressure in multifracture systems. Our results confirm the interpretation by Meyer et al. (2017) that the conditions required to observe pressure drops in wells are very specific and unlikely to be observed in all reservoir formations. For injection wells located at a fracture with high transmissibility (i.e., model “88-60”), pressure drops at the well are potentially observable. However, pressure drops are hardly detectable in situations where the wells are located in low-transmissibility fractures (i.e., model “60-88”). However, as demonstrated by the numerical simulations presented here, pressure drops may occur in the reservoir even if they are not detected at the injection well.

Our simulations were carried out in isothermal conditions and therefore thermal drawdown effects are not modelled. In terms of stress reduction and seismicity, Gan and Elsworth (2014) observed that a second seismic cycle is developed related to the thermal drawdown that could potentially produce a second pressure drop cycle. It would be useful to repeat our analysis with a fully 3D model, since 2D models may enhance the magnitude of early events. Furthermore, the height used in our models (Table 1) is only an assumption required to take into account the third dimension, assuming plain strain for height values much larger than the fracture size (Show and Crouch 1995).

3.6 Conclusions

Using simple fracture geometry configurations, we investigated different hypotheses for the occurrence of fluid pressure drops associated with hydraulic stimulation in Engineered Geothermal Systems (EGS). The results suggest that two fracture sets can influence pressure drops: one system able to be stimulated by shear (that will produce seismic events) and another one able to be stimulated by opening-mode fracturing (that will be aseismic). The tendency of stimulation by shear- or opening-mode fracturing is determined by the operational parameters (i.e., injection pressure, flow rate, etc.) and the stress state.

In the simulations, a pressure drop can be triggered by a seismic event in a shear-stimulated fracture that is hydraulically connected with a tensile or opening-mode fracture. The pressure drop is not produced by the new volume created by dilatancy, but by the opening of the conjugated tensile fracture instead.

This tensile fracture set may be part of the pre-existing fracture network, or alternatively, be developed as a hydrofracture during the stimulation phase. However, in our simulations no pressure drops are observed during hydraulic fracture propagation at the tips of a pre-existing fracture. Nevertheless, once wing cracks are created, it is possible that slip along the natural fracture causes a significant aperture change on the splay fracture that can result in a pressure drop. In addition, we show how seismicity propagates through fracture arrays while poorly oriented segments slip aseismically. Seismicity is concentrated in critically oriented fractures near fracture intersections. The pressurization front propagates non-smoothly and can be affected by the interaction of a conjugate fracture with other fractures with tensional or sliding properties. Our simulation results show that natural fracture/splay fracture interaction is a plausible explanation for the observed pressure drops at the Rittershoffen geothermal site.

3.7 References

- Baujard C, Genter A, Dalmais E, Maurer V, Hehn R, Rosillette R and Vidal J (2017) Hydrothermal characterization of wells GRT-1 and GRT-2 in Rittershoffen, France: Implications on the understanding of natural flow systems in the Rhine graben. *Geothermics* 65:255–268 . doi: 10.1016/j.geothermics.2016.11.001
- Breede K, Dzebisashvili K, Liu X, Falcone G (2013) A Systematic Review of Enhanced (or Engineered) Geothermal Systems: Past, Present and Future. *Geotherm Energy* 1:1–27 . doi: 10.1186/2195-9706-1-4
- Cornet FH, Bérard T, Bourouis S (2007) How close to failure is a granite rock mass at a 5 km depth? *Int J Rock Mech Min Sci* 44:47–66 . doi: 10.1016/j.ijrmms.2006.04.008
- Dempsey D, Suckale J (2015) Induced Earthquake Sequences in Geothermal Settings : Data Trends and Modeling Approaches. Proc 40th Stanford Geotherm Work
- Elders WA, Nielson D, Schiffman P, Schriener A (2014) Investigating ultra high-enthalpy geothermal systems: A collaborative initiative to promote scientific opportunities. *Sci Drill* 18:35–42 . doi: 10.5194/sd-18-35-2014
- Fischer T, Guest A (2011) Shear and tensile earthquakes caused by fluid injection. *Geophys Res Lett* 38:2–5 . doi: 10.1029/2010GL045447
- Gan Q, Elsworth D (2014) Analysis of fluid injection-induced fault reactivation and seismic slip in geothermal reservoirs. 1–26 . doi: 10.1002/2013JB010500.
- Garagash DI, Germanovich LN (2012) Nucleation and arrest of dynamic slip on a pressurized fault. *J Geophys Res B Solid Earth* 117:1–27 . doi: 10.1029/2012JB009209
- Gischig VS (2015) Rupture propagation behavior and the largest possible earthquake induced by fluid injection into deep reservoirs. *Geophys Res Lett* 42:7420–7428 . doi: 10.1002/2015GL065072
- Häring MO, Schanz U, Ladner F, Dyer BC (2008) Characterisation of the Basel 1 enhanced geothermal system. *Geothermics* 37:469–495 . doi: 10.1016/j.geothermics.2008.06.002
- Kinnaert X (2016) Data processing of induced seismicity: estimation of errors and of their impact on geothermal reservoir models. Université de Strasbourg PhD Diss 1-194.
- Király E, Zechar JD, Gischig V, Karvounis D, Heiniger L and Wiemer S (2015) Modeling and Forecasting Induced Seismicity in Deep Geothermal Energy Projects. Proc World Geotherm Congr 19–25
- Kohl T, Mégel T (2007) Predictive modeling of reservoir response to hydraulic stimulations at the European EGS site Soultz-sous-Forêts. *Int J Rock Mech Min Sci* 44:1118–1131 . doi: 10.1016/j.ijrmms.2007.07.022
- Majer EL, Baria R, Stark M, Oates S, Bommere J, Smith B and Asanuma H (2007) Induced seismicity associated with Enhanced Geothermal Systems. *Geothermics* 36:185–222 . doi: 10.1016/j.geothermics.2007.03.003
- Marone C, Scholz CH (1988) The depth of seismic faulting and the upper transition from stable to unstable slip regimes. *Geophys Res Lett* 15:621–624 . doi: 10.1029/GL015i006p00621
- McClure MW (2012) Modeling and Characterization of Hydraulic Stimulation and Induced Seismicity in Geothermal and Shale Gas Reservoirs. Stanford PhD Diss 1–369
- McClure MW (2014) The Potential Effect of Network Complexity on Recovery of Injected Fluid Following Hydraulic Fracturing. SPE Unconv Resour Conf. doi: 10.2118/168991-MS
- McClure MW (2015) Generation of large postinjection-induced seismic events by backflow from dead-end faults and fractures. *Geophys Res Lett* 42:6647–6654 . doi: 10.1002/2015GL065028.Received
- McClure MW, Horne RN (2011) Investigation of injection-induced seismicity using a coupled fluid flow and rate/state friction model. *Geophysics* 76:WC181 . doi: 10.1190/geo2011-0064.1
- McClure MW, Horne RN (2013) Characterizing hydraulic fracturing with a tendency for shear stimulation test. Soc Pet Eng SPE166332:1–17 . doi: 10.2118/166332-MS

- McClure MW, Horne RN (2014) An investigation of stimulation mechanisms in Enhanced Geothermal Systems. *Int J Rock Mech Min Sci* 72:242–260 . doi: 10.1016/j.ijrmmms.2014.07.011
- Meyer G, Baujard C, Hehn R, Genter A and McClure MW (2017) Analysis and Numerical Modelling of Pressure Drops Observed During Hydraulic Stimulation of GRT-1 Geothermal Well (Rittershoffen, France). *Proc 42nd Work Geotherm Reserv Eng* 1:14
- Moeck IS (2014) Catalog of geothermal play types based on geologic controls. *Renew Sustain Energy Rev* 37:867–882 . doi: 10.1016/j.rser.2014.05.032
- Norbeck JH, McClure MW, Horne RN (2018) Field observations at the Fenton Hill enhanced geothermal system test site support mixed-mechanism stimulation. *Geothermics* 74:135–149 . doi: 10.1016/j.geothermics.2018.03.003
- Piris G, Griera A, Gomez-rivas E, et al (2017) Induced Seismicity in pressurised single fractures : a numerical approach. *Geogaceta* 61:95–98
- Prabhakaran R, De Pater H, Shaoul J (2017) Pore pressure effects on fracture net pressure and hydraulic fracture containment: Insights from an empirical and simulation approach. *J Pet Sci Eng* 157:724–736 . doi: 10.1016/j.petrol.2017.07.009
- Rubin AM, Ampuero JP (2005) Earthquake nucleation on (aging) rate and state faults. *J Geophys Res Solid Earth* 110:1–24 . doi: 10.1029/2005JB003686
- Rutledge JT, Phillips WS, Mayerhofer MJ (2004) Faulting induced by forced fluid injection and fluid flow forced by faulting: An interpretation of hydraulic-fracture microseismicity, Carthage Cotton Valley gas field, Texas. *Bull Seismol Soc Am* 94:1817–1830 . doi: 10.1785/012003257
- Schill E, Genter A, Cuenot N, Kohl T (2017) Hydraulic performance history at the Soultz EGS reservoirs from stimulation and long-term circulation tests. *Geothermics* 70:110–124 . doi: 10.1016/j.geothermics.2017.06.003
- Scholz C (2002) *The mechanics of earthquakes and faulting*, 2nd editio. Cambridge University Press, New York
- Segall P (2010) *Earthquake and volcano deformation*. Princeton University Press, New Jersey
- Shou KJ, Crouch SL (1995) A higher order Displacement Discontinuity Method for analysis of crack problems. *Int. J. Rock Mech. Min. Sci. Geomech. Abstr.* 32(1), 49-55. doi: 10.1016/0148-9062(94)00016-V
- Tester JW, Anderson BJ, Batchelor AS, et al (2006) *The Future of Geothermal Energy - Impact of Enhanced Geothermal Systems (EGS) on the United States in the 21st Century*. MIT - Massachusetts Inst Technol 358
- Willis-Richards J, Watanabe K, Takahashi H (1996) Progress toward a stochastic rock mechanics model of engineered geothermal systems. *J Geophys Res* 101:
- Zeeb C, Konietzky H (2015) Simulating the Hydraulic Stimulation of Multiple Fractures in an Anisotropic Stress Field Applying the Discrete Element Method. *Energy Procedia* 76:264–272 . doi: 10.1016/j.egypro.2015.07.859
- Zimmermann G, Reinicke A (2010) Hydraulic stimulation of a deep sandstone reservoir to develop an Enhanced Geothermal System: Laboratory and field experiments. *Geothermics* 39:70–77 . doi: 10.1016/j.geothermics.2009.12.003

Capítol 4

4 On the influence of fault geometry in seismic cycle under fluid injection scenarios: a numerical approach

4.1 Introduction

Field studies reveal that faults are many times non-planar and show complex geometries. For example, the variation in the orientation of fault segments (e.g. ramp-flat geometries in thrust and normal faults), development of step-overs, releasing/restraining bents, branching, or splay in several other faults. As a first approach, a non-planar fault can be described by concatenated planar segments with different orientations. This can be done at different scales, from centimetres to kilometres (e.g. Harris & Day 1993; Brankman & Aydin 2004; Ritz et al., 2015) in a way to describe the roughness and irregularities of faults. These geometrical complexities play an important role in earthquakes because can control the rupture location (e.g. Bie & Ryder, 2014; Hicks et al., 2016), the seismic cycle (i.e. number, magnitude, seismic-aseismic events; Romanet et al., 2018), the propagation of the seismic rupture through different segments (Oglesby, 2005; Oglesby et al., 2003; Oglesby & Mai, 2012), or the earthquakes mechanics (Romanet et al., 2020). For these reasons, the consideration of more realistic fault geometries is important to properly evaluate the Coulomb stress transfer and its effects on seismic production (Mildon et al., 2016). In this way, Zielke et al (2017) proposed that fault roughness and the heterogeneous distribution of strength control the magnitude and static stress drop in natural earthquakes. They showed that smooth, flat faults generate larger magnitude earthquakes than rougher faults under the same tectonic conditions. In the context of thrust systems, Sathiakumar and Barbot (2021) recently suggested that earthquake locations and magnitudes along the Main Himalayan Thrust are controlled by flat-and-ramp geometries, with major production near to abrupt change of orientations.

For scenarios in which the driven energy to destabilize fractures is by anthropic fluid injection, different authors have previously demonstrated that the rupture propagation and the slip behaviour depend on the relative orientation of fault segments to the main stress axes (e.g. Ciardo & Lecampion, 2019; Garagash & Germanovich, 2012; Gischig, 2015; Piris et al., 2018). For example, dynamic aspects such as slip distribution, migration of fluid pressure front, or evolution of the seismicity are highly dependent on fault orientation. However, in general, these studies were focused on single, planar fault scenarios where the variation of fault orientations was not evaluated.

In this work, we evaluate through numerical simulations the influence of the variation of fault segment orientation in the seismic cycles and how it differs from the single-planar fracture solution. Fractures are geometrically represented as periodic releasing or restraining bents (Fig. 1), displaying a macro-roughness that scales from meters to ten meters. The 2D fully coupled hydro-mechanical code CFRAC

(McClure and Horne 2011, 2013) was used. This code uses a discrete element approach to simulate fracture networks and allow to model the stresses variation by fluid injection and to record the seismicity induced.

We focus our analysis on how fault geometry affects seismic production (i.e. hypocentre location and magnitude-frequency), seismic cycle, and the capacity to propagate seismic ruptures. Special attention is focused on the influence of bends (i.e. abrupt change of segment orientations). Unlike other studies where the event location was predefined and nucleated by the increase of shear stress (e.g. Oglesby & Mai, 2012; Romanet et al., 2018), in this work, we simulate seismic events triggered by fluid injection, such as that occurring during the management of enhanced geothermal systems, hydrocarbon reservoirs or storage sites for geo-energy applications (Hearn et al., 2018; Martínez-Garzón et al., 2017). Furthermore, the analysis of the system is evaluated dynamically through time to take into account past effects in order to allow to predict the future behaviour of the system.

4.2 Methodology

The numerical simulations were carried out with the 2D discontinuous element code CFRAC (McClure, 2012). This software can solve the fully-coupled hydro-mechanical problem related to the injection of a fluid through a fracture network embedded in an impermeable matrix and the associated induced seismicity (McClure and Horne 2011, 2013, 2014; among others). These conditions are typically found in deep geothermal reservoirs in crystalline basement rocks, where matrix permeability is nearly zero and fluid flow only occurs on fractures. The full-field fluid flow evolution and the reactivation of pre-existing fractures (by opening and/or sliding) are solved at the same time. In these simulations, a single-phase fluid (liquid water) is assumed and the thermal effects are neglected (i.e. isothermal conditions). The simulation is initialized under a homogeneous and anisotropic stress field, with initial homogeneous fluid pressure distribution. CFRAC can simulate both pre-existing fractures and new hydraulically formed fractures, although the location of potentially new-formed fractures must be pre-defined in advance. The frictional resistance to slip is given by Coulomb's law:

$$|\tau - nv| = \mu_f(\sigma_n - Pf) + S_0 \quad (1)$$

where τ is the shear stress, n is the radiation damping coefficient, v is the sliding velocity of the fracture, μ_f is the friction coefficient, σ_n is the normal stress, Pf is the fluid pressure and S_0 is the fracture cohesion. The evolution of the friction coefficient was defined using a rate-and-state formulation where this parameter depends on the sliding velocity (v) and the sliding history of the fracture (Scholz, 2002; Segall, 2010):

$$\mu_f = f_0 + a \cdot \ln\left(\frac{v}{v_0}\right) + b \cdot \ln\left(\frac{\theta v_0}{d_c}\right) \quad (2)$$

where f_0 is the nominal friction coefficient, a and b are the velocity effect coefficient and the state effect coefficient respectively, v_0 is the reference sliding velocity and θ is the state value.

The code integrates a process that allows simulating the production of seismic events. For our simulations, a microseismic event is considered to begin when the sliding velocity along a fracture exceeds a reference velocity of 5 mm/s. A slip event is considered to have concluded when the highest velocity in the fracture drops below 2.5mm/s (McClure, 2012). The hypocentres of micro-events are located in the element where the reference sliding velocity is exceeded first. The seismic moment magnitude and the seismic moment were defined in order to define the size of the event. The seismic moment (M_0) was defined as a function of the fracture area and its displacement (Stein & Wysession, 2003). This parameter is related to the size and the total energy released by the earthquake and is defined as the integral of the displacement (D) over the fracture area (A) and the shear modulus (G):

$$M_0 = G \int D \cdot dA \quad (3)$$

where, M_0 is expressed in N·m. The seismic moment magnitude (M_w) is correlated with M_0 following the approach by Hanks and Kanamori (1979):

$$M_w = \frac{\log_{10} M_0}{1.5} - 6.06 \quad (4)$$

For a more detailed description of the mathematical formulation used by CFRAC see McClure (2012) or McClure and Horne (2013).

4.3 Model set-up

The initial geometry of the models consisted of a sigmoidal isolated fracture combining segments with two different orientations (Fig. 1A). The angle of fracture segments α was defined as the angle between the segment normal and the maximum compressive stress axis σ_1 . The length of sigmoidal fracture is approximately $L=300\text{m}$, with an envelope angle of $\alpha=74^\circ$. Fractures were defined using linear segments with variable lengths (Fig. 1B) and discretized using element sizes of 20 cm. However, in regions near orientation changes, the element size was refined with shorter lengths (up to 0.10 m) to prevent numerical instabilities. The simulations are two-dimensional and should be interpreted as showing vertical fractures sliding horizontally, viewed from above. A constant out-of-plane height of $h=100\text{m}$ was considered for all models to take into account this third dimension. The Olson (2004) adjustment was used to approximate the effect of a finite formation height on the induced stresses (so that the calculations are pseudo-3D instead of either plane strain or plane stress).

After evaluating a wide range of orientations (α) and the corresponding sliding regimes, the orientations of $\alpha=60^\circ$ and $\alpha=88^\circ$ were selected to define the fault segments (Fig. 2). These orientations represent two contrasted end-members of the seismic behaviours expected for pressurized faults (Garagash &

Germanovich, 2012; Gischig, 2015; Piris et al., 2018). On the one hand, fractures at $\alpha=60^\circ$ are characterized by a critically loaded behaviour, with high seismicity production and ruptures that can propagate through the entire fault with low pressurization region (Fig 2A and 2B). On the other hand, fractures at $\alpha=88^\circ$ are characterized by an aseismic deformation ($v < 1e-3$ m/s), with some peaks of sliding velocities in high-pressurized regions but unable to produce seismicity (i.e. $v > 5e-3$ m/s) (Fig 2E and 2F). Therefore, the combination of segments with these orientations and the same length produces a macroscopic fault with an envelope orientation $\alpha=74^\circ$ (Fig. 1) For a single and flat fracture with $\alpha=74^\circ$, the seismic behaviour is a transition between critically loaded and aseismic, in which seismic ruptures can propagate beyond the pressurized region but not through the entire fracture (Fig. 2C and 2D).

Therefore, the macroscopic fault system shows sharp orientation changes of 28° between the different segments and 14° respect the fault envelope (Fig. 1A). These values are consistent with field observation directional changes observed in natural faults (e.g. Oglesby & Mai, 2012; Perrin et al., 2019; Sathiakumar and Barbot, 2021).

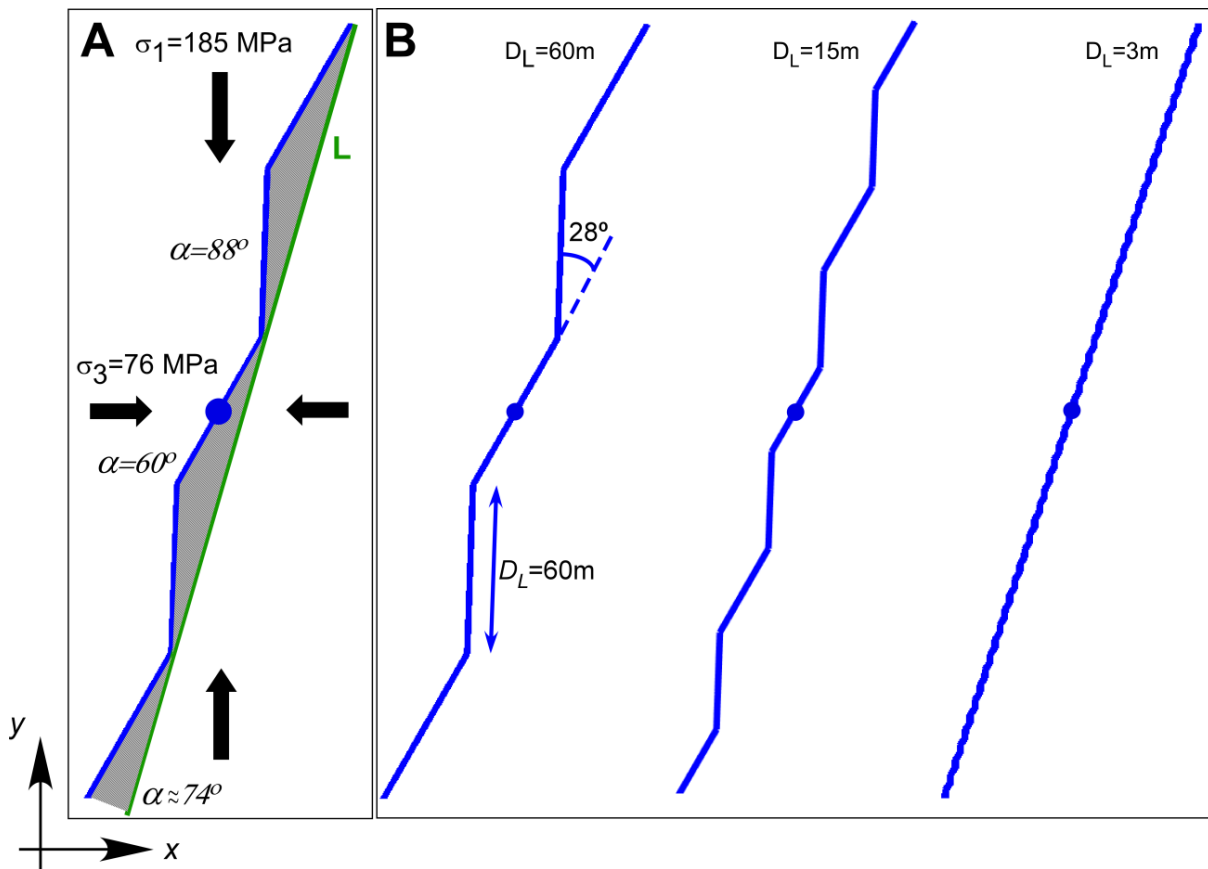


Figure 1. Sketches of simulated fracture networks (blue lines) with the dot as injection point, (A) boundary stress state and reference planar fracture (green line with a longitude L), (B) some examples with different segment sizes ($D_L=60, 15$ and 3 m) for the “60-88” configuration (the central segment is 60 degrees).

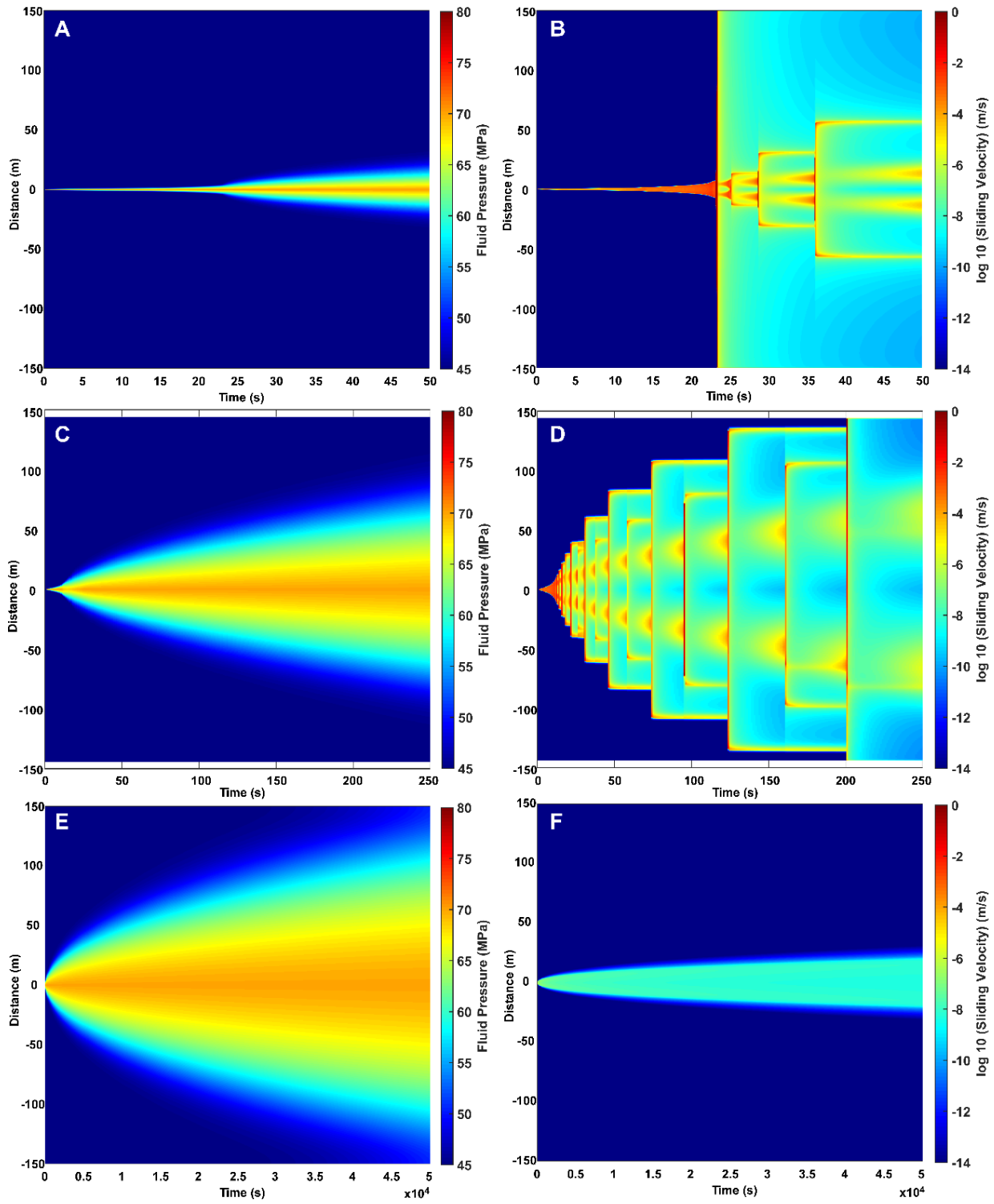


Figure 2. Evolution of the fluid pressure and sliding velocity for the single fault models with orientation $\alpha=60^\circ$ (A and B), $\alpha=74^\circ$ (C and D), and $\alpha=88^\circ$ (E and F). The origin of distance is the injection point located at the centre of the fault. The three examples show different seismic regimes, from critically loaded with uncontrolled rupture beyond the pressurized zone (A and B), pressure-controlled rupture front propagation (C-D), and aseismic behaviour with sliding zone only inside the pressurized region (E-F).

To investigate the effects of geometry changes and scale on the seismic cycle (event locations, magnitude-frequency diagrams, and seismic rupture propagations) models were run with different

lengths of the segments, with lengths ranging between 3 and 60 meters ($D_L = 60, 30, 20, 15, 12, 10, 6$ and 3 meters; e.g., Fig. 1). A series of eight models were run with a central fracture oriented at 60° in the fluid injection point (configuration “60-88”), while an additional series of eight models were run with a central fracture oriented at 88° (configuration “88-60”). The total length L of the macroscopic fault was kept constant and around 300m for all these models. An important parameter to predict the seismic behaviour is the nucleation critical size (L_c), a relationship highly influenced by the parameters of the rate-and-stress law, and expressed as (Scholz, 2002):

$$L_c = \frac{Gd_c}{(\sigma_n - Pf)(b-a)(1-\nu)} \quad (5)$$

where, G is the shear modulus and ν is the Poisson’s ratio. To evaluate the nucleation critical size influence evolution (L_c) with respect to the segment sizes (D_L), different critical distances (d_c) were used to modify the nucleation critical size (L_c) parameter. The range of geometrical and mechanical parameters used in simulations are summarized in Table 1.

Configuration	Segment Size (D_L in m)	d_c (m)	L_c for the 60° segment (m)	Terminology
88_60/60_88	60/30/20/15/12/10/6/3	1e-5/1e-4/1.65e-4/3.3e-4/5e-4/7.5e-4	0.6/6/10/20/30/45	88_60_ D_L _d _c 60_88_ D_L _d _c

Table 1. Different critical distances (d_c) and the associated nucleation critical sizes (L_c) with the equation (4). All the values are in meters. The computed L_c are for the critically loaded configuration (60° segments).

For all the models, the boundary conditions were assumed to be at a depth of 4,500 m, such as roughly that of deep injection projects (Häring et al., 2008; Kwiatek et al., 2019), with initial fluid pressure in the formation defined by the hydrostatic gradient. We assumed a strike-slip regime in which the principal stresses σ_1 and σ_3 are horizontals (i.e. parallel to the y and x -axis of our model, respectively; Fig. 1A), while σ_2 is vertical (oriented out-of-plane in the models). A minimum in-situ stress of 76 MPa was imposed in the x -direction, while the maximum horizontal stress of 185 MPa was applied in the y -direction. A constant injection pressure of 70 MPa was imposed, with a maximum injection rate of 10 kg/s. The simulation time was defined as $5e4$ s for all the simulations.

4.4 Results

A description of the main results is done in this section. Results are shown following three main parameters: (i) the fluid pressure evolution, (ii) seismicity, mainly characterized by the evolution of M_{max} , the total seismic moment, the hypocentre locations, and the seismic vs. slow-slip events, and (iii) the capacity to propagate seismic ruptures through the different fault segments.

4.4.1 Fluid pressure

When injection starts at the centre of the fault (blue dot in Fig.1) and fluid starts to expand through the fracture, the pressurization of the different segments is neither homogeneous nor constant, resulting in sudden pressure drops through the system. (Fig. 3). The pressure drops are related to seismic events, and are detectable by strong decreases of the fluid pressure near the pressurization front. Normally they can propagate along the fault and can in particular conditions be detected at the injection point. Another pattern arising from fluid pressurization is that as the segment size (D_L) is reduced, and therefore there is an increase in the number of directional changes per length, the migration of the pressure front and the pressure gradients are reduced too (Fig. 3).

Fluid pressure curves and patterns are very similar between 88_60 and 60_88 configurations. Some differences are observed in models with $D_L=60$ m because the central segment represents a higher part of the total system. However, as D_L is reduced the influence of the configuration becomes negligible. The main differences are basically related to seismic production during initial stages of the simulation; while the 88_60 configuration starts without seismicity, the 60_88 configuration starts from the beginning with seismic activity.

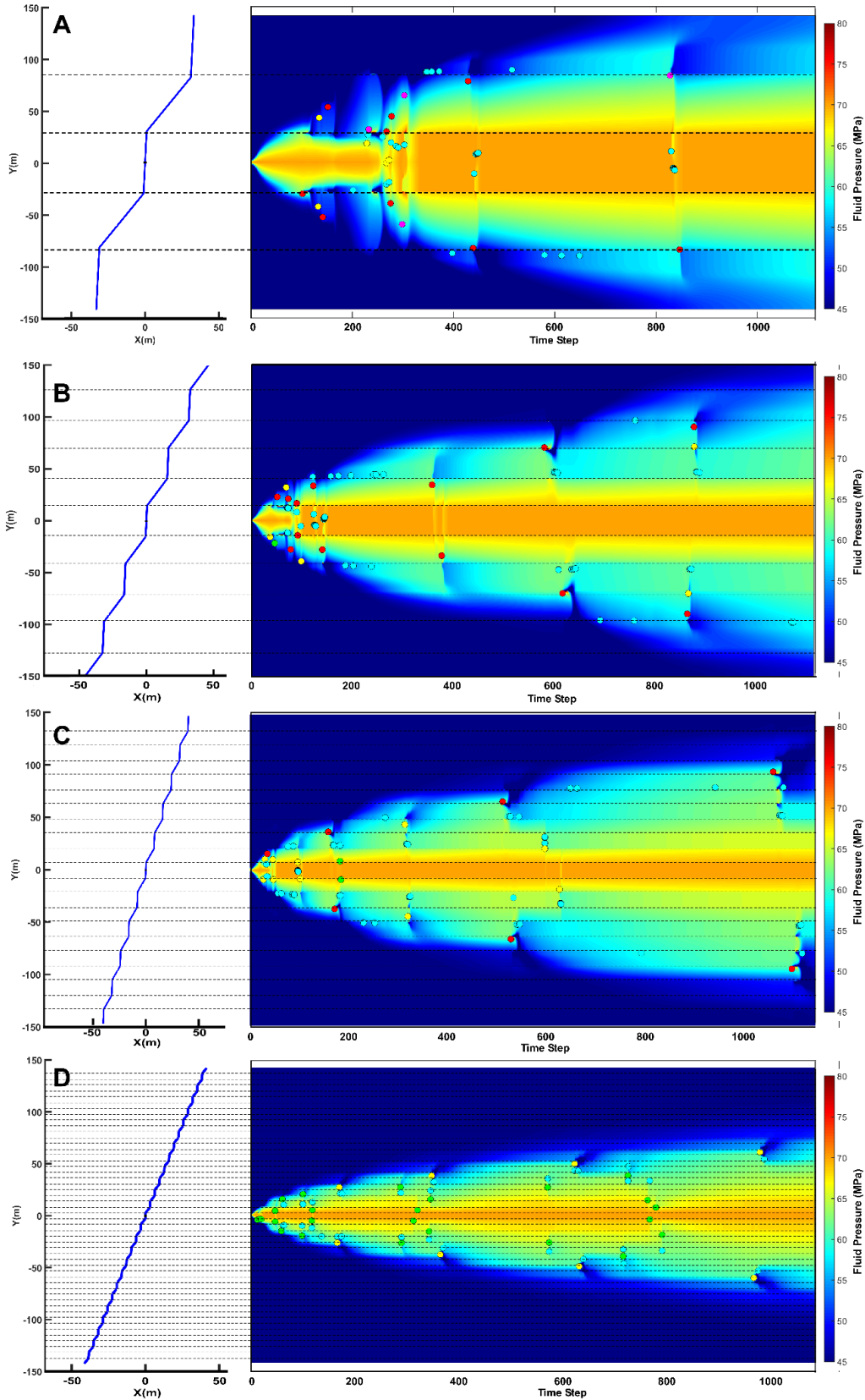


Figure 3. Fluid pressure evolution for different DL (88_60_DL_1e-4). A: DL of 60 meters, B: DL of 30 meters, C: DL of 15 meters and D: DL of 6 meters. Dashed black lines indicate the directional changes or fracture bends. The colour circles are the seismic hypocentres detected using the automatic configuration. Colours indicate the magnitude cyan < 0 , green < 1 , yellow < 1.5 , red < 2 , and magenta ≥ 2 .

4.4.2 Seismicity

The increase of D_L produces an increase in the seismicity production in the model. This can be observed in Table 2, where the data displayed is obtained for the reference models with $d_c=1e-4$ m (or $L_c=6$ m). In terms of maximum magnitude (M_{max}) and total seismic moment, both configurations show similar tendencies. The maximum magnitude ranges from -1.89 to 2.3, with increasing of the maximum magnitude for higher D_L . A similar tendency is observed for the total moment, with values spanning between 10 to $1e7$ MN·m. Similar tendencies are observed using different d_c values. Variation of the total moment is in general proportional to D_L , except for the case with $D_L=3$ with a length size of segments lower than the nucleation length (L_c).

D_L	M_{max}		Total Moment (MN·m)	
	60_88	88_60	60_88	88_60
300	2.42		2.65e+07	
60	2.25	2.32	1.56e+07	1.41e+07
30	2.19	1.95	5.44e+06	6.97e+06
20	2.00	1.92	4.16e+06	5.21e+06
15	1.77	1.77	3.37e+06	3.93e+06
12	1.65	1.65	2.54e+06	2.75e+06
10	1.55	1.55	2.07e+06	2.04e+06
6	1.14	1.10	982007	977506
3	-1.89	-1.48	11.2522	18.581

Table 2. Resume table showing the M_{max} and Total seismic moment (MN·m) for the different configurations 60-88 and 88-60 and for the same $d_c=1e-4$ m.

In terms of hypocentre location, the models reveal that high-magnitude events ($M_w \geq 0$, green, yellow, red and magenta circles in Fig. 3) are located in the proximity of zones where the fault dip changes (Fig. 3), while low-magnitude events ($M_w < 0$, cyan circles in Fig. 3) tend to be located more arbitrarily.

4.4.3 Seismic ruptures propagation

The evolution of slip velocity over time is shown in Fig.4 for models with “88_60” fracture configuration and $d_c=1e-4$ m, for $D_L = 60$ m, $D_L = 30$ m, $D_L = 15$ m, and $D_L = 6$ m. From a general perspective, sliding velocities higher than $1e-3$ m/s are considered seismic events, lower than $1e-3$ m/s are considered aseismic (e.g. Romanet et al., 2018). From the results, it is possible to observe seismic cycles of nucleation, surface rupture propagation, and post-seismic stages that would be considered similar to

those observed in nature. We can observe earthquakes of variable slip velocity and magnitude, with several of them responding to a nucleation stage of slow slip accumulation before triggering an earthquake. In general, stronger seismic events are nucleated in segments with $\alpha=60^\circ$, near fracture intersections.

For all the configurations, and independently of the injection segment orientation, we observed that for first generation events the aseismic segments act as barriers for the event nucleation and propagation (e.g. Fig. 4A first 100 time steps in the injection segment), constraining the event size and the event production to the seismic segment patch, which does not need to be entirely pressurized to slide along all its length (see Figs. 2A, B). However, from this point the fault bends start to play an important role on the seismic cycle. The intersection side corresponding to the aseismic segment starts to slide at low velocities, propagating this sliding towards the aseismic segment. This initial sliding on the aseismic segment starts without needing to be pressurized. On the other hand, the seismic segments always need to have some pressurization to start to slide, although once initiated the rupture propagation can extend beyond the pressurized region (ex. Figs. 2A, B).

When a new event is nucleated (second generation events) on the seismic segment, the region corresponding to the aseismic segment that was sliding at low velocities could slide at seismic velocities, generating a rupture able to go through the zone where the fault orientation changes, resulting in a higher magnitude event.

After this event, a duality of post-seismic behaviour arises between the seismic and aseismic segments. The seismic segment becomes stable due to the stress drop, sliding at velocities near or below the $1e-14$ m/s, and becomes quiet. Contrarily, the aseismic segment remained sliding long periods at low velocities ($1e-5$ to $1e-7$ m/s) after the event, near the segment intersection and on the tip where the event ended (e.g. Fig 4A after time step 400 approx.).

This low velocity sliding in the aseismic segment sometimes can result in low magnitude events that can propagate just in the aseismic segment, or sometimes can propagate to the seismic segments nucleating a new seismic event.

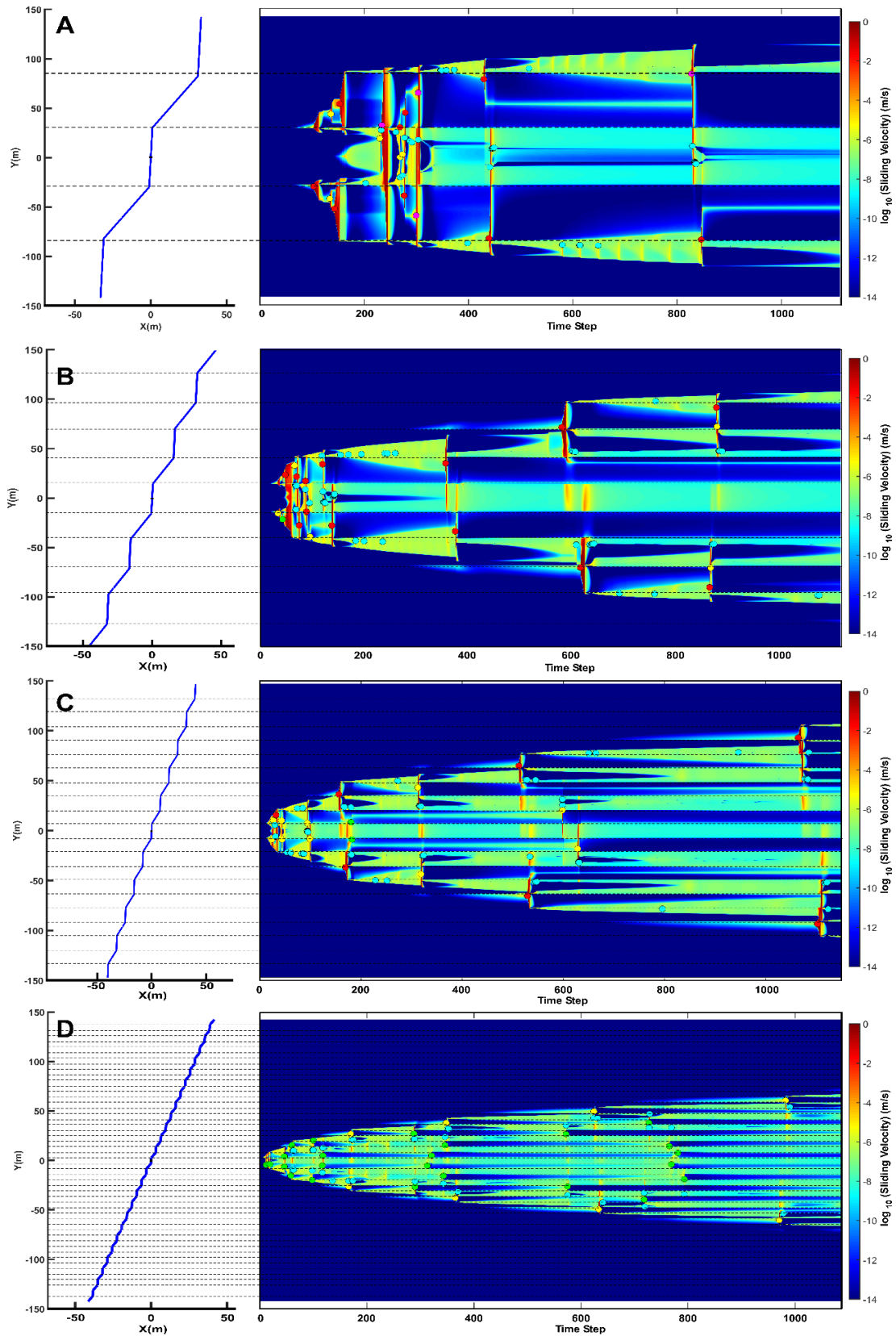


Figure 4. Sliding velocity for different DL (88_60_DL_1e-4). A: DL of 60 meters, B: DL of 30 meters, C: DL of 15 meters and D: DL of 6 meters. Dashed black lines indicate the directional changes or fracture bends. The colour circles are the seismic hypocentres detected using automatic configuration. Colours indicate the magnitude cyan <0 , green <1 , yellow <1.5 , red <2 , and magenta ≥ 2

4.5 Discussion

The results of these series of numerical simulations reveal how fracture bends, expressed as macro-roughness, play a key role in the seismic event production, their propagation, the fracture volume generation, and also are a control on the pressurization of the system. Additionally, the results show that the collective behaviour of a combination of fracture segments with different sliding regimes can be different than that of single segments.

4.5.1 Pressure front propagation

As described in Piris et al. (2018), and as also observed by Deng et al. (2021), fluid pressure drops (Fig. 5) are observed in all the models when a critically loaded segment (i.e. $\alpha = 60^\circ$) slides during a seismic event and tends to open the aseismic and tensional segments ($\alpha = 88^\circ$). These pressure drops are also followed by rapid pressurization due to the constant injection rate. Therefore, pressure drops are physical evidence of the dilatancy process related to mixed stimulation, when sliding along the fracture also produces an opening of the fracture.

The simulations indicate that there is a reduction of the pressurization front velocity with segment size reduction (D_L) and/or increasing the number of bends (Fig. 3 and 5). Both Darcy's law and the analytical expression derived by McClure and Horne (2010) can be used to explain this phenomenon in terms of fluid pressure. The pressure front propagation as a function of time can be calculated as:

$$L_p(t) = \sqrt{\frac{4k_{eq}\rho(1-x)(2+2x)}{\phi c_t \mu (1+x)(1+3x)}} t \quad (6)$$

where $L_p(t)$ is the distance of the pressurization front along the fault, t is time, k_{eq} is the equivalent fracture permeability ($k = b^2/12$, where b is the fracture aperture) after the stimulation process, ρ fluid density, ϕ is the porosity, c_t is the total compressibility, μ is the viscosity and x is the dimensionless pressure parameter defined as:

$$x = \frac{P_{stim} - P_0}{P_{inj} - P_0} \quad (7)$$

where P_{stim} is the fluid pressure at the edge of the stimulated region at the moment at which slip on the next patch of the unstimulated fracture occurs, P_{inj} is the pressure at the injection point and P_0 is the remote fluid pressure. The porosity parameter does not make sense in our simulations because all the fluid is embedded through the fracture and it is assumed to have a value of one, while $P_{inj} = 70\text{MPa}$ and $P_0 = 45\text{MPa}$. For P_{stim} we assigned 54MPa because this is the pressure at which the 60° segments become stimulated and slide. There is no rock compressibility, so that the total compressibility is equal to the compressibility of water. The fluid properties correspond to those of water at 170°C and 70MPa . At those conditions, $c_w = 0.516 \times 10^{-6} \text{ kg/m}^3/\text{MPa}$ (expressed here in units of density per unit pressure), $\rho = 900 \text{ kg/m}^3$ and $\mu = 1.596 \times 10^{-4} \text{ Pa}\cdot\text{s}$.

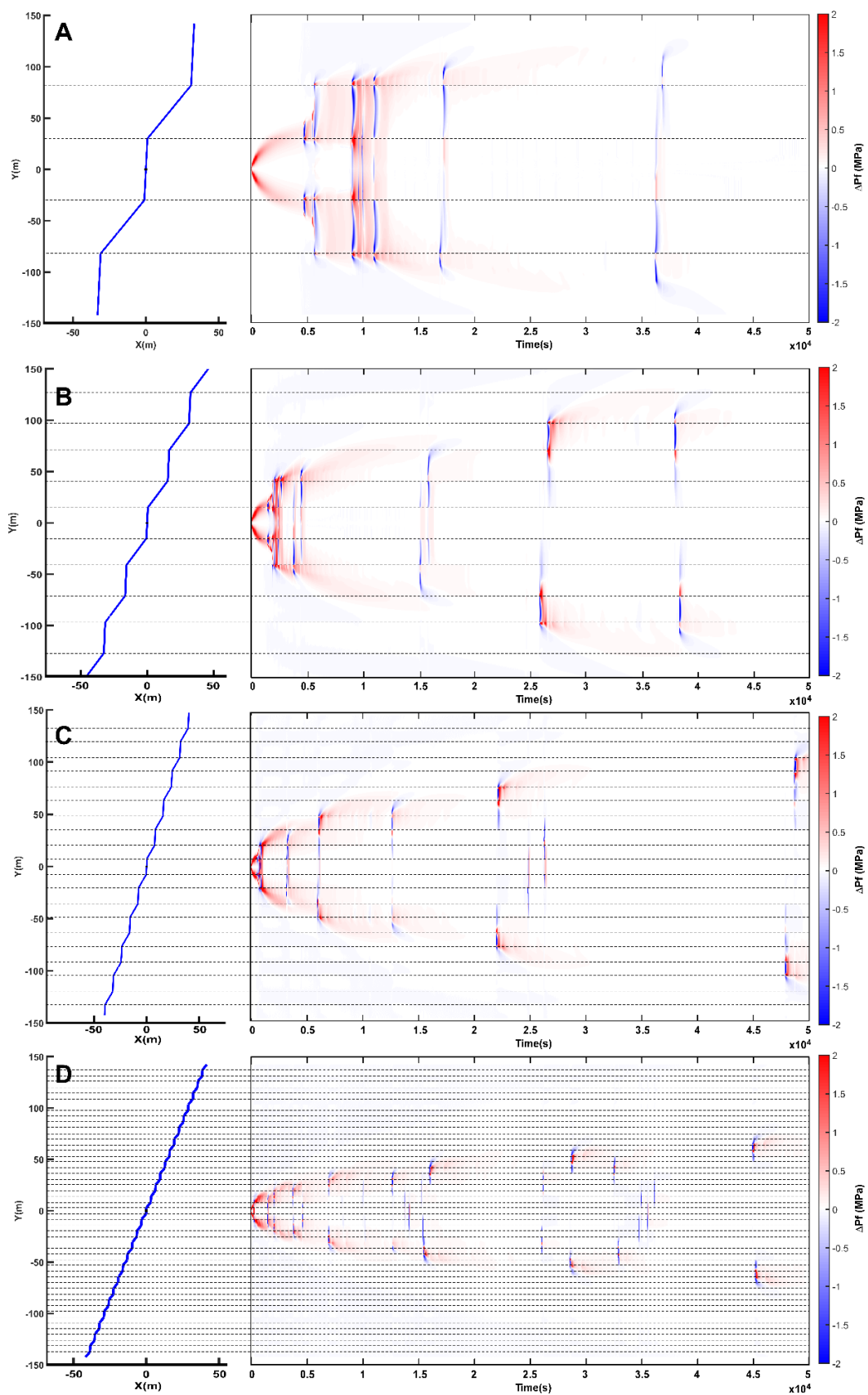


Figure 5. Detail of fluid pressure drops and pressurization for different D_L (88_60_DL_1e-4). A: D_L of 60 meters, B: D_L of 30 meters, C: D_L of 15 meters and D: D_L of 6 meters. Dashed black lines indicate the directional changes or fracture bends.

By solving Eq. (6) we obtain the pressure front propagation with time $L_p(t)$. However here, even assuming x as constant (McClure & Horne, 2010) there is a degree of uncertainty with k_{eq} because this value evolves through time (as the system is stimulated) and is also different through the fault. This value is maximized in the aseismic fault bends (Piris et al., 2018). For this reason, we assume that k_{eq} is the equivalent permeability of the system and can be adjusted to fix the pressure front evolution (black line in Fig. 6). However, this k_{eq} is not able to fully adjust the pressure front due to the pressure drops (Piris et al., 2018; Deng et al., 2021) or the fluid rapid expansion due to the dilatancy process after a seismic stimulation, especially at the beginning of the simulation.

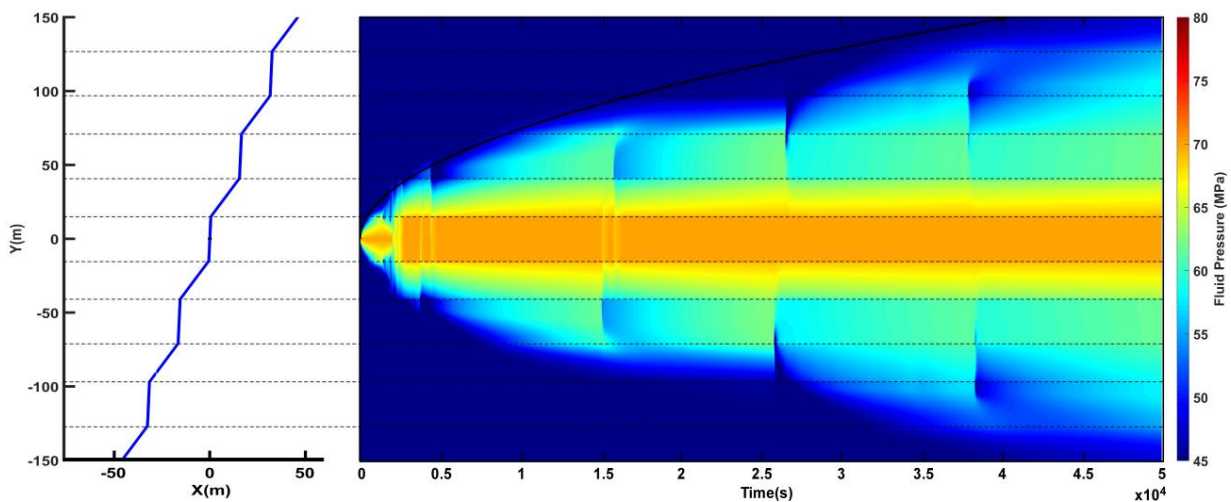


Figure 6. Fluid pressure and Eq. 6 evolution for the 88_60_30_1e-4 model. Dashed black lines indicate the directional changes or fracture bends.

By comparing k_{eq} as a function of D_L we can see how k_{eq} decreases with D_L (Table 3). This also implies a higher number of bends and a decrease of the seismic capacity of stimulation. It is also worth mention that the k_{eq} values obtained for single fractures (e.g., Fig. 2) are two orders of magnitude higher than those obtained for the configurations with fracture directional changes. For a single fracture with $\alpha \approx 74^\circ$ that could be considered as a planar idealization of the different geometries analyzed (Fig. 1 and Fig. 2 C-D). For this situation, the obtained k_{eq} is $1.45e^{-12} \text{ m}^2$, while for $\alpha=60^\circ$ k_{eq} is $1.3e^{-13} \text{ m}^2$ (Fig. 2 A-B) and for $\alpha=88^\circ$ k_{eq} is $2.41e^{-14} \text{ m}^2$ (Fig. 2 E-F). These results show a high dependency of the stimulation capacity to increase permeability with the dilatancy effect.

D_L (m)	60	30	20	15	12	10	6	3
k_{eq} (m^2)	$2.28e^{-14}$	$2.07e^{-14}$	$1.86e^{-14}$	$1.70e^{-14}$	$1.37e^{-14}$	$1.16e^{-14}$	$8.10e^{-15}$	$5.10e^{-15}$

Table 3. Relation between equivalent permeability (k_{eq}) and fracture segment size (D_L) for the 88_60_ D_L _1e-4 models.

To compare if these k_{eq} values have a physical sense we compare them against the real fracture permeability close to the injection point. We can observe that k_{eq} is at least two orders of magnitude lower than the stimulated mean fracture permeability of all the system. This misfit is not observed for single fractures where k_{eq} tend to be similar (same magnitude order). So, this implies that the fracture bends play a role in the fluid pressurization velocity and reduces the capacity of the system to be pressurized.

4.5.2 Seismic production

In order to quantitatively evaluate the location of high-magnitude events and check the influence of fault orientation changes (bends), we computed the distance between each seismic event and the nearest fracture bend (for all the models with a given $d_c=1e-4$ m). This distance was then normalized for each configuration segment size, obtaining a normalized value between -0.5 and 0.5 for all the events and for all the simulations. A value of -0.5 represents that event is located exactly at the centre of an aseismic segment, while a value of 0.5 represents that the event is located exactly at the centre of a seismic segment. Therefore, a value of 0 indicates that the event is located in the fracture bend. Then the seismic moment of all the events, meaning more than 1,000 events, were grouped by intervals of proximity and shown as a histogram diagram. The distribution reveals that the maximum moment is concentrated next to fault bends and along the seismic segments (Fig.7). A strong reduction of the seismic moment is observed near the fault bends located in the aseismic moments.

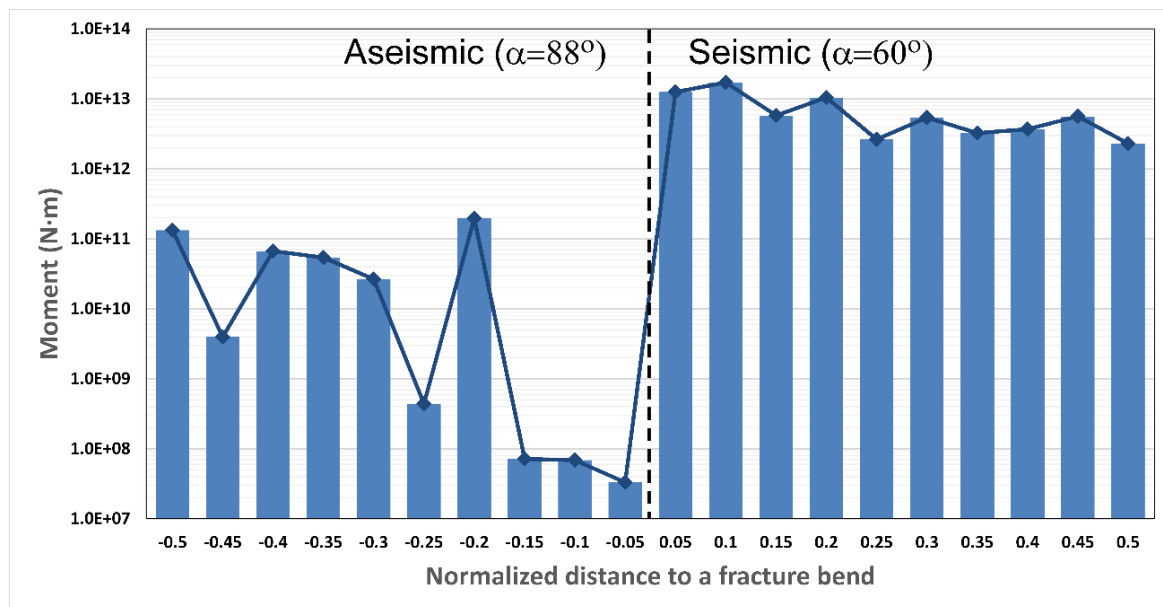


Figure 7. Accumulative seismic moment of all the events grouped by proximity to fracture bends. A value of 0 means that event is located on a fracture bend, a value of -0.5 means that event is located in the middle of an aseismic segment, while a value of 0.5 means that event is located in the middle of a seismic segment.

As shown in Table 2, there is a general tendency to reduce seismicity with the decrease of D_L . A useful approach is to compare the D_L parameter with the theoretical nucleation length (L_c) and, therefore, check if the reduction of the seismic moment is coherent with the convergence of D_L with L_c .

Fig. 8 shows a plot of the total seismic moment for different L_c as a function of the relation D_L/L_c . A sharp decay of the seismic production when the D_L/L_c approaches 0.8 can be observed from the diagram (Fig. 8). From a theoretical point of view, Scholz (2002) proposed that segment sizes below L_c ($D_L/L_c \approx 1$) should not be able to nucleate seismic events. However, this value is reduced to 0.8 for the geometries used in this work. An explanation can be that for our geometries, the segment defined by D_L uses patches beyond the directional changes to nucleate seismic events and, for this reason, it is possible to nucleate events even below $D_L/L_c \approx 1$.

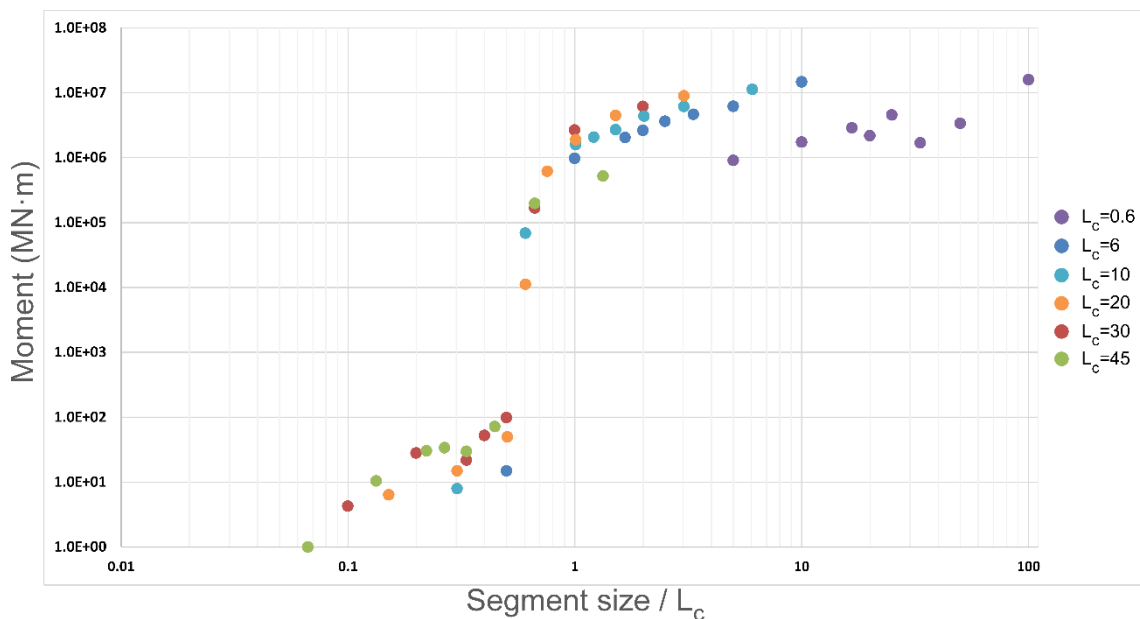


Figure 8. Total simulation magnitude moment (as a result of the average between the 60_88 and the 88_60 configurations) for different L_c .

4.5.3 Seismic front propagation

When injection starts single segments keep their role, seismic segments slide abruptly and aseismic segments arrest the ruptures (Fig. 9, see first time steps, in this case the x axis is defined in time steps to better observe the seismic nucleation, if x axis was defined in seconds the seismic nucleation, which takes one second or less would be masked). Seismic segments slide abruptly to accommodate the instability generated by the fluid pressure increase. However, the aseismic segments are forced to slide at lower velocities to accommodate the instability generated both by the injection pressure and by the differential displacement generated by the sliding of the seismic segments.

The aseismic segment close to the seismic segment starts to slide at low velocity even without an increase of fluid pressure (as also observed by Cappa, 2018), in a way that this slow sliding progressively propagates towards the aseismic segment. This process accommodates with slow sliding the instability of accumulated displacement generated on the system by the sliding on seismic segments. This high gradient forces the aseismic segment to slide, normally with low velocities but sometimes seismically with low-magnitude events (events marked with cyan-coloured symbols in Fig. 9). These slow sliding zones located close to the bends sometimes propagate to the seismic patches nucleating new seismic events (yellow events close to the bends, Fig. 9).

In terms of seismicity, high-magnitude events tend to be preferentially located next to fracture orientation changes, because the side of the aseismic segment keeps sliding continuously as an unstable region and also because there is a high gradient in terms of accumulated sliding in those regions. The side of the aseismic segment close to the orientation change tends to follow an opening mode behaviour (Piris et al., 2018). That should explain why there is a lack of seismicity next to zones of fracture orientation change in the side of the aseismic segment (Fig. 7).

The capacity of aseismic segments to arrest high-velocity ruptures and accommodate them by low-velocity sliding has a side effect and evolves dynamically as more events are produced. In the second generation events, when a new event is produced in the seismic segment, the region that was sliding at low velocities slides now at high velocities (e.g., time step close to 200 and time step close to 700 in Fig. 9), increasing the event size and acting as a bridge to propagate ruptures. After the seismic events, we have observed that the aseismic segments tend to start sliding at low motion again, from the orientation changes, propagating to the rest of the segment at low velocities and in a stationary way, while seismic segments become stable and follow an stick-slip behaviour (Segall, 2010). Accordingly, the seismic instability is followed by a period of no motion during which the friction coefficient is recharged until another seismic instability (the seismic cycle). Thus, when an event is produced in the seismic segments this can propagate through the aseismic segments which was sliding at low velocities and is arrested by the seismic segments which are in the no motion stage or by the aseismic segment in the region that was not sliding at low velocities.

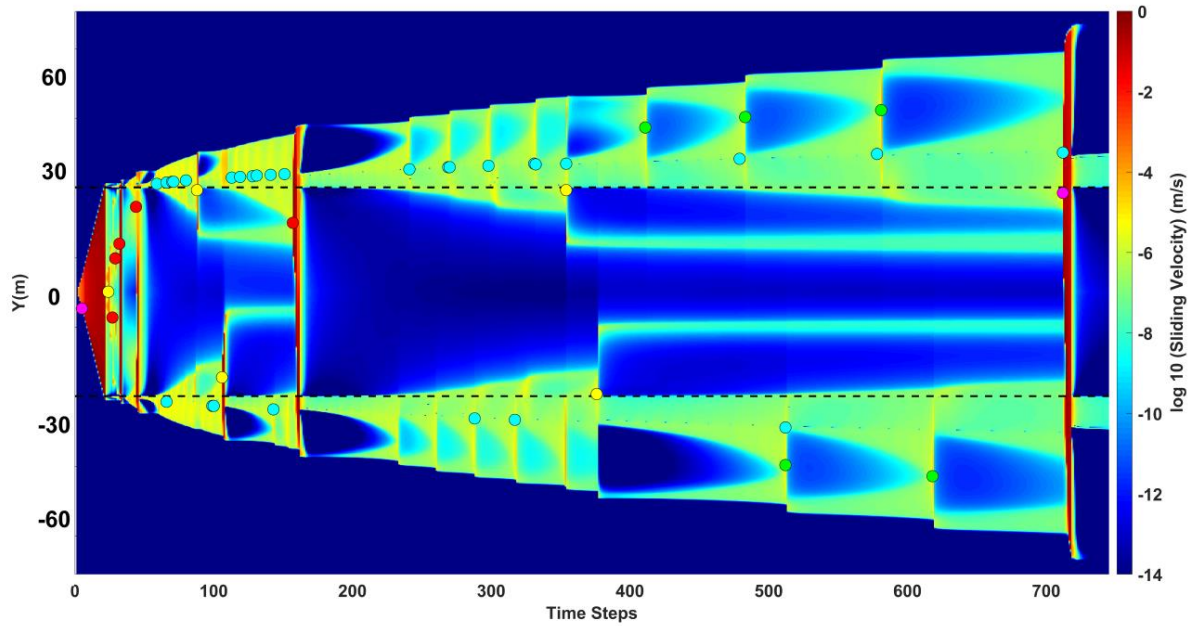


Figure 9. Sliding velocity evolution as a function of time step for the model 60_88_60_1e-4. The injection point is located at $Y=0m$. Dashed black lines indicate the directional changes or fracture bends. The colour circles are the seismic event hypocentres are detected using an automatic configuration. Colours indicate magnitudes as follows: cyan <0 , green <1 , yellow <1.5 , red <2 , and magenta ≥ 2 .

To see this effect we need multi-episodic simulations, because the conditions to propagate the ruptures to the system evolve through time and could be varied from the initial conditions or after the some seismic events. This effect of slow sliding behaviour related also to post- high seismic events, or acting as a precursor for high-magnitude events, was also observed by Luo & Liu (2019) in their study of megathrust earthquakes and their effect on slow sliding patterns. It was also analyzed by Jia et al. (2022) in the South Sandwich Island M_w 8.2 Earthquake, where a slow event was sandwiched between two regular earthquakes.

The complex seismic cycle described before and observed in our simulations, where seismic ruptures and continuous slow sliding are combined motivated solely by the concatenation of segments with different orientations, is coherent with the theory that complex geometry could be enough to trigger seismic cycles which combine slow-slip events (SSE) with seismic events (Romanet et al., 2018). In our simulations, fluid injection into fractures with segment orientation changes is able to produce both SSE and seismic ruptures.

The obtained seismicity can be analyzed from a scaling law point of view (Ide et al., 2007; Gomberg et al., 2016), where the seismic moment of earthquakes scales with the cube of their duration ($M \propto t^3$) whereas the corresponding moment of SSEs is proportional to their duration ($M \propto t$). Although our simulation is basically 2D, the out-of-plane factor ($h=100m$) allows evaluating the relation with the cubic

law instead of the quadratic law (Romanet et al., 2018), assuming that the magnitude of the events for the models with short segments sizes ($D_L = 3\text{m}$) could be oversized.

The events captured by the code in the aseismic segments follow an SSE tendency (called automatic SSE: SSE_AUT and can be observed as cyan circles in Figs. 3, 4 and 9), while the events nucleated in the seismic segments follow an earthquake tendency (called automatic earthquakes: EAQ_AUT and can be observed as green, yellow, red or magenta circles in Fig. 3, 4 and 9). However, the SSE captured by the code automatically were registered considering that a seismic event starts when an element exceeds 5mm/s and finish when the sliding velocity for the last element is below 2.5mm/s. This law generally underestimates both the duration and the magnitude of the SSE (e.g., see cyan-coloured events in Fig. 9, which just take into account the high sliding peak and not all the preceding slow velocity tremor). Although this law can be modified into CFRAC, we have chosen to manually select the SSE from the sliding velocity diagrams (considering SSE velocities from $1\text{e-}3$ to $1\text{e-}6$ m/s or below), and using the Eq. (3) to obtain the seismic moment, to have a better constrain for the SSE. Thus, we obtained another seismic swarm called manual SSE: SSE_MAN. Plotting altogether for the 88_60 models (with the base d_c value) in a moment-time diagram (Fig. 10) each swarm follow the predicted tendency. However, the SSE_AUT are magnitude- and time-truncated due to the seismic law restriction defined by the code and just capture the SSE peak if it reaches the 5mm/s condition. For this reason, the SSE_AUT swarm is located under the tendency of SSE_MAN. Anyway, the observed tendency ($M \propto t$) for SSE_AUT was already indicating that were not conventional seismic earthquakes (Fig. 10).

4.6 Conclusions

We have seen that the fault geometry and the directional change region (step-overs, releasing/restraining bents, branching, or splay fractures) plays an important role in the seismic cycle and on the interaction between seismic events and slow slip events and also that these bend regions tend to concentrate the seismic activity. As an important remark they indicate the role of SSE in the seismic cycle, both as seismic precursors (remaining slow slip regions nucleate new seismic events) and as seismic amplifiers (the remaining slow slip regions are able to slide at high velocities when an seismic event is produced) even in regions preferentially aseismic.

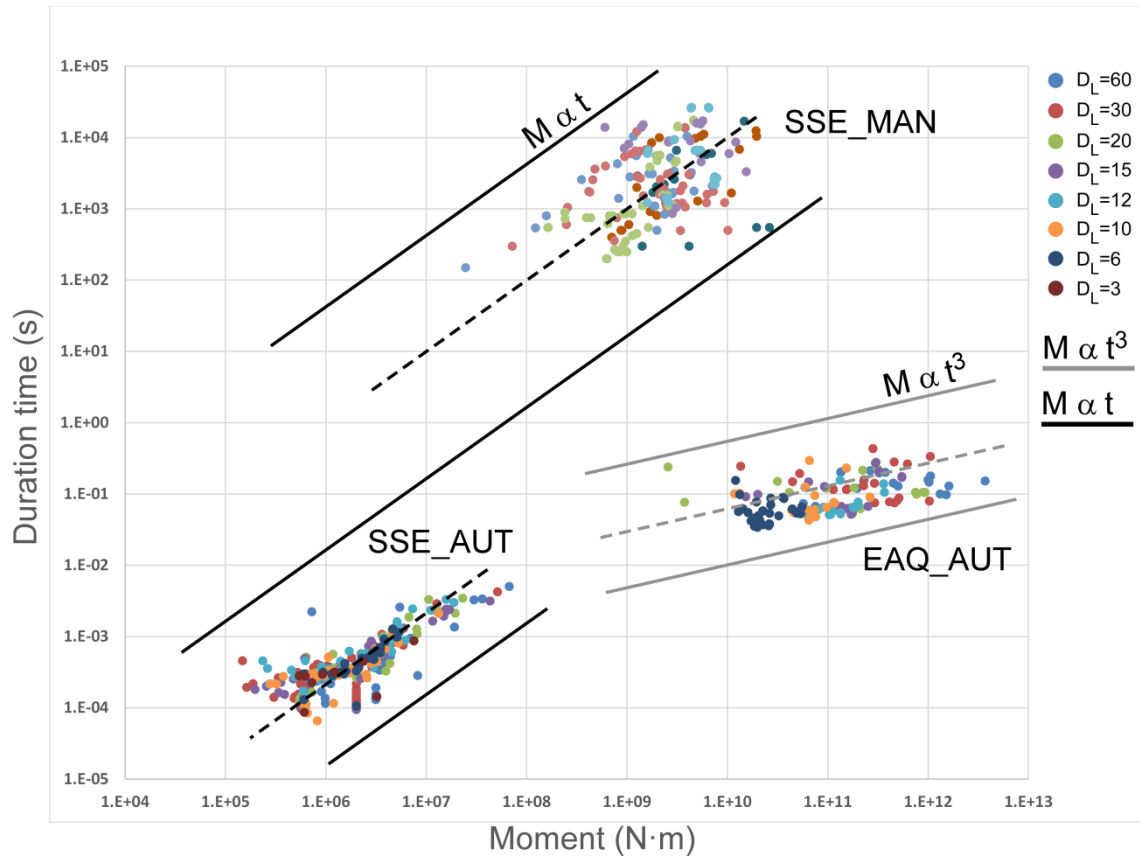


Figure 10. Seismic moment – Duration time diagram where the EAQ_AUT, SSE_AUT and SSE_MAN were plotted. The colours indicate the DL from which the events come. Black and grey lines indicate the $M \propto t$ and $M \propto t^3$ tendency respectively.

Through a simple geometry configuration (faults with directional changes) we have seen the important effect of fault geometry on the seismic cycle. Although the observed slip tendencies for single segments were kept, geometrical complexities introduce variations especially in the aseismic segments. This analysis is coherent with those works that focus on the importance of fault geometry to explain their seismic behaviour (e.g., Mildon et al., 2016) and to produce complex seismic cycles where SSE interact with seismic events (e.g., Romanet et al., 2018). The fault geometry complexity could be complemented with studies that focus on complex friction rheology on planar faults to explain the seismic fault response (e.g. Zielke & Mai, 2016 or Zielke et al., 2017).

The results obtained also reveal the importance of fault geometry on the stimulation capacity of the fault in terms of fluid pressurization velocity and how this behaviour can be modified including macro-roughness into the system, in this case with a fault with directional changes.

Another concept introduced here is the change in the seismic behaviour through the different seismic cycles. The generation of dynamic effects have a future influence on the seismic behaviour of the system, especially with the relationship between SSE and earthquakes. This effect is caused by the

appearance of SEE that become active indefinitely and that can lead to nucleate seismic events or propagate them towards preferentially aseismic regions. The results are coherent with field seismicity observations as for example Luo & Liu (2019), in his study of megathrust earthquakes and their effect on slow sliding patterns or by Jia et al. (2022) in the South Sandwich Island M_w 8.2 Earthquake.

4.7 References

- Bie, L., & Ryder, I. (2014). Recent seismic and aseismic activity in the Ashikule stepover zone, NW Tibet. *Geophysical Journal International*, 198(3), 1632–1643. <https://doi.org/10.1093/gji/ggu230>
- Brankman, C. M., & Aydin, A. (2004). Uplift and contractional deformation along a segmented strike-slip fault system: the Gargano. *Journal of Structural Geology*, 26, 807–824.
- Cappa, F., Guglielmi, Y., Nussbaum, C., & Birkholzer, J. (2018). On the Relationship Between Fault Permeability Increases, Induced Stress Perturbation, and the Growth of Aseismic Slip During Fluid Injection. *Geophysical Research Letters*, 45, 11,012–11,020. <https://doi.org/10.1029/2018GL080233>
- Ciardo, F., & Lecampion, B. (2019). Effect of Dilatancy on the Transition From Aseismic to Seismic Slip Due to Fluid Injection in a Fault. *Journal of Geophysical Research: Solid Earth*, 124, 3724–3743. <https://doi.org/10.1029/2018JB016636>
- Deng, Q., Blöcher, G., Cacace, M., & Schmittbuhl, J. (2021). Modeling of fluid-induced seismicity during injection and after shut-in. *Computers and Geotechnics*, 140(May), 104489. <https://doi.org/10.1016/j.compgeo.2021.104489>
- Garagash, D. I., & Germanovich, L. N. (2012). Nucleation and arrest of dynamic slip on a pressurized fault. *Journal of Geophysical Research: Solid Earth*, 117(10), 1–27. <https://doi.org/10.1029/2012JB009209>
- Gischig, V. S. (2015). Rupture propagation behavior and the largest possible earthquake induced by fluid injection into deep reservoirs. *Geophysical Research Letters*, 42(18), 7420–7428. <https://doi.org/10.1002/2015GL065072>
- Gomberg, J., A.Wech, K. Creager, K. Obara, and D. Agnew (2016), Reconsidering earthquake scaling, *Geophysical Research Letters*, 43(12), 6243–6251, doi:10.1002/2016GL069967.
- Hanks, T. C., & Kanamori, H. (1979). A moment magnitude scale. *Journal of Geophysical Research: Solid Earth*, 84(B5), 2348–2350. <https://doi.org/10.1029/JB084iB05p02348>
- Häring, M. O., Schanz, U., Ladner, F., & Dyer, B. C. (2008). Characterisation of the Basel 1 enhanced geothermal system. *Geothermics*, 37(5), 469–495. <https://doi.org/10.1016/j.geothermics.2008.06.002>
- Harris, R., & Day, S. M. (1993). Dynamic of fault interaction: parallel strike-slip faults. *Journal of Geophysical Research*, 98(No. B3), 4461–4472. <https://doi.org/10.1029/92JB02272>
- Hearn, E. H., Koltermann, C., & Rubinstein, J. R. (2018). Numerical Models of Pore Pressure and Stress Changes Along Basement Faults Due to Wastewater Injection: Applications to the 2014 Milan, Kansas *Earthquake. Geochemistry, Geophysics, Geosystems*, 1178–1198. <https://doi.org/10.1002/2017GC007194>
- Hicks, S. P., Okuwaki, R., Steinberg, A., Rychert, C. A., Harmon, N., Abercrombie, R. E., Bogiatzis, P., Schlaphorst, D., Zahradnik, J., Kendall, J-M., Yagi, Y., Shimizu, K., & Sudhaus, H. (2016). Back-propagating supershear rupture in the 2016 Mw 7.1 Romanche transform fault earthquake. *Nature Geoscience*, <https://doi.org/10.1038/s41561-020-0619-9>
- Ide, S., G. C. Beroza, D. R. Shelly, and T. Uchide (2007), A scaling law for slow earthquakes. *Nature*, 447(7140), 76–79, doi:10.1038/nature05780.
- Jia, Z., Zhan, Z., & Kanamori, H. (2022). The 2021 South Sandwich Island Mw 8.2 Earthquake: A Slow Event Sandwiched Between Regular Ruptures. *Geophysical Research Letters*, 49(3), <https://doi.org/10.1029/2021GL097104>
- Kwiatek, G., Saarno, T., Ader, T., Bluemle, F., Bohnhoff, M., Chendorain, M., Dresen, G., Heikkinen, P., Kukkonen, I., Leary, P., Leonhardt, M., Malin, P., Martínez-Garzón, P., Passmore, K., Passmore, P., Valenzuela, S., & Wollin, C. (2019). Controlling fluid-induced seismicity during a 6.1-km-deep geothermal stimulation in Finland. *Science Advances*, 5(5), eaav7224. <https://doi.org/10.1126/sciadv.aav7224>
- Luo, Y., & Liu, Z. (2019). Slow - Slip Recurrent Pattern Changes: Perturbation Responding and Possible Scenarios of Precursor toward a Megathrust Earthquake. *Geochemistry, Geophysics, Geosystems*, 1–20.

<https://doi.org/10.1029/2018GC008021>

- Martínez-Garzón, P., Kwiatek, G., Bohnhoff, M., & Dresen, G. (2017). Volumetric components in the earthquake source related to fluid-injection and stress state. *Geophysical Research Letters*, 800–809. <https://doi.org/10.1002/2016GL071963>
- McClure, M. W. (2012). Modeling and Characterization of Hydraulic Stimulation and Induced Seismicity in Geothermal and Shale Gas Reservoirs. Stanford PhD Dissertation, 1–369.
- McClure, M. W., & Horne, R. N. (2010). Numerical and Analytical Modeling During Fluid Injection. *Geothermal Resources Council Transactions*, 34, 381–396.
- McClure, M. W., & Horne, R. N. (2011). Investigation of injection-induced seismicity using a coupled fluid flow and rate/state friction model. *Geophysics*, 76(6), WC181. <https://doi.org/10.1190/geo2011-0064.1>
- McClure, M. W., & Horne, R. N. (2013). Characterizing hydraulic fracturing with a tendency for shear stimulation test. *Society of Petroleum Engineers*, SPE166332, 1–17. <https://doi.org/10.2118/166332-MS>
- McClure, M. W., & Horne, R. N. (2014). An investigation of stimulation mechanisms in Enhanced Geothermal Systems. *International Journal of Rock Mechanics and Mining Sciences*, 72, 242–260. <https://doi.org/10.1016/j.ijrmms.2014.07.011>
- Meyer, G., Baujard, C., Hehn, R., Genter, A., & McClure, M. W. (2017). Analysis and Numerical Modelling of Pressure Drops Observed During Hydraulic Stimulation of GRT-1 Geothermal Well (Rittershoffen, France). Proceedings of the 42nd Workshop on Geothermal Reservoir Engineering, 1(1), 14.
- Mildon, Z. K., Toda, S., Faure Walker, J. P., & Roberts, G. P. (2016). Evaluating models of Coulomb stress transfer: Is variable fault geometry important? *Geophysical Research Letters*, 407–414. <https://doi.org/10.1002/2016GL071128>
- Oglesby, D. D. (2005). The dynamics of strike-slip step-overs with linking dip-slip faults. *Bulletin of the Seismological Society of America*, 95(5), 1604–1622. <https://doi.org/10.1785/0120050058>
- Oglesby, D. D., & Mai, P. M. (2012). Fault geometry, rupture dynamics and ground motion from potential earthquakes on the North Anatolian Fault under the Sea of Marmara. *Geophysical Journal International*, 188(3), 1071–1087. <https://doi.org/10.1111/j.1365-246X.2011.05289.x>
- Oglesby, D. D., Day, S. M., Li, Y. G., & Vidale, J. E. (2003). The 1999 Hector Mine earthquake: The dynamics of a branched fault system. *Bulletin of the Seismological Society of America*, 93(6), 2459–2476. <https://doi.org/10.1785/0120030026>
- Olson JE. (2004). Predicting fracture swarms – the influence of subcritical crack growth and the crack-tip process zone on joint spacing in rock. London: Geological Society; 73–88 (Special Publications).
- Perrin, C., Waldhauser, F., Choi, E., & Scholz, C. H. (2019). Persistent fine-scale fault structure and rupture development : A new twist in the Parkfield , California , story. *Earth and Planetary Science Letters*, 521, 128–138. <https://doi.org/10.1016/j.epsl.2019.06.010>
- Piris, G., Griera, A., Gomez-Rivas, E., Herms, I., McClure, M. W., & Norbeck, J. H. (2018). Fluid pressure drops during stimulation of segmented faults in deep geothermal reservoirs. *Geothermal Energy*, 6(24). <https://doi.org/10.1186/s40517-018-0110-7>
- Ritz, E., Pollard, D. D., & Ferris, M. (2015). The influence of fault geometry on small strike-slip fault mechanics. *Journal of Structural Geology*, 73, 49–63. <https://doi.org/10.1016/j.jsg.2014.12.007>
- Romanet, P., Sato, D. S., & Ando, R. (2020). Curvature, a mechanical link between the geometrical complexities of a fault: application to bends, kinks and rough faults. *Geophysical Journal International*, 223(1), 211–232.
- Romanet, P., Bhat, H. S., Jolivet, R., & Madariaga, R. (2018). Fast and slow earthquakes emerge due to fault geometrical complexity. *Geophysical Research Letters*. <https://doi.org/10.1029/2018GL077579>
- Sathiakumar, S., Barbot, S. (2021). The stop-start control of seismicity by fault bends along the Main Himalayan Thrust. *Communications Earth and Environment*, 2, 87. <https://doi.org/10.1038/s43247-021-00153-3>

- Scholz, C. (2002). *The mechanics of earthquakes and faulting* (2nd editio). New York: Cambridge University Press.
- Segall, P. (2010). *Earthquake and volcano deformation*. New Jersey: Princeton University Press.
- Stein, S., & Wysession, M. (2003). *An Introduction to Seismology, Earthquakes, and Earth Structure* (Vol. 74). Malden, MA: Blackwell Science. <https://doi.org/10.1785/gssrl.74.6.824>
- Zielke, O., Galis, M., & Mai, P. M. (2017). Fault roughness and strength heterogeneity control earthquake size and stress drop. *Geophysical Research Letters*, 777–783. <https://doi.org/10.1002/2016GL071700>
- Zielke, O., & P. M. Mai (2016), Subpatch roughness in earthquake rupture investigations. *Geophysical Research Letters*, 43, 1893–1900, doi:10.1002/ 2015GL067084.

Capítol 5

5 3DHIP-Calculator - A new tool to stochastically assess deep geothermal potential using the Heat-In-Place method based on 3D geological models

5.1 Introduction

Deep geothermal energy exploration and exploitation activities have vigorously grown during the last decade worldwide [1–3]. One of the key tasks during the early evaluation stages of deep geothermal plays is the assessment of the base resource in terms of the energy stored in the reservoir [4]. This quantification is an essential step to estimate the energy that can be produced from the geothermal reservoir for power generation or direct uses (district heating, greenhouses, etc.), and is key for carrying out preliminary evaluations of the project feasibility based on the required investment and the exploitation cost of the geothermal resource. However, there are uncertainties in the geological knowledge that must be considered when carrying out these preliminary assessments during the early stages of exploration of the geothermal resource. These uncertainties are mainly related to the prediction of the reservoir geometry, petrophysical properties, and temperature distribution.

The volumetric “Heat-In-Place” (HIP) method, implemented by the United States Geological Survey (USGS) [5], together with its subsequent revisions [6–10], is still the most widely used evaluation technique for the estimation of the available stored heat and the recoverable heat fraction (Hrec) of deep geothermal reservoirs [11–16]. This method considers the volume of the reservoir (surface and thickness), the petrophysical properties (e.g., rock type, porosity, specific heat capacity, etc.), fluid properties (e.g., fluid density, etc.), as well as the reservoir and reinjection (or reference) temperatures. Due to the potential influence of these parameters and their uncertainty, Nathenson [17] considered the need to follow a stochastic approach through Monte Carlo simulations [18]. This approach systematically varies the parameters considered over a defined range of values by using probability distribution functions (PDF) (e.g., triangular, normal, lognormal, etc.) [8,19,20].

Traditionally, common commercial software designed for risk and decision analysis purposes, such as @Risk [21] and Crystal Ball [22], have been used for geothermal resource assessment. They apply the volumetric method using Monte Carlo simulations (i.e., stochastic calculations implementing PDFs for the variables). Both tools run as Microsoft Excel add-ins, and calculations are normally applied at the scale of the entire reservoir or to a specific part of it, where the selected volume is conceptually treated as a single voxel [23–26]. In terms of open-source software, Pocasangre et al. [27] have more recently developed the ‘GPPeval’ application (Geothermal Power Potential assessment), a Python-based stochastic library for the assessment of the geothermal power potential using the volumetric method in a liquid-dominated reservoir. A handicap of these applications is that the analyzed domain must be treated

as a lumped parameter model, i.e., with a homogeneous distribution of parameters in the whole volume considered. However, local variabilities are expected in reservoirs, mainly due to the variation of the petrophysical properties, temperature distribution, and reservoir geometry (thickness, depth, etc.). For this reason, approaches based on GIS (Geographic Information System) coupled with 3D subsurface models are promising, because they explicitly allow the application of the volumetric method using 3D voxel models as inputs. Several authors have used 3D geological models to calculate the volume of a reservoir to subsequently apply the HIP volumetric method in a deterministic way by assigning values to parameters of each unit to estimate, quantify, and map a first estimation of the geothermal reserve [28,29].

A more sophisticated approach is that applied by the VIGORThermoGIS code [12], an implementation of the ThermoGIS TNO code [30–32]. This tool was implemented specifically to assess prospective areas for geothermal development in the Netherlands and in southern Italy during the VIGOR Project [12]. The codes and the methodology implemented in these two tools can be considered nowadays as a reference for the scientific community working on the evaluation of resources at the regional scale. These tools demonstrated the use of methods that couple 3D subsurface data with GIS tools to stochastically assess the deep geothermal potential. Nevertheless, their implementation was limited to their case study areas and specific datasets. Therefore, there is still a need for a standard and freely available tool for the whole geothermal community in order to be able to estimate the HIP using Monte Carlo simulations, and in which any 3D geological and 3D thermal models can be utilized to assess case studies.

A gap is identified between what the geoscience community working in geothermal energy would need (including geological surveys, universities, research institutes, or consulting companies) and what is currently offered by free commercial or open-source software packages to assess deep geothermal potential at the regional scale in three-dimensions and by stochastically using the volumetric method. To close this gap, a novel and free software called the ‘3DHIP-Calculator’ is presented here. This tool allows for estimating the geothermal potential of a reservoir using the volumetric Heat-In-Place (HIP) method, originally implemented by the United States Geological Survey (USGS) [5], combined with a Monte Carlo simulation approach [17] and using 3D geological and 3D thermal models based on a voxel format as inputs.

The 3DHIP-Calculator application has many competitive advantages. Firstly, the source code and the installation files are accessible for all users and developers from open-source repositories such as GitHub. Secondly, as the tool allows importing 3D models that integrate previously generated geological, petrophysical, and thermal data, it considers the whole geological heterogeneity of the reservoir to estimate the geothermal potential using the HIP method. Finally, the results can be exported in ASCII format for their subsequent post-processing in other environments, such as GIS software packages. This

allows generating maps of the assessed deep geothermal potential at the regional scale, and to use 3D visualization tools and statistical packages, such as R [33], for further evaluations. All these advantages open a wide range of possibilities, including the construction of GIS-based maps or to conduct feasibility studies of the deep geothermal potential through risk analysis approaches.

This contribution presents the structure, capabilities, and use of the 3DHIP-Calculator and its graphical user interface (GUI). Moreover, the method is demonstrated through a case study of the Reus-Valls Basin (RVB) [34]. The RVB is part of the Neogene extensional basins of the Catalan Coastal Ranges (NE of the Iberian Peninsula, Spain), which, according to previous studies [35–37], has a high potential for the development of deep geothermal energy for direct heat or power generation. However, the lack of enough subsurface information (from deep appraisal wells) results in a relatively large uncertainty for the assessment of its geothermal potential. The RVB case is a useful example of deep geothermal potential assessment at the regional scale, where the 3DHIP-Calculator can offer a first estimate of the spatial distribution of the deep geothermal resource based on the existing geological knowledge and its associated uncertainty.

5.2 Materials and methods

5.2.1 Mathematical background of the HIP method

The 3DHIP-Calculator is based on the HIP approach, which allows estimating the geothermal resource and the recoverable fraction of a subsurface reservoir [5,10–12]. The HIP (kJ) is calculated according to Equation (1):

$$HIP = V \cdot [\phi \cdot \rho_F \cdot C_F + (1 - \phi) \cdot \rho_R \cdot C_R] \cdot (Tr - Ti) \quad (1)$$

where V is the voxel volume (m^3), ϕ is the rock porosity (parts per unit), ρ is the rock density (kg/m^3), C is the specific heat capacity ($kJ/kg \cdot ^\circ C$), and the F and R sub-indexes account for the fluid and host rock, respectively. Tr is the reservoir temperature ($^\circ C$) and Ti refers to either the re-injection, reference, or abandonment temperature ($^\circ C$). Therefore, Ti can refer to the threshold of economic or technological viable temperature, the ambient temperature (i.e., the annual mean surface temperature value), or a temperature value defined according to other criteria [11]. Equation (1) is solved within the 3DHIP-Calculator for each voxel in the model that satisfies the condition that $(Tr - Ti) \geq 5 \text{ }^\circ C$. Otherwise, the HIP for that voxel is not evaluated and is set to zero. The HIP is expressed in kJ.

Then, the obtained HIP value is used to calculate the recoverable heat (H_{rec}) following Equation (2), which accounts for the producible thermal power during a given plant or project lifetime (T_{live}):

$$H_{rec} = \frac{HIP \cdot C_e \cdot R}{T_{live} \cdot P_f} \quad (2)$$

where the HIP resulting from Equation (1) is scaled by a recovery factor (R , in parts per unit) to represent the part of the heat that can be extracted. This first estimation of the recovery factor (R) requires special attention because it depends on many factors, including the hydrogeological characteristics of the reservoir and the current drilling technology. Some authors suggest using R values between 0.02 and 0.2 [38] or close to 0.01 [12] for studies where there is no previous information. A recovery factor for a geothermal doublet (with a production borehole and an injection borehole) was defined at 0.33 according to the Atlas of Geothermal Resources in Europe [16,39], based on Muffler and Cataldi [5] and Lavigne [40]. Williams et al. [6,7,41] proposed a range of R values according to the geothermal reservoir type: a range from 0.08 to 0.2 for fracture-dominated reservoirs, 0.01 for Enhanced Geothermal Systems [42], and from 0.1 to 0.25 for sediment-hosted reservoirs with a maximum value of 0.5 [3]. Additionally, a conversion efficiency factor (C_e , in parts per unit) is used to incorporate the effect of the efficiency of the heat exchange from the geothermal fluid to a secondary fluid in a thermal plant. C_e can vary as a function of geothermal exploitation (e.g., heat or electricity production). Finally, since most of the direct heat applications of geothermal energy (such as district heating, greenhouse heating, etc.) do not operate continuously throughout the year, a plant factor (P_f , in parts per unit) is included. This factor considers the fraction of the total time in which the geothermal plant is in operation. Thus, H_{rec} is expressed in kW.

5.2.2 Mathematical background of the Monte Carlo method

The Monte Carlo method, i.e., a multiple probability simulation, is a mathematical solution widely used to estimate the possible outcomes of an uncertain event. Unlike a normal forecasting model, Monte Carlo simulations predict a set of outcomes based on an estimated range of values versus a deterministic or fixed input value. This method is used in the 3DHIP-Calculator to probabilistically evaluate the uncertainty associated with the input parameters and the corresponding geothermal potential results [18]. The first step is to link a probability distribution function (PDF) to each parameter, to infer the unknown quantities of the samples, and to take into account the range and pattern of variation of the different parameters [43]. Thus, Equations (1) and (2) are applied using a stochastic approach, instead of a deterministic one, so that their input values are not fixed parameters yielding a unique result. The calculations based on these two equations are repeated as many times as desired (N , number of simulations), producing a large number of likely outcomes, using random values extracted from probability distribution functions assigned to the parameters and predefined depending on the pattern variation. The application allows selecting normal or triangular PDFs for the input parameters of Equations (1) and (2). The mean and standard deviation are used to define normal distributions, while the lower, most probable, and upper values are for triangular distributions. The required input data for the calculations are 3D geological models (3DGM), 3D thermal models (3DTM), and random values within the selected PDF for each parameter. The values of the variables defined in a deterministic way (i.e., without assigning PDFs) are considered as fixed. Accordingly, the application calculates as many

different HIP and Hrec values as the number of simulations defined by the user for each voxel of the model. The results of the calculations are also expressed as PDFs.

5.2.3 Program description

The 3DHIP-Calculator (Figure 1) was developed using MATLAB[®] (v. R2019b) [44] based on the MATLAB App Designer, and then compiled for Windows as a standalone application. The installation files, as well as the user manual and examples, can be freely downloaded from the “Deep geothermal energy” web page of the Institut Cartogràfic i Geològic de Catalunya (ICGC) (under the Creative Commons license Attribution 4.0 International, CC BY 4.0). The source code can also be downloaded from <https://github.com/OpenICGC/3DHIP-Calculator> (accessed on 15 April 2022).

An easy-to-use graphical user interface (GUI) was implemented and organized in six main steps, as shown in the workflow of Figure 2. The first part comprises the pre-processing step, that includes the selection of input parameters (step 1 in Figure 2). In this step, the input 3D geological and 3D thermal models (referred to as 3DGM and 3DTM, respectively) are converted to a matrix, where each row corresponds to one voxel in the 3D model and the columns are the petrophysical/reservoir parameters. Using depth ranges and geological units, the target volume of the whole model is defined. The parameters that are not included as initial data in the 3D models are defined using PDFs (2, Figure 2).

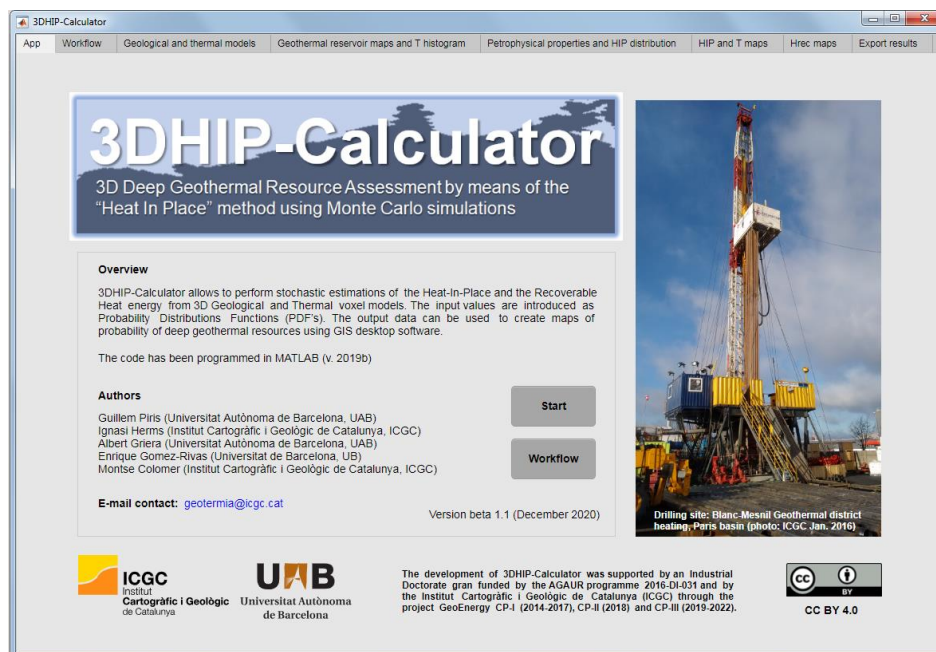


Figure 1. Screenshot of the main GUI window. The 3DHIP-Calculator is organized in eight tabs.

During the processing step, the HIP and Hrec calculations are carried out using Equations (1) and (2), and performed as many times (M) as desired (3, Figure 2). The full results from the N simulations are stored for each voxel of the model and include the entire uncertainty obtained from the Monte Carlo method. Then, the results are statistically compiled to obtain a cumulative probability distribution (CDF)

for each voxel, from which the representative probability values are extracted. The voxels corresponding to the target volume are also summed and compiled statistically to obtain the probability results for the entire target reservoir (4, Figure 2). Finally, the post-processing allows visualizing the probability results (4 and 5, Figure 2) and exporting the original data and the stochastic results to ASCII files (6, Figure 2).

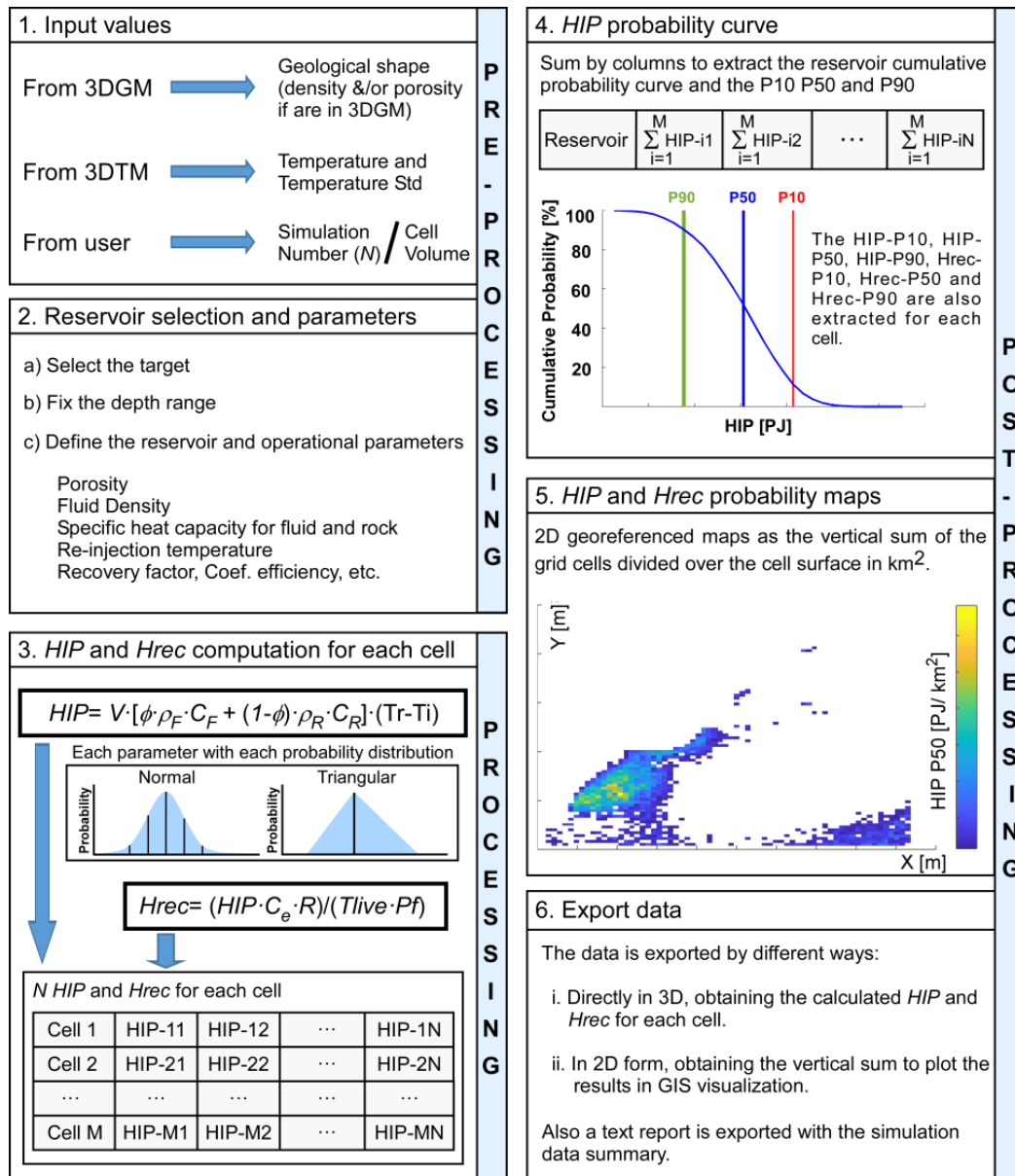


Figure 2. 3DHIP-Calculator workflow. It is divided into six main steps: (1) input values, (2) reservoir selection and parameters, (3) HIP and Hrec computation, (4) HIP probability curve, (5) HIP and Hrec probability maps, and (6) export data (modified from Herms et al., 2021 [34]).

5.2.3.1. Pre-processing: Input data

An essential step to run the application is to choose and upload the imported 3DGM and 3DTM. The application allows for loading data using ASCII text files, delimited by tabulators, spaces, or commas. A 3DTM is not always required, and alternatively, an approach based on a linear geothermal gradient

according to depth can be used, if a 3DTM is not available. When this option is chosen, the temperature of each voxel is calculated according to Equation (3):

$$T_z = T_0 + \Delta T \times Dz \tag{3}$$

where T_z is the estimated temperature at depth z , T_0 is the mean annual surface temperature, ΔT is the measured thermal regional gradient in C/km, and Dz is the depth z of the target according to the preliminary 3D model. This approach assumes a conductive steady-state regime and is indicated for geothermal plays in passive tectonic settings where no asthenospheric anomalies occur [45].

The 3DGM and 3DTM files should follow certain rules in terms of data organization (e.g., Figure 3). Particularly, they need to include at least one line of column headers before listing the data. The file is organized in a way that each column contains a variable, and each line corresponds to a voxel. The columns normally correspond to (in this order): voxel coordinates (X , Y , and Z , usually corresponding to its centroid) in UTM or geographic coordinates in decimal degrees, and a numerical identifier to differentiate the geological units (e.g., lithology, formation, reservoir, target, etc.). Additionally, the 3DGM can contain petrophysical parameters such as density (in g/cm^3) and porosity (parts per unit) that can vary for each voxel. The 3DTM should include the voxel coordinates (X , Y , and Z), the temperature (in $^\circ\text{C}$), and the temperature standard deviation (in $^\circ\text{C}$) for each voxel. The temperature standard deviation is an optional parameter that can be set to zero if it is unknown. Furthermore, the voxel position and resolution (in X , Y , and Z) of the geological and thermal models must be identical and match each other.

A	1	X, Y, Z, Lithology, Density
	2	317027.9125, 4540905.475, -6967.857143, 1, 2.90372729
	3	317721.7375, 4540905.475, -6967.857143, 1, 2.99401951
	4	318415.5625, 4540905.475, -6967.857143, 1, 2.68000007
	5	319109.3875, 4540905.475, -6967.857143, 1, 2.75085641
B	1	X, Y, Z, Mean_Lithology, Mean_Temperature, Stddev_Temperature
	2	317027.9125, 4540905.475, -6967.857143, 1, 180.15632, 1.52323
	3	317721.7375, 4540905.475, -6967.857143, 1, 180.26542, 1.36252
	4	318415.5625, 4540905.475, -6967.857143, 1, 180.65485, 2.01631
	5	319109.3875, 4540905.475, -6967.857143, 1, 180.90902, 1.86546

Figure 3. Internal structure of the data files of the voxel-based geological (A) and thermal (B) models that the 3DHIP-Calculator needs to be imported.

These input files for the voxel-based 3DGM and 3DTM can be generated using common commercial geological modeling software, such as GeoModeller3D (©BRGM, Intrepid-Geophysics) or SKUA-GOCAD® (Paradigm), or GemPy, an open-source 3D geological model based on Python [46], among many other packages able to export 3D models in this format. The files for the testing case presented in this paper were generated using GeoModeller3D (v 4.0.8).

5.2.3.2. Post-processing: Output data

The outputs from the stochastic simulations are utilized to:

- Generate a CDF for each voxel, from which a probability 10% (P10) (very low confidence of the estimation and high values), P50, and P90 (high confidence of the estimation and low values) are extracted. Furthermore, the mean and standard deviation are also calculated.
- Generate a CDF for the entire investigated target (e.g., geological unit, reservoir, etc.) summing the voxel values, and the P10, P50, and P90 are calculated. This approach is only used for the HIP calculation and not for the Hrec one.
- Generate 2D maps using the relationship between the vertical sum of the values calculated in each voxel with respect to the area occupied by the voxel (in km²). The P10, P50, and P90 of HIP and Hrec are then estimated.
- The application allows exporting two ASCII files with all results for further post-processing and generates an automatic report that summarizes the input data and the main results.

One of these files is the 3D model with all the voxels of the selected target. Each output register for each voxel contains the initial data (*X*, *Y*, *Z*, and geology and thermal properties) plus the HIP (PJ) and Hrec (kW) calculations. The HIP and Hrec are expressed in terms of P10, P50, P90, mean, and standard deviation. This file can be exported again to 3D geological modeling software for subsequent post-processing, or to other environments, such as GIS suites (e.g., the results of this study are presented in maps using the free and open-source QGIS 3.16.1 ‘Hannover’ version), 3D visualization tools, or statistical packages such as R [33]. The second file is the 2D model with the vertical summation of the HIP (PJ) and Hrec (kW) values of each voxel and their coordinates (in this case only *X* and *Y*), which can also be used for further geospatial analysis in GIS for mapping. The values of HIP and Hrec are not divided by the voxel area, and they are expressed as they have been calculated, i.e., in P10, P50, and P90. Finally, the last file contains a brief report in text format that includes the data and parameters used for the simulation, as well as the main results obtained.

5.2.3.3. Modelling scenarios depending on data availability

The software can be used for different situations and contexts, depending on the availability of data. The optimal scenario is when both a 3DGM containing the distribution of petrophysical parameters (e.g., density, porosity) and a 3DTM with the same voxel structure that includes the temperature distribution with depth are available. An intermediate case would be when only a 3DGM is available and the temperature information of the study region is estimated using the mean geothermal gradient. In that case, the 3DHIP-Calculator can be run using a linear geothermal gradient instead of a thermal model. The worst scenario would be when the reservoir volume and temperature are roughly known, and the rest of the parameters need to be inferred. The 3DHIP-Calculator can also be used in these cases, although the uncertainty of the variables and resulting PDFs increase.

5.3 Example case study—The Reus-Valls Basin (NE, Spain)

This section demonstrates the use and capabilities of the 3DHIP-Calculator assessing the geothermal potential of the Reus-Valls Basin (RVB) based on the geological and thermal models presented by Herms et al. [34]. The Triassic and Jurassic units were selected as potential targets. As the main goal is to show the capabilities of the tool, the stratigraphic complexity of Triassic and Jurassic units was simplified in the model used for this analysis. The three scenarios described in the previous section are considered here to calculate the geothermal potential of the RVB. A fourth scenario that also includes the calculation of the recoverable heat is also considered here.

5.3.1 Geological setting

The RVB is part of a set of SW–NE oriented extensional basins of the Catalan Coastal Ranges (Figure 4), which were formed during the Neogene rifting related to the opening of the Western Mediterranean and the Valencia Trough. The basin has a half-graben geometry strongly tilted towards its NW margin, where it is limited by the Camp Fault, which controls the basin depocenters [47]. This is an extensional NE-trending and SE-dipping basement fault [48] that was active from the early Miocene to the Quaternary. The fault separates the Prades-Llaberia and Miramar ranges (where the Mesozoic cover and the Paleozoic basement rocks crop out) and the Neogene sedimentary infill of the basin. These Neogene sediments reach a maximum thickness of about 2000 m near La Selva del Camp and Montbrío del Camp towns [47]. The Neogene sediments unconformably overlay the Mesozoic and the Paleozoic basement. Paleogene deposits are not preserved within the RVB, but such sediments lie unconformably on top of the Mesozoic succession in the Ebro Basin, NW of the study area.

There is no evidence of hydrothermal activity in the RVB except for the western limit of the basin, where there is a shallow hydrothermal aquifer controlled by W edge faults of the basin (called the ‘Camp Fault’) in the surroundings of the town of Montbrío del Camp. The hydrothermal aquifer shows an upward groundwater thermal flow of deep origin and a temperature of 81 °C at a 52 m depth. This fault-controlled hydrothermal aquifer is used nowadays by a thermal spa located within the town, exploiting its hot groundwaters.

Moreover, there is no evidence of magmatic activity, and it can be assumed that the main heat transport mechanism for the entire sedimentary basin at the regional scale is conduction. This is controlled by the thermal conductivity distribution of the lithologies that fill the basin and by the radiogenic heat production from the underlying granites. Therefore, the system can be classified as a conduction-dominated geothermal play in an intracratonic basin for the Mesozoic aquifers, which corresponds to a CD-1 of the catalog of geothermal play types based on geologic controls defined by Moeck [45,49] and CD-3 for the crystalline basement rocks.

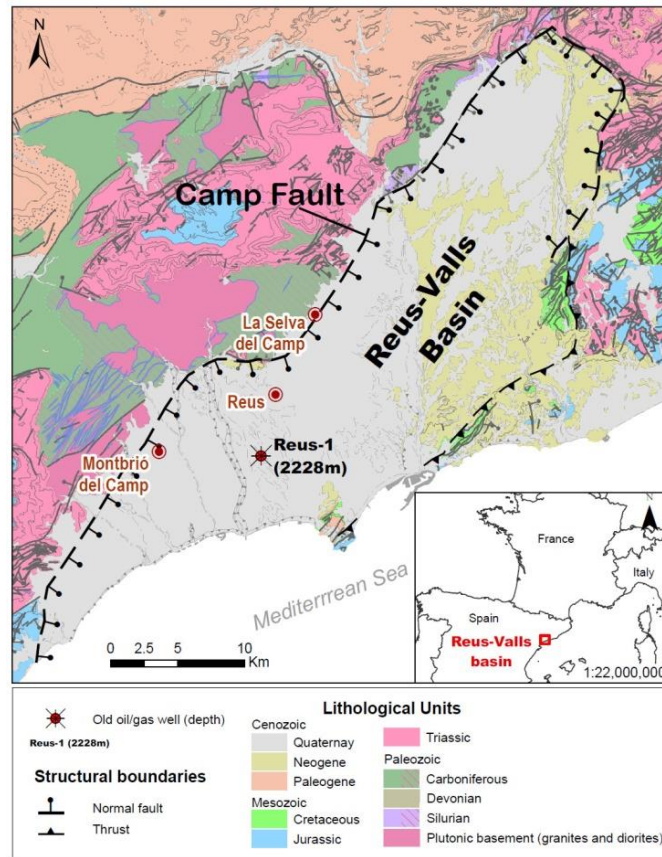


Figure 4. Geological map with the delimitation of the Reus-Valls Basin (modified from [50]). Source of EU map: © EuroGeographics for the administrative boundaries, European Commission, Euro-stat/GISCO.

5.3.2 The potential hot deep sedimentary aquifers

The main deep aquifers acting as targets in the test case are in the Jurassic and Triassic limestones and sandstones. Currently, their deep geothermal energy potential is still untapped. It is well-known that these aquifers are geothermal reservoirs that have been exploited for a long time in other places of central and western Europe, such as the Malm limestones of the Molasse Basin in Germany [51], the Dogger limestones of the Paris Basin [52], and the Buntsandstein sandstones in northern Germany [53] and the Upper Rhine Graben [54].

The Jurassic sequence of the RVB is defined by a basal layer of brecciated dolostones followed by a carbonate interval constituted by limestones and sandy limestones with widespread dolomitization and karstification. In the old Reus-1 well (Figure 4), which was drilled for oil/gas exploration [55,56], these materials correspond to a 261 m thick unit of partially karstified dolostones, with an estimated porosity ranging between 11% and 21% and an average value of 16%, according to available data measured in the same facies of nearby offshore fields [56]. This unit was considered a possible reservoir target for an underground gas storage project in the 90's due to its hydraulic properties.

The Middle Triassic corresponds to the Muschelkalk facies. These are defined from bottom to top by a basal interval of limestones and dolostones (Lower Muschelkalk), an intermediate interval of continental red fine sandstones, mudstones, and gypsum layers, and finally, an interlayered interval of limestones-dolostones and siltstone layers (Upper Muschelkalk). The total thickness of the unit is irregular in all the Catalan Coastal Ranges, and is about 359 m in the Reus-1 well. The basal dolostone (Lower Muschelkalk) is about 81 m thick in this well [55,56]. The main characteristics for inferring the reservoir porosity are the karstification of carbonates and the intense fracturing related to the Alpine exhumation and Neogene extension periods. Thus, the available data measured in nearby areas show values of primary porosity ranging between 7% and 12% (Ebro-1 and Fraga wells) [57], which can be considerably increased by secondary porosity. Finally, Buntsandstein facies (Lower Triassic) are composed of red detrital sediments formed by heteromeric conglomerates and fine sandstones, grading to mudstones at the top. The sedimentary sequence is constituted (from bottom to top) by a few meters of basal breccia, conglomerates, red sandstones, and a unit of interlayered siltstones with carbonate and evaporitic levels (Röt facies). Accordingly, the potential reservoir horizons that must be considered (in terms of host rock and fracture porosity) are the conglomerates and especially the sandstones of the lowest part of the sequence, with a total thickness range between 60 and 130 m in the Tarragona region [58]. The basal conglomerate has an irregular surface distribution and its porosity can be altered by its siltstone portion [59]. Moreover, the fluvial sandstones may have high porosity, as suggested by data from oil exploration wells (Ebro-1 and Ebro-2) in a nearby area, with average values of porosity ranging from 5.5% to 12.1%, with maximum values of 18% [57]. Attending to the range of measured porosities in the formations considered, a triangular distribution is consistent with the actual porosity pattern and is selected to be used for the reported examples (Table 1).

The 3DGM used for the RVB was built using the GeoModeller3D software (v 4.0.8) after several iterative steps including additional geological and geophysical data [34]. First, a reference model was generated using a Digital Terrain Model 15 × 15 [60], the geological map 1:50.000 of the area [61], data from the surface-based 3D regional geological model of Catalunya [62], unpublished geological cross-sections, information from deep oil/gas borehole (Reus-1 well; BTH depth -2228 m and Z: +74.26 m a.s.l.), interpreted horizons from 2D seismic profiles, as well as complementary information from the borehole database of Catalonia [63]. To refine this model, a full gravity/magnetic litho-constrained stochastic geophysical inversion approach was carried out using a Bayesian inference scheme implemented in the geologic modeling package of GeoModeller3D based on Markov Chain Monte Carlo simulations [64,65]. The gravity and magnetic raw data used in the inversion process were obtained from the geophysical database of Catalonia [66]. The 3D inversion modeling was applied to fit the most probable 3DGM using a stochastic approach [34]. The resulted 3DGM honors all the available geological constraints (well data, density values, stratigraphic order, and surface geology), and the gravity and magnetic data.

The 3DTM was also prepared using GeoModeller3D, applying a forward modeling approach using the quasi-stochastic methodology called *Parameter Sweep*—an algorithm for heat resource uncertainty studies in steady-state. In this approach, we assumed that the main heat transport mechanism in the basin is thermal conduction. Dirichlet boundary conditions were assigned at the top and bottom of the model, with a pre-fixed temperature of 15 °C corresponding to the mean annual surface temperature on top, and 176 °C at a 7 km depth. The bottom temperature boundary condition of the model was set from a generalized 3D lithospheric scale steady-state conductive heat transfer model for the whole territory of Catalonia (NE, Spain), previously built with the software LitMod_3D, and assuming local isostasy [67]. This model considered three layers: two layers model the crust with constant values of radiogenic heat production and thermal conductivity, and a third layer models the upper mantle without radiogenic heat production and constant thermal conductivity. The LitMod_3D approach considers, among others, the effect of gravity, geoid, surface heat flow, and petrological and seismic data [68]. Several temperature layers were obtained from this model at the base of the crust and at 15, 7, and 3 km depths, with a corresponding temperature of 176 °C at a 7 km depth, which are currently published on the ICGC website [35].

Assuming an average ambient air temperature of 15 °C and a ground temperature of 176 °C at a 7 km depth, the resulting average thermal gradient is estimated at 23 °C/km considering the whole thickness of the model. However, if the calculation focuses on specific depths, the thermal gradient distribution can vary slightly with respect to this value due to the heterogeneous vertical distribution of thermal properties across the different lithologies. For example, the contrast between the lower thermal conductivity distribution in Neogene and Mesozoic sediments compared to the Paleozoic basement induces a local gradient of 28.3 °C/km, from the surface to the top of the Jurassic reservoir in the Reus-1 well. The petrophysical parameters, i.e., the mean value of thermal conductivity, the heat production rate, and their corresponding standard deviation, for each lithology were obtained from previous works and the literature [34]. As stated above, the 3DHIP-Calculator can be used in different contexts according to the available data and assumptions. To introduce the different options, different scenarios of data availability were considered.

5.3.2.1. Example 1: Using a single-voxel 1D geological model

The first case considered here corresponds to the worst-case scenario, where a voxel-based 3DGM is not available. In this case, we assume an idealized reservoir defined only by a single voxel, prepared in a simple way. We impose a fixed value for the reservoir whole volume and the parameters are defined according to the PDF. This approach can be useful to obtain a first-order estimation of the HIP when the geometry and temperature of the target reservoir and the model must be idealized as a single-voxel reservoir. This case is equivalent to those considered in the literature when using commercial applications such as @Risk (Palisade) or Crystal Ball (Oracle) [23–25], and by the ‘GPPeval’ Python-

based stochastic library [27]. These software packages cannot consider the distributed 3D geometry of the reservoirs and therefore must assume the reservoir as a single volume.

Since the geological and thermal models are simplified to a single voxel, it is necessary to determine the total target reservoir volume in the calculations. The petrophysical and operational properties are introduced to indicate the corresponding triangular or normal distribution functions (Table 1). The results generated by the 3DHIP-Calculator tool are limited to the HIP histogram and the CDFs with the corresponding P10, P50, and P90 for the entire target (such as shown in Figure 5b for example 2).

5.3.2.2. Example 2: Using a 3DGM but not a 3DTM

The second scenario assumes a 3DGM that contains only information of the lithology class of each voxel, but not of its petrophysical parameters (such as rock density, porosity, and thermal properties) or specific temperature data from a calibrated 3D thermal model to estimate the temperature distribution in all the voxels of the model. To address the thermal context in this scenario, a regional gradient is assumed using Equation (3). In this example, a regional geothermal gradient of 30 °C/km and a mean annual surface temperature of 15 °C are assumed. Thus, the depth–temperature profile directly results from Equation (3) (Figure 5a).

After uploading the 3DGM and providing an input value for the geothermal gradient (30 °C/km), a total of $N = 10,000$ realizations were carried out. This number of simulations is accepted by different authors as high enough for Monte Carlo evaluations [4,19,27,43]. For this example, we considered the Triassic unit as the geothermal target reservoir.

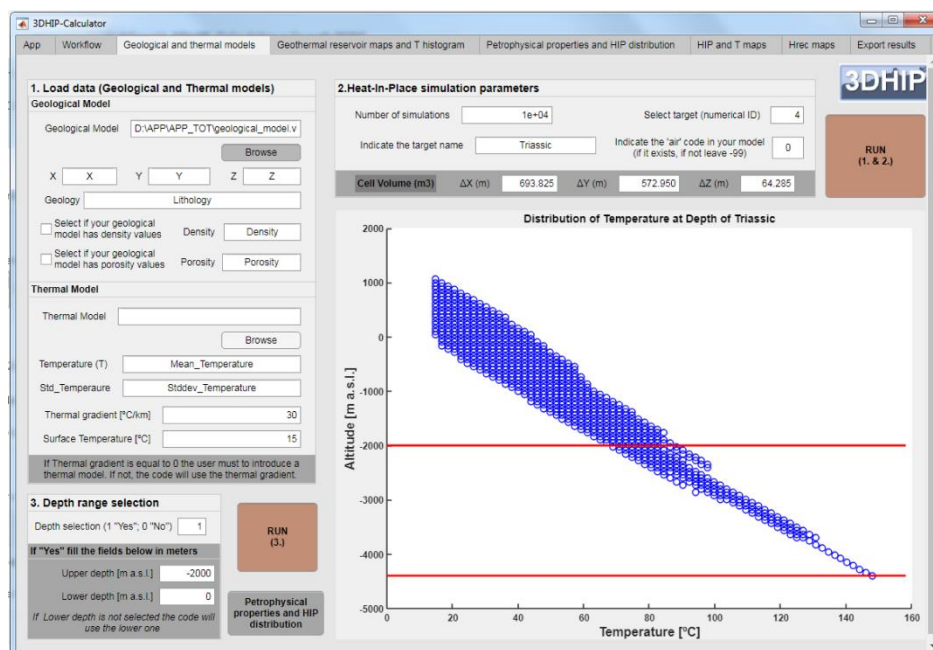
The selected depth range of the Triassic reservoir is indicated by two red lines in Figure 5. We selected the lower limit as the bottom of the model, while the upper depth corresponds to –2000 m a.s.l. The upper depth range was chosen as the limit where the reservoir temperature is >60 °C, a standard lower cut-off temperature for district heating stations [69]. The summary of petrophysical and operational properties, and their corresponding PDFs, are displayed in Table 1 and Figure 5b.

The values of the different parameters have been defined according to the available data, as well as from the scientific literature. The range of porosity values for the Buntsandstein and Muschelkalk units assumes a triangular PDF with porosity values of 7%, 12%, and 18% for the lowest, most probable, and highest values, respectively. Other parameters were obtained from the general literature, including the fluid density [70], fluid specific heat capacity [71], rock density [72], and rock specific heat capacity [73]. Considering the large uncertainty of the recovery factor (R), we used a triangular PDF with a lower value of 0.08, a most probable value of 0.12, and an upper value of 0.15, according to a conservative setting.

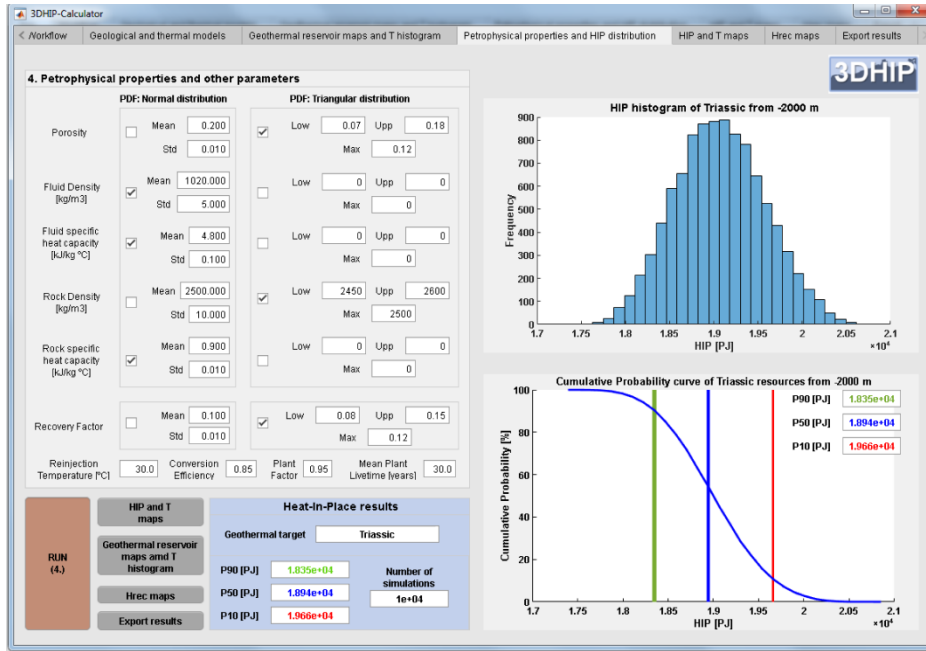
	Property	Units	PDFs	Values
Petrophysical	Porosity	-	Triangular	Low: 0.07, Max: 0.12, Upp: 0.18
	Fluid Density	kg/m ³	Normal	Mean: 1020, SD: 5
	Fluid specific heat capacity	kJ/kg.°C	Normal	Mean: 4.8, SD: 0.1
	Rock density	kg/m ³	Triangular	Low: 2450, Max: 2500, Upp: 2600
	Rock specific heat capacity	kJ/kg.°C	Normal	Mean: 0.9, SD: 0.01
Operational	Recovery factor	-	Triangular	Min: 0.08, Max: 0.12, Upp: 0.15
	Reinjection temperature	°C	-	30
	Conversion efficiency	-	-	0.85
	Plant factor	-	-	0.95
	Mean plant lifetime	years	-	30

Table 1. Petrophysical and operational parameters used for the HIP and Hrec calculations in example 2 (Low and Upp correspond to the minimum and maximum temperature values assigned to the triangular distribution with lowest frequencies; Max—the value with the highest frequency; PDF—probability distribution function; SD—standard deviation).

The results of the HIP and Hrec parameters can be displayed as histograms of their frequency and/or CDFs with P10, P50, and P90 values for the target reservoir (Figure 5b). Alternatively, the resulting HIP and Hrec values (P10, P50, and P90) can also be recalculated and displayed in 2D maps as the vertical summation of the calculated values assigned to each voxel divided by the voxel area in km² (see Figure 6 for an example of HIP). In these maps, the voxels with a zero value were left without color. Finally, the results can be exported to GIS software packages for post-processing (e.g., QGIS), as shown in Figure 7, where an isoline map of the HIP_P90 is plotted to highlight the probability results.



(a)



(b)

Figure 5. (a) Depth–temperature distribution for the Triassic unit using a linear geothermal gradient (example 2). Each blue circle corresponds to a temperature value of each of the voxels that discretize the Triassic unit. The red lines indicate the fixed depth range for the HIP and Hrec calculations. (b) Petrophysical and operational properties, and the corresponding PDFs used for this example. On the right-side: the HIP histogram and its CDF (blue curve) with the P10 (red line), P50 (blue line), and P90 (green line) for the entire targeted reservoir.

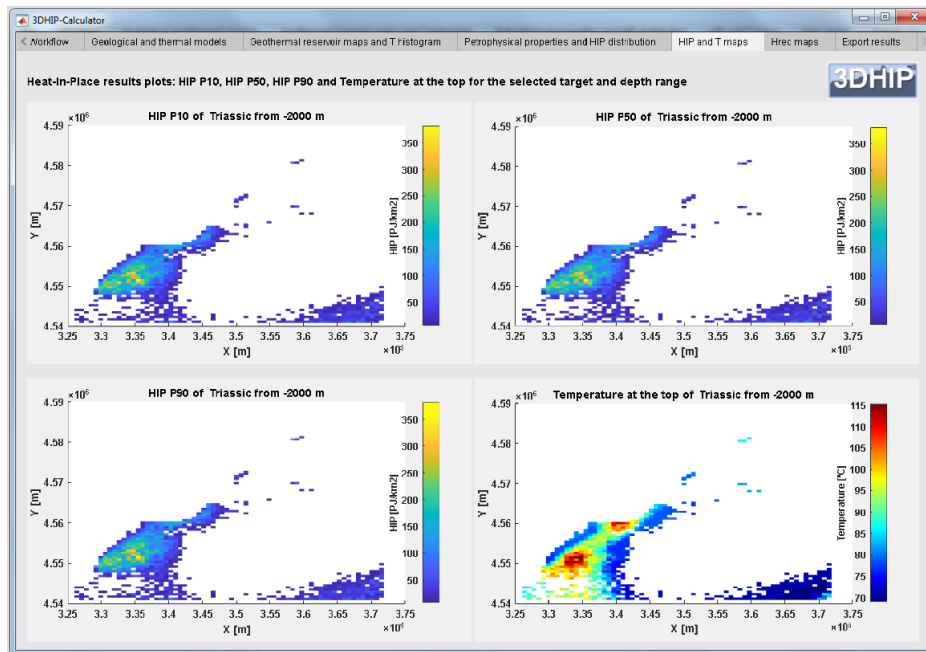


Figure 6. 2D maps of the HIP results of the P10, P50, and P90, and the temperature distribution at the top of the Triassic units below the pre-fixed depth range. For the HIP parameters, the values were calculated as an integration over the depth range and normalized by the voxel area. Units are in PJ/km² and °C, respectively.

The maximum geothermal potential in the study area (approximately 320–340 PJ/km²) is concentrated near the Vinyols town (Figure 7). This region coincides with the zone where the RVB is deeper and

Triassic attains its higher thickness at the regional scale. This spatial distribution of the results shows not only an estimation of the geothermal potential but also reveals where the prospective zones for geothermal energy production are located within the RVB. This demonstrates the importance of using 3D georeferenced data as inputs, containing the spatial geological information in three dimensions.

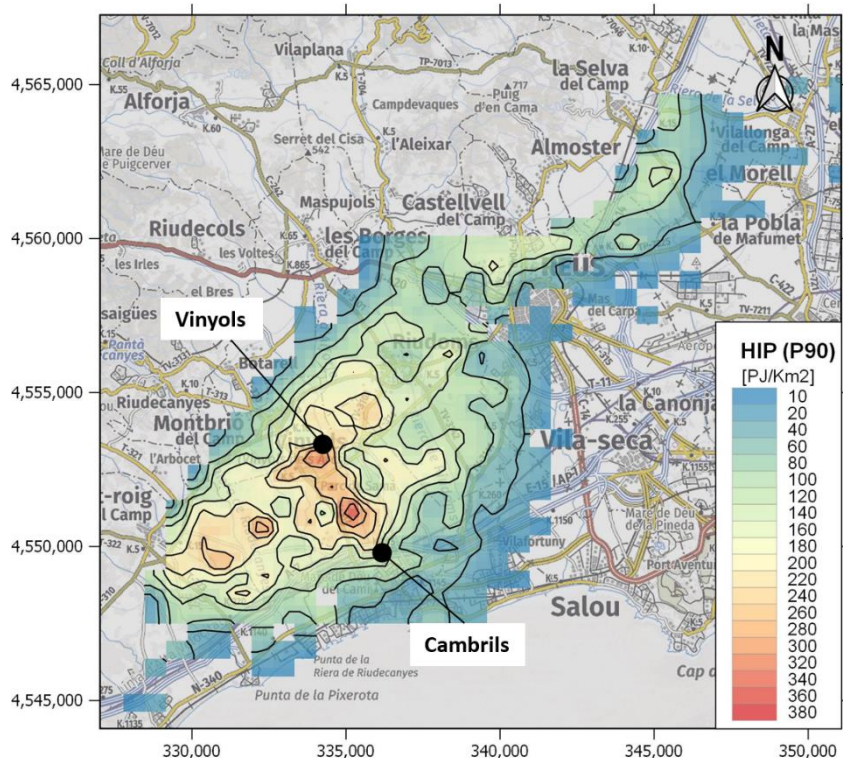


Figure 7. The HIP with P90 for the Triassic unit (example 2). The map was plotted with constant contour lines (20 PJ/Km²) following the described second example (i.e., with a 3DGM but not a 3DTM).

5.3.2.3. Example 3: Using both a 3DGM and a 3DTM

The third scenario corresponds to a case in which a 3DGM, which includes petrophysical data (e.g., density), and a 3DTM, with the temperature and its standard deviation for each voxel, are available. The number of simulations and the reservoir target are the same as those of the previous example. Figure 8 shows a graph of the temperature distribution against depth for all the voxels corresponding to the target reservoir. As the temperature distribution in depth is the result of a 3DTM, the temperature dispersion is lower than that of the previous example and less affected by topography. The reservoir top, base, vertical thickness, and temperature distribution are shown in Figure 9 for the selected target and depth range. A summary of the parameters and PDFs used in this scenario and the resulting HIP frequency and CDFs are displayed in Figure 10.

The HIP and Hrec results are displayed in a georeferenced map (Figure 11) to provide a background of geographical context, and this allows for further analysis. The highest values (260–300 PJ/km²) were observed southwest of the basin, concentrated around the town of Vinyols. However, in this scenario,

the estimation of HIP values was sensibly lower than those of the previous example. This is because the 3DTM mean gradient is lower than that of the previous scenario.

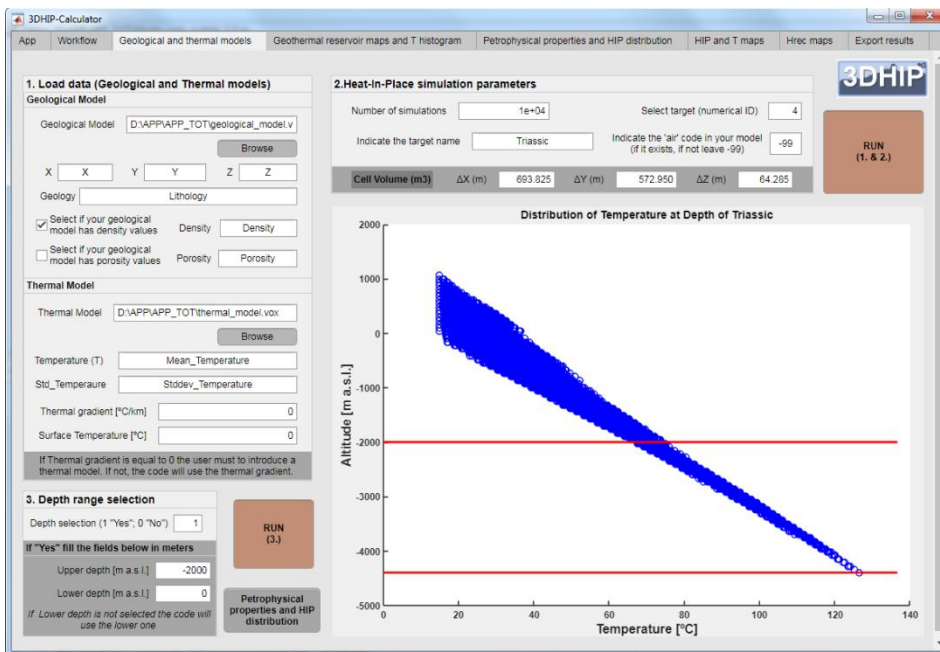


Figure 8. Altitude with respect to the temperature distribution for the selected target in example 3 (Triassic unit). Each blue circle corresponds to a voxel temperature value within the target reservoir. The red lines indicate the depth range fixed for performing calculations.

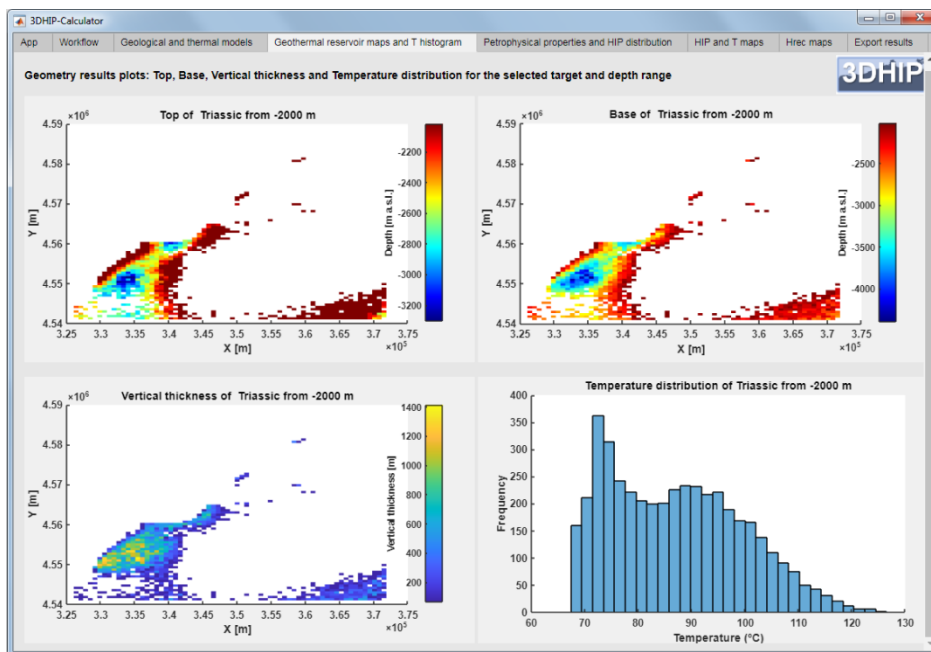


Figure 9. 2D distribution map of the top, base, and vertical thickness of the Triassic unit. Maximum depth and thickness are observed SW of the basin. The temperature distribution for the Triassic unit is shown in the bottom right diagram.

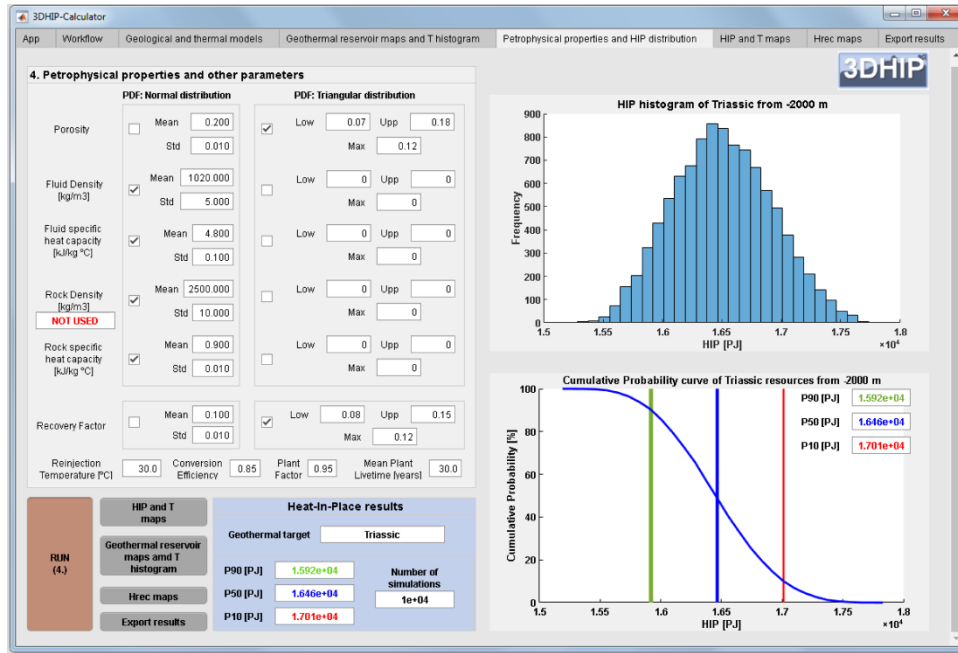


Figure 10. Summary of the petrophysical and operational parameters and PDFs used in example 3. For this example, the 3D geological model includes a rock density value for each voxel, and for this reason, it was not stochastically simulated using a pre-scribed PDF. On the right: the HIP histogram and the HIP CDF's results for the entire target reservoir (P10, P50, and P90).

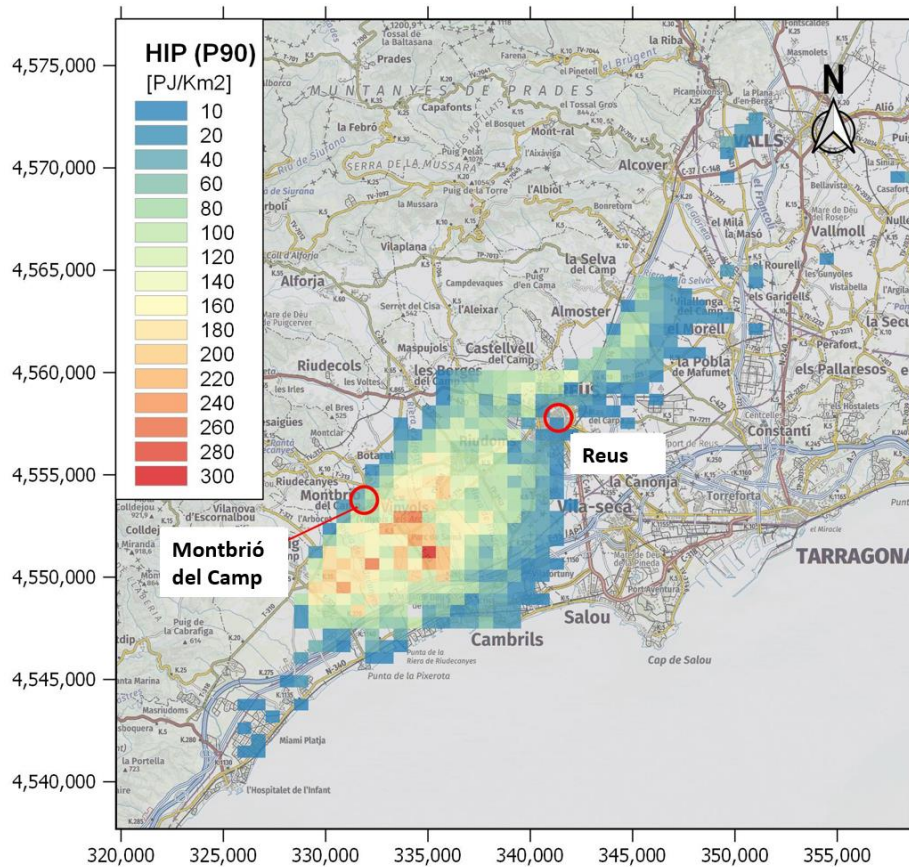


Figure 11. 2D georeferenced map showing the HIP results obtained using example 3. The resulting HIP (P90) values are divided by the voxel area to express the results in PJ/km². Only on-shore values are displayed.

5.3.2.4. Example 4: The use of the Recoverable Heat (Hrec) values

The last scenario corresponds to a case in which the recoverable heat (Hrec) is also estimated. The results provide a first estimation of the percentage of the urban thermal demand that could be covered with the thermal energy recovered from a hypothetical geothermal doublet, where production and injection wells are typically separated from 1 to 2 km [72]. The Jurassic unit was considered as the target reservoir and the well locations were assumed to be next to the old Reus-1 oil well, where the Jurassic thickness is about 250 to 300 m from 1430 to 1700 m depth [54,55]. The example uses the same data assumption as that in example 3 (3DGM, which includes petrophysical data (e.g., density), and a 3DTM, with the temperature and its standard deviation for each voxel). For this case, the formation temperature oscillates between 55 and 65 °C and the rock porosity follows a normal distribution with a mean of 16% and a standard deviation of 5% [55]. Table 1 shows the other values used for the calculation.

Here, we compared the obtained Hrec with respect to the urban heat demand of the city of Reus (Figure 12). We compared the sum of the obtained Hrec for the different probabilities, Hrec_P10, Hrec_P50, and Hrec_90, under the influence radius of the hypothetical production deep well. Considering that the influence radius of the exploitation area in the reservoir has a value of half of the spacing between the injection and extraction wells (e.g., of up to 0.5 to 1 km), we obtained that the Hrec can range from 927 kW (P90 with 0.5 km of influence in the injection well) to 6.1 MW (P10 with 1 km of influence in the injection well). The heat demand density information was gathered from the Hotmaps EU project (<https://www.hotmaps-project.eu> (accessed on 15 April 2022)). The total heat energy demand obtained for the city of Reus was 391.05 GWh/year. Considering as a hypothesis that this demand concentrates during the colder part of the year (6 months) and with heaters working 12 h per day (2160 h/year), we can estimate the demand of thermal heat power capacity. In this case, the Hrec results suggested that a geothermal production well of a doublet in the Jurassic reservoir in this location could cover a range of 0.51% to 3.38% of the total heat demand of this city (Table 2 and Figure 12).

Hrec—Recoverable Heat vs. Estimated R— Radius of Influence	Hrec P10 (kWt)	Hrec P50 (kWt)	Hrec P90 (kWt)
R = 0.5 km	1337	1140	927
R = 1 km	6127	5185	4211

Table2. Estimated probable heat recovery capacity as a function of the influence radius for a hypothetical geothermal doublet well in the Jurassic reservoir close to the Reus-1 well.

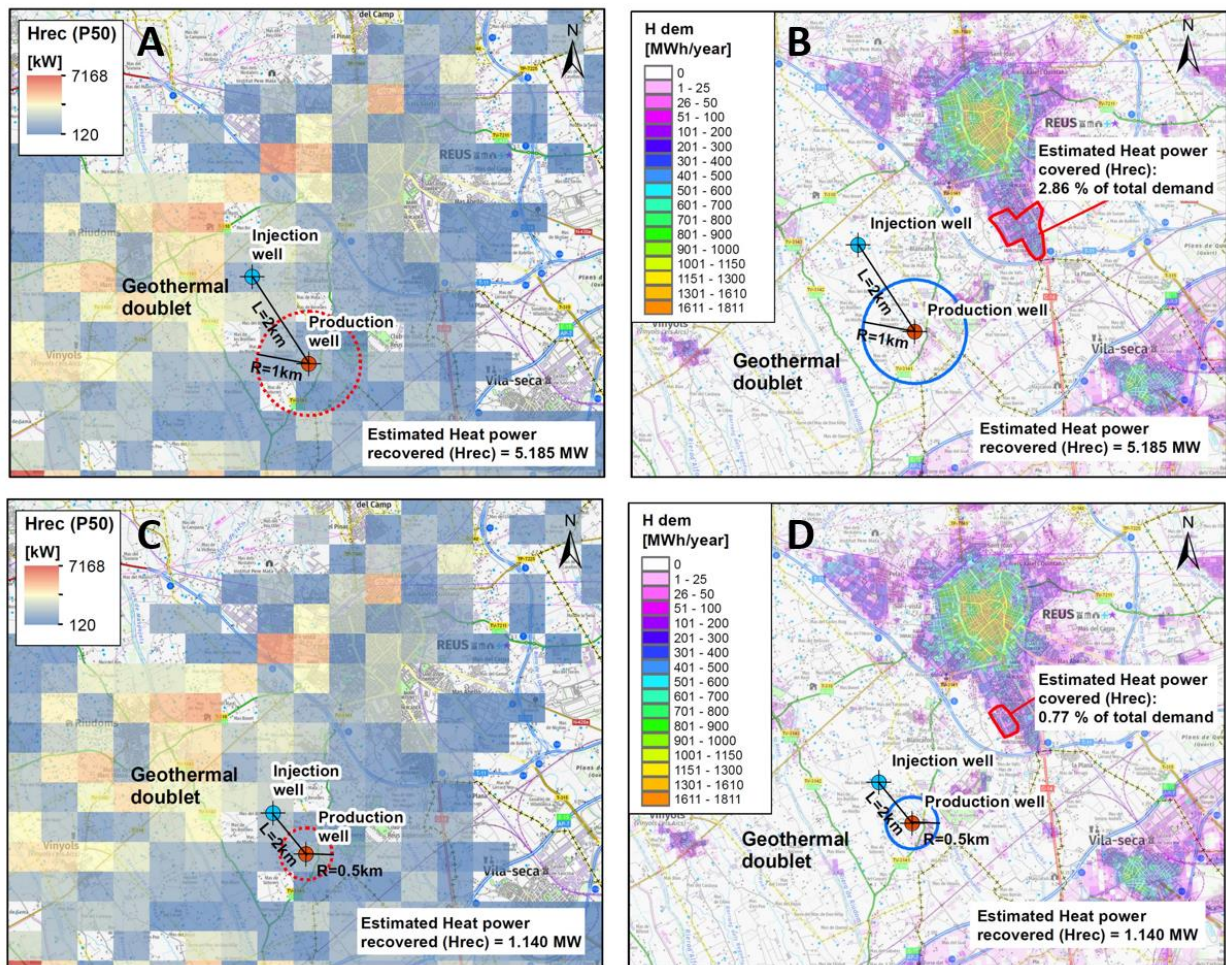


Figure 12. Two geothermal doublet scenarios comparing the Hrec_P50 (A–C) with the heat demand of the city of Reus (B–D): the red polygon shows the covered area of the Reus total demand. (A,B) The injection and production wells are separated by 2 km and the radius of influence into the reservoir is considered to be 1 km. (C,D) The injection and production wells are separated by 1 km and the well influence radius into the reservoir is 0.5 km.

The Hrec results also suggest that the geothermal potential is much higher in the northwest of the Reus-1 well. This can be explained due to the fact that to the NW, the Jurassic formation lies deeper, up to 2000 m, and thus its temperature, following the 3DTM, oscillates between 70 and 80 °C. However, we considered a location close to the Reus-1 oil well to use its data.

5.4 Discussion and conclusions

This paper describes a novel and freely available tool named the 3DHIP-Calculator, which is used to assess the deep geothermal energy potential of hot aquifers. The tool allows applying the HIP method to calculate the HIP and the Hrec of a target reservoir following a Monte Carlo stochastic approach, and using 3D geological and 3D thermal models as inputs. The HIP method [5] is widely known and used in geothermal energy studies. The tool can be used to generate probability maps, which are of particular importance during the preliminary assessment of geothermal resources, mainly at the regional scale. In this work, the operation and workflow of the 3DHIP-Calculator tool have been presented. Its use has been demonstrated through an example of an area identified with deep geothermal potential in Mesozoic

aquifers located in the NE of the Iberian Peninsula (Reus-Valls Basin), and from considering four different conceptual scenarios based on the available data.

The 3DHIP-Calculator covers the need to have a standard and freely available tool for the whole geothermal community with which users can estimate the HIP using Monte Carlo simulations and where they can use their 3D models to assess their case studies. In this regard, the 3DHIP-Calculator is the only free tool that allows to carry out estimations of the geothermal potential assessment at the same time, either considering a homogeneous distribution of parameters (i.e., lumped parameter models) in the whole reservoir or including spatial variability of petrophysical properties through the considered reservoir (e.g., density and porosity). Moreover, the 3DHIP-Calculator is not regionally constrained and can be used to perform geothermal potential assessment exercises independently from where their data is. Additionally, the 3DHIP-Calculator simulations are not limited to a specific case study and the initial input data can change and incorporate data as these are refined or obtained through the reservoir characterization. The link between the 3DGM and 3DTM (examples 2 and 3), and the corresponding 3D geothermal potential assessment model (3DGPAM), represents an important step forward with respect to scenarios such as that of example 1, where the reservoir is represented as a single voxel and the geothermal potential results are limited to a single CDF with values of P10, P50, and P90 for the entire target reservoir, and where the option to include more data as the reservoir knowledge increases is truncated.

The results of the 3DGPAM can also again be exported back into 3D geological modeling software to carry out further steps of geothermal exploration of a specific project, or simply exported in 3D visualization software to plot the obtained results (e.g., the open-source, multi-platform data analysis and visualization application, such as ParaView).

The 3DHIP-Calculator is designed to assess and map geothermal resources at the regional scale. It bridges the gap between the first phases of field exploration and geological 3D modeling, and the necessary phase of quantification of the geothermal heat available in deep hot reservoirs, maintaining the uncertainty of the data. Therefore, it should be considered a complementary tool to the well-known open-source software DoubletCalc 2D [74], which allows calculating the hydraulic performance around geothermal doublets (producing well and injector) over time, and that is also based on stochastic simulations (Monte Carlo). Indeed, this analysis corresponds to a more advanced and detailed phase in the development of geothermal projects, considering, for example, that it is required for many grant applications related to specific geothermal projects in the Netherlands. The 3DHIP-Calculator is not designed to calculate the hydraulic performance of a doublet or to directly calculate the flow, temperature, and therefore the potential energy recovered from them, as other already available tools do

for these purposes. However, it is able to make a first estimation from a hypothetical geothermal doublet, as shown in example 4.

The results obtained in the test case of the Reus-Valls Basin (NE, Spain) demonstrate how the 3DHIP-Calculator can satisfactorily evaluate and map the deep geothermal potential of reservoirs in a distributed manner from 3D models. In the presented test case study, the results reveal the existence of a high geothermal potential located between the villages of Vinyols and Cambrils (e.g., Figure 7). Although the exploration phase is in a preliminary stage, the results obtained considering the 3D modeling and the stochastic approach will allow progress in the decision-making process for the design of new exploratory campaigns, and thus increase the precision of the predictions. This modeling workflow has improved the estimates from previous studies based exclusively on a deterministic and a basin-wide aggregate approach [36,37,75].

The examples presented here demonstrate how geoscientists and engineers can use the 3DHIP-Calculator to easily evaluate the geothermal potential from their 3D geological models in a repeatable and systematic manner following a stochastic approach. The tool will help investors and research organizations determine the suitability of continuing to advance with new investments in pre-feasibility studies of future deep geothermal projects.

5.5 References

1. Bertani, R. Geothermal Power Generation in the World 2010–2015 Update Report. Proceedings World Geothermal Congress 2015 Melbourne, Australia. 19–25 April 2015; pp. 19–25.
2. Sigfússon, B.; Uihlein, A. 2015 JRC Geothermal Energy Status Report; EUR 27623 EN; Joint Research Center: Petten, The Netherlands; p. 59. <https://doi.org/10.2790/757652>
3. van Wees, J.-D.; Boxem, T.; Angelino, L.; Dumas, P. A Prospective Study on the Geothermal Potential in the EU. GEOLEC Project; EC, Utrecht, The Netherlands, 2013; p. 97.
4. Agemar, T.; Weber, J.; Moeck, I. Assessment and Public Reporting of Geothermal Resources in Germany: Review and Outlook. *Energies* 2018, 11, 332. <https://doi.org/10.3390/en11020332>.
5. Muffler, P.; Cataldi, R. Methods for Regional Assessment of Geothermal Resources. *Geothermics* 1978, 7, 53–89. [https://doi.org/10.1016/0375-6505\(78\)90002-0](https://doi.org/10.1016/0375-6505(78)90002-0).
6. Williams, C.F. Updated Methods for Estimating Recovery Factors for Geothermal Resources. In Proceedings of the Thirty-Second Workshop on Proceedings, Geothermal Reservoir Engineering, Stanford University, Stanford, CA, USA, 22 January 2007; p. 7.
7. Williams, C.F.; Reed, M.J.; Mariner, R.H. A Review of Methods Applied by the U.S. Geological Survey in the Assessment of Identified Geothermal Resources; U.S. Geological Survey: Reston, Virginia, 2008; p. 30.
8. Garg, S.K.; Combs, J. Appropriate Use of USGS Volumetric “Heat in Place” Method and Monte Carlo Calculations. In Proceedings of the Thirty-Fourth Workshop on Geothermal Reservoir Engineering, Stanford University, Stanford, CA, USA, 1 February 2010; p. 7.
9. Garg, S.K.; Combs, J. A Reexamination of USGS Volumetric “Heat in Place” Method. In Proceedings of the Proceedings Thirty-Sixth Workshop on Geothermal Reservoir Engineering, Stanford University, Stanford, CA, USA, 31 February 2011; p. 5.
10. Garg, S.K.; Combs, J. A Reformulation of USGS Volumetric “Heat in Place” Resource Estimation Method. *Geothermics* 2015, 55, 150–158. <https://doi.org/10.1016/j.geothermics.2015.02.004>.
11. Limberger, J.; Boxem, T.; Pluymaekers, M.; Bruhn, D.; Manzella, A.; Calcagno, P.; Beekman, F.; Cloetingh, S.; van Wees, J.-D. Geothermal Energy in Deep Aquifers: A Global Assessment of the Resource Base for Direct Heat Utilization. *Renew. Sustain. Energy Rev.* 2018, 82, 961–975. <https://doi.org/10.1016/j.rser.2017.09.084>.
12. Trumpy, E.; Botteghi, S.; Caiozzi, F.; Donato, A.; Gola, G.; Montanari, D.; Pluymaekers, M.P.D.; Santilano, A.; van Wees, J.D.; Manzella, A. Geothermal Potential Assessment for a Low Carbon Strategy: A New Systematic Approach Applied in Southern Italy. *Energy* 2016, 103, 167–181. <https://doi.org/10.1016/j.energy.2016.02.144>.
13. Miranda, M.M.; Raymond, J.; Dezayes, C. Uncertainty and Risk Evaluation of Deep Geothermal Energy Source for Heat Production and Electricity Generation in Remote Northern Regions. *Energies* 2020, 13, 4221. <https://doi.org/10.3390/en13164221>.
14. Arango-Galván, C.; Prol-Ledesma, R.M.; Torres-Vera, M.A. Geothermal Prospects in the Baja California Peninsula. *Geothermics* 2015, 55, 39–57. <https://doi.org/10.1016/j.geothermics.2015.01.005>.
15. Pol-Ledesma, R.-M.; Carrillo-de la Cruz, J.-L.; Torres-Vera, M.-A.; Membrillo-Abad, A.-S.; Espinoza-Ojeda, O.-M. Heat Flow Map and Geothermal Resources in Mexico / Mapa de Flujo de Calor y Recursos Geotérmicos de México. *Terra Digit.* 2018. <https://doi.org/10.22201/igg.25940694.2018.2.51.103>.

16. Hurter, S.; Schellschmidt, R. Atlas of Geothermal Resources in Europe. *Geothermics* 2003, 32, 779–787. [https://doi.org/10.1016/S0375-6505\(03\)00070-1](https://doi.org/10.1016/S0375-6505(03)00070-1).
17. Nathenson, M. Methodology of Determining the Uncertainty in the Accessible Geothermal Resource Base of Identified Hydrothermal Convec-Tion Systems; Open-File Report; U.S. Geological Survey: Menlo Park, CA, USA, 1978; p. 51.
18. Rubinstein, R.Y.; Kroese, D.P. *Simulation and the Monte Carlo Method*; Wiley Series in Probability and Statistics; 3rd ed.; Wiley: Hoboken, NJ, USA, 2017; ISBN 978-1-118-63220-8.
19. Shah, M.; Vaidya, D.; Sircar, A. Using Monte Carlo Simulation to Estimate Geothermal Resource in Dholera Geothermal Field, Gujarat, India. *Multiscale Multidiscip. Model. Exp. Des.* 2018, 1, 83–95. <https://doi.org/10.1007/s41939-018-0008-x>.
20. Trota, A.; Ferreira, P.; Gomes, L.; Cabral, J.; Kallberg, P. Kallberg Power Prod. Estim. From Geothermal Resources by Means of Small-Size Compact Climeon Heat Power Converters: Case Studies from Portugal (Sete Cidades, Azores and Longroiva Spa, Mainland). *Energies* 2019, 12, 2838. <https://doi.org/10.3390/en12142838>.
21. Palisade Corporation. @Risk for Excel; Palisade Corporation: Ithaca, NY, USA, 2014.
22. Oracle. Oracle Crystal Ball Spreadsheet Functions for Use in Microsoft Excel Models; Oracle: Austin, TX, USA, 2014.
23. Arkan, S.; Parlaktuna, M. Resource Assessment of Balçova Geothermal Field. Proceedings World Geothermal Congress. 2005 Antalya Turkey. 24–29 April 2005.
24. Yang, F.; Liu, S.; Liu, J.; Pang, Z.; Zhou, D. Combined Monte Carlo Simulation and Geological Modeling for Geothermal Resource Assessment: A Case Study of the Xiongxi Geothermal Field, China. Proceedings World Geothermal Congress 2015 Melbourne, Australia 19–25 April 2015; pp. 19–25.
25. Halcon, R.M.; Kaya, E.; Penarroyo, F. Resource Assessment Review of the Daklan Geothermal Prospect, Benguet, Philippines. Proceedings World Geothermal Congress 2015 Melbourne, Australia 19–25 April 2015; pp. 19–25.
26. Barkaoui A.-E.; Zarhloule, Y.; Varbanov, P.S.; Klemes, J.J. Geothermal Power Potential Assessment in North Eastern Morocco. *Chem. Eng. Trans.* 2017, 61, 1627–1632. <https://doi.org/10.3303/CET1761269>.
27. Pocasangre, C.; Fujimitsu, Y. Geothermics A Python-Based Stochastic Library for Assessing Geothermal Power Potential Using the Volumetric Method in a Liquid-Dominated Reservoir. *Geothermics* 2018, 76, 164–176. <https://doi.org/10.1016/j.geothermics.2018.07.009>.
28. Zhu, Z.; Lei, X.; Xu, N.; Shao, D.; Jiang, X.; Wu, X. Integration of 3D Geological Modeling and Geothermal Field Analysis for the Evaluation of Geothermal Reserves in the Northwest of Beijing Plain, China. *Water* 2020, 12, 638. <https://doi.org/10.3390/w12030638>.
29. Calcagno, P.; Baujard, C.; Dagallier, A.; Guillou-Frottier, L.; Genter, A. Three-Dimensional Estimation of Geothermal Potential from Geological Field Data: The Limagne Geothermal Reservoir Case Study (France). Proceedings of the Geothermal Resources Council GRC Annual Meeting, Reno, USA, October 4-7, 2009. Page 326
30. van Wees, J.-D.; Juez-Larre, J.; Bonte, D.; Mijnlief, H.; Kronimus, A.; Gesse, S.; Obdam, A.; Verweij, H. ThermoGIS: An Inte-grated Web-Based Information System for Geothermal Exploration and Governmental

- Decision Support for Mature Oil and Gas Basins. In Proceedings of the World Geothermal Congress 2010, Bali, Indonesia, 25 April 2010; p. 7.
31. Kramers, L.; van Wees, J.-D.; Pluymaekers, M.P.D.; Kronimus, A.; Boxem, T. Direct Heat Resource Assessment and Subsurface Information Systems for Geothermal Aquifers; the Dutch Perspective. *Neth. J. Geosci.* 2012, 91, 637–649. <https://doi.org/10.1017/S0016774600000421>.
 32. Vrijlandt, M.A.W.; Struijk, E.L.M.; Brunner, L.G.; Veldkamp, J.G.; Witmans, N.; Maljers, D.; van Wees, J.D. ThermoGIS Update: A Renewed View on Geothermal Potential in the Netherlands. In Proceedings of the European Geothermal Congress 2019, Den Haag, The Netherlands, 11 June 2019; p. 10.
 33. R Core Team. R: A Language and Environment for Statistical Computing; R Foundation for Statistical Computing: Vienna, Austria, 2013.
 34. Herms, I.; Piris, G.; Colomer, M.; Peigney, C.; Griera, A.; Ledo, J. 3D Numerical Modelling Combined with a Stochastic Approach in a MATLAB-Based Tool to Assess Deep Geothermal Potential in Catalonia: The Case Test Study of the Reus-Valls Basin. In Proceedings of the World Geothermal Congress 2020 + 1, Reykjavik, Iceland, 24-27 October 2021; p. 9.
 35. ICGC Geothermal Atlas of Catalonia: Geoindex-Deep-Geothermal 2020. Available online: <https://www.icgc.cat/en/Public-Administration-and-Enterprises/Tools/Geoindex-viewers/Geoindex-Deep-geothermal-energy> (accessed on 15 October 2021).
 36. Colmenar-Santos, A.; Folch-Calvo, M.; Rosales-Asensio, E.; Borge-Diez, D. The Geothermal Potential in Spain. *Renew. Sustain. Energy Rev.* 2016, 56, 865–886. <https://doi.org/10.1016/j.rser.2015.11.070>.
 37. Arrizabalaga, I.; De Gregorio, M.; De Santiago, C.; Pérez, P. Geothermal Energy Use, Country Update for Spain. In Proceedings of the European Geothermal Congress 2019, Den Haag, The Netherlands, 11 June 2019; p. 9.
 38. Beardsmore, G.R.; Rybach, L.; Blackwell, D.; Baron, C. A Protocol for Estimating and Mapping Global EGS Potential. *Geotherm. Resour. Counc. Trans.* 2010, 34, 301–312.
 39. Hurter, S.; Haenel, R. Atlas of Geothermal Resources in Europe; Official Publications of the European Communities, European Commission: Luxembourg, 2002.
 40. Lavigne, J. Les Ressources Géothermiques Françaises- Possibilités de Mise En Valeur. *Ann. Des Mines*, 1977, 41 pages.
 41. Williams, C.F. Development of Revised Techniques for Assessing Geothermal Resources. In Proceedings of the Twenty-Ninth Workshop on Geothermal Reservoir Engineering, Stanford University, CA, USA, 26 January 2004; p. 5.
 42. Lund, J.W.; Boyd, T.L. Direct Utilization of Geothermal Energy 2015 Worldwide Review. *Geothermics* 2016, 60, 66–93. <https://doi.org/10.1016/j.geothermics.2015.11.004>.
 43. Wang, Y.; Wang, L.; Bai, Y.; Wang, Z.; Hu, J.; Hu, D.; Wang, Y.; Hu, S. Assessment of Geothermal Resources in the North Jiangu Basin, East China, Using Monte Carlo Simulation. *Energies* 2021, 14, 259. <https://doi.org/10.3390/en14020259>.
 44. MathWorks. MATLAB; The MathWorks, Inc.: Natick, MA, USA, 2019.
 45. Moeck, I.; Beardsmore, G.R. A New ‘Geothermal Play Type’ Catalog: Streamlining Exploration Decision Making. In Proceedings of the Thirty-Ninth Workshop on Geothermal Reservoir Engineering, Stanford University, Stanford, CA, 24 February 2014; p. 8.

46. de la Varga, M.; Schaaf, A.; Wellmann, F. GemPy 1.0: Open-Source Stochastic Geological Modeling and Inversion. *Geosci. Model Dev.* 2019, 12, 1–32. <https://doi.org/10.5194/gmd-12-1-2019>.
47. Massana, E. L'activitat Neotectònica a Les Cadenes Costaneres Catalanes. Ph.D. Thesis, University of Barcelona: Barcelona, Spain, 1995.
48. Cabrera, L.; Calvet, F. Onshore Neogene record in NE Spain: Vallès–Penedès and El Camp half-grabens (NW Mediterranean). In *Tertiary Basins of Spain*; Friend, P.F., Dabrio, C.J., Eds.; Cambridge University Press: Cambridge, UK, 1996; pp. 97–105. ISBN 978-0-521-46171-9.
49. Moeck, I.S. Catalog of Geothermal Play Types Based on Geologic Controls. *Renew. Sustain. Energy Rev.* 2014, 37, 867–882. <https://doi.org/10.1016/j.rser.2014.05.032>.
50. ICGC Base Geològica 1:50.000 de Catalunya. Administration-and-Enterprises/Downloads/Geological-and-geothematic-cartography/Geological-cartography/Geological-map-1-50-000 (accessed on 1 January 2021).
51. Moeck, I.S.; Dussel, M.; Weber, J.; Schintgen, T.; Wolfgramm, M. Geothermal Play Typing in Germany, Case Study Molasse Basin: A Modern Concept to Categorise Geothermal Resources Related to Crustal Permeability. *Neth. J. Geosci.* 2019, 98, e14. <https://doi.org/10.1017/njg.2019.12>.
52. Lopez, S.; Hamm, V.; Le Brun, M.; Schaper, L.; Boissier, F.; Cotiche, C.; Giuglaris, E. 40 Years of Dogger Aquifer Management in Ile-de-France, Paris Basin, France. *Geothermics* 2010, 39, 339–356. <https://doi.org/10.1016/j.geothermics.2010.09.005>.
53. Blöcher, G.; Reinsch, T.; Hennings, J.; Milsch, H.; Regenspurg, S.; Kummerow, J.; Francke, H.; Kranz, S.; Saadat, A.; Zim-mermann, G.; et al. Hydraulic History and Current State of the Deep Geothermal Reservoir Groß Schönebeck. *Geothermics* 2016, 63, 27–43. <https://doi.org/10.1016/j.geothermics.2015.07.008>.
54. Haffen, S.; Géraud, Y.; Diraison, M.; Dezayes, C.; Siffert, D.; Garcia, M. Temperature Gradient Anomalies in the Buntsandstein Sandstone Reservoir, Upper Rhine Graben, Soultz, France. In *Proceedings of the Tu D203 09 -76th EAGE Conference & Exhibition 2014, Amsterdam, The Netherlands, 16 June 2014*.
55. Zapatero, M.A.; Reyes, J.L.; Martínez, R.; Suárez, I.; Arenillas, A.; Perucha, M.A. Estudio Preliminar de las Formaciones Favorables para el Almacenamiento Subterráneo de CO₂ en España; Instituto Geológico y Minero de España (IGME): Madrid, Spain, 2009; p. 135.
56. Aurense Proyecto de Almacenamientos Subterráneos de Gas. Reus; Auxiliar de Recursos y Energía, S.A.: Madrid, España, 1996; p. 65.
57. Campos, R.; Recreo, F.; Perucha, M.A. AGP de CO₂: Selección de Formaciones Favorables en la Cuenca del Ebro; Informes Técnicos Ciemat; CIEMAT: Madrid, España, 2007; p. 124.
58. Marzo, M. El Bundstandstein de los Catalánides: Estratigrafía y Procesos Sedimentarios. Ph.D. Thesis, Universitat de Barcelona: Barcelona, Spain, 1980.
59. Zapatero, M.A.; Suárez, I.; Arenillas, A.; Marina, M.; Catalina, R.; Martínez-Orío, R. Proyecto Europeo GeoCapacity. Assessing European Capacity for Geological Storage of Carbon Dioxide; Instituto Geológico y Minero de España (IGME): Madrid, España, 2009; p. 162.
60. ICGC Model d'Elevacions Del Terreny de Catalunya 15 × 15 metres (MET-15) v2.0. 2018. <https://www.icgc.cat/Descarregues/Elevacions/Model-d-elevacions-del-terreny-de-15x15-m> (accessed on 11 January 2021).

61. ICGC Mapa Geològic Comarcal de Catalunya. Full Del Baix Camp 2006. <https://www.icgc.cat/en/Public-Administration-and-Enterprises/Downloads/Geological-and-geothematic-cartography/Geological-cartography/Geological-map-1-50-000> (accessed on 11 January 2021).
62. ICGC Model 3D Geològic de Catalunya 2013. <https://www.icgc.cat/Administracio-i-empresa/Descarregues/Cartografia-geologica-i-geotematica/Cartografia-geologica/Model-geologic-3D-de-Catalunya> (accessed on 15 January 2020).
63. ICGC Base de Dades de Sondejors de Catalunya (BDSoc) 2015. <https://www.icgc.cat/ca/Administracio-i-empresa/Eines/Visualitzadors-Geoindex/Geoindex-Prospeccions-geotecniques> (accessed on 15 January 2020).
64. Scott, S.W.; Covell, C.; Júlíusson, E.; Valfell, Á.; Newson, J.; Hrafnkelsson, B.; Pálsson, H.; Gudjónsdóttir, M. A Probabilistic Geologic Model of the Krafla Geothermal System Constrained by Gravimetric Data. *Geotherm. Energy* 2019, 7, 29. <https://doi.org/10.1186/s40517-019-0143-6>.
65. Scott, S.; Covell, C.; Juliusson, E.; Valfell, Á.; Newson, J.; Hrafnkelsson, B.; Pálsson, H.; Gudjónsdóttir, M. A Probabilistic Geologic Model of the Krafla Geothermal System Based on Bayesian Inversion of Gravimetric Data. In *Proceedings of the World Geothermal Congress 2020 + 1; Reykjavik, 24-27 October 2021*; p. 13.
66. ICGC Base de Dades Geofísica de Catalunya 2013. <https://www.icgc.cat/Administracio-i-empresa/Serveis/Geofisica-aplicada/Geoindex-Tecniques-geofisiques> (accessed on 15 January 2020).
67. Fullea, J.; Afonso, J.C.; Connolly, J.A.D.; Fernández, M.; García-Castellanos, D.; Zeyen, H. LitMod3D: An Interactive 3-D Software to Model the Thermal, Compositional, Density, Seismological, and Rheological Structure of the Lithosphere and Sublithospheric Upper Mantle: LITMOD3D-3-D Interactive code to model lithosphere. *Geochem. Geophys. Geosystems* 2009, 10, n/a-n/a. <https://doi.org/10.1029/2009GC002391>.
68. Carballo, A.; Fernández, M.; Jiménez-Munt, I. Corte Litosférico al Este de La Península Ibérica y Sus Márgenes. *Modelización de Las Propiedades Físicas Del Manto Superior. Física Tierra* 2011, 23, 131–147. https://doi.org/10.5209/rev_FITE.2011.v23.36915.
69. Agemar, T.; Weber, J.; Schulz, R. Deep Geothermal Energy Production in Germany. *Energies* 2014, 7, 4397–4416. <https://doi.org/10.3390/en7074397>.
70. Oldenburg, C.M.; Rinaldi, A.P. Buoyancy Effects on Upward Brine Displacement Caused by CO₂ Injection. *Transp. Porous Media* 2011, 87, 525–540. <https://doi.org/10.1007/s11242-010-9699-0>.
71. Lukosevicius, V. Thermal Energy Production from Low Temperature Geothermal Brine—Technological Aspects and Energy Efficiency; ONU Geothermal Training Programme; Orkustofnum—National Energy Authority: Grensasvegur, Reykjavik, Iceland, 1993; p. 42.
72. Ayala, C. Basement Characterisation and Cover Deformation of the Linking Zone (NE Spain) from 2.5D and 3D Geological and Geophysical Modelling. In *Proceedings of the 8th EUREGEO, Barcelona, Spain, 15-17 June 2015*; p. 23.
73. Willems, C.J.L.; Nick, H.M. Towards Optimisation of Geothermal Heat Recovery: An Example from the West Netherlands Basin. *Appl. Energy* 2019, 247, 582–593. <https://doi.org/10.1016/j.apenergy.2019.04.083>.
74. Veldkamp, J.G.; Pluymaekers, M.P.D.; van Wees, J.-D. *DoubletCalc 2D (v1.0) Manual*; TNO 2015 R10216; TNO: Utrecht, Netherlands, 2015.

75. Arrizabalaga, I.; De Gregorio, M.; De Santiago, C.; García de la Noceda, C.; Pérez, P.; Urchueguía, J.F. Country Update for the Spanish Geothermal Sector. In Proceedings of the World Geothermal Congress 2020 + 1, Reykjavik, Iceland, 24-27 October 2021.

Capítol 6

6 Discussion and Conclusions

This thesis focusses on the development of methodologies, tools and workflows for geothermal reservoir analysis from a numerical approach. The study is based on two main concepts: (i) the analysis of processes related to induced seismicity associated with fluid injection and (ii) the assessment of the deep geothermal potential.

To achieve the objectives outlined in **chapter 1** several numerical modelling tools were used, including codes already available as CFRAC (**chapters 2, 3 and 4**), existing codes that have been modified in this PhD thesis such as TF3D (**chapter 2**) and new software that has been developed within this project, such as 3DHIP-Calculator (**chapter 5**).

In terms of induced seismicity due to fluid injection, the thesis **chapter 2** explores how the fracture orientation affects the slip regimes and the transition between seismic and aseismic slip using the dynamic friction coefficient as the rate-and-state law. The results reveal a range of slip regimes, from those in which there is abrupt sliding with low pressurized patches to those in which there is aseismic slide with low velocities to accommodate the fluid pressurization.

The different slip regimes can be correlated with the fracture or fault orientations with respect to the stress state, allowing the evaluation of the system seismic response in advance. In EGS it is possible to evaluate those slip regimes, as well as the capacity to be stimulated or to slide abruptly in a seismic response, by constraining the stress state and the main fault structure orientation. This evaluation is a crucial step for the development of this type of geothermal project. The slip regimes have been evaluated using both continuous (TF3D) and discontinuous (CFRAC) models. The continuum 3D modelling approach (TF3D), which has been modified to include a dynamic rate-and-state friction law, tends to attenuate the friction hardening and weakening, introducing higher background oscillations. The pseudo 3D discrete fracture network (CFRAC) tends to accommodate the friction changes in single abrupt episodes. Although both codes reproduce the different sliding regimes, the adaptive time step in TF3D is not able to drastically reduce the time step to accurately simulate the production/nucleation events and sliding details compared to CFRAC. A future improvement of the capacity of TF3D to nucleate events will be the implementation of a fine adaptive time step, able to significantly reduce the time step as a function of parameters related to seismicity.

Once the foundations of the slip regimes have been laid a step forward was taken to analyze different processes related to induced seismicity in deep geothermal reservoirs, in this case, using CFRAC as a modelling tool (**chapter 3**). Simple fracture configurations were used to investigate the fluid pressure

drops associated with hydraulic stimulations observed in the Rittershoffen geothermal reservoir (an EGS located in NE France). The results suggest that two fracture sets can influence pressure drops: one system can be stimulated by shear (that will produce seismic events) while the other one can be stimulated by opening-mode (aseismic) fracturing. The tendency of stimulation by shear- or opening-mode fracturing is determined by the operational parameters (*i.e.*, injection pressure, flow rate, etc.) and the stress state. This tensile fracture set may be part of the pre-existing fracture network or, alternatively, be developed as a hydrofracture during the stimulation phase. In the simulations, a pressure drop can be triggered by a seismic event in a shear-stimulated fracture that is hydraulically connected to a tensile or opening-mode fracture. Nevertheless, once wing cracks are created, it is possible that slip along the natural fracture causes a significant aperture change on the splay fracture that can result in a pressure drop. The pressure drop is not produced by the new volume created by dilatancy, but by the opening of the conjugated tensile fracture instead.

The simulation results are coherent with the mixed stimulation theory, which considers that pre-existing fractures and hydraulic fracturing generation interact to increase the reservoir permeability. In this work the models use simplified geometries and intend to investigate and understand physical processes rather than providing a perfect representation of a specific real system. We chose not to use a model with complex multifracture networks in order to isolate the main processes controlling pressure drops and seismicity. With a more complex network, the superposition of effects could attenuate the phenomena. However, modelling more complex systems could provide a better description of what is happening in a multifracture network and expand the results exposed here.

The interaction between different sliding regimes and the results obtained to explain the fluid pressure drops in EGS were used to focus on seismic cycles in non-planar faults and faults or fractures with segments with different orientations (**chapters 4**). Although this part of the thesis is less specifically related to geothermal reservoirs, the seismic events triggered by fluid injection can be evaluated as those that take place during the management of enhanced geothermal systems, hydrocarbon reservoirs or storage sites for geo-energy applications. The results reveal the importance of considering the fault or fracture macro-roughness both for fluid pressurization and seismic production. Also, the directional changes, step-overs, releasing/restraining bends, branching, or splay fractures (in real cases) play an important role in the seismic cycle and with the interaction between seismic events and slow slip events. Slow slip events, which can dissipate the energy even sliding at low velocities, can act as earthquake precursors or amplify the seismic ruptures preferentially to aseismic patches. Another aspect resulting from this part of the thesis for rough fractures or faults is the dynamic seismicity evolution and how it should be taken into account. The seismic behaviour is different at the beginning of the pressurization process than once it is pressurized, and therefore past events are useful for the prediction of the future behaviour of the system.

To complete the analysis of the geothermal reservoirs and focusing on the second objective (deep geothermal potential assessment) the geothermal reservoirs were analyzed as an energy deposit, independently of whether the reservoir is hydrothermal or petrothermal. For this reason, the thesis (**chapter 5**) addresses one of the key tasks during the early evaluation stages of deep geothermal plays: the assessment of the base resource in terms of the energy stored in the reservoir. This quantification is an essential step to estimate the energy that can be produced from the geothermal reservoir for power generation or direct uses (district heating, greenhouses, etc.), and is key for carrying out preliminary evaluations of the project feasibility based on the required investment and the exploitation cost of the geothermal resource. However, there are uncertainties in the geological knowledge that must be considered when carrying out these preliminary assessments during the early stages of exploration of the geothermal resource. A new tool called 3DHIP-Calculator was developed and freely distributed to increase the capacity to perform deep geothermal potential estimations, following these boundary conditions and taking into account that a) the reference tools for deep geothermal potential evaluation currently use GIS (Geographic Information System) coupled with 3D subsurface models, and b) these evaluations must be done in probabilistic terms to include uncertainty.

The software package 3DHIP-Calculator has been developed within this PhD project to meet the need to have a standard and freely available tool for the whole geothermal community with which the users can estimate the volumetric “Heat-In-Place” method, which was implemented by the United States Geological Survey (USGS) (reference method used in geothermal energy studies), coupled with Monte Carlo simulations. In this regard, 3DHIP-Calculator allows carrying out estimations of the geothermal potential at the same time, either considering a homogeneous distribution of parameters in the whole reservoir (i.e., lumped parameter models) or including spatial variability of petrophysical properties through the considered reservoir (e.g., density and porosity). Moreover, 3DHIP-Calculator is not regionally constrained and can be used to carry out geothermal potential assessment exercises independently from where their data is. The Reus-Valls Basin (RVB, NE of the Iberian Peninsula, Spain) was used for testing 3DHIP-Calculator to perform geothermal potential evaluations of this promising basin in terms of deep geothermal potential. Although the current data of the RVB is limited, and that means it has uncertainty, this chapter presents an evaluation of the geothermal potential for the Triassic unit and the heat percentage of the Reus city that could be covered with a geothermal well in that unit.

The 3DHIP output data is organized in a way that it can be easily managed in Geographic Information System software to develop maps or to be uploaded in specialized 3D visualization software. The current version of the software, presented in this work, is not designed to calculate the hydraulic performance of a doublet or to directly calculate the heat flow, temperature, and therefore the potential energy recovered from them. These parameters need to be evaluated during post-processing based on the output data.

However, the available source code allows include new steps or functionalities to obtain better predictions of the recoverable deep geothermal energy.

Geothermal energy presents and represents a key piece in the energy transition that has recently begun. The two aspects analyzed seek to generate knowledge with the aim of bringing deep geothermal energy closer to society and thus encourage its use and the development of projects that take it into account.

Thus, the main conclusions of the thesis are:

- The dynamic friction coefficient rate-and-state law can be used to numerically analyze (through continuous and discontinuous models) dynamic ruptures and the existence of different slip regimes, from aseismic to seismic slip. This transition can be correlated with fault or fracture orientations respect to the stress state. Chapter 2.
- The relation between faults or fractures able to be stimulated by shear (that will produce seismic events) and those able to be stimulated by opening-mode fracturing (and which are thus aseismic) can be used as a plausible explanation for the observed pressure drops at the Rittershoffen geothermal site. Chapter 3.
- Fault geometry and the directional changes region (step-overs, releasing/restraining bents, branching, or splay fractures) plays an important role in the seismic cycle and with the interaction between seismic events and slow slip events. Chapter 4.
- 3DHIP-Calculator is able for the assessment of the deep geothermal potential at the regional scale using the volumetric method based on a stochastic approach and using 3D geological and 3D thermal voxel models as input data. Chapter 5.

Acknowledgments / Agraïments

7 Acknowledgments / Agraïments

La tesi que aquí es presenta, i els projectes paral·lels que s'han anat generant seguint la mateixa metodologia són la demostració del triomf d'una idea: afrontar els reptes conceptuals i socials que ens envolten s'ha de fer a través de la ciència i el coneixement. Aquesta idea, que fa ja uns anys neix i s'aplica dins de l'Àrea de Geofísica i Sismologia a través del Dr. Xavier Goula (ara jubilat) i de l'Àrea Recursos Geològics a través del Sr. Ignasi Herms (futur doctor) de l'Institut Cartogràfic i Geològic de Catalunya (ICGC) ha permès en relativament poc temps crear una base de projectes i de coneixement que impulsen la ciència en el nostre territori. No obstant, per a que aquesta idea arrel·li, cal que aquesta ciència i coneixement es vagi a buscar a través d'un sistema universitari capaç d'afrontar reptes, a vegades, no exclusivament científics. Aquí és on apareix la Unitat de Geotectònica de la Universitat Autònoma de Barcelona representada pel Dr. Albert Griera per nodrir de coneixement aquest projecte i al que també s'hi suma el Dr. Enrique Gómez Rivas. Un projecte que busca aportar coneixement per al desenvolupament de reservoris geotèrmics.

Així, el primer gran agraïment és per aquestes persones, i que ja, a part de mentors, professors, directors i tutors són amics. Per creure en aquesta idea, per fer-la realitat a través d'un doctorat industrial i per deixar-me ser-hi partícip.

Després d'aquesta petita introducció, em permetreu que faci una mica de retrospectiva per retrocedir en el temps fins a l'inici de l'etapa universitària i agrair aquí m'ha acompanyat per aquest trajecte. Per que encara que una de les coses que la universitat t'ensenya, és, que sempre s'ha de continuar aprenent, aquesta tesi si que representa un punt i a part en la vida universitària. L'inici de la vida universitària, comença en el meu cas, lluny de casa, lluny de la Val d'Aran, a Barcelona. Aquest fet es possible, gràcies a l'esforç de la meva família, els meus pares i avis que em brinden la oportunitat de poder estudiar i de fer-ho allà on volia. Així, el segon gran agraïment i més profund és sens dubte per la meva família, Mama, Papa, Quim, Padrí, Padrina, Abuelo i Abuela que m'obren la porta a un món increïble que es diu universitat i coneixement (encara que com més aprens, més petit ets sents en aquest món). Aquesta etapa universitària, també representa l'inici d'una relació que s'ha anat forjant a base d'exàmens i treballs, d'esperes, sacrificis, viatges, alegries i canvis i que avui representa el lligam més fort que tinc, aquella constant de les grans equacions que per a mi representes tu Pati i sense la qual, no seria on soc, ni de bon tros. Així, el meu agraïment constant, passat, present i futur és per tu.

La etapa universitària comença plena de sorpreses i reptes, com quan entres en un bosc al que mai has estat, però aviat aprens a gaudir d'aquests reptes i aprendre a superar-los hàbilment. Aquí, juguen un paper fonamental tots aquells professors i professores, que dia rere dia van dedicar temps a l'ensenyament. Entre ells, el Dr. Albert Soler a qui a part del seu coneixement, també he d'agrair els

seus consells (tenies raó amb l'Enginyeria Geològica) i la seva amistat, la Dra, Anna Serra, el Dr. Ramon Codina, el Dr. Maarten Saaltink, el Dr. Carlos Ayora i al Dr. Joan Martínez i molts i moltes altres, a qui he d'agrair la seva paciència i dedicació per ensenyar. També a tu Jean, que al llarg del camí per l'Escola de Camins de la UPC i per la Facultat de Geologia de la UB em vas ensenyar que si vols arribar lluny, has de formar equip.

Així, de ràpid o de lent, s'acaba una llicenciatura i es comença amb la vida laboral, en aquest cas, com a becari a l'ICGC on un grup meravellós de persones a la Àrea de Sismologia m'ensenyen a treballar i a veure els terratrèmols de manera diferent. L'efecte del cas Castor sacseja encara l'àmbit sismològic i a través de la idea exposada al principi s'inicien dos projectes per aportar-hi coneixement a través de treballs de final de màster, una mes vesada a l'àmbit sismològic a través de la Dra Tànit Frontera i en Lluís Saló (aviat doctor al MIT) i l'altra per analitzar la sismicitat induïda a través de modelitzacions numèriques a través del Dr. Albert Griera, Dr. Enrique Gómez Rivas, Sr. Ignasi Herms, Dr. Xavier Goula i jo mateix. Agrair tot el suport a aquestes persones per continuar ensenyant-me a aprendre i per confiar en mi per iniciar un projecte com aquest.

Aquesta línia no s'atura i fructifica en un doctorat industrial entre la Universitat Autònoma de Barcelona i l'ICGC. Quin univers el doctorat, la teva feina és investigar i anar plasmant el que veus en documents, és fàcil de dir però molt difícil de fer. Per això, l'ambient de treball i companyerisme al Departament de Geologia de la UAB a través dels seus professors i professores Dr. David Gómez, Dra. Maria Luisa Arboleya, Dr. Toni Teixell i dels seus doctorands i doctorandes, especialment la ja Dra. Laura Burrel i molt aviat Dr. Xavier Coll, Marc Guardia, Norbert Caldera, Gerard Casado ha sigut fenomenal des del primer dia fins a l'últim, que espero que trigui en arribar. El temps i les vivències, ens han fet passar de companys a amics.

Aquest ambient també l'he trobat a la Unitat d'Hidrogeologia i Geotèrmia de l'ICGC, gràcies Montse i Georgina per ajudar-me al llarg del doctorat i per fer-me l'estada a l'ICGC tan agradable i enriquidora. Moltes gràcies Ignasi per tot el suport, ajuda i pro activitat que demostres cada dia i amb tots els projectes en els que estàs involucrat. Cal seguir empenyent la geotèrmia i vosaltres sou un exemple de com fer-ho a tots els nivells, local, regional i europeu, com el projecte HotLime al que us dono les gràcies per deixar-m'hi participar dins el doctorat.

El doctorat, m'ha permès viatjar i conèixer nous entorns i persones, I am especially thankful with Dr. Quan Gan from his support during the Aberdeen stay and with his lessons about Tough-Flac code. Also, with Mark McClure and Jack Norbeck for share and teach about CFRAC, for their idea of collaboration. All of them are an example of science is collaboration and share. Thank you so much.

Thank you Martina for your lessons about faith, and your conversations under the leaking roof.

Com he comentat, aquesta tesi no hauria sigut possible sense els meus directors Albert i Enrique, que sempre han estat allí quan els necessitava, amb la porta oberta, independentment de l'hora i el mitjà de comunicació, per respondre les meves preguntes i per revisar documents. Sou un exemple de dedicació a la causa de l'ensenyament i la investigació. Gràcies per permetre'm seguir amb el doctorat des de la distancia. I, encara que la bateria sigui a punt d'esgotar-se, sempre trobeu energia per tornar-la a carregar i seguir avançant. De veritat mil gràcies, aquí em teniu i em tindreu, pel que faci falta.